University of California

Los Angeles

Constraining the Intergalactic Magnetic Field Through its Imprint on Gamma Ray Data from Distant Sources.

A dissertation submitted in partial satisfaction

of the requirements for the degree

Doctor of Philosophy in Physics

by

Timothy Christian Arlen

2013

© Copyright by
Timothy Christian Arlen
2013

Abstract of the Dissertation

Constraining the Intergalactic Magnetic Field Through its Imprint on Gamma Ray Data from Distant Sources.

by

Timothy Christian Arlen

Doctor of Philosophy in Physics

University of California, Los Angeles, 2013

Professor Vladimir V. Vassiliev, Chair

Gamma ray photons, with energies $\geq$ TeV propagating cosmological distances will be attenuated by pair production with diffuse extragalactic background photon fields-both the cosmic microwave background (CMB) radiation and the UV – far-IR extragalactic background light (EBL). The produced electron/positron pairs will subsequently inverse Compton scatter background photons up to GeV–TeV energies, and some of these upscattered photons may also initiate pair production in the formation of an electromagnetic cascade. If an intergalactic magnetic field (IGMF) exists on cosmological length scales of relevance to the cascade, it will deflect the electrons and positrons and will leave an imprint on the resulting spectral, angular, and temporal properties of the cascade radiation. The primary goal of this study was to constrain the properties of the IGMF using data from known sources of TeV gamma-rays.

This thesis describes the construction of a high precision, 3-dimensional, particle-tracking Monte Carlo simulation code to model the intergalactic electromagnetic cascade, and uses it to systematically explore the effects of the IGMF on

the cascades in multiple observational domains. We then compare the simulations with gamma-ray data from current generation ground-based gamma-ray instruments such as VERITAS, HESS, and MAGIC, sensitive to TeV-scale energies, as well as the *Fermi* satellite, sensitive to the GeV-scale.

This novel technique of constraining the IGMF has rapidly emerged over the last decade as gamma-ray instruments have become more sensitive and as theoretical understanding of the cascade process has progressed. This emerging field has proven to be richly complex and we find that the data from current generation gamma-ray instruments do not allow for an unambiguous upper or lower limit to be placed on the IGMF at present. We do find it likely that the next generation ground based gamma-ray observatory, the Cherenkov Telescope Array (CTA) will be able to detect unambiguous signatures of gamma-ray cascading if the IGMF magnitude is within a certain range, and thus provide a robust constraint on IGMF properties.

The dissertation of Timothy Christian Arlen is approved.

Robert L. McPherron

Zvi Bern

Matthew A. Malkan

Vladimir V. Vassiliev, Committee Chair

University of California, Los Angeles

2013

To my wife Lucy,

my parents,

brother, and sisters.

Table of Contents

List of Figures

List of Tables

Acknowledgments

There are many people I wish to thank who have positively influenced me and helped me throughout my graduate career. Above all, special thanks to my advisor, Prof. Vladimir V. Vassiliev whose patience, intellectual stimulation, and rigorous guidance has helped shape this thesis into its present form. His scientific and personal influence will remain with me, long after I leave UCLA. I'd also like to thank Prof. Rene Ong for his advice and encouragement regarding my present and future work. Special thanks also goes to my friend and colleague, Matthew Wood, for his unending patience, especially regarding my many computing questions and VERITAS analysis questions. I'd like to thank everyone in the UCLA VERITAS group for their support and kindness, particularly those who have tangibly contributed to this project: Stephen Fegan and Yusef Shafi.

I wish to thank the funding agency that has supported this work, the National Science Foundation under grant award number 0969948, and acknowledge that the many simulations in my thesis were performed on the UCLA hoffman2 cluster.

I'd also like to thank my collaborators at the University of Chicago, particularly Tom Weisgarber for closely working together with me to ensure the accuracy of our simulations, and also to Prof. Scott Wakely and Hao Huan.

Additional thanks is in order to the rest of my colleagues in the VERITAS collaboration, who have all contributed in some ways to the data used in this thesis, and additionally to those who have contributed to enjoyable times spent on site taking data and running the instrument for a few weeks out of the year.

I wish to thank the rest of the UCLA Astronomy department for welcoming me into their fold, and for their contribution to an enjoyable work environment- not least of which includes our wonderful intramural teams, the Supernovas and

Blue Stragglers.

A very special thank you is in order to my parents, who were my first educators-tirelessly homeschooling me and my siblings from the very beginning through middle school. In particular, special thanks to my Dad, my first science teacher, for helping to cultivate a curiosity and wonder about the natural world that remains to this day. I also thank my brother-my roomate for two years at UCLA, and my four sisters. Finally, I'd like to thank my wife Lucy, whose love, patience, and support throughout the ups and downs of graduate student life and thesis writing has brought me much joy and satisfaction.

Vita

2006 B.S. (Physics, minor in Mathematics)
California Polytechnic University, San Luis Obispo, CA

Publications

Arlen, T. C., Vassiliev, V. V., Weisgarber, T., Wakely, S. P., and Shafi, S. Y., "Intergalactic Magnetic Fields and Gamma Ray Observations of Extreme TeV Blazars", 2013, *The Astrophysical Journal*. Submitted.

Huan, H., Weisgarber, T., **Arlen, T. C.**, and Wakely, S. P., "A New Model for Gamma-Ray Cascades in Extragalactic Magnetic Fields.", 2011, *Astrophysical Journal Letters*, 735, L28.

List of Abbreviations

ACD	Anti-coincidence detector
BBN	Big bang nucleosynthesis
CMB	Cosmic microwave background radiation
CTA	Cherenkov Telescope Array
DAQ	Data acquisition system
DEC	Declination (-90 deg to 90 deg), sim. to longitude
dFED	Differential flux energy density (energy time^{-1} area^{-1})
EBL	(UV – far-IR) Extragalactic background light
EDF	Event data file
eV	Electron volts
FOV	Field of view
FRW	Friedmann-Robertson-Walker
FSRQ	Flat spectrum radio quasar
FWHM	Full width at half maximum
GeV	Giga electron volts. 1 GeV = 10^9 eV
GRB	Gamma-ray burst
HE	High energy, 100 MeV $\lesssim$ E $\lesssim$ 100 GeV
$H0$	"$B_{IGMF} = 0$ hypothesis"
IACT	Imaging atmospheric telescope
IC	Inverse Compton
IGM	Intergalactic medium
IGMF	Intergalactic magnetic field
IR	Infrared
IRF	Instrument response function
kpc	Kiloparsec

LAT	Large area telescope (aboard the *Fermi* satellite
MeV	Mega electron volts
MHD	Magnetohydrodynamics
MJD	Modified Julian day
Mpc	Megaparsec
OS	Optical System
PMT	Photomultiplier tube
PSF	Point spread function
QCD	Quantum chromodynamics
QED	Quantum electrodynamics
RA	Right ascension (0 to 24 hr), sim. to latitude
R_{68}	68 % containment radius
SDF	Spacecraft data file
SED	Spectral energy density
TeV	Tera electron volts. 1 TeV = 10^{12} eV
UV	Ultraviolet
VHE	Very high energy. E $\gtrsim$ 100 GeV

CHAPTER 1

Intergalactic Magnetic Fields

Magnetic fields are pervasive in nature. With few exceptions, typical astronomical objects observed have a magnetic field associated with it-planets, stars, pulsars, galaxies, galaxy clusters, AGN jets, etc. Where did these fields from? What is their history in the formation and evolution of these objects, and what is the origin of magnetic fields in gas and plasma from which these objects were formed in the universe? This chapter provides an introduction to the observational evidence of magnetic fields in galaxies and clusters and it highlights theoretical arguments for the presumed existence of intergalactic magnetic fields (IGMFs). Briefly, in order to explain the microgauss-level magnetic fields which are observed in nearly all galaxies and some galaxy clusters, it is necessary that a significantly weaker but non-zero magnetic field must have been present at the epoch of galaxy formation. These primordial fields have undergone a much simpler evolution in the cosmological volumes outside of the galaxies and galaxy clusters, and they might be detectable today in the Cosmic Voids where these fields should have survived at some level to the present day. Several plausible theoretical models speculate that primordial magnetic fields might have been generated at various epochs during cosmological history. These fields may have seeded magnetic fields in the galaxies observed today, and they may have affected other processes in the early universe. Therefore, detecting these large-scale (of order Mpc or larger) intergalactic magnetic fields in cosmological voids-outside of galaxies and galaxy

clusters-provides insights into the astrophysics of galaxy magnetic field generation and their role in cosmology. Furthermore, the detection of intergalactic magnetic fields would have implications for the propagation of Ultra High Energy Cosmic Rays ($E \gtrsim 10^{18}$ eV) from extragalactic sources.

This chapter is structured as follows: the first section provides an overview of the current status of observations of galaxy and galaxy cluster scale magnetic fields (galactic scale and larger), and associated detection techniques required to make these observations. In section 1.2, we summarize the essential ideas for two major classes of theoretical models which have been put forward to explain the observations of galactic magnetic fields, highlighting the fact that nearly all of these models require a seed magnetic field, present at the epoch of galaxy formation. Section 1.3 presents an overview of some plausible models and constraints of primordial magnetic fields in the early universe, at high redshifts. Finally, section 1.4 introduces the ideas which form the basis of this thesis, speculating about the possibility of a new observational window for the intergalactic magnetic fields at low redshift, through detecting the secondary radiation of electromagnetic cascades initiated by TeV-scale gamma-rays from extragalactic sources.

1.1 Galactic Magnetic Fields: Overview of Observations

Generic observational properties of galactic and extragalactic magnetic fields on scales of order a kpc and higher can be summarized as the following [Wid02, CT02, KZ08, WRS12]

1. In spiral galaxies, including our own Milky Way, magnetic fields with a magnitude of about 1 – 10 μG are observed. These fields include a large scale component whose coherence length is on the order of the size of the

visible disk, and smaller scale tangled fields with an energy density of the same order as the coherent component, of about 3×10^{-14} erg cm^{-3}. The coherent component seems to exhibit patterns of either an axially symmetric or sign-alternating bisymmetric spiral structure (see Fig. 1.2).

2. The magnetic field in the Milky Way is known in greater detail. In addition to exhibiting the above features, the energy density of the coherent and turbulent components of the fields appear to be in approximate equipartition with the kinetic energy density of the turbulent gas in the galaxy. Anisotropic fluctuations to the random component might also be present, with more power parallel to the mean field of the galaxy than perpendicular to it.

3. In elliptical galaxies, smaller scale tangled fields are observed, but a mean component on the scale of the galaxy is generally undetectable. This lack of a galactic scale magnetic field is a major difference between elliptical and spiral galaxies.

4. There is a robust measurement of μG-level magnetic field in one galaxy at redshift $z \approx 0.4$ [KPZ92]. Separate Faraday Rotation studies have found evidence of μG-level magnetic fields in samples of galaxies with redshift around $z \approx 1.3$ [BML08]. Detection was not possible due to our incomplete knowledge of the magnetic field of our own galaxy.

5. In most galaxy clusters, the estimates of the magnetic fields range from about 0.1 μG to $\sim$ 10 μG. The spatial extent of these fields is generally of order Mpc, and the coherence length is comparable to the spatial extent of the member galaxies in the clusters. Although several theoretical models have been put forward to explain the magnetic fields in the clusters as a

leakage of galactic magnetic fields, the origin of these fields is not definitively settled [CT02].

Knowledge of galactic and extragalactic magnetic fields relies on four primary observational methods [Kro94, Wid02, KZ08]. Zeeman splitting and Faraday rotation measures the average magnetic field component integrated along the line of sight, so that regions of opposite magnetic field tend to cancel each other. Measurements from polarized synchrotron radiation and polarized starlight emission absorption by magnetically aligned dust grains yield the line of sight integrated magnetic field component in the plane of the sky, in which case, regions of oppositely directed magnetic field contribute to an amplification of the signal. Each of these four techniques is briefly described below.

1.1.1 Zeeman Splitting

In principle, Zeeman splitting provides the most direct way to measure an extraterrestrial magnetic field. Indeed, the first measurement of a magnetic field external to the Earth was the discovery of the Zeeman effect in sunspots of a Gauss-level magnetic field in 1908 by George Hale [Wid02]. The physical mechanism for the Zeeman effect is the fact that a magnetic field breaks the degeneracy in the electronic energy levels of an atom or molecule. The energy difference between neighboring levels of

$$\Delta E = g\mu B = 6 \times 10^{-9} g \left(\frac{B}{1\mathrm{G}} \right) \mathrm{eV},$$

where g is the Landé factor of order 1 and μ is the Bohr magneton. For the galactic and extragalactic magnetic fields of less than 10 μG Zeeman splitting is a very small perturbation on the fine or hyperfine structure of atomic or molecular

levels ($\sim 10^{-5}$ eV), known as the weak Zeeman splitting regime. In this regime, there are $2j + 1$ energy states for the Hamiltonian interaction term of $\mu\vec{B} \cdot (\vec{J} + \vec{S})$. Typically, low frequency (radio) singlet transitions between fine or hyperfine structure levels are used to detect Zeeman splitting, in which case the ν_{mn} line is split in triplet

$$\nu = \nu_{mn} \pm \frac{eB}{(4\pi mc)}\text{Hz},$$

where ν_{mn} is a singlet transition and B is measured in Gauss. The weak Zeeman effect is very difficult to observe, because the relative line shift associated with this spilitting is of order

$$\frac{\Delta\nu}{\nu} \approx 1.4g \left(\frac{B}{\mu\text{G}}\right) \left(\frac{\text{Hz}}{\nu}\right).$$

The two most common spectral lines in Zeeman effect observations are the 21 cm hyperfine structure line from neutral hydrogen, and the 18 cm molecular line seen in OH clouds, each of which give a relative line shift of only

$$\frac{\Delta\nu}{\nu} \approx 10^{-9} g \left(\frac{B}{\mu\text{G}}\right).$$

Comparing this to the broadening due to Doppler shifting of the gas, $\Delta\nu/\nu \approx 10^{-6}(T/100\text{ K})^{1/2}$, where T is the mean temperature of the atoms, and it is clear that Zeeman splitting is actually a broadening of the already Doppler shifted line. This makes it difficult to observe except in low temperature, relatively high magnetic field systems. Radio observations of the Zeeman effect have provided excellent measurements of the magnetic field in our own galaxy, but so far there are no robust detections of Zeeman splitting in other galaxies.

1.1.2 Faraday Rotation

Faraday rotation is a phenomenon that occurs when electromagnetic waves propagate through an electron plasma in the presence of a magnetic field. The left and right circular polarization states propagate with different phase velocities, along the direction of the magnetic field, which for linearly polarized light of wavelength λ, results in a rotation of the electric field vector over a path length L,

$$\Delta\varphi = (\mathrm{RM})\,\lambda^2,$$

$$\mathrm{RM} = \frac{e^3}{2\pi m_e^2 c^4}\int_0^L n_e(l)B_\parallel(l)dl \approx 81\frac{\mathrm{mrad}}{\mathrm{cm}^2}\int_0^L \left(\frac{n_e}{\mathrm{cm}^{-3}}\right)\left(\frac{B_\parallel}{\mu\mathrm{G}}\right)\left(\frac{dl}{\mathrm{kpc}}\right),$$

where n_e is the local density of non-relativistic electrons, $B_\parallel$ is the line of sight component of the magnetic field, and L is the total path length of the electromagnetic wave. In general, to estimate the magnetic field strength, one must obtain an independent measurement of the electron density along the line of sight, which is rarely available. For our galaxy, this can be reasonably well-established, but for astrophysical systems outside our own galaxy, this information is difficult to obtain. In addition, uncertainties in the RM integral of our own galaxy represent an irreducible foreground error in measurements of weak extragalactic (outside of the milky way) magnetic fields. This effectively sets a lower bound on the extragalactic magnetic field strength that one could probe using this method ($B_{min} \gtrsim 0.1\mu\mathrm{G}$).

1.1.3 Synchrotron Emission

Synchrotron radiation is produced by relativistic particles in their accelerated motion on helical trajectories along magnetic field lines. From the frame of reference at the gyrocenter of the motion, the radiation appears to be beamed within

a cone of opening angle γ^{-1}, whereas an observer will receive pulses separated in time by $\tau = 2\pi/\omega_B$, with pulse width of $\gamma^{-3}\tau$, where $\omega_B = |q|B/(\gamma mc)$ is the relativistic Larmor frequency. The spectrum of received emission is peaked around the characteristic frequency, which for electrons is

$$\nu_c = \frac{3\gamma^2|e|B_\perp}{4\pi m_e c} \approx 0.3 \left(\frac{\gamma}{10^4}\right)^2 \left(\frac{B_\perp}{\mu\mathrm{G}}\right) \mathrm{GHz},$$

where $B_\perp$ is the magnetic field strength, m_e and e are the electron mass and charge. The angle-averaged value of the received power per particle for an isotropic distribution of electrons with energy $\gamma m_e c^2$ is given by

$$\frac{dE}{dt} = \frac{4}{3}\beta^2\gamma^2 c\sigma_T U_B \approx 10^{-19} \left(\frac{\gamma}{10^4}\right)^2 \left(\frac{B}{\mu\mathrm{G}}\right)^2 \mathrm{erg\ s^{-1}},$$

where $\beta = v/c$, U_B is the energy density of the magnetic field, and σ_T is the Thomson cross-section.

For a population of electrons, the total synchrotron emission depends both on the number density of electrons, as well as the strength of the local magnetic field, projected onto a direction in the plane of the sky. Detailed modeling of synchrotron radiation is complex (see e.g. [Shu91]), and only the generic features are outlined here. For a power law distribution of electrons (valid over some energy range)

$$n_e(E)dE = n_{e0} \left(\frac{E}{E_0}\right)^{-\gamma} dE,$$

the synchrotron emissivity, defined as the amount of power radiated per volume of the electron distribution is proportional to

$$j_\nu \propto n_{e0}\nu^{(1-\gamma)/2} B_\perp^{(1+\gamma)/2}.$$

Thus, the synchrotron emission spectrum can be related to the number (or energy) density of the relativistic electrons and the strength of the magnetic field. In astrophysical environments, these two quantities are generally not known separately, and an additional assumption such as the equipartition of energy is frequently used to estimate the magnetic field strength, purely based on the detection of synchrotron radiation. Since synchrotron radiation occurs where interactions between cosmic rays, shock fronts, and magnetic fields are redistributing energy, the equipartition of energy condition is often violated, sometimes very strongly, although arguments can be made that in all but the most extreme conditions, it is not violated to greater than a factor of 10 in either direction [Wid02]. Within our own galaxy, this equipartition of energy condition can be tested, and indeed, observations are in excellent agreement with its predictions.

1.1.4 Polarization of Optical Starlight

Due to the presence of dust and its interaction with magnetic fields in astrophysical systems, it is possible to extract magnetic field information from the polarized light from stars in our own galaxy and in nearby galaxies. If a magnetic field permeates interstellar space where populations of dust exist, elongated dust grains would have a preferred direction in space, so that one of the short axes would coincide with the magnetic field direction. Although the precise mechanism by which dust grains are oriented in a magnetic field is not well understood [Wid02], it is known that these dust grains in turn, preferentially absorb light polarized along its long axis, prependicular to the magnetic field. This results in a polarization of the transmitted radiation along the direction parallel to the magnetic field line. Some galaxies, including our own, have been observed to exhibit a spiral pattern of optical polarization, showing evidence for a spiral, coherent μG-level

magnetic field, within the disk. Unfortunately, this method has limited value as a probe of extragalactic magnetic fields for three reasons. 1) There is at least one other effect which can lead to the polarization of starlight, and that is anisotropic scattering in the interstellar medium. 2) The starlight polarization effect is necessarily self-obscuring, because it depends on extinction of some of the radiation. For example, a 10 % polarization effect must go hand in hand with a reduction in the luminosity of radiation by a factor of 20. 3) The precise mechanism of dust grain orientation in a magnetic field is not well-understood and therefore quantifying this effect makes a number of assumptions. Despite these drawbacks, however, it remains a good diagnostic to study magnetic fields in our own galaxy.

1.2 Galactic Magnetic Fields: Generation and Evolution Models

A wealth of observations of galactic scale magnetic fields combined with energy equipartition observed in the Milky Way and nearby galaxies suggests that galactic magnetic fields might have played an important role in galaxy formation and evolution. In fact, the modeling of galactic magnetic fields provides one of the primary theoretical motivations to undertake the search for IGMFs. At present, it is believed that these fields must have existed at some level to provide seed fields for galactic magnetic field formation. In order to gain an understanding of the origin and persistence of $\sim$ 10 kpc-scale galactic magnetic fields, and thus to understand this argument, it is first necessary to outline the relevant concepts in magnetohydrodynamics (MHD) and plasma physics.

1.2.1 Magnetohydrodynamics and Plasma Physics Background Relevant to Galactic Magnetic Field Generation

Relevant MHD Equations for Galactic Magnetic Field Evolution

The equations of Magnetohydrodynamics (MHD) describe the interactions between electromagnetic fields and the motion of charged fluids[1]. In general, the plasma will be composed of multiple particle species (in our case, electrons and ions-the ions being protons, unless stated otherwise). Using the Boltzmann equation, one derives the hydrodynamic approximation of the equation of motion for each particle species. For example, for electrons

$$m_e n \left[\partial_t \mathbf{v}_e + (\mathbf{v}_e \cdot \nabla)\mathbf{v}_e\right] = -en(\mathbf{E} + \mathbf{v}_e \times \mathbf{B}) - \nabla P - n(n+\delta n)\frac{e^2}{\sigma}\left(\mathbf{v}_e - \mathbf{v}\right), \quad (1.1)$$

where n, m_e, e, $\mathbf{v}_e$ are the electron number density, mass, electric charge, and average velocity of the electron fluid. $\mathbf{E}$ and $\mathbf{B}$ are the electric and magnetic field respectively, and P is the pressure of the plasma. The bulk velocity of the proton fluid is denoted by $\mathbf{v}$, and its density is $n + \delta n$; for the case of no charge separation, $\delta n = 0$. σ is the electrical conductivity, and the term which includes it describes the exchange of momentum due to collisions between these two fluids. A similar equation can be written for the proton fluid. Since the electron mass is much smaller than the proton mass, one can separate the timescales of various processes in the plasma. One "slow" timescale is associated with the bulk flow of the plasma, and the "fast" timescale is associated with the electrons adjusting to the slowly changing densities and velocities driven by this plasma flow. This corresponds to neglecting the inertia of the electrons, $m_e = 0$ resulting in the

[1]Much of this material was adapted from [Kul05] and [Bit04].

following equation:

$$0 = \mathbf{E} + \mathbf{v}_e \times \mathbf{B} + \frac{\nabla P}{en} + \frac{en}{\sigma}(\mathbf{v}_e - \mathbf{v}). \tag{1.2}$$

where we assumed no charge separation, $\delta n = 0$. It is now convenient to introduce the current density vector, $\mathbf{J} = -en(\mathbf{v}_e - \mathbf{v})$, and rewrite this equation in the following form

$$\mathbf{J} - \frac{\sigma}{en}\mathbf{B} \times \mathbf{J} = \sigma \mathbf{F}, \tag{1.3}$$

where $\mathbf{F} = \mathbf{E} + \mathbf{v} \times \mathbf{B} + \nabla P/(en)$. Equation 1.3 is known as Ohm's Law with the Hall Effect term. The second term on the left is the Hall Effect term, which in application to the evolution of galactic scale magnetic fields can be neglected, $\sigma|\mathbf{B}|/(en) \ll 1$. In principle, this equation can be solved for $\mathbf{J}$, without this approximation, by taking the scalar and vector products of this equation with respect to $\mathbf{B}$. We further neglect the pressure term (which will later be important for understanding Biermann battery effects), and we derive the familiar version of Ohm's Law

$$\mathbf{J} = \sigma \left(\mathbf{E} + \mathbf{v} \times \mathbf{B}\right). \tag{1.4}$$

For cases where the Maxwell current term in Ampere's Law can be neglected, $\mathbf{J} = \nabla \times \mathbf{B}/\mu_0$ (valid for all but the "fastest" processes which may be associated with charge separation), Ohm's law can be combined with Ampere's Law, and taking the curl of both sides gives

$$\frac{\partial \mathbf{B}}{\partial t} = \nabla \times (\mathbf{v} \times \mathbf{B}) + \eta_m \nabla^2 \mathbf{B}, \tag{1.5}$$

where $\eta_m = 1/(\mu_0 \sigma)$ is the magnetic viscosity. This equation describes the evolution of the magnetic field due to two effects. The first term on the right hand

side, referred to as the "flow term", describes the magnetic field evolution due to the plasma flow, and the second term describes the diffusion of the magnetic field. To obtain an order of magnitude estimate of the relative importance of the two terms for galactic magnetic field evolution, we approximate

$$|\nabla \times (\mathbf{v} \times \mathbf{B})| \approx \frac{vB}{L}$$

$$\eta_m \left|\nabla^2 \mathbf{B}\right| \approx \eta_m \frac{B}{L^2}.$$

where L is the characteristic length in the system. The ratio of these two terms, often called the magnetic Reynolds number, R_m is given by

$$R_m = \frac{vL}{\eta_m}.$$

When the flow term dominates, that is when $R_m \gg 1$, to first order the diffusive term, which is due to the resistivity of the plasma, can be neglected and the resulting equation implies that for highly conducting (low resistivity) fluids, the magnetic field lines move along exactly with the fluid, rather than diffusing out away from the plasma. In other words, the field lines are "frozen in" to the conducting fluid. Thus, the fluid can flow freely along field lines, but any motion perpendicular to them carries the field lines with it.

When resistive decay dominates the dynamics, that is when $R_m \ll 1$, the diffusion term defines the magnetic field evolution, with the characteristic decay time of $\tau_D = L^2/\eta_m$, which for the conditions of plasma similar to those existing in our own galaxy gives

$$\tau_D \approx 10^{26} \left(\frac{L}{\mathrm{pc}}\right)^2 \mathrm{yr}.$$

It appears that the characteristic diffusion time is much larger than the Hubble

time, and therefore, the diffusive effects could have played only a sub-dominant role in the evolution of galaxy-size magnetic fields, as was first pointed out by [Fer49]. Since the "flow" or inductance term dominates the magnetic field evolution, it is very difficult to come up with a theory of galactic field origins, because to get any currents started in the first place, a very strong generator is required to balance the huge back EMF produced when the currents rise.

MHD Dynamos

The above zeroth-order treatment of the field generation and decay is known to be an incomplete description however, because it treats the system containing the magnetic field (the galaxy) as quasistatic (changing on slow time scales), whereas it is in fact a fluid and decay of the magnetic field can occur over timescales much faster than the characteristic resistive decay time. However, when a conducting fluid moves across a magnetic field, it produces an electric field of $\mathbf{E} = -\mathbf{v} \times \mathbf{B}/c$. Such a system is referred to as a "magnetic dynamo". The electric field created in it, is necessary to balance the magnetic field against resistive decay and also to balance the inductance. The induced currents can amplify and maintain the original magnetic field. The main problem in dynamo theory is to find a realistic fluid velocity that will properly balance the inductive and resistive effects that occur during field evolution, and maintain the magnetic field for long timescales, usually required for significant field amplification.

To describe the maintenence of the much smaller spatial scale magnetic field of the Earth and Sun, a refined theory for dynamos, the mean field theory (see e.g., [Kul05]) has become widely accepted as describing the generic properties of the observed magnetic field. In the galactic setting, it is more difficult, but it was first shown by two groups independently-by [Par71] in the U.S. and by [VR72] in

Russia-that similar motions exist in the galaxy which could overcome the large inductance and amplify and maintain the magnetic field of the galaxy.

Following [Wid02] and [KZ08], the essential features of the standard galactic dynamo model, known as the $\alpha-\Omega$ dynamo are summarized briefly here, and then more detail is given later in section 1.2.3. Turbulent motions in the Interstellar Medium, driven e.g. by Stellar Winds, Supernova explosions, and hydrodynamic instabilities, carry loops of toroidal magnetic field out of the plane of the disk (see Fig 1.1). These loops are twisted into the poloidal plane by the Coriolis effect, while the toroidal field is regenerated from the poloidal field by differential rotation in the disk. This $\alpha-\Omega$ dynamo operates in any differentially rotating, turbulent fluid.

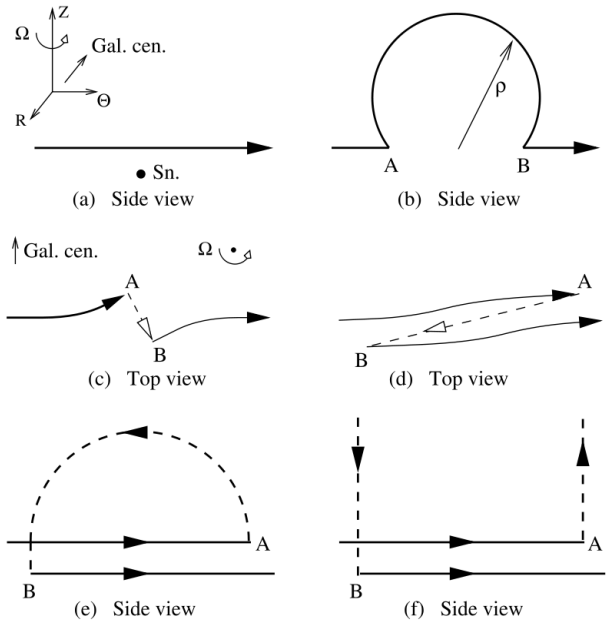

Figure 1.1 (Figure taken from [KZ08]). The operation of the $\alpha-\Omega$ dynamo. In (a) and (b) a supernova (noted as Sn) blows the magnetic loop. It is twisted into the poloidal plane by Coriolis forces as is seen in the top view of (c). The dashed line represents the upper part of the loop. In (d) the lower part of the line is stretched by differential rotation. Then the upper part of the line is removed to infinity as in (e) and (f).

Because a straightforward application of the standard $\alpha - \Omega$ dynamo to the galactic magnetic field problem is more complicated, numerous variations on this standard theme have been proposed. Overall though, the general idea that galactic fields are maintained by differential rotation and small-scale velocity field fluctuations seems to be an essential feature of the galactic magnetic field evolution. Although the dynamo mechanism appears viable, it does not still resolve the primary origin question of 1) whether the galactic field was produced from an initially weak field present or generated somehow during galaxy formation, or 2) whether there was already a strong magnetic field present during the collapse of the protogalactic disk and subsequent formation of the galaxy.

Biermann Battery Mechanism

The Biermann battery process is a mechanism by which a magnetic field can be produced from zero. If the conditions were always such that Eq. 1.5 applied, then a magnetic field could not be started up from zero, due to flux conservation. In other words, the solution $\mathbf{B} = 0$ would always be a solution, for all times. In deriving this equation, we have neglected a term, $\nabla P/(en)$, which when included becomes

$$\frac{\partial \mathbf{B}}{\partial t} = \nabla \times (\mathbf{v} \times \mathbf{B}) + \eta_m \nabla^2 \mathbf{B} + \frac{1}{en^2} \nabla n \times \nabla P. \tag{1.6}$$

In the isothermal plasma with no charge separation, ∇P is always aligned with ∇n, and therefore, the contribution of this term is zero. However, when charge separation effects are not negligible ($\delta n \neq 0$), the misalignment of these gradients is possible, and therefore, this term becomes the source of magnetic field generation, known as the Biermann battery mechanism. One can see that this very same source term is also responsible for the charge separation. To demonstrate

this, we take the divergence of Ohm's Law,

$$\frac{1}{\sigma}\nabla\cdot\mathbf{J}=\nabla\cdot\mathbf{F}=\nabla\cdot\mathbf{E}+\nabla\cdot(\mathbf{v}\times\mathbf{B})+\nabla\cdot\frac{\nabla P}{en}.$$

Utilizing the continuity equation, $\nabla\cdot\mathbf{J}=-e(\partial\delta n/\partial t)$, and Gauss's Law, $\nabla\cdot\mathbf{E}=e\delta n/\varepsilon_0$, we derive the evolution equation for the separation of charges

$$\frac{\varepsilon_0}{\sigma}\frac{\partial}{\partial t}(e\delta n)+e\delta n=\varepsilon_0\left(\frac{1}{\eta_m}\mathbf{v}\cdot\mathbf{E}-\mathbf{B}\cdot(\nabla\times\mathbf{v})-\nabla\cdot\left(\frac{\nabla P}{en}\right)+\frac{1}{\eta_m}\mathbf{v}\cdot\frac{\nabla P}{en}\right).$$

The terms on the right function as the sources of charge separation. For example, in settings with non-zero pressure and density gradients, or non-zero voticity ($\nabla\times\mathbf{v}$), charge separation will arise. In astrophysical environments on small spatial scales, for example, in the propagation of shock waves, temperature gradients may arise, which will lead to misalignment between the pressure gradient and the density gradient, also resulting in the generation of magnetic field from zero.

1.2.2 Galactic Magnetic Fields: Strong Primordial Field Hypothesis

The essential feature of the dynamo mechanism in explaining the observations of galactic magnetic fields is its ability to regenerate large-scale magnetic field continuously, starting from a (possibly much) weaker seed magnetic field. The alternative scenario is that the galactic magnetic fields are relics of strong primordial magnetic fields created in the early universe and which are maintained today by differential rotation and turbulent diffusion, which we explain in this section.

A magnetic field permeating the protogalactic medium will be amplified by adiabatic compression and differential rotation during the formation and rotation of the disk. The generic features of an idealized model for the primordial-strong

field hypothesis are discussed below, in the limit that the dynamo mechanism is not the dominant effect. Consider a differentially rotating disk with angular velocity, $\omega = \omega(r)$, using cylindrical coordinates r, ϕ, z. Initially, there exists a uniform magnetic field (for example, in the $\mathbf{e}_x$ direction) in the plane of the disk of the protogalaxy, so that $\mathbf{B}(\mathbf{x},0) = \mathrm{B}_0\mathbf{e}_x$. When magnetic diffusion is negligible, the time evolution of the field satisfies [Wid02]

$$\mathbf{B}(r,\phi,t) = B_0 \left(\mathbf{b}(r,t) + t\frac{d\omega(r)}{d\ln r}\left[\cos(\omega(r)+\phi t)\right]\mathbf{e}_\phi \right),$$

where $\mathbf{b}(r,t) = \cos[\omega(r)t]\mathbf{e}_x + \sin[\omega(r)t]\mathbf{e}_y$. The field lines before and after differential rotation at a given time slice of the galactic disk are shown in Fig. 1.2.

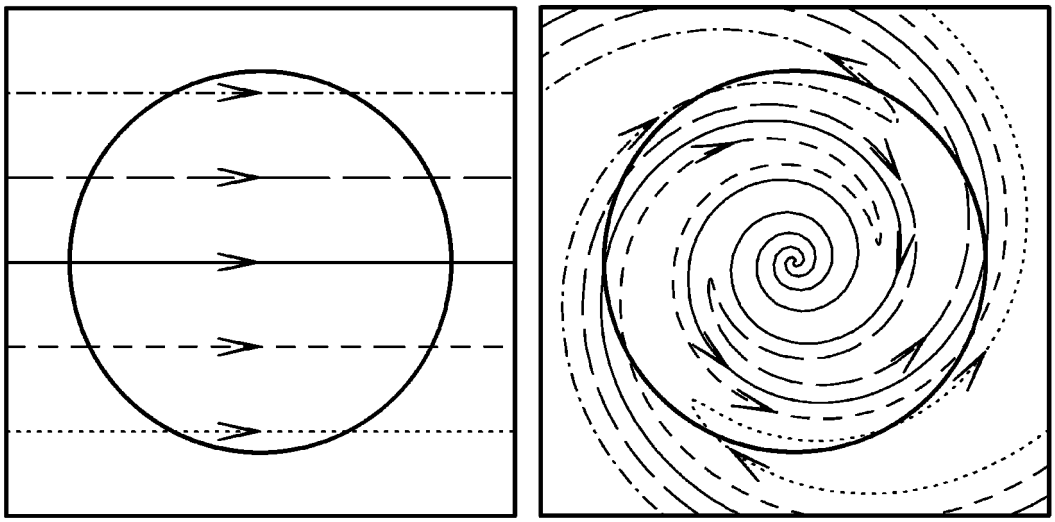

Figure 1.2 (Figure taken from [Wid02]). Distortion of magnetic-field lines under the action of differential rotation. The left panel shows the initial homogeneous magnetic field configuration. The different line types are for visualization purposes. The right panel shows the same field lines after they have been distorted by differential rotation.

A distinguishing prediction of this hypothesis is that differential rotation will mix the field at different radii, so that the final field configuration is bisymmetric.

This hypothesis has been criticized on at least two grounds: 1) that turbulent diffusion (within the protogalaxy) may destroy primordial magnetic fields on short timescales [Par79], and 2) it appears that the bisymmetric field prediction is not observed, but given the current resolution of the magnetic field measurements in galaxies including our own milky way, this cannot be definitively ruled out [HK97].

For this model of the galactic magnetic field to work, one needs to start with strong primordial fields, since no dynamo amplification occurs during the galaxy evolution. One possibility is that a field is generated at moderate redshift (z $\sim$ 5) by turbulence which occurs during structure formation in the protogalaxy. Another possibility is that perhaps there is a two stage process for the formation of most galaxies today, in that the first stage occured with little or zero magnetic field, but widespread starburst galaxy activity and radio jet quasar activity seeded a large percentage of the IGM with μG-level magnetic field. Subsequent generations of galaxies then perhaps formed in this environment. If this is true, then the IGMF in voids could be as high as around a 10s of nG. This scenario is discussed by a number of authors [RS68, DL90, FL01], but so far, the details of the filling of the universe with magnetic flux have not yet been worked out with enough precision to assess its plausibility.

1.2.3 Galactic Magnetic Fields: Weak Primordial Seed Field Hypothesis

An alternative hypothesis to strong primordial fields can be developed by invoking the Dynamo amplification mechanism, in which case a much weaker seed magnetic field would be required to explain its significantly amplified present day value. To apply dynamo theory to the galactic case, a systematic treatment of

turbulent amplification of magnetic fields is required. Specifically, a mean-field approximation is employed to describe the effects of turbulence, which is called the "Mean Field Dynamo Theory". Here we illustrate a very simplified model, with a number of assumptions that in many cases is impossible to verify experimentally. Turbulent patches of the disk are quantified by the kinetic helicity, $\mathbf{v} \cdot \nabla \times \mathbf{v}$, and its effect on the magnetic field is quantified by the α term, where α is defined as

$$\alpha = -\frac{\tau}{3}\langle \mathbf{v} \cdot \nabla \times \mathbf{v} \rangle.$$

The brackets denote turbulent ensemble averages, τ is the decorrelation time of turbulent motion, and isotropic turbulence is assumed (so that α is a scalar). Qualitatively, the α-effect can be understood as the distortion of a magnetic field line by a localized helical disturbance, such as is demonstrated in Fig.1.1.

Because of the small (assumed) resistivity of the fluid, the turbulent resistivity is introduced in the form of the β term defined as

$$\beta = \frac{\tau}{2}\langle v^2 \rangle.$$

The β term is an effective mixing term produced by random turbulent motions and smooths out the field on scales larger than that of the turbulent motion. It can be understood as the effect of the random walk, since τv is the displacement Δr, $\beta \approx (\Delta r)^2/\tau$ is effectively a diffusion coefficient.

In the kinematic limit, that is if the initial magnetic field of the protogalaxy was so small that motion of the fluid can be considered to be independent of the magnetic field, Eq 1.5 describes the evolution of the magnetic field, where the diffusion term is negligible because of the (assumed) small resistivity of the turbulent fluid. At this point, the velocity and magnetic field are divided into a

component associated with turbulent motions ($\delta\mathbf{v}$, $\delta\mathbf{B}$) and a smooth, coherent component ($\mathbf{v}$, $\mathbf{B}$). Substitution into Eq 1.5 and averaging over turbulent motion scales gives

$$\frac{\partial \mathbf{B}}{\partial t} = \nabla \times (\mathbf{v} \times \mathbf{B}) + \nabla \times (\langle \delta\mathbf{v} \times \delta\mathbf{B} \rangle). \tag{1.7}$$

For $\delta\mathbf{v} = \delta\mathbf{B} = 0$, this equation reduces to Eq. 1.5 in which magnetic viscosity is neglected. The quadratic term in the magnetic field fluctuations and the random velocities of the turbulent fluid has been added to the mean, smoothed magnetic field evolution. Following [Kul05], it can be shown that

$$\langle \delta\mathbf{v} \times \delta\mathbf{B} \rangle = \alpha\mathbf{B} - \beta\nabla \times \mathbf{B},$$

leading to the well known mean-field dynamo equation

$$\frac{\partial \mathbf{B}}{\partial t} = \nabla \times (\mathbf{v} \times \mathbf{B}) + \nabla \times (\alpha\mathbf{B}) + \beta\nabla^2\mathbf{B}. \tag{1.8}$$

For the application to the galactic disk evolution, we introduce cylindrical coordinates (r, ϕ, z), and keep only the derivatives in the thin vertical direction (z). The solutions for the mean radial and azimuthal field components satisfy

$$\frac{\partial B_r}{\partial t} = -\frac{\partial}{\partial z}(\alpha B_\phi) + \beta\frac{\partial^2 B_r}{\partial z^2} \tag{1.9}$$

$$\frac{\partial B_\phi}{\partial t} = \Omega B_r + \beta\frac{\partial^2 B_\phi}{\partial z^2}, \tag{1.10}$$

where the galactic rotation velocity $\mathbf{v} = r\Omega\vec{e}_\phi$ and $\partial\Omega/\partial r = -\Omega/r$ have been substituted in addition to dropping the small term, $\partial_z(\alpha B_r)$, in Eq 1.10.

To find an increment of the magnetic field growth one looks for a mode proportional to $e^{\gamma t}$ and solves equations 1.9 and 1.10 as an eigenvalue problem. The

boundary conditions most often invoked are that the disk is confined to a small region in z, $-h < z < h$, presuming that the diffusion coefficient, β, is very large outside the disk, and the magnetic field is taken to be zero for $|z| > h$, so that $B_r = B_\phi = 0$ in this region, which is known as the vacuum boundary conditions. We refer to [RSS88] for the full eigenvalue equation for γ with the given boundary conditions. To make an order of magnitude estimate, we follow [RSS88] and speculate that if

$$\frac{\Omega \alpha h^2}{\beta^2} \approx 1,$$

then $\gamma \approx \beta/h^2$. The growth time of the mode can be estimated roughly for our own galaxy assuming a turbulent velocity of $\delta v \approx 10$ km s^{-1}, correlation length $\delta v \tau \approx 100$ pc, $h \approx 300$ pc, which gives $1/\gamma \approx 5 \times 10^8$ yr, and there could be about 20 amplification times, $1/\gamma$, throughout the age of the galactic disk. This could raise an initial field by a factor of $\sim 10^8$, from about 10^{-14} G to its present value. However, the uncertainties in the above parameters, including the validity of the vacuum boundary conditions are significant, so that a large range of initial magnetic fields are allowed by the mean field dynamo, if it indeed operates throughout the lifetime of the galaxy. The increment of instability, γ, is an indicator of the initial growth rate. However, the $\alpha - \Omega$ dynamo must saturate eventually, and that is expected to happen when conditions in the turbulent motions of the galactic disk are such that α and β are "non-linearly quenched", see e.g. [BF99]. The primary question is whether the dynamo quenches when the mean field comes to equipartition with turbulence, which appears to be the case in our own galaxy, or whether the small scale fields suppress the dynamo long before reaching equipartition. [BS05] offer a detailed discussion of these aspects of the theory.

One of the most severe criticisms of the mean field dynamo model as applied

to our own galaxy is the problem of expelling negative flux from the plane of the disk. In order for the dynamo to operate as illustrated in Fig 1.1, negative flux must be expelled from the plane of the galaxy after the field lines have been twisted in the toroidal direction to amplify the magnetic field in the disk. If this is the case, then flux freezing implies that any flux that escapes must be embedded within interstellar matter. To be more quantitative, let f be the fraction of interstellar medium which must be removed for every efolding of the magnetic field. Then, if the field strength increases from B_0 to B_1, the mass of the interstellar medium decreases from M_0 to $M_1 = M_0(B_1/B_0)^f$. To increase $B_0 = 10^{-16}$G to $B_1 = 10^{-6}$G, with $f = 1/3$, it would require $M_0 \approx 10^3 M_1$, which seems untenable and inconsistent with observations. Thus, resolving the flux expulsion problem is an issue of active research and debate.

In summary, the $\alpha - \Omega$ dynamo mechanism appears to have much plausibility and can be studied in detail numerically, but significant uncertainties remain which makes it difficult to assess its viability as an explanation. Particularly, many detailed observations are missing regarding critical parameters related to determining the dynamo growth rate, the detailed present-day configuration of the magnetic field in the disk, and the possibility of flux expulsion from the disk. Thus, the complexity of the dynamo amplification mechanism, observational uncertainties, and a large sensitivity of the results to these uncertainties do not allow for a definitive statement to be made regarding the magnitude of the seed field during galaxy formation if this mechanism is the primary one responsible for the generation and maintenance of the galactic magnetic fields.

1.3 Primordial Magnetic Fields: Observational Constraints and Models

The leading explanations of the origins of the galactic magnetic fields require a seed field to be present at the time of galaxy formation. The significant complexity of the magnetic field amplification mechanisms which could have taken place in the galaxies makes it nearly impossible to estimate the amplitude of these seed fields, even with a few orders of magnitude accuracy. A natural question would be where did these fields come from, and perhaps also, are these fields observable in the present day universe? These fields could have produced secondary observational effects, for example, by changing primordial nucleosynthesis, or leaving an imprint in the CMB fluctuations. These fields may still be preserved in relatively intact form in the gravitationally unbound structures in the universe, such as cosmic voids, since they have undergone relatively simple evolution there. Up until now, they have not been measured; however, upper and lower bounds have been derived at various epochs and utilizing a wide range of observational techniques.

There is a vast literature on the subject of various models of primordial magnetic field production, including as far back as the epoch of inflation (see e.g. [GR01] section 4.5). Here we only summarize some characteristic examples of the types of models that are invoked for the generation of a primordial field as well as some cosmological tests of their existence and bounds. For a detailed treatment of this subject, one may consult the *Physics Report* of [GR01] or the more recent work of [DN13]. We begin this section with a brief outline of the main mechanisms of primordial magnetic field evolution throughout Cosmological history.

Table 1.1. Relevant properties to the evolution of magnetic fields in the universe, including the present day voids. All parameters are given in the lowest redshift in the epoch unless otherwise noted by the $\rightarrow$ which denotes how the parameter changes from the highest to the lowest redshift in the epoch. (Note that $\tau = (n_\gamma \sigma_T c)^{-1}$, and $\tau_C = (n_e \sigma_C v_e)^{-1}$).

Free Electron Plasma Parameters of the Universe			
Parameter	Epoch I ($z \gtrsim 1100$)	Epoch II ($1100 \gtrsim z \gtrsim 10$)	Epoch III ($z \lesssim 10$)
n_e (cm^{-3})	$2 \times 10^{-7}(1+z)^3$	$2 \times 10^{-10}\ (1+z)^3$	$2 \times (10^{-8} - 10^{-10})\ (1+z)^3$
v_e (m/s)	3.7×10^5	$3.7 \times 10^5 \rightarrow 3.7 \times 10^4$	$2.2 \times 10^6 \rightarrow 3.7 \times 10^5$
τ_T (s)	91	$91 \rightarrow 9.1 \times 10^7$	$9.1 \times 10^7 \rightarrow 1.2 \times 10^{11}$
τ_C (s)	2.4×10^2	$2.4 \times 10^5 \rightarrow 2.4 \times 10^8$	$\gtrsim 4 \times 10^{11} \rightarrow 3 \times 10^{12}$
σ (s^{-1})	700	0.7	70
η_m (m^2/s)	1.1×10^3	1.1×10^6	1.1×10^4

1.3.1 Primary Evolution Mechanisms of Primordial Mangetic Fields

The evolution of the mangetic fields in voids from the epoch of reionization until now, is driven by two effects-cosmological expansion and interaction with plasma in the voids. Since the energy density of the magnetic field scales as $(1+z)^4$, the cosmological evolution of the magnetic field is described by

$$B(z) = B_0\,(1+z)^2 \tag{1.11}$$

where B_0 is the magnetic field in the present epoch. The interaction of the magnetic field with the plasma in the voids, is driven by Eq. 1.5. To estimate the relative importance of the flow and diffusion terms, we estimate the electron conductivity, and the magnetic field diffusion coefficient. Thomson scattering off CMB photons is the dominant contributor to the electron resistivity, so $\tau \simeq$

$(n_\gamma \sigma_T c)^{-1}$, where σ_T is the Thomson cross section and n_γ is the CMB photon number density. Therefore the electrical conductivity of the plasma is determined by

$$\sigma = \frac{n_e e^2 \tau}{m_e} = \frac{n_e e^2}{m_e n_\gamma \sigma_T c}.$$

It is important to note that the ratio of electron density to photon density is redshift independent, and thus, the evolution due only to cosmological expansion, proceeds with constant σ. Assuming the present day plasma density in the voids, in the range of $2 \times 10^{-2} - 2 \times 10^{-4}$ m^{-3}, one finds that $\sigma \approx 0.7$ - 70 s^{-1} and the magnetic diffusion coefficient, $\eta_m \approx 10^4 - 10^6$ m^2/s. Thus, since the epoch of reionization ($z \approx 10$), the characteristic diffusion scale of the magnetic field can be estimated as

$$L_0 \approx \left(\frac{\eta_m}{H_0}\right)^{1/2} \left(\frac{z}{\Omega_m}\right)^{1/4}$$

where H_0 is the hubble constant, Ω_m is the present day matter density parameter, and the assumption is made that the universe's expansion is approximately dominated by the matter density. The estimation of the length scale gives $L \approx 2 \times 10^{11}$ m. This suggests that magnetic field diffusion, which took place since the reionization epoch has erased magnetic field structures only on very small spatial scales, of less than 1 astronomical unit. Comparing the flow term with the characteristic thermal velocities of the plasma (with temperature of a few thousand K) to the diffusion term, suggests that magnetic field on the scale larger than 1 astronomical unit is driven by the plasma evolution and the diffusion process can be neglected at spatial scales larger than this. For example, depletion of the matter in the cosmic voids due to negative gravitational potential, will be accompanied by proportional depletion of its magnetic field. In other words, the underdensity of the matter in the void can be used to estimate the underdensity of the magnetic field as well.

Similar considerations for the flow and diffusion terms of magnetic field evolution for the period since recombination to reionization can be used to estimate the diffusion length scale of about 30 astronomical units, for the electron density of $2 \times 10^{-4}(1+z)^3$ m^{-3}. The conductivity is independent of cosmological expansion and evolution of magnetic fields on the spatial scales larger than this is dominated by the interaction with plasma flows. This indicates that during the large scale structure formation, magnetic field was frozen into the gas due to the conductivity of the residual low density electron plasma, and therefore, it could naturally provide a seed field for the galactic magnetic fields. The rough estimate of relative energy density of these seed fields and the energy density of magnetic fields in the voids is determined by the ratio of matter density in these cosmic objects. As structures form, processes other than Thomson scattering of CMB photons may start to dominate the electron resistivity (for example, electron-electron or electron-proton collisions), and therefore the relatively simple picture of the magnetic field evolution described above for the case of voids will no longer be applicable for galaxy formation when the gas densities increase. Additionally, the expulsion of the magnetic field together with plasma from galaxies into the voids (e.g. due to AGN activity or starburst galaxies), may take place, and this has been proposed by several authors [RS68, DL90, FL01], as a mechanism for potentially altering the intergalactic magnetic field.

Prior to the recombination epoch, the electron density was $0.2(1+z)^3$ m^{-3} [KT90], and the electron resistivity was dominated by Thomson scattering off photons in thermal equilibrium with the plasma, and this dominance only increases at higher redshifts. Despite the simplicity of the conductivity in the electron plasma, the evolution of large scale magnetic fields may be very different from Eq 1.5. At certain epochs in the early universe, magnetic field energy can be efficiently converted into heat. The damping of different MHD modes is a complex problem

discussed in e.g. [JKO98], but the important conclusion for the discussion here is that modes whose wavelength is greater than a comoving length of about 50 Mpc are unaffected, but damping of MHD modes below this wavelength depends on the type of mode and field strength. In addition, the condition for the generation of magnetic field via the Biermann battery mechanism without a seed field, may arise during this epoch. The underlying cause of these processes is related to a slightly different coupling of photons to electrons and protons (see section 1.3.4).

More exotic magnetic field dissipation mechanisms can also take place which can signficantly deviate magnetic field evolution from cosmological rescaling, eq 1.11. For example, the existence of magnetic monopoles in nature would cause a dramatic decrease of magnetic fields, due to energy transfer to accelerating monopoles [Par70]. Extremely large magnetic fields may also trigger QED processes spontaneously converting electromagnetic energy into electron positron pairs. In general, relatively large magnetic fields present at the critical events in the history of the universe, such as nucleosynthesis or recombination might have left astrophysical imprints observable today.

1.3.2 Limits from CMB Anisotropy

A major source of cosmological data, the cosmic microwave background (CMB), carries information about the plasma distribution in the universe at the time of decoupling and recombination ($z \sim 1100$) and may contain imprints of a primordial magnetic field. If primordial magnetic fields existed prior to this epoch, then it would have interacted with the primordial plasma in the universe.

A recent extensive review of observational constraints on primordial magnetic fields is provided in [DN13]. The effect of the primordial magnetic fields lead to perturbations in the density and polarization of the CMB. For example, the

magnetic field energy momentum tensor perturbs the geometry of the universe and may also alter the behavior of the cosmic plasma at the time of recombination (e.g. Alfven waves, etc.) and this induces corresponding density perturbations. Magnetic fields may impact large scale structure formation, for example formation of galaxy clusters and thus may leave an imprint on the CMB by the SZ effect. Faraday rotation will evidently lead to the effects on the CMB polarization. All of these effects and more subtle ones are discussed in [DN13] where references to the original works can be found. In general, because the fluctuations in the CMB are on the order of 10^{-5}, and the energy density in the primordial magnetic field is

$$\Omega_B \approx 10^{-5} \left(\frac{B}{10^{-8} G} \right)^2 \Omega_\gamma,$$

it is expected that magnetic fields of order a nG (at present) may leave an imprint in the CMB anisotropies of the order of 1 %, depending on the details and duration of CMB interactions with the plasma at that epoch. Thus, most limits derived from CMB observations on a primordial magnetic field have been on this order or larger (e.g. [PF11]). The Planck[2] satellite is expected to improve current limits by a factor of two, but so far these constraints have not been published.

1.3.3 Limits from Big Bang Nucleosynthesis

Big bang nucleosynthesis (BBN), the process by which atomic nuclei are created from pre-existing nucleons, took place around $10^{-2} - 1$ sec after the big bang, and is responsible for primordial formation of the ^{4}He, ^{3}He, D, and ^{7}Li in the Universe. The reactions responsible for the chemical equilibrium of neutrons and

[2] http://www.esa.int/Our_Activities/Space_Science/Planck

protons in the early Universe are the weak processes:

$$n + e^+ \leftrightarrow p + \bar{\nu}_e$$

$$n + \nu_e \leftrightarrow p + e^-$$

$$n \leftrightarrow p + e^- + \bar{\nu}_e.$$

The presence of strong magnetic fields at this epoch alters the equilibrium of these reactions through interaction of spin-1/2 particles with the magnetic fields and therefore alters the predictions of the theory, so that the agreement between theoretical predictions and experimental observations of chemical abundances provides a limit on the magnetic field strength at that time. The two primary effects of a magnetic field at nucleosynthesis are 1) it modifies the chemical reaction rates and 2) the magnetic energy density leads to an increased expansion rate. Numerous numerical simulations in the 1990s were carried out [CST94, COS96, GR96, KSV96] and largely converged on the fact that the dominant effect comes from the change in the expansion rate due to the presence of magnetic field energy.

The first effect of the magnetic field on nucleosynthesis is in changing the neutron fraction through changing the electron density of states. The helical motion of an electron in a magnetic field can be decomposed into motion along the field and circular motion perpendicular to the field. According to quantum mechanical principles, the energy associated with the circular motion is quantized and the total energy of the particle can be written as

$$E = (p_z^2 c^2 + m_e^2 c^4 + 2eB\hbar c n_s)^{1/2},$$

where n_s is the quantum number for different energy eigenstates known as Landau levels. These levels become available when $B \gtrsim B_c = m_e c^3/e\hbar = 4.4 \times 10^{13}$G. The resulting quantization of the electron energy changes the density of states of the electrons, resulting in an increase of the neutron decay rate. If this were the only effect of the magnetic field, it would lead to an decrease in the number of neutrons present at BBN and a decrease in the ^{4}He abundance.

The second effect of a magnetic field at BBN is the contribution of the field to the energy density of the Universe, which affects the expansion rate, changing the temperature-time relationship. Thus, the overall expansion rate of the universe is increased with this extra magnetic energy, decreasing the amount of time over which nucleosynthesis can occur, and in particular the time during which neutrons can decay, resulting in an increase in the ^{4}He abundance. The He abundance is fixed when the age of the Universe is around $\simeq$ 1 sec at a temperature of $kT \simeq 1$MeV. At this time, the energy density of the Universe is 2×10^{25} erg cm^{-3}, comparable to the energy density in a magnetic field of 10^{13}G. Thus, the magnetic field must be less than this value so as not to change the BBN predictions, which results in a limit of around $B < 10^{-6}$G today assuming only the cosmological expansion effect and no other evolution of these fields.

1.3.4 Models of Primordial Magnetic Field Generation

The first magnetic fields may have been produced during inflation, an early universe phase transition, or at recombination. In what follows, some post-inflation scenarios for magnetic field generation are highlighted, following [Wid02, GR01, DN13], followed by a brief discussion of more speculative, though intriguing inflationary scenarios [DN13]. Early universe phase transitions typically involve fundamental changes in the nature of particles and fields as well as a significant

release of free energy over a relatively short time, leading naturally to electric currents and magnetic field induction. These scenarios typically rely on statistical fluctuations of strong small spatial-scale fields to yield weak large spatial-scale fields or dynamical processes, such as an inverse cascade of magnetic energy, to channel field energy from small to large scales.

The QCD phase transition is one such example of where cosmological magnetic fields may have been produced. At high temperatures, $kT \gtrsim kT_{QCD} \backsimeq 150$ MeV, the universe made a transition from a quark-gluon plasma, where quarks and gluons existed as nearly free particles, to the hadronic phase. The order of this thermodynamic transition is unknown, but if it is second order, the transformation occurs in such a way that approximate thermodynamic equilibrium is maintained locally and at each instant of the transition, and the phases are not separated by the boundary. This turns out to be important for the possibility of magnetic field generation which can occur at the phase boundary separation. For example, in the first order transition, bubbles of hadronic phase nucleate and grow when the universe cools to T_{QCD}. Shocks develop at bubble walls, latent heat is released, and various regions of the universe reheat back to T_{QCD}. The two phases coexist but they are separated by boundaries and the hadronic region grows at the expense of regions still existing in the quark-gluon plasma.

[Hog83] investigated the possibility that magnetic fields are generated during such a first order phase transition, and found that battery and dynamo processes create and amplify magnetic fields, within each bubble, of magnitude B_B. When the bubbles collide, the fields of each bubble are "stitched" together by magnetic reconnection. In this way, field lines, following random paths can be extended to much larger scales than the characteristic bubble scale, L_B. Detailed computations were carried out by [QLS89] which demonstrated how the

Biermann battery might have operated during the QCD phase transition. To summarize these conclusions, the baryon asymmetry implies that there exists more quarks than anti quarks, and if the number density of the up (+2/3), down (-1/3), and strange (-1/3) quarks were equal, then the quark-gluon plasma would be electrically neutral. But because the strange quark is heavier and therefore less abundant, there is a net positive charge for the quarks which is compensated by an excess of negatively charged leptons (matter asymmetry). Shocks developing during the hadronic bubble nucleation process and characterized by strong pressure gradients, misalign the quarks' and leptons' number density gradients. Electric currents are then induced due to the Biermann battery process (see section 1.2.1) as bubble walls sweep through the quark-gluon plasma. These currents induce stochastic magnetic fields of order $\sim$ 5 G, which at the recombination epoch are only $\sim 10^{-31}$ G at 100 kpc scales. However, [CO94] and [SOJ97] estimated stronger fields, leading to an estimated strength of $\sim 10^{-23}$ G at recombination, at 100 kpc (galactic) scales. Again the assumption being made here is that the magnetic fields were not amplified in further evolution and only underwent cosmological amplification.

A similar scenario is at work if the electroweak phase transition is first order. Although the transition appears to be weakly first order or second order (see [BBM96] and references therein), when the plasma supercools below the electroweak phase transition temperature of $T_{EW} \backsimeq 100$ GeV, bubbles of broken electro-weak symmetry phase may be able to nucleate and expand, eventually filling the entire plasma. If a field is produced under this scenario, estimates differ as to its magnitude at the time of decoupling on comoving galactic scales (100 kpc), but one typical computation by [Vac91] gives $B \backsimeq 10^{-23}$ G.

One recent model of magnetic field generation between the QCD phase tran-

sition but prior to recombination was proposed by [ITO06]. The idea is that the cosmological density fluctuations that explain the large-scale structure of the Universe can produce magnetic fields on cosmological scales prior to the epoch of recombination, when second order couplings between photons and electrons are considered. Prior to recombination, the temperature is great enough that Compton and Coulomb scattering is so efficient that photons, protons, and electrons are approximated as a tighly coupled fluid. If these three types of fluid moved in exactly the same way, no magnetic fields would be generated, but due to the fact that photons scatter off of electrons preferentially compared to protons, small differences in velocity between protons and electrons are generated, yielding electric currents. This anisotropic photon pressure causes a rotation of the electric current that generates the magnetic field through a Biermann battery mechanism. However, the rotation (or vector) mode of perturbations in linear order is known to be damped away during the expansion of the universe [TIO05]. Thus, it is necessary to consider the second order couplings in the Compton scattering term, which gives rise to magnetic fields which are correlated to temperature fluctuations at recombination, because the electric current is associated with the density perturbations of photons. The resulting magnetic field spectrum is turbulent, and dominated by the energy density at small comoving length scales (with respect to the size of voids), but the field amplitude is approximately 10^{-20} G for coherence lengths of about a Mpc [ITS07].

None of the above models of magnetic field generation detailed above, however, can generate fields much larger than around 10^{-20} G. Another approach to producing a magnetic field at the very earliest phases of the Universe, is the possibility of the coupling of the inflation field to the electromagnetic field (see, for example, the class of models of this kind discussed by [DN13]). Since there is a vast uncertainty regarding the type of coupling of the Electromagnetic field

to the inflation field, various models of the evolution of the magnetic field during inflation can be devised. If these models are tuned properly, it is possible to generate magnetic fields on the order of about a nG or lower today. These fields would not violate the lower limits due to Big Bang Nucleosynthesis (see section 1.3.3). Therefore, if the IGMFs are indeed as high as this, it may be a relic of interesting physics at the inflationary epoch.

1.4 Primordial Magnetic Fields: A New Observational Technique

Due to the vast uncertainty of modeling the dynamo amplification mechanism in the galaxies, simulations predict a magnetic field amplification factor ranging from 10^4 - 10^6 and higher. This combined with the present-day μG scale magnetic fields argues that the seed field in the protogalactic disk might have been 10^{-10} G or lower. The present day magnetic fields in the voids should therefore be further decreased by the compression factor of $10^3 - 10^4$, estimated by the ratio of the matter density in the protogalactic gas and the voids. The prospects for direct detection of such a weak field, $\lesssim 10^{-12}$G have been elusive until recently, since no conventional observational technique (see section 1.1) would be sensitive enough to detect them.

During the past few years, a new measurement technique has emerged which may be able to constrain or measure these low IGMFs in voids. This technique relies on observations of Very High Energy (VHE; $E \gtrsim 100$ GeV) sources of gamma-rays, and the generic effects are illustrated in figure 1.3. Briefly, sources of VHE photons (for example, blazars, a class of active galactic nuclei) emit VHE gamma-rays which then interact with the EBL, pair producing an electron

and positron. These charged particles are deflected in opposite directions by the IGMF and then Inverse Compton (IC) scatter CMB and EBL photons producing secondary gamma-rays of a lower energy than the primary. As a result, an electromagnetic cascade occurs, and if it primarily develops within cosmic voids, then the spectral, angular, and temporal properties of the cascade emission at the GeV scale carry information about the intergalactic magnetic field.

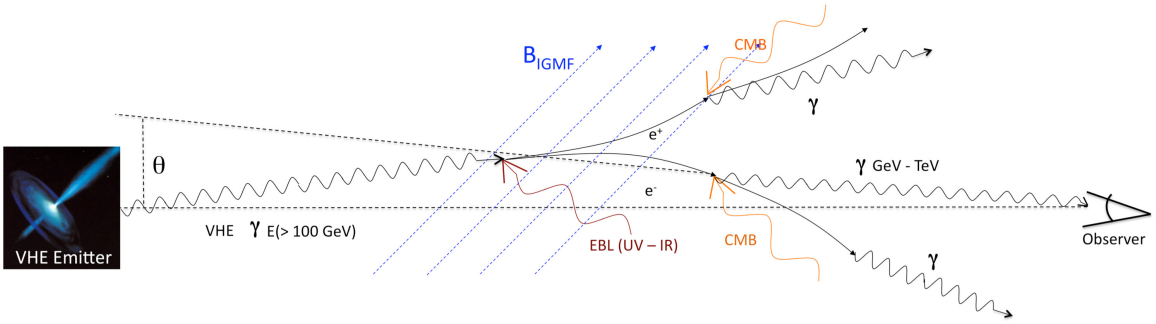

Figure 1.3 Schematic overview of the electromagnetic cascading in intergalactic space.

In this emerging field, many recent works have been published attempting to both characterize the effects of the cascading process from a theoretical and numerical point of view, as well as compare the results of these computations and simulations to data, to argue for a lower limit on the IGMF. A preliminary investigation into the effects of the cascading process on the temporal profile of the cascade radiation, or "echo" emission, was performed by [Pla95], and around the beginning of current generation gamma-ray detector technology, several other studies have been performed to characterize this echo emission and argue for a lower bound on the IGMF of around 10^{-20} G (e.g. [IIT08, MTI08, TMI12, TMI13]). The angular profile, or "halo" emission has also been studied from a computational point of view, beginning with the original paper of [ACV94] and followed up in much more detail with predictions for current generation gamma-

ray detectors by [NS09, DKO09, Ahl11].

The observational characteristic that has received the greatest amount of attention in the past few years, however, is the effect of the spectral modification due to cascading. The basic idea here is that through pair production of the highest energy gamma-rays (the TeV band), the cascade redistributes flux from the TeV band to lower energies, provided that a strong magnetic field which would isotropize the electrons and positrons is absent. If a relatively high amount of TeV flux from a source has survived extinction through the EBL to reach the earth, then a much greater amount must have undergone pair production with EBL photons and have been redistributed to lower energies. If this amount of predicted cascaded flux exceeds the amount measured at GeV energies, for a given range of magnetic field, then this range of IGMF would be inconsistent with the data, and in this way a lower limit can be derived.

A brief historical overview of this avenue of investigation begins with the work of [NV10], who through the use of a simple geometric model, and making the explicit assumption that the measured VHE spectrum has been approximately constant over millions of years, deomonstrated that a lower limit on the order of 10^{-15} G on a uniform IGMF could be placed. Several other papers appeared to confirm these results (e.g. [TGF10, TGB11]). However, [DCR11] speculated that if the VHE activity of the blazar sources of gamma-rays had only been constant over a few years during which time the sparse VHE-band observations have been made, a less constraining lower limit on the IGMF of 10^{-18} G remains, and semi-analytic calculations, expanding on these simplified geometric models confirmed these predictions [HWA11]. Finally, Monte Carlo simulations which numerically compute much of the relevant physics were used by [DKO11] and [TVN11] to confirm and improve the results of simplified geometric semi-analytic models,

and a lower limit on the IGMF of about 10^{-18} G, appeared to be consistent with the data, provided that the assumptions going into these calculations are correct.

The complexity of the physics involved in these calculations, however, as well as the many systematic uncertainties of the data, has not allowed for a unique interpretation of this data, nor has it allowed for a model-independent lower bound on the IGMF at this point. The purpose of this thesis within this emerging study is to provide an account of the state of the present data, investigating the applicability of assumptions which have gone into the presently derived lower limits on the IGMF, and to predict prospects for future instruments, which is accomplished through the use of a newly developed state of the art 3-D particle tracking Monte Carlo simulation code, taking into account all of the relevant physics of electromagnetic cascades.

The outline of this thesis is as follows. Chapter 2 describes the essential physics of the simulation code, including a description of the pair production and inverse Compton scattering processes, the cosmological expansion effects, and the algorithm for the computation of the time delay of each particle in the cascade. Chapter 3 describes the implementation of the primary input parameters-the EBL modeling, the IGMF modeling, and the gamma-ray source modeling-for which significant uncertainty exists. Chapter 4 provides an overview of the current generation gamma-ray instruments covering the approximate energy range of $\sim$ 100 MeV - 10 TeV, relevant for the study of intergalactic electromagnetic cascading. Chapter 5 investigates the lower limits on the IGMF from model-dependent predictions in the literature, investigating how the effect of systematic uncertainties in the astrophysical parameters as well as the gamma-ray data affect these results. Chapter 6 overviews the angular extension and time delay effects of the secondary radiation, and makes predictions for the possible detection of

these effects with future generation technology. Finally, chapter 7 discusses the results and addresses some alternative physics models which have been offered as an explanation of the gamma-ray data.

CHAPTER 2

Gamma-Ray Cascading: Development of the Simulation Code

In order to explore in detail the potentially observable spectral, angular, and temporal effects of cascading in intergalactic space, it is necessary to develop and utilize fully 3-dimensional Monte Carlo simulations. In this chapter, the physics of electromagnetic cascading in intergalactic space is described, which forms the basis of the simulation code, in particular, the QED scattering processes, the details of tracking individual particles, and cosmological effects. The primary contributors to the development of the simulation code which was used to study these cascades were Tim Arlen and Vladimir Vassiliev, with contributions from Stephen Fegan and Yusef Shafi. This chapter serves the function of both explaining the relevant physics of the cascade code, as well as providing documentation for some of the most important details of the implementation in the simulations.

The modeling of gamma ray cascading in the intergalactic space induced by the beam of very high energy photons produced by AGN is broken up into several steps. The flux of source gamma-ray photons is simulated according to an AGN model, with several free parameters, as described in chapter 3. For each photon of energy E_e emitted by the source at redshift z_e, the algorithm illustrated in figure 2.1 is perfomed: the astrophysical input parameters are specified by the user-the model for the Extragalactic Background Light (EBL) and parameters

for the IGMF, both of which are described in detail in chapter 3. In step 1, the optical depth for the interaction of a gamma-ray photon with a low energy EBL photon is sampled from an exponential distribution. The redshift z_i (> 0), of the interaction point is determined or it is assumed that the photon reaches the observer redshift of z = 0 ($z_i < 0$). In the latter case, the parameters of the photon crossing the z = 0 surface are saved to a ROOT[1] data file. In the former case, step 2 is invoked, which determines the 4-momentum of the interacting EBL photon from the QED pair-production cross section, by sampling the marginal probability distribution functions (p.d.f). In step 3, the outgoing 4-momenta of the electron/positron pair (in this section, hereafter referred to as "electrons") is determined from the relativistic kinematics equations and sampling of free parameters. In step 4, the electron propagation length until it interacts with the background photon (CMB or EBL) is sampled from the exponential distribution, and if its position at interaction has $z < 0$, it is dropped. The electron propagated to the interaction point is influenced by the IGMF and cosmological expansion effects. Step 5 determines the 4-momentum of the background photon which interacted with the electron, again by sampling the appropriate marginal p.d.f. Step 6 determines the kinematics of the interaction, namely the outgoing 4-momenta of the electron and photon after IC scattering. If the electron energy is above the electron tracking energy threshold provided by the user, the electron is placed on a stack otherwise it is dropped. The gamma-ray photon is put back through the cycle at step 1, if it is above the photon tracking energy threshold provided by the user. After a gamma ray photon has crossed the z = 0 surface, the simulation checks for any electrons remaining in the stack, and if so, starts over at step 4 with the electron taken from the stack.

The decomposition of the cascade into single primary photons enables the

[1] http://root.cern.ch/drupal/content/documentation

simulation to be carried out on multiple parallel processors in a computing cluster (in this case, the UCLA hoffman2 cluster[2]). The output of the secondary photons from a given energy primary photon is saved in its own ROOT data file. For each energy bin of the source, the code simulates a given number of primary photons, and the results of all produced secondary photons are collected and placed into storage trees, which are optimized for enhanced access speed and reduced disk space, and are saved as ROOT files. These files are generated for each EBL model, IGMF model, and source redshift. Utilizing this information, it is possible to sample the cascading process for a variety of source models, as described later.

2.1 Fundamental Physical Processes

Throughout the cascade simulation, it is necessary to compute the parameters of each particle undergoing a scattering process, sampled from their underlying marginal p.d.f., utilizing their full QED interaction cross sections. The two fundamental interactions in the cascade are pair production and inverse Compton (IC) scattering, which are described below.

2.1.1 Pair Production Propagation Length and Kinematics

It has long been suggested that the attenuation of a gamma ray flux occurs as VHE gamma ray photons propagate cosmological distances due to interactions with background photon fields, namely the UV to far infrared diffuse Extragalactic Background Light (EBL) [GS67]. Such photon photons collisions lead to the annihilation of the photons and the production of an electron and positron pair. The Feynman diagrams for this process are given in Figure 2.2a, and using the

[2] https://idre.ucla.edu/hoffman2

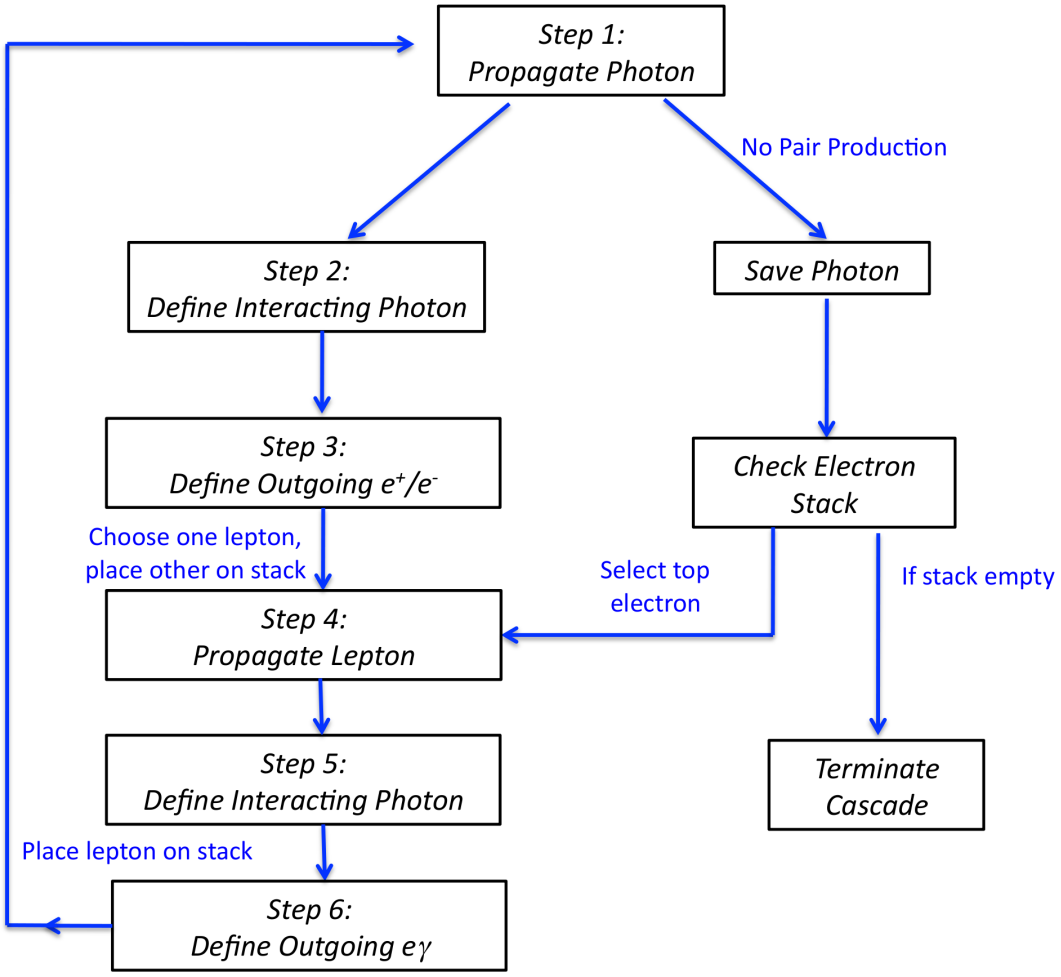

Figure 2.1 Functional diagram of the simulation code of the cascade process.

Feynman rules for the QED Lagrangian, the scattering cross section for $\gamma\gamma$ pair production can be derived (see, e.g. the textbook [PS95])

$$\sigma(\epsilon) = \pi r_o^2 \epsilon \left\{ \left(1 + \epsilon - \frac{\epsilon^2}{2}\right) \ln\left[\frac{1 + (1-\epsilon)^{1/2}}{1 - (1-\epsilon)^{1/2}}\right] - (1+\epsilon)(1-\epsilon)^{1/2} \right\}, \qquad (2.1)$$

where the parameter $\epsilon = 2m_e^2c^4/E_\gamma\varepsilon(1-\cos\vartheta)$, m_e is the electron mass, and r_o is the classical electron radius, E_γ is the energy of the hard gamma photon and ε is the energy of the soft background photon, and ϑ is the polar scattering angle

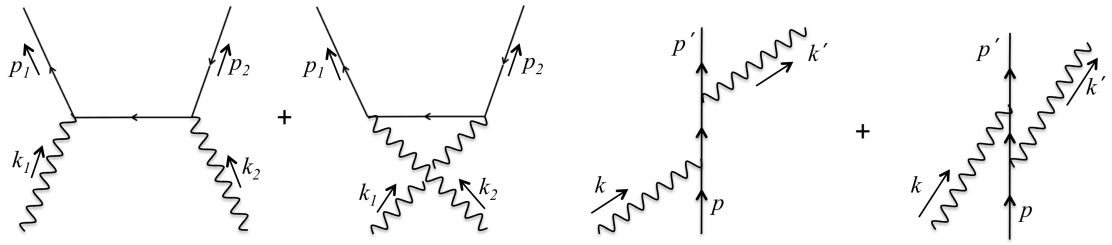

Figure 2.2 Feynman Diagrams for the two QED processes of interest in the cascade simulations: (a) (left) Pair Production and (b) (right) inverse Compton Scattering.

between the hard and soft photon momentum vectors.

2.1.1.1 Pair Production Propagation Length

Let us denote the probability of finding a gamma-ray photon of energy E propagating with the speed of light at a distance ℓ from the emission position, L_e, as $P(\ell)$. The change of this probability is

$$dP(\ell) = -P(\ell)\frac{d\ell}{\lambda},$$

where $P(\ell)$ is the probability of a photon reaching the distance ℓ and $d\ell/\lambda$ is the probability of photon interaction and disappearance in the interval $d\ell$. The parameter λ is the mean free path for the interaction. The well-known solution of this equation is

$$P(E; L_e, L_i) = P(E; L_e) \exp\left(-\int_{L_e}^{L_i} \frac{d\ell}{\lambda(E)}\right) = P(E; L_e) e^{-\tau(E, L_e, L_i)}, \qquad (2.2)$$

where τ is the optical depth, which depends on the energy of the VHE photon. For an isotropic distribution of background target photons with differential number

density, $dn(\varepsilon)/d\varepsilon$, the differential optical depth is given by

$$d^4\tau = \sigma(\epsilon)c(1-\cos\vartheta)\frac{d\ell}{c}\frac{dn(\varepsilon)}{d\varepsilon}d\varepsilon\frac{d\varphi d\cos\vartheta}{4\pi},$$

where $\sigma(\epsilon)$ is the interaction pair production cross section, ϑ is the polar angle between momentum vectors of the incident and target photons, $c(1-\cos\vartheta)$ is the relative velocity of two photons projected onto the direction of the incident photon, and $d\ell/c$ is the time interval. Thus,

$$\frac{d\tau(E)}{d\ell} = \frac{1}{\lambda(E)} = \int\int \sigma(\epsilon)\frac{dn(\varepsilon)}{d\varepsilon}(1-\cos\vartheta)\left(\frac{d\cos\vartheta}{2}\right)d\varepsilon,$$

where the φ-dependence has been integrated out.

Since the cross-section, $\sigma(\epsilon)$, depends on both variables of integration, the order of integration can be changed to decouple the integrals, with $(1-\cos\vartheta) = 2q/\epsilon$ where $q = m_e^2c^4/E\varepsilon$ and ε. Using these definitions, the inverse mean free path can be written as

$$\frac{1}{\lambda(E)} = \frac{3}{8}\sigma_T\int_{\varepsilon_{thr}}^{\infty} F(q)\frac{dn(\varepsilon)}{d\varepsilon}d\varepsilon,$$

where $\sigma_T = 8\pi r_o^2/3$ is the Thomson cross section, $\varepsilon_{thr} = m_e^2c^4/E$ is the minimum energy of soft photon which can contribute to the pair production process, and

$$F(q) = 2q^2\int_q^1 \epsilon^{-2}\left[(1+\epsilon-\frac{\epsilon^2}{2})\ln\left(\frac{1+(1-\epsilon)^{1/2}}{1-(1-\epsilon)^{1/2}}\right)-(1+\epsilon)(1-\epsilon)^{1/2}\right]d\epsilon$$

contains the integral over the incident angle of the background photon (since $\epsilon = 2q/(1-\cos\vartheta)$).

To include the effects of cosmological evolution of the EBL photon field, one needs to include both the expansion of spacetime as well as the comoving evolu-

tion of the EBL due to changing sources of radiation. In this study, we neglect the latter, due to the relative proximity of AGN used (z < 0.3). Under this approximation, the differential number density of EBL $dn(\varepsilon, z)/d\varepsilon = (1+z)^2 dn(\varepsilon_0)/d\varepsilon_0$, where $\varepsilon_0 = \varepsilon/(1+z)$ is the present day EBL photon energy and $dn(\varepsilon_0)/d\varepsilon_0$ is the present day differential number density. Utilizing the Friedmann equation, it can be shown that

$$\frac{d\ell}{dz} = -\frac{c}{H_o}\frac{1}{1+z}\frac{1}{Q(z)},$$

$$Q(z) = \sqrt{\Omega_r(1+z)^4 + \Omega_m(1+z)^3 + \Omega_\Lambda + (1-\Omega_0)(1+z)^2}, \tag{2.3}$$

in which H_0 denotes the Hubble constant and Ω_i, $i = r, m, \Lambda, 0$ represent the unitless radiation, matter, Lambda, and total energy density at the present time (z $= 0$). Hence, the optical depth as a function of emission, z_e, and interaction, z_i, redshift and energy is

$$\tau\left(E; z_e, z_i\right) = \frac{3c\sigma_T}{8H_o}\int_{z_i}^{z_e}\frac{(1+z)^2}{Q(z)}dz\int_{\frac{m_e^2c^4}{E(1+z)^2}}^{\infty}\frac{dn(\varepsilon_0)}{d\varepsilon_0}d\varepsilon_0 F\left(\frac{m_e^2c^4}{E\varepsilon_0(1+z)^2}\right), \tag{2.4}$$

where

$$E = \frac{E_e}{(1+z_e)} = \frac{E_i}{(1+z_i)},$$

where E is the energy of the photon at z $= 0$, and E_e and E_i are the photon energy at emission and interaction redshifts. Utilizing equation 2.4, one can sample the interaction redshift $\hat{z}_i$ as

$$\hat{\chi} = \exp(-\tau(\hat{z}_i)) \Rightarrow -\ln(\hat{\chi}) = \tau(\hat{z}_i), \tag{2.5}$$

$$\hat{\tau}\left(E; z_e, \hat{z}_i\right) = \frac{3}{8}\sigma_T\frac{c}{H_o}\int_{\hat{z}_i}^{z_e}\frac{(1+z)^2}{Q(z)}dz\int\frac{dn(\varepsilon_0)}{d\varepsilon_0}d\varepsilon_0 F\left(\frac{m_e^2c^4}{E\varepsilon_0}\frac{1}{(1+z)^2}\right) \tag{2.6}$$

where $\hat{\chi}$ is a uniformly distributed random number between 0 and 1. Figure 2.3

illustrates lines of constant optical depth, τ= 0.5, 1, 3 for a photon of energy E (z = 0) (y-axis) and redshift, z_e, (assuming $z_i = 0$) (x-axis), using the standard model for the EBL as described in chapter 3.

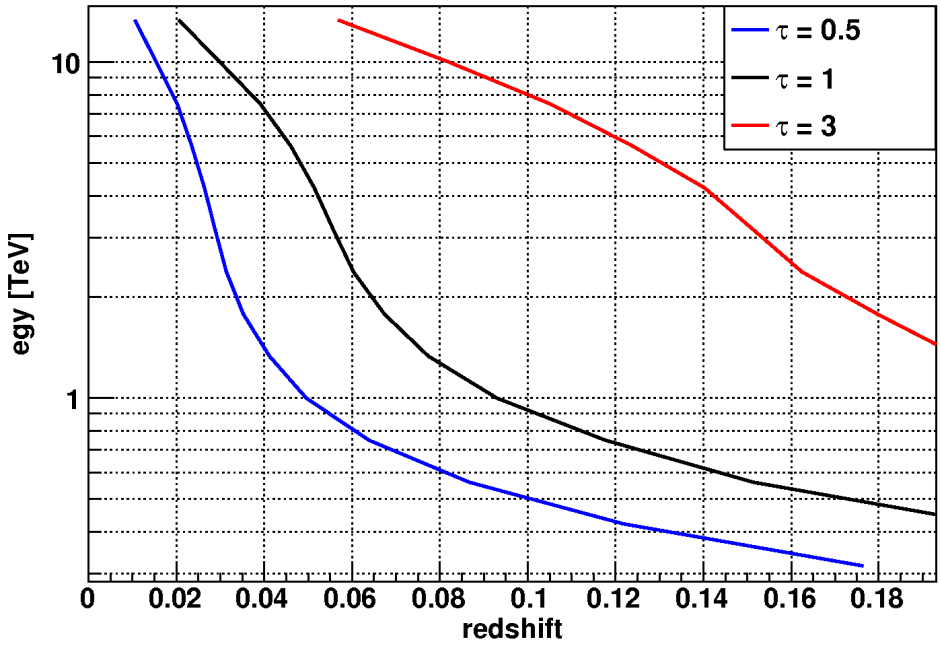

Figure 2.3 Lines of constant optical depth over a range of redshifts and energies of interest to this work.

2.1.1.2 Energy of Background Target Photon

Equations 2.5 and 2.6 are utilized in the code to determine the interaction redshift, z_i. To sample the energy of the background photon, $\hat{\varepsilon}$, which the gamma-ray interacts with, we form a marginal distribution utilizing the second integral of Eq 2.4

$$\hat{\chi_\varepsilon} = \frac{\int_{\varepsilon_{thr}}^{\hat{\varepsilon}} \frac{dn(\varepsilon_0)}{d\varepsilon_0} F(q)\, d\varepsilon_0}{\int_{\varepsilon_{thr}}^{\infty} \frac{dn(\varepsilon_0)}{d\varepsilon_0} F(q)\, d\varepsilon_0},$$

where $\hat{\chi_\varepsilon}$ is a uniformly distributed random number between 0 and 1, and where $q = m_e^2 c^4/(E\varepsilon_0(1+z_i)^2)$.

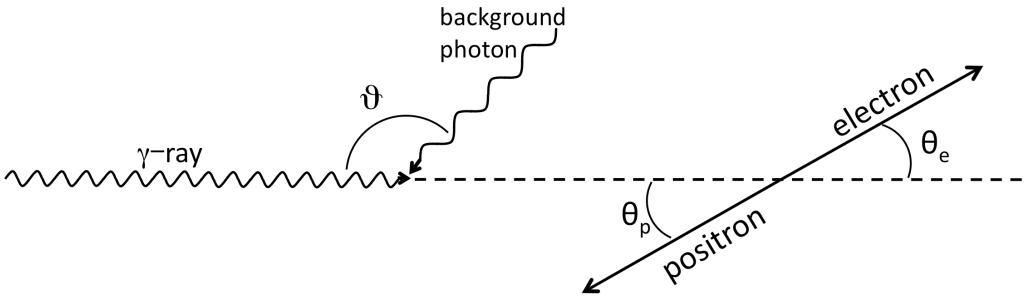

Figure 2.4 Angles of interest in the Pair Production scattering process. The left hand side depicts the incident γ-ray and the background target photon in the lab frame, whereas the right hand side shows the outgoing electron and positron in the center of mass frame.

2.1.1.3 Momentum Direction of Target Photon

The innermost integral in Eq. 2.4, $F(q)$ determines the impact angle, ϑ of the background photon (see Figure 2.4). As before, to sample $\hat{\vartheta}$, we form the marginal distribution,

$$\hat{\chi}_{\vartheta} = \frac{\int_q^{\hat{\epsilon}} \epsilon^{-2} \left[(1+\epsilon-\frac{\epsilon^2}{2}) \ln\left(\frac{1+(1-\epsilon)^{1/2}}{1-(1-\epsilon)^{1/2}}\right) - (1+\epsilon)(1-\epsilon)^{1/2} \right] d\epsilon}{\int_q^{1} \epsilon^{-2} \left[(1+\epsilon-\frac{\epsilon^2}{2}) \ln\left(\frac{1+(1-\epsilon)^{1/2}}{1-(1-\epsilon)^{1/2}}\right) - (1+\epsilon)(1-\epsilon)^{1/2} \right] d\epsilon}, \tag{2.7}$$

in which the random number $\hat{\chi}_{\vartheta}$ is uniformly distributed between 0 and 1, $\hat{\varepsilon}$ is found by solving this equation, and $(1-\cos\hat{\vartheta}) = 2q/\hat{\epsilon}$. The details of the method implemented to rapidly and precisely integrate this function are somewhat complicated and the implementation is described in the appendix A. In addition to this, the axial angle ϕ is sampled from a uniform distribution between 0 and 2π.

2.1.1.4 Kinematical Parameters of Electron Positron Pair

The 4-momenta of the outgoing electrons and positrons are determined utilizing the center of mass reference frame, in which the direction of momentum vectors

are oppositely directed and randomly sampled from a uniform distribution of solid angle. The resulting 4-momenta are boosted back into the lab reference frame to compute the outgoing kinematical parameters of the electron and positron pair.

2.1.2 Inverse Compton Scattering Propagation Length and Kinematics

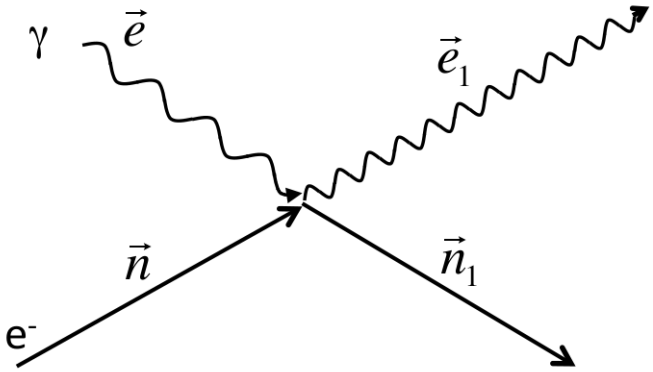

Figure 2.5 (Lab frame) direction vectors of the inverse Compton scattering process, for both the incident and scattering particles.

The GeV - TeV e^+/e^- pairs created in the pair production process dissipate their energy dominantly through the inverse Compton interaction with the background photons fields, CMB and EBL. The Feynman diagrams for IC scattering are given in Figure 2.2b, and using the Feynman rules for the QED Lagrangian, the Klein-Nishina formula for the differential cross section for unpolarized radiation can be derived (see, e.g. the textbook of [PS95]):

$$\frac{d\sigma}{d\Omega} = \frac{r_0^2}{2}\frac{\epsilon_1^2}{\epsilon^2}\left(\frac{\epsilon}{\epsilon_1} + \frac{\epsilon_1}{\epsilon} - \sin^2\theta\right), \tag{2.8}$$

where ϵ is the incident energy of the photon and ϵ_1 is the scattered energy of the

photon in the rest frame of the electron, given by

$$\epsilon_1 = \frac{\epsilon}{1 + \frac{\epsilon}{m_e c^2}(1 - \cos\theta)},$$

and r_0 is the classical electron radius, and θ is the outgoing polar angle of the photon in the electron rest frame. Integrating over the solid angle gives the total cross section for $e\gamma$ Compton scattering

$$\begin{aligned}\sigma(x) = \frac{3}{4}\sigma_T \Bigg[\frac{1}{x}\ln(1+x) - \frac{4}{x^2}(\ln(1+x) - x) - \\ \frac{8}{x^3}\left(\ln(1+x) - x + \frac{x^2}{2}\right) + \frac{2+x}{2(1+x)^2}\Bigg],\end{aligned} \tag{2.9}$$

where $\sigma_T = 8\pi r_0^2/3$ is the Thomson cross section, and the parameter $x = 2\epsilon/m_e$. Similar to the discussion in section 2.1.1.1, one can define the differential optical depth for electron scattering off of an isotropic photon field

$$d^4\tau = \frac{dn(\varepsilon)}{d\varepsilon d\Omega} d\Omega_{inc} d\varepsilon \frac{d\sigma(\varepsilon)}{d\Omega_{scat}} d\Omega_{scat} \left|\frac{v_{rel}}{v}\right| d\ell, \tag{2.10}$$

where $dn(\varepsilon)/(d\varepsilon d\Omega)$ is the number density of target (incident) photons per energy per solid angle, $d\Omega_{inc} = -d(\cos\eta)d\psi$, $d\Omega_{scat} = -d(\cos\theta)d\varphi$ correspond to the differential solid angle of incident and scattered photons respectively, and $v_{rel} = |\beta c - c\cos\eta|$ is the relative speed of the electron and photon projected onto the direction of the electron. Integrating over $d\psi$ and $d\Omega_{scat}$ gives

$$\tau = 2\pi \int_{L_e}^{L_i} d\ell \int \frac{1}{4\pi}\frac{dn(\varepsilon)}{d\varepsilon} d\varepsilon \int_0^\pi \sigma(x(\eta)) \left|\frac{\sqrt{\gamma^2 - 1} - \gamma\cos\eta}{\sqrt{\gamma^2 - 1}}\right| \sin\eta d\eta, \tag{2.11}$$

where $x(\eta) = 2\epsilon/(m_e c^2) = 2\varepsilon(\gamma - \sqrt{\gamma^2 - 1}\cos\eta)/(m_e c^2)$. Using a substitution,

$y = \gamma - \sqrt{\gamma^2 - 1}\cos\eta$, $\cos\eta = (\gamma - y)/\sqrt{\gamma^2 - 1}$

$$\tau = \frac{1}{2}\int_{L_i}^{L_2} d\ell \int \frac{dn(\varepsilon)}{d\varepsilon} d\varepsilon \int_{\gamma(1-\beta)}^{\gamma(1+\beta)} \sigma(2\frac{\varepsilon y}{m_e c^2}) \frac{\gamma}{(\gamma^2-1)^{3/2}} \left| y - \frac{1}{\gamma} \right| dy.$$

Applying a Mellin integral transform for σ, it is possible to separate the integration over y and ε, given by

$$\sigma(q) = \frac{\sigma_T}{2\pi i}\int_{c-i\infty}^{c+i\infty} q^{-\mu}\Sigma(\mu)d\mu, \quad 0 < c < 1, \tag{2.12}$$

with $\Sigma(\mu)$ defined as

$$\Sigma(\mu) = \int_0^\infty \frac{\sigma(x)}{\sigma_T} x^{\mu-1} dx.$$

This integral, using equation 2.9 for $\sigma(x)$-the total cross section for Compton scattering-can be evaluated analytically. Leaving the details of this calculation to appendix B, we quote the result

$$\Sigma\left(\mu\right) = \frac{3}{4}\left(\frac{1}{1-\mu} + \frac{4}{2-\mu} - \frac{8}{3-\mu} + \left(1 - \frac{\mu}{2}\right)\right)\frac{\pi}{\sin\pi\mu} \tag{2.13}$$

The remaining integral over y can be performed analytically, and is a function of γ and μ, which is denoted as $\Pi(\gamma, \mu)$,

$$\Pi(\gamma,\mu) = \frac{\gamma}{(\gamma^2-1)^{\frac{3}{2}}}\left[\begin{array}{c} \frac{1}{2-\mu}\left(\left(\gamma+\sqrt{\gamma^2-1}\right)^{2-\mu} + \left(\frac{1}{\gamma+\sqrt{\gamma^2-1}}\right)^{2-\mu} - 2\left(\frac{1}{\gamma}\right)^{2-\mu}\right) \\ -\frac{1}{1-\mu}\frac{1}{\gamma}\left(\left(\gamma+\sqrt{\gamma^2-1}\right)^{1-\mu} + \left(\frac{1}{\gamma+\sqrt{\gamma^2-1}}\right)^{1-\mu} - 2\left(\frac{1}{\gamma}\right)^{1-\mu}\right) \end{array}\right].$$

The resulting expression for the optical depth becomes

$$\tau = \frac{\sigma_T}{2}\int_{L_i}^{L_2} d\ell \int_{\varepsilon_1}^{\varepsilon_2} \frac{dn(\varepsilon)}{d\varepsilon} d\varepsilon \frac{1}{2\pi i}\int_{\frac{1}{2}-i\infty}^{\frac{1}{2}+i\infty} \left(2\frac{\varepsilon}{m_e c^2}\right)^{-\mu} \Sigma(\mu)\Pi(\gamma,\mu)d\mu, \tag{2.14}$$

where for definiteness, in the Mellin integral transform we have set $c = 1/2$. As in the case of producing the outgoing electron and positron from the pair production computation step (see section 2.1.1), the parameters of the interacting particles are randomly sampled from their underlying marginal probability density functions and the outgoing particles' kinematic parameters are computed. The steps to accomplish this are outlined below, but most of the details are left to the appendices.

2.1.2.1 Inverse Compton Propagation Length

The optical depth can be written in terms of the mean free path as follows: $\tau = \ell/\lambda_{\rm mfp}$, where ℓ is the distance propagated and $\lambda_{\rm mfp}$ is the mean free path. Thus, the mean free path for an IC interaction is given by

$$\frac{1}{\lambda_{\rm mfp}} = \frac{\sigma_T}{2}\int_0^\infty \frac{dn(\varepsilon)}{d\varepsilon}d\varepsilon \frac{1}{2\pi i}\int_{\frac{1}{2}-i\infty}^{\frac{1}{2}+i\infty}\left(2\frac{\varepsilon}{m_e c^2}\right)^{-\mu}\Sigma(\mu)\Pi(\gamma,\mu)d\mu. \tag{2.15}$$

To compute the random distance to an IC interaction $\hat{\ell}$, a random number $\hat{\chi}$, uniformly distributed between 0 and 1 is generated

$$\hat{\chi} = \exp(-\hat{\tau}) = \exp(-\hat{\ell}/\lambda_{\rm mfp}) \Rightarrow \hat{\ell} = -\lambda_{\rm mfp}\cdot\ln(\hat{\chi}).$$

There are two distinct integrals to be evaluated, one over target photon energy, ε, and another over the mellin transform variable, μ. The first integral over ε must be done numerically, since both CMB photons and EBL photons are included as background photons for IC scattering. However, the second integral which we

denote as

$$U\left(\frac{2\varepsilon}{m_e c^2}, \mu\right) = \frac{1}{2\pi i}\int_{\frac{1}{2}-i\infty}^{\frac{1}{2}+i\infty}\left(\frac{2\varepsilon}{m_e c^2}\right)^{-\mu}\Sigma(\mu)\Pi(\gamma,\mu)d\mu, \tag{2.16}$$

must be carefully treated to optimize speed and accuracy of computations. Evaluation of this integral is discussed in the following section.

2.1.2.2 Energy of Background Target Photon

Once the interaction distance is computed, the next parameter to sample is the energy of the background target photon. This is accomplished by forming the marginal distribution utilizing the integrals from Eq. 2.15

$$\hat{\chi}_\varepsilon = \frac{\int_0^{\hat{\varepsilon}} \frac{dn(\varepsilon)}{d\varepsilon} d\varepsilon U\left(\frac{2\varepsilon}{m_e c^2}, \mu\right)}{\int_0^{\infty} \frac{dn(\varepsilon)}{d\varepsilon} d\varepsilon U\left(\frac{2\varepsilon}{m_e c^2}, \mu\right)} \tag{2.17}$$

where $\hat{\chi}_\varepsilon$ is a uniformly distributed random number between 0 and 1. The evaluation of the integral U is lengthy and the details of this are provided in appendix C.

2.1.2.3 Momentum Direction of Target Photon

The next step is to find the momentum direction of the photon which interacts with the electron. Recalling that η is the polar interaction angle between the incoming electron and photon, and that it is related to integration variable y by $\cos\eta = (\gamma - y)/\sqrt{\gamma^2 - 1}$, we form the marginal probability density function for

$\hat{y}$,

$$\hat{\chi}_y = \frac{\frac{1}{2\pi i}\int_{\frac{1}{2}-i\infty}^{\frac{1}{2}+i\infty} \Sigma(\mu)\left[\left(\frac{2\hat{\varepsilon}}{m_e c^2}\right)^{-\mu}\int_{\frac{1}{\gamma+\sqrt{\gamma^2-1}}}^{\hat{y}} y^{-\mu}\frac{\gamma}{(\gamma^2-1)^{\frac{3}{2}}}\left|y-\frac{1}{\gamma}\right| dy\right] d\mu}{U\left(\frac{2\hat{\varepsilon}}{m_e c^2},\gamma\right)}, \tag{2.18}$$

where $\hat{\chi}_y$ is a uniformly distributed random number between 0 and 1, and where $y \in \left[(\gamma+\sqrt{\gamma^2-1})^{-1}, \gamma^{-1}\right]$. Finally, the azimuthal angle is sampled from a uniform distribution between 0 and 2π.

2.1.2.4 Compton Scattering to Determine Outgoing Angles

Once all the interaction parameters are defined, the boost into the electron rest frame is determined, then it becomes a straightforward Compton scattering computation, where the differential scattering cross section (Klein-Nishina formula), Eq 2.8 is used to determine the outgoing angles of the photon. Finally, the resulting 4-momenta are boosted back into the lab frame to compute the outgoing kinematical parameters of each particle, concluding the simulation of the inverse Compton scattering interaction.

The above equations are derived without accounting for cosmological expansion. As before, assuming no evolution in the comoving frame, we can make the straightforward substitution of $dn/d\varepsilon$ and ε in terms of $dn/d\varepsilon_0$ and ε_0 for the isotropic diffuse background photon fields (CMB and EBL). The correction for the path length $d\ell(z)$ is more complicated, and is derived in the next section. The primary reason for the necessity to account for the change in path length due to cosmological expansion concerns the accurate computation of time delays of secondary particles. These so called "echo" effects, carry information about

the magnetic fields and need to be computed accurately down to the minute time scale over distances of the order of a Hubble length; hence, it is necessary to achieve a very high degree of precision in the particle 4-position and momentum tracking and to work out where possible the exact solution for an electron propagating in curved spacetime.

2.2 Cosmology and Geometry

In order to accurately compute the path length propagated by charged particles following curved trajectories deflected by a magnetic field in the expanding spacetime of the universe, it is necessary to derive and solve the equations of motion. The Lagrangian (in SI units) for a charged particle propagating in the presence of an electromagnetic field, with potentials $\varphi(\vec{r},t)$ and $\vec{A}(\vec{r},t)$ defined so that $\vec{E} = -\nabla\varphi - \frac{\partial}{\partial t}\vec{A}$ and $\vec{B} = \nabla \times \vec{A}$ is given by

$$L = -mc^2\sqrt{1 - \frac{1}{c^2}\left(\frac{d\vec{r}}{dt}\right)^2} - e\varphi\left(\vec{r},t\right) + e\left(\frac{d\vec{r}}{dt}, \vec{A}\left(\vec{r},t\right)\right),$$

which yields the standard Lorentz force law

$$\frac{d}{dt}\left(\frac{m}{\sqrt{1 - \frac{1}{c^2}\left(\frac{d\vec{r}}{dt}\right)^2}}\frac{d\vec{r}}{dt}\right) = e\vec{E} + e\frac{d\vec{r}}{dt} \times \vec{B}.$$

To include the effects of curved space time, we rewrite the Lagrangian in a manifestly covariant form of the action integral

$$S = \int_{t_1}^{t_2} L(t)dt = -\int_{t_1}^{t_2}\left[mc\sqrt{g^{\alpha\beta}\frac{dx_\alpha}{dt}\frac{dx_\beta}{dt}} + e\frac{dx_\alpha}{dt}A^\alpha(x)\right]dt. \tag{2.19}$$

Considering flat Euclidean space with a Friedmann-Robertson-Walker (FRW) metric,

$$ds^2 = c^2dt^2 - a(t)^2d\vec{r}^2$$

where $a(t)$ is the scale factor, $dx^\mu = (cdt, d\vec{r})$, and $A^\mu = (\varphi(\vec{r},t)/c, \vec{A}(\vec{r},t))$, one can rewrite equation 2.19 to yield

$$L\left(t\right) = -mc^2\sqrt{1 - \left(\frac{a(t)}{c}\right)^2\left(\frac{d\vec{r}}{dt}\right)^2} - e\varphi(\vec{r},t) + ea(t)^2\left(\frac{d\vec{r}}{dt}, \vec{A}(\vec{r},t)\right). \quad (2.20)$$

We solve the equations of motion for the charged particle assuming that the magnetic field is constant in the comoving frame and the electric field is negligible

$$\vec{A}(\vec{r},t) = \frac{1}{2}\left(\vec{B}\times\vec{r}\right); \varphi(\vec{r},t) = 0.$$

Then the Lagrangian can be rewritten with these definitions as

$$L(\vec{r},\dot{\vec{r}}) = -mc^2\sqrt{1 - \frac{a^2}{c^2}\dot{\vec{r}}^2} + \frac{e}{2}a^2\left[\dot{\vec{r}}\cdot\left(\vec{B}\times\vec{r}\right)\right]. \quad (2.21)$$

Since $a^2\vec{B}$ is constant in time (see equation 1.11), the Euler-Lagrange equations of motion are

$$\frac{d}{dt}\left(\frac{ma^2\dot{\vec{r}}}{\sqrt{1 - \frac{a^2}{c^2}\dot{\vec{r}}^2}}\right) = e\left(\dot{\vec{r}}\times a^2\vec{B}\right), \quad (2.22)$$

which reduce to the Minkowski space result, when $a = 1$. It is evident that the Lorentz force is applied perpendicular to the velocity, $\dot{\vec{r}}$, and therefore, generalized momemtum of the particle is conserved

$$p_0 = \frac{ma^2v}{\sqrt{1 - \frac{a^2}{c^2}v^2}} = \text{const} \quad (2.23)$$

so that the particle's speed as a function of time (redshift) can be obtained from the above equation. The derivations of the particle velocity ($\vec{n}$) and position as a function of time ($r(\vec{t})$) are provided in appendix D and here we quote the relevant final results. The propagation track length in the comoving frame is given by

$$l(z_{i+1}, z_i) = R_H \int_{z_{i+1}}^{z_i} \frac{(1+z)}{\sqrt{\left(\frac{mc}{p_0}\right)^2 + (1+z)^2}} \frac{dz}{Q(z)}. \tag{2.24}$$

Introducing the unit vector along the direction of the magnetic field line at a given spacetime point as $\vec{e}_B$, the particle velocity vector as it propagates from redshift z_i to z_{i+1} is

$$\begin{aligned}\vec{n}(z_{i+1}) = (\vec{n}(z_i) - (\vec{n}(z_i)\cdot\vec{e}_B)\,\vec{e}_B)\cos(\kappa_0 l) + \\ [\vec{n}(z_i)\times\vec{e}_B]\sin(\kappa_0 l) + (\vec{n}(z_i)\cdot\vec{e}_B)\,\vec{e}_B.\end{aligned}$$

The comoving position vector is

$$\begin{aligned}\vec{r}(z_{i+1}) = \vec{r}(z_i) + \vec{n}(z_i)l + (\vec{n}(z_i) - (\vec{n}(z_i)\cdot\vec{e}_B)\vec{e}_B)\left[\frac{\sin(\kappa_0 l) - \kappa_o l}{\kappa_0}\right] \\ + (\vec{n}(z_i)\times\vec{e}_B)\left[\frac{1-\cos(\kappa_0 l)}{\kappa_0}\right],\end{aligned}$$

where l is the propagated track length and $\kappa_0 = e|B_0|/p_0$. Utilizing these equations, one can rewrite the equation for the IC optical depth derived in the previous section (Eq. 2.14), for the case of particle motion in a constant magnetic field and expanding universe. The integrals over the track length dl are converted to integrals over redshift.

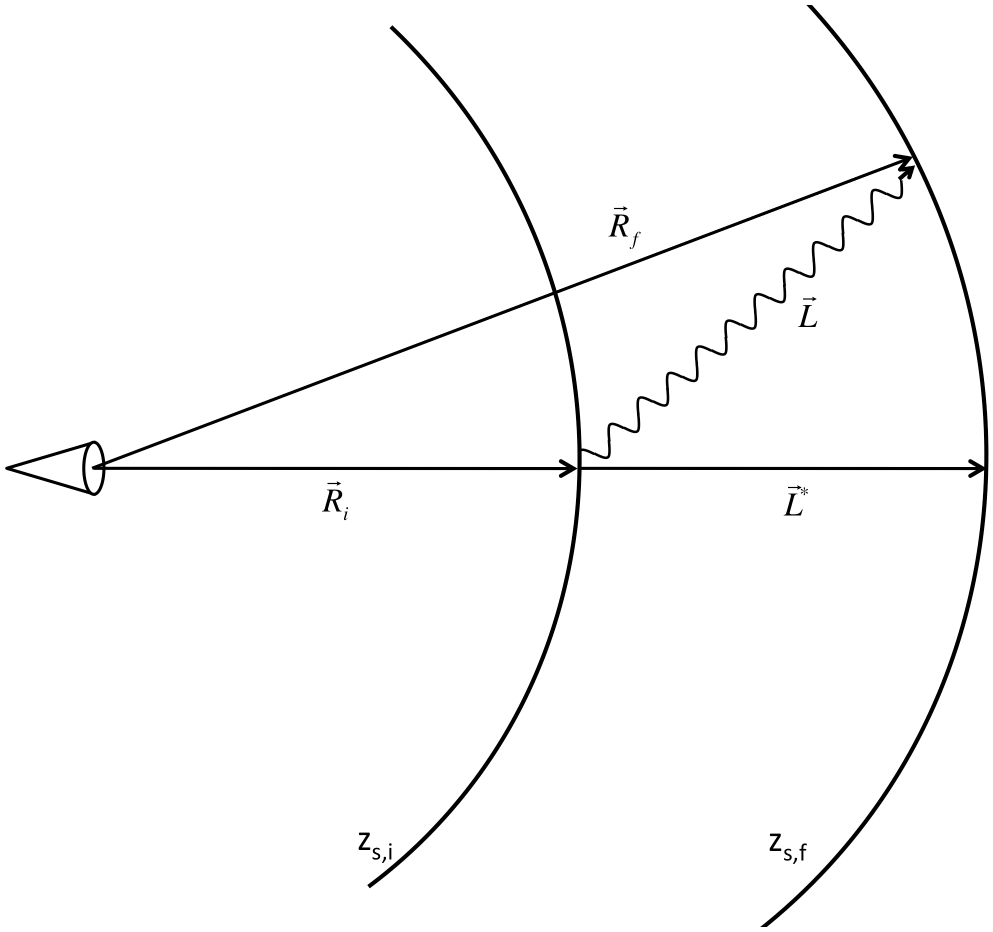

Figure 2.6 Definitions for the computation of time delays and accurately tracking the position of secondary particles. $z_{s,i}$ and $z_{s,f}$ denote z_s surfaces i and f respectively.

2.3 Propagation and Time Delay

One of the goals of this study is to understand the effect of secondary cascading on the temporal profile of variable sources of TeV gamma-rays and use the simulations to search for time delay signatures of an IGMF. Because the brightest flares from TeV blazars have been accurately resolved on $\sim$ minute timescales, it is desirable to accurately track the time delay of the particles down to minute time scales (or better). Over propagation distances of the order of the Hubble

radius, this corresponds to a numerical accuracy of about 1 part in 10^{16} or 10^{17}, and therefore, great care is required to achieve this precision.

The general idea is that when each particle in the cascade takes a propagation step from the emitted redshift to the interaction redshift ($z_e \rightarrow z_i$) along some arbitrary (non-radial) direction, we compute the difference of propagation time rather than total travel time, between the particle and a photon which moves radially from z_e to z_i. In this stepwise fashion, the time delay of each secondary particle in the cascade is calculated relative to a photon directly propagating from the redshift of the source to the observer, arriving at time = 0. To aid the computations, we introduce a global variable, z_s, which defines a spherical surface of constant redshift, centered on the source corresponding to the redshift of a radially propagating photon. Figure 2.6 illustrates a photon propagating along a trajectory, $\vec{L}$, from position $\vec{R}_i$ at global redshift $z_{s,i}$ to $\vec{R}_f$ at $z_{s,f}$ and also displays the path $\vec{L}^*$ which a radial photon would traverse. The algorithm for computing the time difference of these two paths is explained below, first for the photon, and next for the electron.

The tracking of secondary particles is done most conveniently in the comoving frame. The coordinate system is defined so that the location of the source with redshift z is at the position of the origin, and the observer is located on the sphere with comoving radius equal to the proper distance at present. The proper distance from the source to observer, for flat Euclidean space with a FRW metric is given by

$$R = \int_0^R \frac{dr}{a(t)} = c\int_z^0 (1+z)\frac{dt}{dz}dz = R_H \int_0^z \frac{dz}{Q(z)} \tag{2.25}$$

where $Q(z)$ is defined in equation 2.3.

A secondary photon produced by IC scattering will propagate non-radially until it either pair produces with a background photon at z_f or until it reaches

the observer redshift, as given by Eq. 2.6. Thus, in general, one must compute the comoving distance L (where $\vec{L} = L\vec{e}$) that corresponds to a change in redshift, $\Delta z = z_i - z_f$. From Fig 2.6, we see that L can be computed from

$$\left(\vec{R}_i + L\vec{e}\right)^2 = \vec{R}_f^2$$

so that

$$L = \sqrt{(\vec{R}_i \cdot \vec{e})^2 + R_f^2 - R_i^2} - \left(\vec{R}_i \cdot \vec{e}\right) = R_H \int_{z_f}^{z_i} \frac{dz}{Q(z)}. \tag{2.26}$$

And the amount of cosmic time traveled by the photon is

$$T = \frac{1}{H_0} \int_{z_f}^{z_i} \frac{1}{(1+z)} \frac{dz}{Q(z)}. \tag{2.27}$$

Furthermore, for the radial photon, the distance traveled is

$$L^* = |\vec{L}^*| = |\vec{R}_f| - |\vec{R}_i|,$$

and so the global redshift can be determined from

$$L^* = R_H \int_{z_{s,f}}^{z_{s,i}} \frac{dz}{Q(z)} \tag{2.28}$$

and used to determine the amount of cosmic time taken by the direct photon,

$$T^* = \frac{1}{H_0} \int_{z_{s,f}}^{z_{s,i}} \frac{1}{(1+z)} \frac{dz}{Q(z)}. \tag{2.29}$$

Equations 2.26 – 2.29 determine the particle tracking and what remains is to evaluate $T - T^*$ as well as the length integrals, to sufficient accuracy and speed. For small steps in redshift, $\Delta z \ll 0.1$, the integral of Eq. 2.26 and Eq. 2.27 can be evaluated using a Taylor Series expansion about the starting redshift, z_i, keeping

a sufficient number of terms. Defining the unitless propagation length $\ell = L/R_H$ and propagation time $t = H_0 T$ and the integrand functions $F(z) = 1/Q(z)$, $\Phi(z) = (Q(z)(1+z))^{-1}$ of equations 2.26 and 2.27, we have that

$$\ell = \int_{z_i - \Delta z}^{z_i} F(z)dz \simeq a\Delta z - \frac{b}{2}(\Delta z)^2 + \frac{c}{6}(\Delta z)^3 - \frac{d}{24}(\Delta z)^4 + ...$$

$$t = \int_{z_i - \Delta z}^{z_i} \Phi(z)dz \simeq \alpha\Delta z - \frac{\beta}{2}(\Delta z)^2 + \frac{\gamma}{6}(\Delta z)^3 - \frac{\delta}{24}(\Delta z)^4 + ...,$$

where $(a, b, c, d) = (F(z_i), F'(z_i), F''(z_i), F'''(z_i))$ and similarly, $(\alpha, \beta, \gamma, \delta) = (\Phi(z_i), \Phi'(z_i), \Phi''(z_i), \Phi'''(z_i))$. (Analogous equations can be written for the radial photon, ℓ^* and t^*). Once ℓ is determined, ℓ^* (the unitless propagation length of the radial photon) can be calculated directly using

$$\ell^* = \frac{|\vec{R}_f| - |\vec{R}_i|}{H_0} = \sqrt{r_i^2 + 2(\vec{r}_i \cdot \vec{\ell}) + \ell^2} - r_i,$$

where $r_i = |\vec{R}_i|/H_0$. ℓ^* can then be used to find the global redshift difference the radial photon propagated, $\Delta z^* = z_{s,i} - z_{s,f}$. Rather than obtaining it from Eq. 2.28 directly, an accurate and relatively quick way to compute Δz^* is to express it as a perturbation expansion in powers of ℓ^*, because Δz^*, $\ell^* \ll 1$. This gives

$$\Delta z^* \approx A^*\ell^* + B^*(\ell^*)^2 + C^*(\ell^*)^3 + D^*(\ell^*)^4,$$

where

$$A^* = \frac{1}{a^*}$$

$$B^* = \frac{1}{2a^{*3}} b^*$$

$$C^* = -\frac{1}{6a^{*4}} c^* + \frac{1}{2a^{*5}} b^{*2}$$

$$D^* = \frac{1}{24a^{*5}}d^* - \frac{5}{12a^{*6}}b^*c^* + \frac{5}{8a^{*7}}b^{*3}.$$

Finally, the time delay for a non-radial secondary photon, $\Delta T = H_0(t - t^*)$, is computed as

$$(t-t^*) = (\alpha\Delta z - \alpha^*\Delta z^*) - \frac{1}{2}(\beta(\Delta z)^2 - \beta^*(\Delta z^*)^2) + \frac{1}{6}(\gamma\,(\Delta z)^3 - \gamma^*\,(\Delta z^*)^3) - \frac{1}{24}(\delta\,(\Delta z)^4 - \delta^*\,(\Delta z^*)^4).$$

Electron time delays are calculated in a very similar way to the Photon time delays detailed above, the one major change being that the formula for the length propagated from redshift z_i to z_{i+1} changes from 2.26 to that of Eq 2.24, and the time taken to propagate a redshift difference Δz changes from Eq 2.27 to

$$T = \frac{1}{H_o}\int_{z_i-\Delta z}^{z_i} \frac{1}{\sqrt{\left(\frac{mc}{p_0}\right)^2 + (1+z)^2}} \frac{dz}{Q(z)}. \tag{2.30}$$

Because the propagation step due to IC scattering is generally so small ($\Delta z \sim 10^{-7}$), for all values tested (and run in the simulation), a second order Taylor expansion for Eq 2.24 and 2.30 and a third order perturbation expansion for Δz^* was sufficient to achieve the desired accuracy in the electron time delay calculation.

CHAPTER 3

Modeling and Implementation of the Input Parameters

In the previous chapter, the particle interactions and tracking in the cascade was described in detail, incorporating known physics from QED and Cosmology. In the present chapter, the three essential input parameters required for the modeling of actual astrophysical sources of gamma rays are described-the spectral energy density of the EBL, the model for the intergalactic magnetic field, and the model for the gamma-ray emission at the source. These range from mildly constrained to completely unconstrained, and the strategy employed throughout the simulation code was to model these objects as generically as possible, so that the widest range of parameters could be searched over and tested.

3.1 Extragalactic Background Light Model

Diffuse radiation fields fill the universe at all wavelengths. These radiation fields carry information regarding the formation and evolution of structures on various spatial scales and on the physical mechanisms responsible for them. The most well-known, intense, and precisely measured of these is the cosmic microwave background radiation (CMB), which yields information regarding the early Universe, prior to about 300,000 years after its beginning. The diffuse background

radiation over the UV - far-IR wavelength range is called the extragalactic background light (EBL) and is the second most intense background photon field to the CMB, although it is signficantly less precisely measured. The primary importance of the EBL is that it carries information about the galaxy and star formation history of the Universe, although other factors, like emission from AGN and quasars, also contributes to its SED. The EBL is characterized by two humps in its SED, a peak somewhere in the near-IR (around 1 μm) due to the direct redshifted emission of starlight, and a peak in the far-IR (around 100 μm) due to the reprocessing of this starlight by galactic dust.

Direct detection of the EBL is very difficult, mostly due to the strong uncertainty in the foreground emission of zodiacal light, which is orders of magnitude more intense than the EBL in the IR. Some measurements have been made in the Optical-UV and in the far-IR, but there is a general lack of agreement in the IR, the vast majority of the SED of the EBL. Models of the EBL based on various observational methods as well as current upper and lower limits on its intensity can be found in, e.g., [MR07, FRV08, KD10, DPR11]. Fig 3.1 shows a summary of recent experimental upper and lower limits on the EBL as well as some recent models for the EBL spectral energy density in the current epoch (z = 0), taken from [DPR11].

The EBL affects the propagation of extragalactic sources of gamma-rays in the approximate energy range of > 10 GeV, as described in section 2.1.1. Sources where a large percentage of the total power emitted at greater than these energies are primarily blazars, which are believed to be AGN whose jets are oriented along the line of sight towards the Earth. These photons are attenuated primarily through the $\gamma + \gamma \rightarrow e^- + e^+$ pair production process. In principle, observations of the energy spectrum in this waveband carries information regarding the

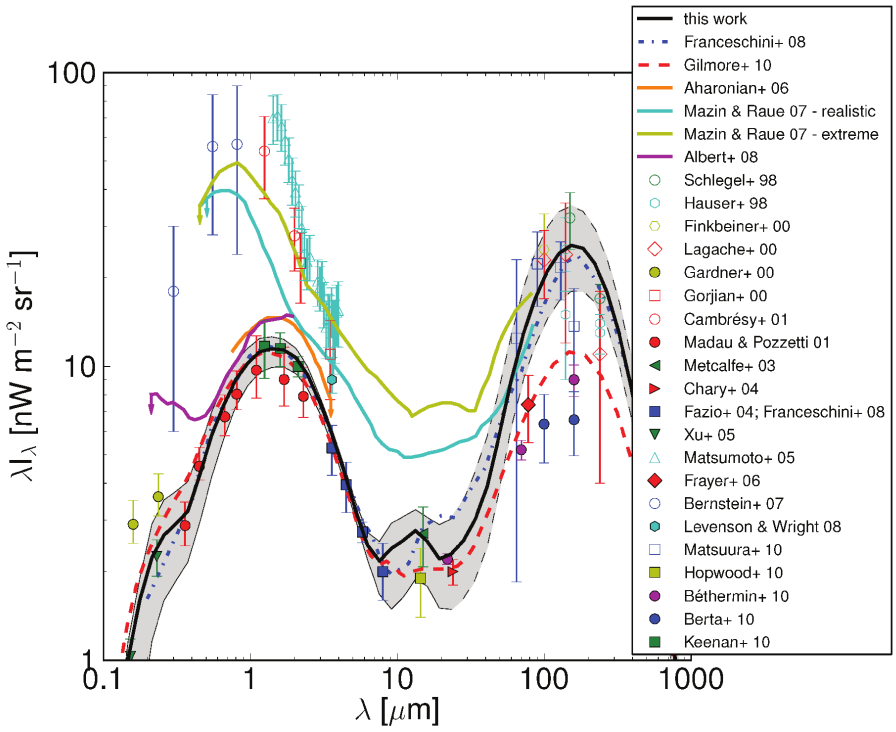

Figure 3.1 Figure taken from [DPR11], showing the various experimental limits from a vast array of measurements, as well as some recent model predictions for the EBL SED in the present epoch (z = 0).

intrinsic spectra of blazars, the intensity of the EBL, and the IGMF.

In the simulation code, to model the extragalactic background light spectral energy density, the user inputs 5 or more data points, bounded by the relatively well-measured point at 240 μm, and a wavelength in the UV, at 0.1216 μm. The code then uses a cubic spline to interpolate the value at each intermediate wavelength, and at the end points, it extrapolates a logarithmic cutoff to wavelengths < 0.1216 μm and > 240 μm. For the majority of the results in this work, a standard EBL model was used, from now on denoted as "EBL Model 1", with six energy density points at ($I_\lambda(240\mu\text{m}) = 15.9$ nW m^{-2} sr^{-1}, $I_\lambda(60) = 7.3$, $I_\lambda(12) = 2.0$, $I_\lambda(2.5) = 9.4$, $I_\lambda(0.38) = 3.2$, $I_\lambda(0.12) = 0.43$). Two additional EBL models are used prominently, one which will be called "EBL model 2" with

a substantially lower dust peak, and another called "EBL model 3", with a reduced stellar peak. These three models are shown in Fig 3.2, along with the EBL model of [DPR11], which is a typical recently computed EBL model based on recent observations.

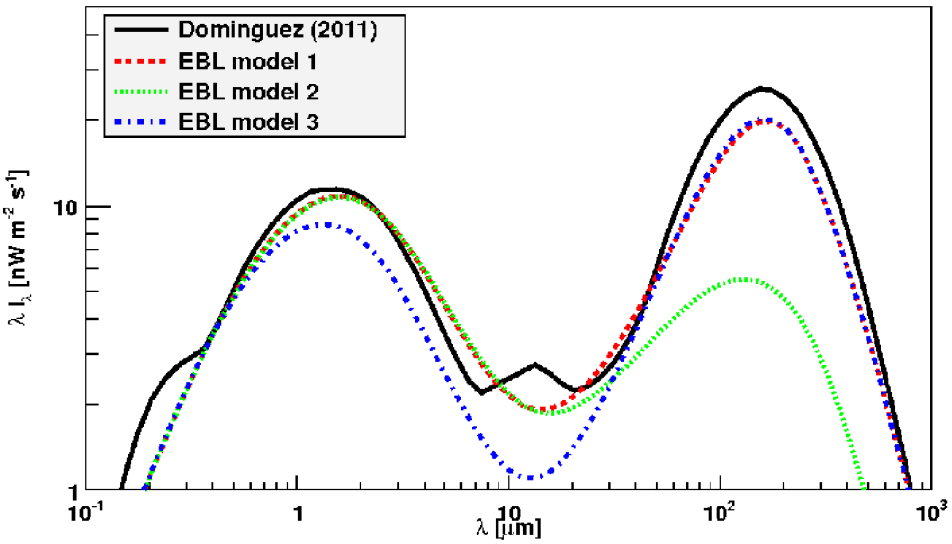

Figure 3.2 Comparison between the EBL model of [DPR11] and the 3 EBL models used in the present work-a typical EBL model (EBL model 1), one chosen with a low dust peak (EBL model 2), and one chosen with a low stellar peak (EBL model 3).

3.2 Magnetic Field Model

The observational effects of magnetic fields in the gamma-ray signal of extragalactic sources originate in the deflection of the charged particles from the trajectory of the primary photon and deflection of the direction of the secondary IC scattered photons. Different regimes of influence of the IGMF can be determined by exploring the interplay between the characteristic coherence lengths of the IGMF ($L_{\rm coh}$), the $e^{\pm}$ IC cooling length ($L_{\rm IC}$), and the distance from the interaction

point to the observer $D(z)$. For sources of interest in this work, sources with redshift $z \gtrsim 0.1$ are investigated, and so $D(z) \approx$ few hundred Mpc - 1 Gpc. In the simulations, electrons are tracked down to energies of 75 GeV, since below these energies, the amount of secondary photons with energies relevant to this study ($E > 100$ MeV) is negligible. A typical 1 TeV electron will lose its energy to IC scattering on the CMB over a characteristic length of $L_{\rm IC} \approx 0.4$ Mpc, and where $L_{\rm IC} \propto E_e^{-1}$. For the coherence length of magnetic fields, $L_{\rm coh} \gg L_{\rm IC}$, the IC scattering effectively happens in the environment of nearly constant B_{IGMF}. For $L_{\rm coh} \ll L_{\rm IC}$, the deflection of charged particles occurs in the non-coherent regime and leads to smaller deflection. In this work, the coherence length of the IGMF is conservatively chosen to be 1 Mpc, which corresponds to coherent scattering for all photons of interest (with energies > 100 MeV). It has been observed that the reversal field length of the magnetic fields in clusters of galaxies is on the scale of 10 - 100 kpc ([GR01]) and reflects the spatial scales of the distribution of plasma. Thus, the magnetic fields in the voids with significantly larger characteristic plasma distribution scales, are likely to have coherence lengths much larger than this.

The IGMF is modeled in the code as a system of cubic cells with the cube edge length approximately corresponding to the coherence length of the IGMF and magnetic field magnitudes which are equal in value but randomly oriented in direction (see Fig 3.3). To preserve cosmic variance, each cell is assigned an orientation when the first particle of the electromagnetic cascade propagates through it. If the cascade develops over a large number of these magnetic field cells, the observable effects of the IGMF are randomized. However, if the distance to the observer is comparable to the size of the magnetic field domain, the observational effects of the randomly chosen direction become significant. For this study, we analyze sources at distances greater than a few hundred Mpc ($z > 0.1$), and the

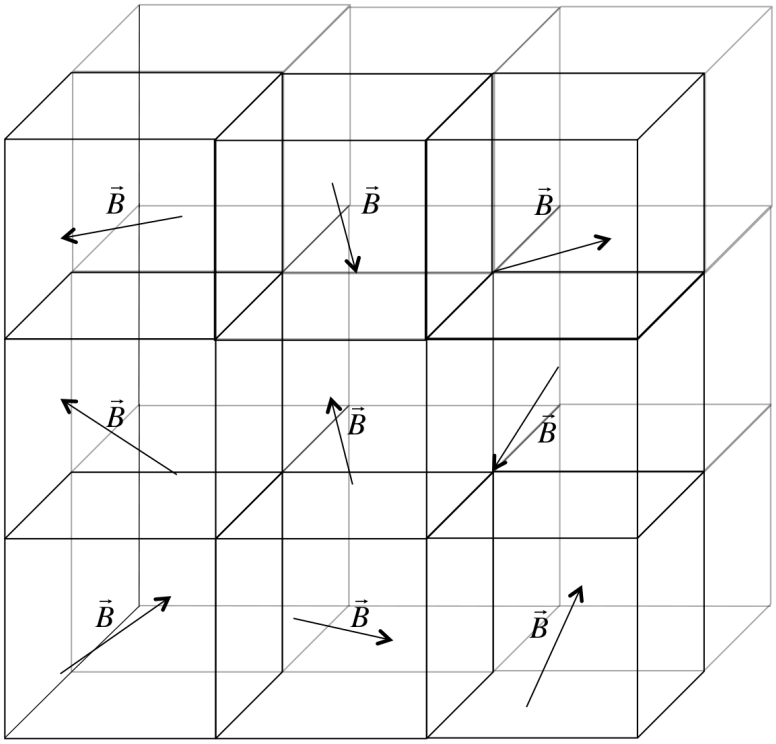

Figure 3.3 The magnetic field model employed in the code divides up space into cubic cells and seeds each one with a randomly oriented magentic field of constant magnitude.

size of the domains and the magnetic field value are evolved with the standard $(1+z)^{-1}$ and $(1+z)^2$ dependencies. The values of the magnetic field reported will always refer to the values at $z = 0$.

Figure 3.4 illustrates the mean time delay of secondary photons produced by a monoenergetic beam of 100 TeV primary photons at a redshift of $z = 0.13$. The photons arriving at the observer are integrated over an aperture radius of 10.0°. For each of the energy bins (4 per decade), the mean delay time is computed for 6 magnetic fields including the zero field case. The time delay for the latter is due to QED scattering of the secondary particles of the pair production and IC scattering processes. For a 10 GeV photon, the time delay amounts to about

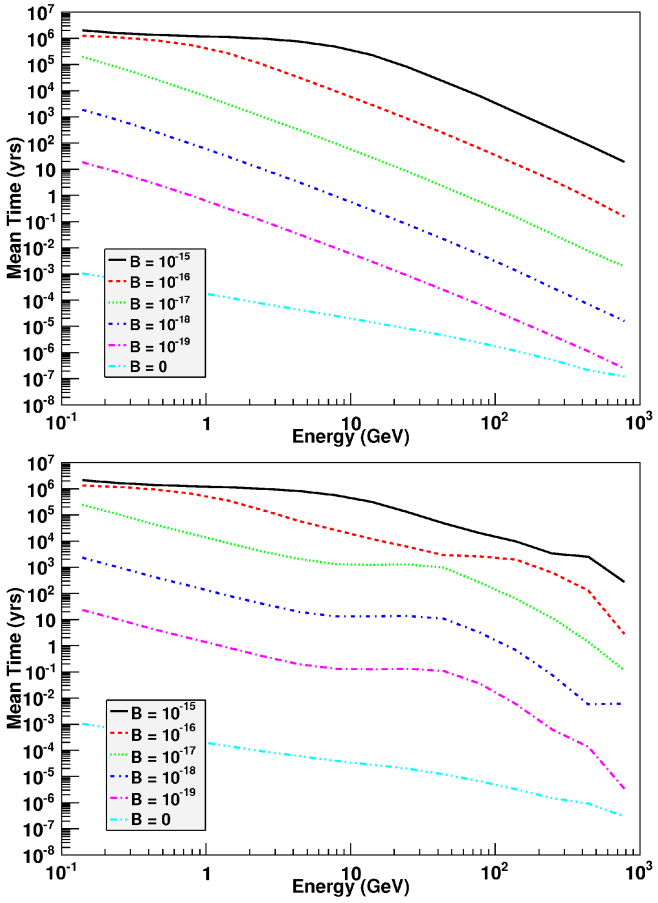

Figure 3.4 Mean time delay of secondary gamma-rays produced by a monoenergetic beam of 100 TeV photons at a redshift of $z = 0.13$, for a varying B_{IGMF} with (a) (top) the EBL excluded as a target photon field in the IC scattering of electrons and (b) (bottom) with the EBL included as a target field.

a half hour and for 0.1 GeV photons, the time delay is about 10 hours. The saturation effect at low energies is due to the aperture cutoff. Figure 3.4a shows the mean time delay with no EBL photons as IC targets in the simulations. It follows the spectrum of $T_{delay} \propto E^{-\frac{5}{2}}$, derived analytically by making several simplifications, as explained in [NS09]. Figure 3.4b shows the result when the EBL field is included. The time delay for a non-zero field of secondary photons with energies above 10 GeV is significantly increased, because electrons can move

farther from the position of pair production and still scatter higher energy EBL photons towards the observer increasing the average time delay in a given energy bin. The effect can be seen more clearly in Figure 3.5, which shows the distribution of arrival times of secondary photons in a single energy bin of 10.0 - 17.78 GeV with and without the target EBL photons for IC scattering.

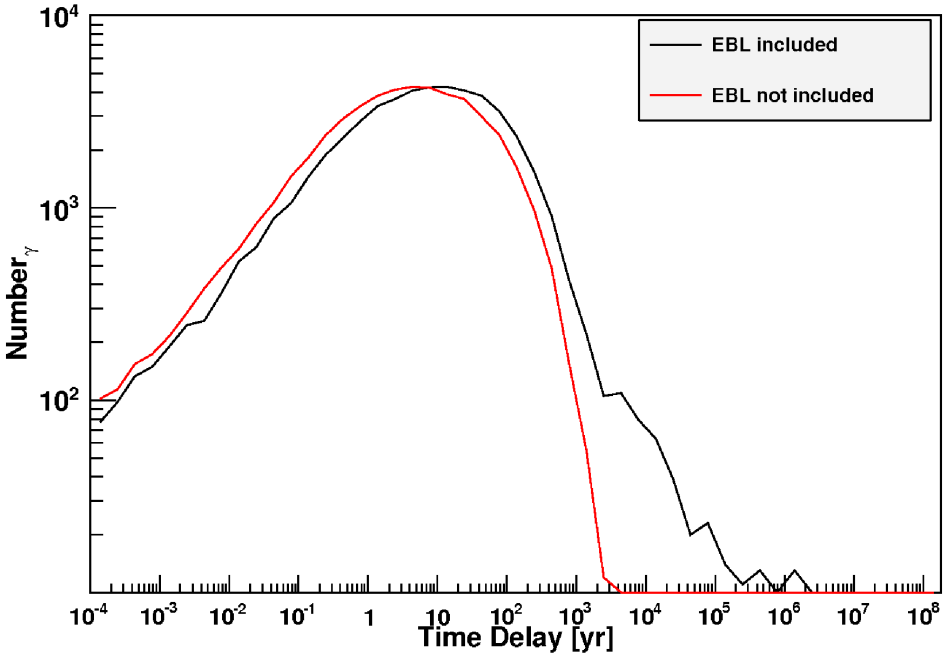

Figure 3.5 Distribution of arrival times of secondary photons in a single energy bin of 10.0 - 17.78 GeV at $B_{IGMF} = 10^{-17}$ G with and without the EBL photons included as a target for the IC scattering computation.

In the code, the magnetic field model is implemented as a C++ STL map, and when running on a cluster with a large number of parallel processors, care must be taken to ensure that no race conditions occured throughout the simulation, or to ensure that the first particle entering a cell would in fact define the cell's orientation once and for all. To ensure that this would be the case, one text file for a specific source redshift z, B_{IGMF}, and $L_{\rm coh}$containing the orientation of each cell that has ever been defined was kept as a global data file, available to all the

processes. At the start of each simulation, the information from this text file is loaded into the map, so that if the cell has previously been defined, it would be known by each process. If a particle enters a cell which has not been previously defined, the process will lock the text file, check to see if another process has already defined that cell in the meantime, and if it has not defined it, it will define the field orientation, print it to the file, then re-load the updated contents back into the map. For long coherence lengths ($L_{\rm coh}\sim$ Mpc) and secondarily for low magnetic fields ($B_{IGMF} \lesssim 10^{-15}$ G) this procedure is not a significant cost in the overall time to run the simulation. But when the above parameters of the magnetic field are not satisfied, this algorithm can be a significant fraction of the total time spent in the simulation, and the parallelization gain can decrease considerably. So this method is best suited to studies of longer coherence length magnetic fields. For magnetic fields where $L_{\rm IC} \ll L_{\rm coh}$, an algorithm that employs a random walk in deflection angle would be a more optimal solution.

3.3 Gamma Ray Source Model

In the first stage of the cascade simulation, monoenergetic beams of photons are simulated, and the parameters of each secondary photon in the cascade are saved for later use with a realistic model of an extragalactic astrophysical source of gamma rays, at the simulated redshift. This section describes the methodology and analytical formulas for converting the raw output of the simulations into a realistic source model for the emission of gamma-rays.

The highest energy of the photon escaping the local AGN host galaxy is determined by the spectral energy density of background photons of the host galaxy. A 30 TeV photon progagating through a Milky Way-like galaxy will have an optical depth of ~ 1, based on rough estimates of the energy density of the

Galaxy in the far infrared ($\sim 100\ \mu m$). Photons with energies higher than this will either be absorbed by interactions with the galactic light or the CMB, on spatial scales less than the size of the galaxy (≤ 1 Mpc). These photons will initiate cascades under the influence of galactic magnetic fields ($\sim 10^{-5} - 10^{-6}$G, see, e.g. [Wid02]) which are strong enough to isotropize the secondary photons of the cascade ([ACV94]). Thus, there is a natural high energy cutoff of around this energy, depending on the exact characteristics of the AGN host galaxy.

In the simulations, primary gamma-rays are emitted along $\vec{e}_z = (0, 0, 1)$, with a specific energy, ε, at the source redshift, z, and at time = 0. After cascading, the detected photon position on the surface of zero redshift is given by $\vec{e}_r = (\sin\theta\cos\varphi, \sin\theta\sin\varphi, \cos\theta)$, and its direction vector is given by $\vec{e}_p = (\sin\theta_p\cos\varphi_p, \sin\theta_p\sin\varphi_p, \cos\theta_p)$. At the end of a single primary photon simulation, the following secondary photon parameters are saved: E, θ, φ, T, θ_p, φ_p, where T is the delay time with respect to a primary photon. A Green's function for this process can be introduced, which describes the system's response to a single primary gamma ray of energy ε at redshift z. It is the 6-dimensional probability distribution function of the secondary photons, G and is defined from

$$dN = G(E, \theta, \varphi, T, \theta_p, \varphi_p; \varepsilon, z)\frac{dE}{E}\sin\theta d\theta d\varphi dT \sin\theta_p d\theta_p d\varphi_p \tag{3.1}$$

where N is the number of secondary photons detected with given parameters E, θ, φ, T, θ_p, φ_p and G can be determined from the simulations. From this point forward, we assume that there is axial symmetry in the distribution of source photons, which reduces the dimensionality of G so that

$$dN = G(E, \theta, T, \theta_p, \xi_p; \varepsilon, z)\frac{dE}{E}\sin\theta d\theta dT \sin\theta_p d\theta_p d\xi_p \tag{3.2}$$

where $\xi = \varphi_p - \varphi$.

The source at redshift z emits primary photons with an axially symmetric probability distribution function, so that the number of emitted primary photons, n, is given by

$$dn(\varepsilon, \tau, \theta_s) = f(\varepsilon(1+z), \frac{\tau}{1+z}, \theta_s, \varphi_s)\frac{d\varepsilon}{\varepsilon}\frac{d\tau}{1+z}\sin\theta_s d\theta_s d\varphi_s \tag{3.3}$$

where $d\tau$ is the observed time bin, related to the time bin at the source by $d\tau/(1+z)$. A photon leaving the source along an arbitrary direction, $\vec{e}_\gamma = (\sin\theta_s\cos\varphi_s, \sin\theta_s\sin\varphi_s, \cos\theta_s)$ is related to the primary photon leaving the source along $\vec{e}_z$ in the simulation by two rotation matrices

$$\vec{e}_\gamma\,(\theta_s, \varphi_s) = \begin{pmatrix} \cos\varphi_s & -\sin\varphi_s & 0 \\ \sin\varphi_s & \cos\varphi_s & 0 \\ 0 & 0 & 1 \end{pmatrix} \begin{pmatrix} \cos\theta_s & 0 & \sin\theta_s \\ 0 & 1 & 0 \\ -\sin\theta_s & 0 & \cos\theta_s \end{pmatrix} \begin{pmatrix} 0 \\ 0 \\ 1 \end{pmatrix} \Rightarrow$$

$$\vec{e}_\gamma\,(\theta_s, \varphi_s) = R_z(-\varphi_s)R_y(\theta_s)\vec{e}_z$$

Then $\vec{e}_r$ and $\vec{e}_p$ from the simulation can be rotated in the same way. Thus,

$$\vec{e}_r\,(\theta_s, \varphi_s) = R_z(-\varphi_s)R_y(\theta_s)(\sin\theta\cos\varphi, \sin\theta\sin\varphi, \cos\theta)$$

$$\vec{e}_p\,(\theta_s, \varphi_s) = R_z(-\varphi_s)R_y(\theta_s)(\sin\theta_p\cos\varphi_p, \sin\theta_p\sin\varphi_p, \cos\theta_p)$$

It is now convenient to define a projection of the momentum vector onto the observer field of view (FOV). Figure 3.6 shows the geometry of the source and observer. The projections of $\vec{e}_p$ and $\vec{e}_z$ onto the FOV of the observer are

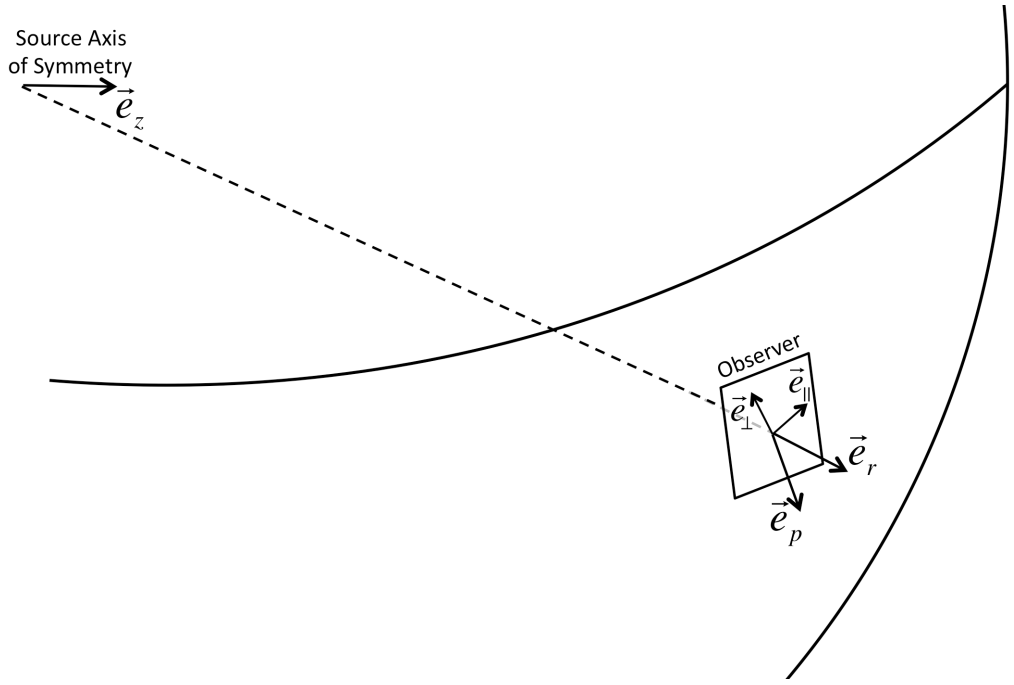

Figure 3.6 Source-observer geometry. A primary photon leaves along $\vec{e}_z$, and reaches the observer with momentum in the direction $\vec{e}_p$. The momentum vector is reconstructed in the field of view of the observer along the angle parallel ($\vec{e}_\parallel$) and perpendicular ($\vec{e}_\perp$) to the source axis of symmetry projected onto the observer surface.

$$\vec{e}_{p,FOV} = \vec{e}_p - (\vec{e}_p \cdot \vec{e}_r)\vec{e}_r$$

$$\vec{e}_{z,FOV} = \vec{e}_z - (\vec{e}_z \cdot \vec{e}_r)\vec{e}_r.$$

This allows a definition of a unit vector in the direction parallel to the source axis of symmetry projected onto the FOV

$$\vec{e}_\parallel = \frac{\vec{e}_z - (\vec{e}_z \cdot \vec{e}_r)\vec{e}_r}{\sqrt{1 - (\vec{e}_z \cdot \vec{e}_r)^2}} \tag{3.4}$$

and a unit vector perpendicular to this direction, in the FOV of the observer

$$\vec{e}_{\perp} = \vec{e}_{\parallel} \times \vec{e}_r. \tag{3.5}$$

Therefore, for this decomposition, the two angles in the direction parallel and perpendicular to the source axis of symmetry are defined by

$$\tan \vartheta_{\parallel} = \frac{(\vec{e}_p \cdot \vec{e}_z) - (\vec{e}_r \cdot \vec{e}_z)(\vec{e}_p \cdot \vec{e}_r)}{(\vec{e}_p \cdot \vec{e}_r)\sqrt{1 - (\vec{e}_r \cdot \vec{e}_z)^2}},$$

and

$$\tan \vartheta_{\perp} = \frac{(\vec{e}_p \cdot [\vec{e}_z \times \vec{e}_r])}{(\vec{e}_p \cdot \vec{e}_r)\sqrt{1 - (\vec{e}_r \cdot \vec{e}_z)^2}}.$$

For the final geometrical consideration, note that the viewing angle, θ_v is defined as

$$\cos \theta_v = (\vec{e}_r \cdot \vec{e}_z) = \cos\theta \cos\theta_s - \sin\theta \sin\theta_s \cos\varphi.$$

At this point, an expression can be derived for the total number of secondary gamma-rays arriving at the observer with time t, energy E, and with arrival angles $\vartheta_{\parallel}$ and $\vartheta_{\perp}$ detected by an instrument at viewing angle θ_v in terms of N_{γ} s^{-1} m^{-2} rad^{-2}. The total number of all secondary photons arriving at the observer surface ($z = 0$) is

$$N = \int \cdots \int dN\left(E, T, \theta, \theta_p, \xi_p; \varepsilon, z\right) dn\left(\varepsilon, \tau, \theta_s; z\right),$$

where integration takes place over the arguments of both dN and dn, at the observation surface and at the source. The photons arriving at the observer at time $t = \tau + T$ within an interval dt are given by

$$dN\left(t\right) = dt \int \cdots \int \delta\left(t - \tau - T\right) dN\left(E, T, \theta, \theta_p, \xi_p; \varepsilon, z\right) dn\left(\varepsilon, \tau, \theta_s; z\right).$$

The integration over the source azimuthal angle is trivial, because of the assumption of axial symmetry. Thus, this can be removed from the integral (see Eq 3.3) and rewritten as an observer angle, so that the solid angle of the observer can be introduced, $d\Omega_v = d(-\cos\theta_v)d\varphi_v$. Similar rewriting of the equation gives

$$
\begin{aligned}
d^6N\left(t, E, \vartheta_{\parallel}, \vartheta_{\perp}, \Omega_v\right) = dt\frac{dE}{E}d\left(\tan\vartheta_{\parallel}\right)d\left(\tan\vartheta_{\perp}\right)d\Omega_v \\
\int\cdots\int f\left(\varepsilon\left(1+z\right), \frac{\tau}{1+z}, \theta_s\right)\frac{d\varepsilon}{\varepsilon}\frac{d\tau}{1+z}\sin\theta_s d\theta_s \\
\delta\left(\cos\theta_v - \cos\theta\cos\theta_s + \sin\theta\cos\varphi\sin\theta_s\right) \\
\delta\left(\tan\vartheta_{\parallel} - \frac{\left(\vec{e}_p\cdot\vec{e}_z\right) - \cos\theta_v\left(\vec{e}_p\cdot\vec{e}_r\right)}{\left(\vec{e}_p\cdot\vec{e}_r\right)\sin\theta_v}\right) \\
\delta\left(\tan\vartheta_{\perp} - \frac{\left(\vec{e}_p\cdot\left[\vec{e}_z\times\vec{e}_r\right]\right)}{\left(\vec{e}_p\cdot\vec{e}_r\right)\sin\theta_v}\right) \\
\delta\left(t-\tau-T\right) \\
\\
G\left(E, T, \theta, \theta_p, \xi_p; \varepsilon\right)dT\sin\theta d\theta d\varphi\sin\theta_p d\theta_p d\xi_p,
\end{aligned}
$$

which is an expression for the number of photons arriving at the observer location with momentum characterized by the FOV angles $\vartheta_{\parallel}$ and $\vartheta_{\perp}$, per time, per solid angle. Since the delta functions depend non-trivially on all of the angular integration variables, performing this integral is complicated. Details of this procedure can be found in the internal memo, called "Green's Functions", but the derived formulas are given below after a few comments. 1) The restriction of θ_s, θ, $\theta_v \leq \pi/2$, is placed. This is justified for the cases of interest, since otherwise we would be considering photons that had started out moving backwards with respect to the direction of the observer, and only in the highest field cases would this be relevant, and even then it is a second order effect. It does rule out viewing angles close to perpendicular, but again this situation need not be considered for

the purposes of this research. 2) The integration parameters $\tan\vartheta_\perp$ and $\tan\vartheta_\perp$, which are projections of the momentum vector onto the FOV of the observer are converted to polar coordinates using the transformation $d(\tan\vartheta_\parallel)d(\tan\vartheta_\perp) \rightarrow \tan\vartheta d(\tan\vartheta)d\varphi_\vartheta$, so that the angles $\tan\vartheta$, φ_ϑ are now used. With these changes, the expression for the number of photons arriving at the observer with the given parameters becomes

$$\begin{gathered} d^6N(t,E,\vartheta,\varphi_\vartheta,\Omega_v) = dt\frac{dE}{E}\tan\vartheta d(\tan\vartheta)d\varphi_\vartheta d\Omega_v \\ \int\ldots\int f\left(\varepsilon(1+z),\frac{\tau}{1+z},\cos\theta_s=\cos\overline{\theta}_s\right)\frac{d\varepsilon}{\varepsilon}\frac{d\tau}{1+z} \\ \delta\left(\tan^2\vartheta-(t_\perp^2+t_\parallel^2)\right) \\ \delta\left(t-\tau-T\right) \\ G(E,T,\theta,\theta_p,\xi_p;\varepsilon)dT\sin\theta d\theta\sin\theta_p d\theta_p d\xi_p, \end{gathered} \tag{3.6}$$

where

$$\cos\overline{\theta}_s = \cos\left(\theta_v+\theta\right)\sin^2(\frac{\varphi_\vartheta-\varphi_t}{2}) + \cos(\theta_v-\theta)\cos^2(\frac{\varphi_\vartheta-\varphi_t}{2})$$

$$t_\perp = \frac{\sin\theta_p\sin\xi_p}{\cos\theta\cos\theta_p+\sin\theta\sin\theta_p\cos\xi_p}$$

$$t_\parallel = \frac{\sin\theta\cos\theta_p-\cos\theta\sin\theta_p\cos\xi_p}{\cos\theta\cos\theta_p+\sin\theta\sin\theta_p\cos\xi_p}$$

$$\varphi_t = \cos^{-1}\left(\frac{t_\parallel}{\sqrt{t_\parallel^2+t_\perp^2}}\right).$$

In order to more easily compare the model with experimental results, it is now convenient to convert this expression to a flux of gamma-rays in terms of number per time per area per solid angle. Using the relationship $d\Omega_v = A(E)/(4\pi D_L^2)$,

where D_L is the luminosity distance to the source, Eq 3.6 can be rewritten as

$$\begin{gathered} d^4F(t,E,\vartheta,\varphi_\vartheta,\Omega_v) = dt\frac{dE}{E}\tan\vartheta d(\tan\vartheta)d\varphi_\vartheta = \\ \frac{1}{4\pi D_L^2}\int\ldots\int f\left(\varepsilon(1+z),\frac{\tau}{1+z},\cos\theta_s=\cos\overline{\theta}_s\right)\frac{d\varepsilon}{\varepsilon}\frac{d\tau}{1+z} \\ \delta\left(\tan^2\vartheta-(t_\perp^2+t_\parallel^2)\right) \\ \delta\left(t-\tau-T\right) \\ G(E,T,\theta,\theta_p,\xi_p;\varepsilon)dT\sin\theta d\theta\sin\theta_p d\theta_p d\xi_p. \end{gathered} \tag{3.7}$$

With this formalism, a generic axially-symmetric source model can be used in conjunction with Eq. 3.7 to predict the flux of gamma-rays at observing angle θ_v.

3.3.1 Standard Model of Source Emission: Broken Power Law with Exponential Cutoff

In this section, we present the standard source spectral model which we used to fit the simulations to the data, particularly in chapter 6. Consider a distribution of photons, which is isotropic in its own rest frame (the primed frame). Then the differential number of photons with momentum in the interval $d^3\vec{p'}$ is given by

$$f(\vec{p'})d^3p' = f(p')p'^2dp'\sin\theta' d\theta' d\varphi'$$

where $f(\vec{p'})$ is the probability distribution, describing a photon with momentum in interval dp', and where the photon energy is $\varepsilon' = p'c$. Assume for simplicity that the distribution of the photon gas is described by a single power law with differential spectral index α and normalization constant F_0 so that the distribution becomes

$$f(\vec{p'})d^3p' = \frac{F_0}{c^3}\left(\frac{\varepsilon'}{\varepsilon_0}\right)^{-\alpha-2}\varepsilon'^2 d\varepsilon' \sin\theta' d\theta' d\varphi'.$$

Supposing that this distribution of photons is boosted along the z-axis with some bulk Lorentz factor, Γ, the distribution in the observer reference frame becomes

$$f\left(\vec{p}\right)d^3\vec{p} = \Gamma\left(1-\beta\cos\theta_s\right)\frac{F_0}{c^3}\left(\frac{\varepsilon\Gamma\left(1-\beta\cos\theta_s\right)}{\varepsilon_0}\right)^{-\alpha-2}\varepsilon^2 d\varepsilon \sin\theta_s d\theta_s d\varphi_s$$

suggesting a source model of a single power law distribution of photons in analogy with Eq. 3.3 of

$$f\left(\vec{p}\right)d^3\vec{p} = \frac{F_0}{c^3}\left(\Gamma\left(1-\beta\cos\theta_s\right)\right)^{-\alpha-1}\left(\frac{\varepsilon}{\varepsilon_0}\right)^{-\alpha+1}\frac{d\varepsilon}{\varepsilon}\sin\theta_s d\theta_s d\varphi_s.$$

There is an inherent ambiguity in modeling the highest energy ($\gtrsim 5$ TeV) end of most VHE sources, since it is usually underdetermined by the data, owing to the decreasing flux of astrophysical sources of gamma-rays at these energies and the decreasing sensitivity of current instruments. Additionally, according to the argument presented at the beginning of the current section, an exponential cutoff due to the infrared light near the galaxy is expected if high enough energy photons are prodced within these sources. To model this, we introduce an exponential cutoff factor of $\exp(-\varepsilon/\varepsilon_c)$, where ε_c is the cutoff energy so that the source model distribution becomes

$$f\left(\vec{p}\right)d^3\vec{p} = \frac{F_0}{c^3}\left(\Gamma\left(1-\beta\cos\theta_s\right)\right)^{-\alpha-1}\left(\frac{\varepsilon}{\varepsilon_0}\right)^{-\alpha+1}\exp\left(-\frac{\varepsilon}{\varepsilon_c}\right)\frac{d\varepsilon}{\varepsilon}\sin\theta_s d\theta_s d\varphi_s. \tag{3.8}$$

This four parameter fit (δ, ε_c, F_o, α) is sufficient to model the VHE part of the spectrum ($\varepsilon \gtrsim 100$ GeV). Since the energy range of interest for this study covers more than 5 decades of energy (from 0.1 GeV to $>$ 10 TeV), the high energy

part of the source spectrum ($\lesssim$ 100 GeV) is allowed to obey a power law with a different spectral index, γ, below a break energy ε_B in order to model as generic a source spectral shape as possible. The model then becomes

$$f\left(\vec{p}\right) d^3\vec{p} = \frac{F_0}{c^3}\delta^2 \begin{cases} \left(\frac{\varepsilon}{\varepsilon_B \delta}\right)^{-\gamma+1} \exp\left(-\frac{\varepsilon}{\varepsilon_c}\right) & \frac{\varepsilon}{\varepsilon_B \delta} < 1 \\ \left(\frac{\varepsilon}{\varepsilon_B \delta}\right)^{-\alpha+1} \exp\left(-\frac{\varepsilon}{\varepsilon_c}\right) & \frac{\varepsilon}{\varepsilon_B \delta} > 1 \end{cases}, \tag{3.9}$$

where $\delta = (\Gamma(1 - \beta\cos\theta_s))^{-1}$, is the usual kinematic Doppler factor. This 6-parameter gamma-ray source spectrum is given at the redshift of the host galaxy and is necessary and sufficient to satisfy the observational data of TeV blazars in both the HE and VHE regimes.

To illustrate the effects of different gamma-ray source model parameters, simulations are shown for z=0.13, B=10^{-15} G, ϵ_c = 30 TeV, $\alpha = \gamma = 1.5$. Figure 3.7 shows the observed spectra of a source with the above parameters when it is viewed at different angles and Lorentz factors. All photons arriving within an aperture of 5° around the source are integrated. The black (solid) line shows the spectrum of the prompt photons reaching the observer, which is modified by absorption on the EBL. It is assumed that this observed spectrum is the same for different viewing angles and different Lorentz factors. Figure 3.7a shows the spectrum of secondary photons when the source is viewed at $\theta_{\rm v}$ = 0°, 2°, 5°, 10° and Figure 3.7b shows the spectrum of secondary photons for Γ = 5, 10, 30, 100. Viewing a source with the same prompt differential flux energy density (dFED), but with increasing viewing angle or Lorentz factor implies the power in the jet must increase.

The higher energy end of the secondary photon spectrum ($\gtrsim$ 20 GeV) is unchanged for different viewing angles and jet Lorentz factors because photons at these energies are generated from primary photons leaving the source with nearly

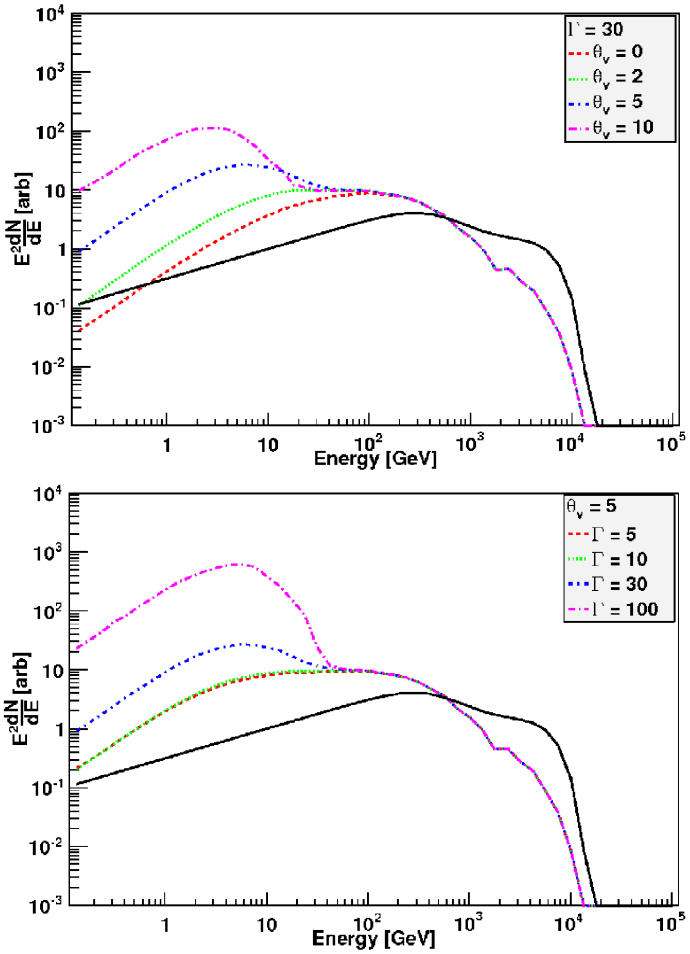

Figure 3.7 Simulations of a source at z=0.13, with $\alpha = \gamma = 1.5$, $\epsilon_c = 30$ TeV, and $B_{IGMF}=10^{-15}$ for a) (top) $\Gamma = 30$ and four different viewing angles and b) (bottom) $\theta_v = 5°$ and four different jet boost factors.

zero deflection from the angle to the observer and the flux of these photons is directly proportional to that of the prompt photons. The lower energy end of the spectrum ($\lesssim$ 20 GeV) is generated by secondary electrons of lower energies, the trajectories of which are significantly deflected from that of the primary photon producing them. Additionally, the cooling length due to IC losses increases inversely proportionally to energy, allowing significantly larger deflection angles. The position of the peak of the SED is correlated to the value of the magnetic

field, and its intensity is proportional to the overall power in the jet which increases with larger viewing angle or Lorentz factors. When the characteristic angular size of the jet becomes larger than the viewing angle ($1/\Gamma > \theta_{\rm v}$), the SED is nearly independent of the Lorentz factor.

One final example of the simulation code, which illustrates the importance of including higher order cascading in the simulations to correctly describe secondary photons with energies $\gtrsim$ 200 GeV, is presented in figure 3.8. Multiple generations of the cascade are not included in analytical and semi-analytic models out of necessity, but can be naturally accomodated in the 3D particle tracking Monte Carlo code presented in this work. Figure 3.8 shows the results of simulations of secondary photons produced for a source at z=0.3, with $\mathrm{B}_{IGMF} = 10^{-16}$ G, $\theta_{\rm v} = 0$, and $\Gamma = 10$. The two panels display different intrinsic spectra for the source; panel a) is obtained with $\alpha = 1.5$ and $\epsilon_c = 30$ TeV, and panel b) corresponds to $\alpha = 1.5$ and $\epsilon_c = 5$ TeV. Both panels show the direct dFED of the source together with the time-integrated secondary dFED, within 0.5° from the position of the source. The two lines of the secondary dFED shown on the figure are obtained with second order cascading included or not included in the simulation. It is evident that the secondary dFED $\gtrsim$ 200 GeV is strongly affected by this assumption and if this simplification is made, the Monte Carlo simulations may over-predict the total dFED in the VHE energy range.

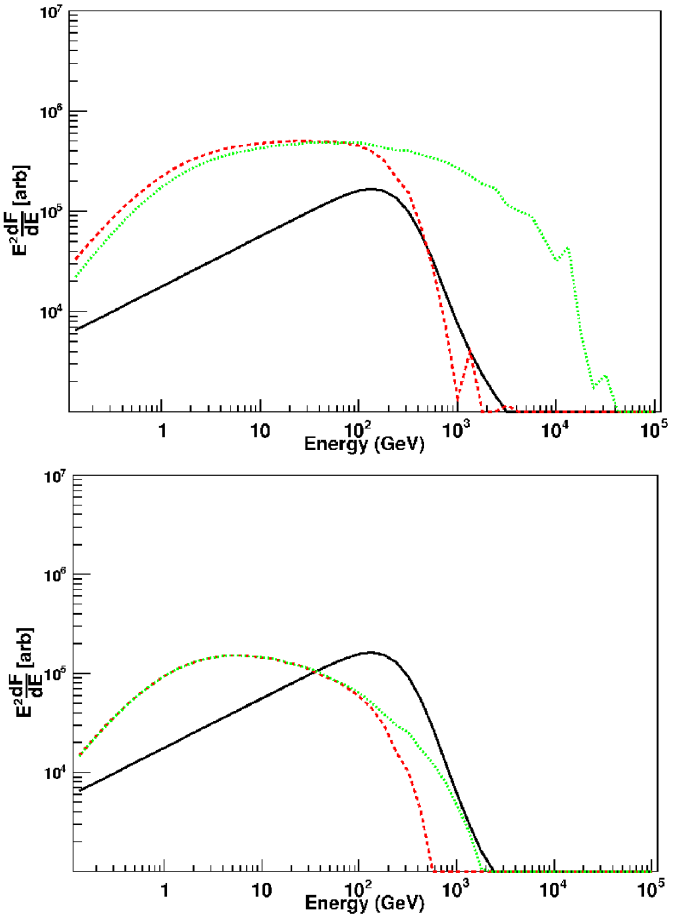

Figure 3.8 Comparison of spectra produced by both neglecting and including multiple generations in the cascade for a source at z=0.3, with $B_{IGMF} = 10^{-16}$ G, $\theta_v = 0$, and $\Gamma = 10$. (integrated over a 0.5 deg aperture). The black (solid) line is the prompt, direct spectrum, the red (long dashed) line shows the secondary spectrum produced when multiple generations of the cascade are included, and the green (small dashed) line shows the secondary spectrum when only a single generation of cascading is allowed in the simulations. Two different source spectra were used a) (left) spectral index $\alpha = 1.5$, cutoff energy, $\epsilon_c = 30$ TeV and b) (right) $\alpha = 1.5$, $\epsilon_c = 5$ TeV.

CHAPTER 4

Current Gamma Ray Instruments

To study electromagnetic cascades produced by the high energy TeV photons interacting with the background photon fields, it is necessary to sample the broad-band spectrum from MeV to TeV energies. The prompt radiation is emitted in the TeV band, usually above 1 TeV, and the sources which have a hard spectrum (with significant amount of the total power of the source emitted in the TeV energy band) will have the greatest chance of producing detectable levels of secondary cascade emission, which is typically peaked around 1 GeV. Thus, it is necessary to measure the energy density of prompt radiaiton in the TeV band, since these measurements determine the characteristics of the cascade emission in the GeV band. Such observations are carried out by two types of instruments, utilizing different experimental techniques-space-based satellites and ground-based imaging atmospheric Cherenkov telescopes (IACTs).

Space-based gamma-ray instruments, such as those aboard the past mission EGRET [TBD95] and the current mission *Fermi*, [AAA09b] detect gamma-rays through pair-conversion of the gamma-ray into an electron and positron and by measuring the geometry of the secodary electromagnetic cascade and amount of electromagnetic energy deposited into the calorimeter. The size of these instruments has been limited to $\lesssim 1$ m^2, due to the high cost of launching the detector into orbit. This collecting area combined with the typical luminosity of the gamma-ray astrophysical sources sets a practical upper limit of ~ 100 GeV,

on the energy of gamma-rays observable with such instruments due to the rapidly decreasing fluxes. The small collecting area is partially compensated for by the large field of view ($\sim$ 2 steradians) of the detector, high duty cycle, and excellent background rejection, as these instruments are designed to conduct full sky surveys.

Ground-based IACTs detect the Cherenkov light emitted by secondary particles in the electromagnetic cascades initiated when gamma-rays interact with the Earth's atmosphere. The electrons and positrons in the cascade polarize the atmosphere and thus emit Cherenkov radiation when their velocity exceeds the speed of light in the medium. Cherenkov light takes the form of a cylindrical wave propagating at an angle of $\theta = \cos^{-1}[1/(n\beta)]$ with respect to the particle's trajectory, where n is the index of refraction of the atmosphere (a function of height) and βc is the particle's speed. The observable Cherenkov light (which does not get absorbed by molecules in the atmosphere when reaching the IACT) peaks at $\sim$ 330 nm. The primary mechanisms in the development of the cascade are pair production and Bremsstrahlung radiation. The energy of the primary particle is efficiently subdivided by these mechanisms resulting in a corresponding increase in the number of particles in the cascade. This cascade grows until the particle energies fall below the threshold at which the dominant energy loss mechanism becomes ionization, which occurs around $\sim$ 80 MeV. The number of particles in the shower (above $\sim$ 80 MeV) has a logarithmic dependence on energy, and the shower maximum-the height at which the number of particles in the cascade is greatest-can be computed as a function of energy, atmospheric density, and height above sea level. For a 300 GeV photon, it would occur around a height of around 10 km. The distribution of Cherenkov light on the ground is determined by the interplay of two effects-the growing/decreasing number of particles in the cascade as it develops/decays and the changing Cherenkov emission angle as a function

of atmospheric height. The combination of these effects leads to the distribution of Cherenkov light within a pool with radius of $\sim$ 130 m at sea level, which is relatively insensitive to the primary particle energy. The corresponding area of the Cherenkov light pool, $\sim 10^5$ m^2, determines the characteristic collecting area of the IACT. In the following two sections, features of the *Fermi*-LAT instrument and the VERITAS IACT important for this study are described.

4.1 Fermi-LAT Overview: A HE Gamma-Ray Detector

For the correct interpretation of *Fermi* data, it is important to know some details of how a photon interacts with the LAT. The primary instrument aboard the *Fermi* satellite is the Large Area Telescope (LAT), which is a wide field of view (FoV), high energy gamma-ray imaging detector, sensitive over the approximate energy range of 20 MeV to $\sim$ 100 GeV. *Fermi* is on an elliptical orbit located at a height of about 565 km off the surface of the Earth at a 25.5° inclination, orbiting the Earth in around 96 min. It is pointed away from the Earth at all times, so that the Earth does not block its view of the sky. The primary observation mode for *Fermi* is the "scanning" mode in which the normal to the front of the instrument on alternate orbits is pointed from +35° from the zenith to -35° from zenith on the subsequent orbit. In this way, every 3 hours, nearly uniform sky exposure is achieved. When a strong GRB occurs, *Fermi* orients itself to point in the location of the burst for a few extra hours to collect data. *Fermi* collaboration publications, such as [AAA09b] describe the detailed technical specifcations and operation of the LAT. Here, some important features of the instrument for the detection of gamma-rays and our study of intergalactic cascades are outlined.

A photon entering the LAT will pass through the *Anti-coincidence detector* (ACD) enclosing the instrument and interact with an atom inducing electron

positron pair production in the LAT Tracker-converter [ABB07]. The Tracker is segmented into 16 "towers" or modules arranged in a 4 by 4 configuration in the LAT. Gamma-rays entering through one of these 16 modules will strike a nucleus within one of the 16 high-Z tungsten plane layers and produce an electron-positron pair (see Fig. 4.1). The charged particles subsequently pass through up to 36 planes of position-sensitive Silicon detectors interspersed throughout the tower behind each tungsten plane. As the charged particles propagate through the module, their "tracks" are recorded and their trajectories point back to the direction of the gamma-ray that entered the tracker.

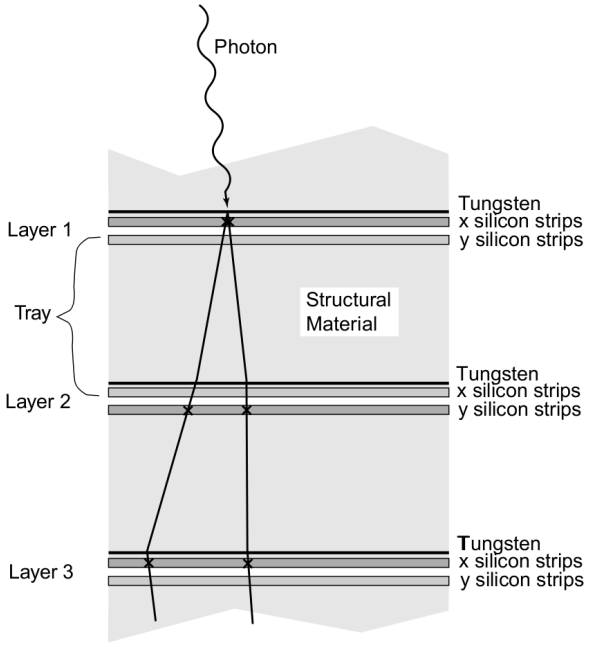

Figure 4.1 Depiction of the measurement of gamma-ray pair conversion within a tracker module. Most of the angular information comes from the first two points on the track, because multiple scattering in successive layers of Tungsten degrades the angular resolution. (Figure taken from [ABB07]).

The instrument was designed to balance the need for good angular resolution to low energy and increased effective area to higher energy gamma-rays. Because

the overall PSF is primarily determined by the $\sim 1/E$ dependence on multiple scatterings within a tungsten layer in the tracker, the thinner the tungsten converter planes are, the better the PSF will be, but the reduced photon absorption optical depth of the detector will lower the overall collecting area at high energies. To achieve this balance, the tracker was divided into a "front" region consisting of 12 thin converters (0.03 radiation lengths each) to optimize the PSF at low energies, and a "back" region where each of the 4 tungsten plane converters are ~ 6 times thicker than the front, maximizing the effective area at the expense of less than ~ 2 in angular resolution (at 1 GeV) for photons converting in this region. The LAT sensitivity to point sources is approximately equally balanced between the front and back sections.

Upon exiting the tracker, gamma-rays enter the *Calorimeter* located underneath the tracker modules. The primary purpose of the LAT calorimeter (for a full technical description, see [JGP97]) is to measure the energy deposited by the gamma-ray into the electromagnetic cascade of the electron-positron pairs. The Calorimeter also images the shower development profile and applies shower leakage corrections, which provides an additional background discrimination. The total vertical depth of the calorimeter is 8.6 radiation lengths, for a total instrument depth of 10.1 radiation lengths. Each of the 16 calorimeter modules (attached to each tracker module) consists of 96 long, narrow CsI scintillators, stacked in 8 layers of 12 crystals each of alternating orientation to determine the location and spread of the deposited energy of the showers. This shower imaging capability and photon absorption optical depth enables the high energy reach of the LAT and contributes to efficient background rejection. For the higher energy showers in particular, the energy resolution is greatly enhanced through the application of shower leakage corrections.

The LAT ACD encloses the tracker and calorimeter and operates as a charged-particle veto against cosmic rays entering the tracker [MHO07]. Incoming gamma-rays pass freely through this thin plastic scintillator material, while cosmic rays cause a flash of light, allowing for effective cosmic ray discrimination. It is composed of 89 individual sections surrouding the top and four sides of the LAT, requiring a total active area of ~ 8.3 m^2. The LAT specification of keeping the residual background of "fake photons" at the level of < 10 % of the diffuse γ-ray background intensity, combined with the fact that the cosmic rays outnumber gamma-rays by on average a factor of $10^3 - 10^5$ throughout the energy range of LAT sensitivity requires that the total cosmic ray rejection must be greater than about a factor of 10^6. Since protons outnumber electrons by about a factor of 10^2, the cosmic ray proton rejection must be greatest. Since the LAT calorimeter and tracker provide suppression of the proton background at the level of $> 10^3$, the ACD provides the additional factor of 10^3. Since gamma-ray and electron-induced showers look very similar in the calorimeter, it cannot be used to reject the electron background. The tracker provides relatively little rejection, since many gamma-ray events would be lost to achieve a high degree of electron/gamma-ray separation. Thus, the ACD provides the bulk of the electron rejection, and the overall efficiency for detecting a singly-charged relativistic particle entering from the top or sides is at the level of 0.9997.

Data from the Tracker, Calorimeter, and ACD subsystems are sent to the Data Acquisition System (DAQ), which implements the multi-event trigger to provide onboard event processing. The DAQ has two other purposes-to run filter algorithms to reduce the number of downloaded events and to rapidly search for transients. The onboard processing of events is designed to reduce the event rate from $2-4$ kHz to ~ 400 Hz that is then downloaded for processing on the ground.

In this work, we make use of the LAT data and its performance characteristics in two ways. First, we simulate the LAT response to the electromagnetic cascades which we simulate with the given properties of the source to infer characteristics of the intergalactic magnetic fields. For this, we use the high level public performance characteristics of the LAT, such as the effective collecting area and point spread function. We also use the LAT data to infer the spectral, angular, and temporal characteristics from real astrophysical sources, in which case, we use high level data products provided by the LAT team to the public. Here we summarize the relavant LAT performance and data analysis products.

4.1.1 Fermi-LAT Performance

The main performance characteristic is the Intsrument Response Functions (IRFs) which characterizes the LAT response-such as effective collecting area, point spread function, and energy resolution-as a function of photon energy, incidence angle, conversion point within the instrument, and other important parameters. This thesis utilizes the IRFs produced by the LAT team, which corresponds to the analysis *P7SOURCE_V6* was optimized for point-like sources and the production of the second LAT source catalog (2FGL).

The LAT effective area sensitively depends on the gamma-ray energy and the polar angle of incidence from which it enters the LAT, but also depends weakly on the azimuthal angle of incidence. Figure 4.2 displays the effective area vs Energy for photons of normal incidence, as well as the effective area vs. polar angle of incidence (θ), for front and back-detected photons individually and as the total (front plus back).

Unlike previous versions of the IRFs, the LAT Point Spread Function (PSF) for version P7SOURCE_V6 is derived using in-flight data, and does not include

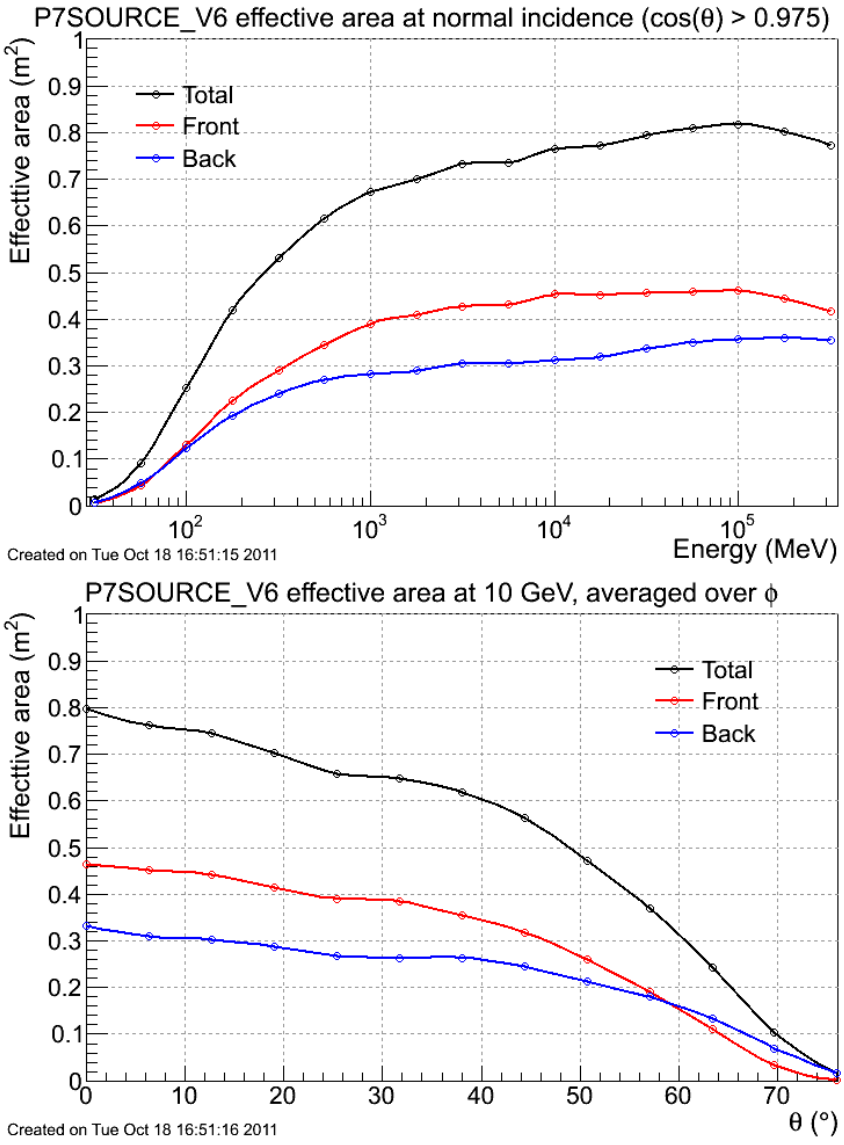

Figure 4.2 LAT Effective Area curves as a function of various parameters. (top) The Effective Area as a function of energy for photons impinging on the LAT at an angle defined by $\cos\theta > 0.975$. (bottom) Effective Area as a function of polar incidence angle, for photons of energy 10 GeV.

any dependence on the off-axis angle, which has implication for studies of HE transients, which we do not conduct in this work. The 68 % and 95 % containment angles of the reconstructed incident photon direction for normally incident photons is shown in Figure 4.3. The total (front plus back) 68 % containment angle of the PSF falls roughly linearly (in log-angle log-energy space) from about 6° at 100 MeV, to about 0.4° at 3 GeV, then slowly varies to around 0.2° at 100 GeV, comparable to the PSF of most IACTs.

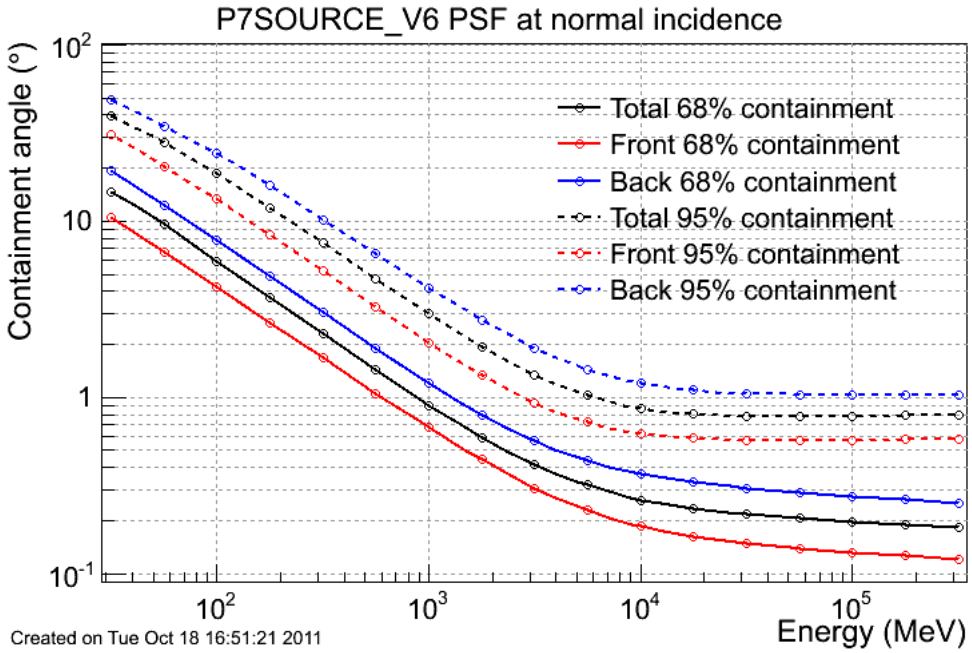

Figure 4.3 LAT PSF as a function of the incident photon energy for front and back converted photons and the total.

The LAT energy resolution is the parameter which demonstrates the ability of the LAT to correctly reconstruct the initial energy of incoming photons. Figure 4.4 shows a plot of the 68 % containment of the reconstructed incoming photon energy as a function of energy for normally-incident photons. The energy resolution very weakly depends on whether the photon converted in the front or back section of the tracker, but it does depend strongly at lower energies until

about a GeV, at which point, it remains approximately constant at the 10 % level until 100 GeV. For higher energies, the energy resolution degrades.

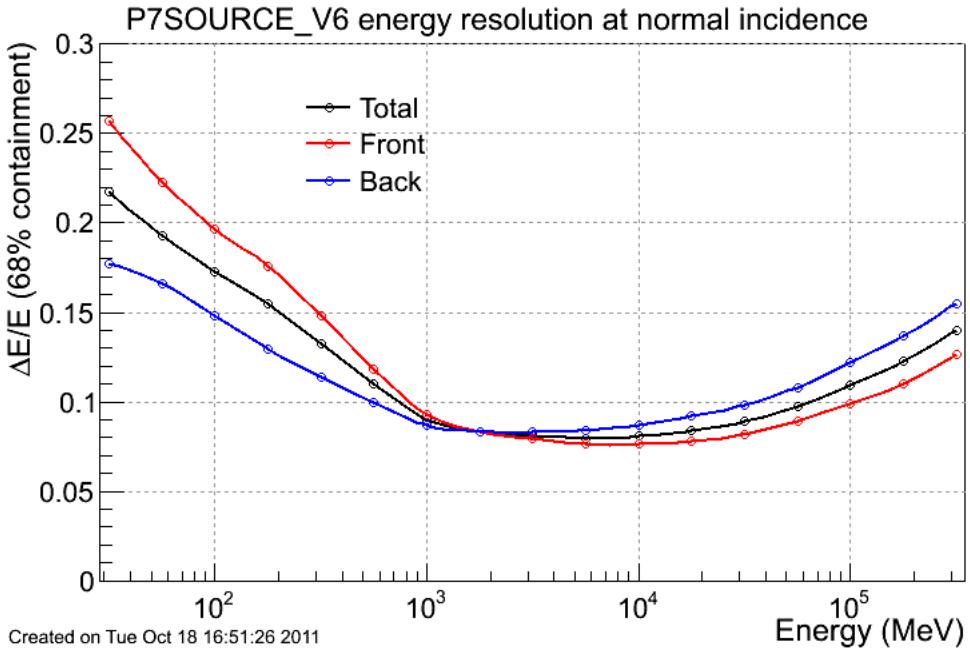

Figure 4.4 LAT Energy Resolution

4.1.2 Fermi-LAT Data Analysis

The *Fermi*-LAT team provides the scientific community with the *event data files* (EDF) and *spacecraft data files* (SDF). The EDFs contain information about the detected photons such as the energy of the event, RA and DEC, galactic coordinates (which are utilized to later compute the galactic and extragalactic diffuse backgrounds), the arrival time, the measure of photon identification probability (event class), instrument pointing and the Earth's position at the time of the detection, and some other parameters. The spacecraft data files provide information on the pointing and exposure of the spacecraft in a particular direction.

In addition to the high level data products, EDFs and SDFs, the LAT team

provides a suite of science tools to perform the source detection, flux determination, and spectral modeling of *Fermi*-LAT sources. These science tools employ an unbinned maximum likelihood optimization technique[1], to determine various parameters of a source in question, given the current galactic and extragalactic diffuse background models derived from simulations, and some parameters of all astrophysical sources in its neighborhood, such as the location in the sky and constraints on spectral properties (normally within a 10° field of view). The steps required for source detection and flux determination are as follows:

1. Select data from EDFs based on set of cuts on pointing with respect to the Earth, spacecraft orientation, etc.

2. Generate raw count maps from the EDFs 4.5

3. Compute exposure map using SDFs

4. Create a list of sources within the 10° neighborhood of the source in question utilizing the LAT two year point source catalog[NAA12], which includes spectral properties in addition to the coordinates of the sources.

5. Define parameters of the source in question e.g. spectral flux, spectral index or a different Spectral Energy Density.

6. Run the *gtlike* tool to obtain a global fit of the model of the source in question and its neighborhood sources to the data.

At the completion of these steps, parameters of the sources (such as integral flux and spectral index) are estimated utilizing the maximaum likelihood method. These data together with the TS value, which is approximately equal to σ^2 in the regime when the number of counts is much larger than 1, are produced.

[1] http://fermi.gsfc.nasa.gov/ssc/data/analysis/documentation/Cicerone/Cicerone_Likelihood/

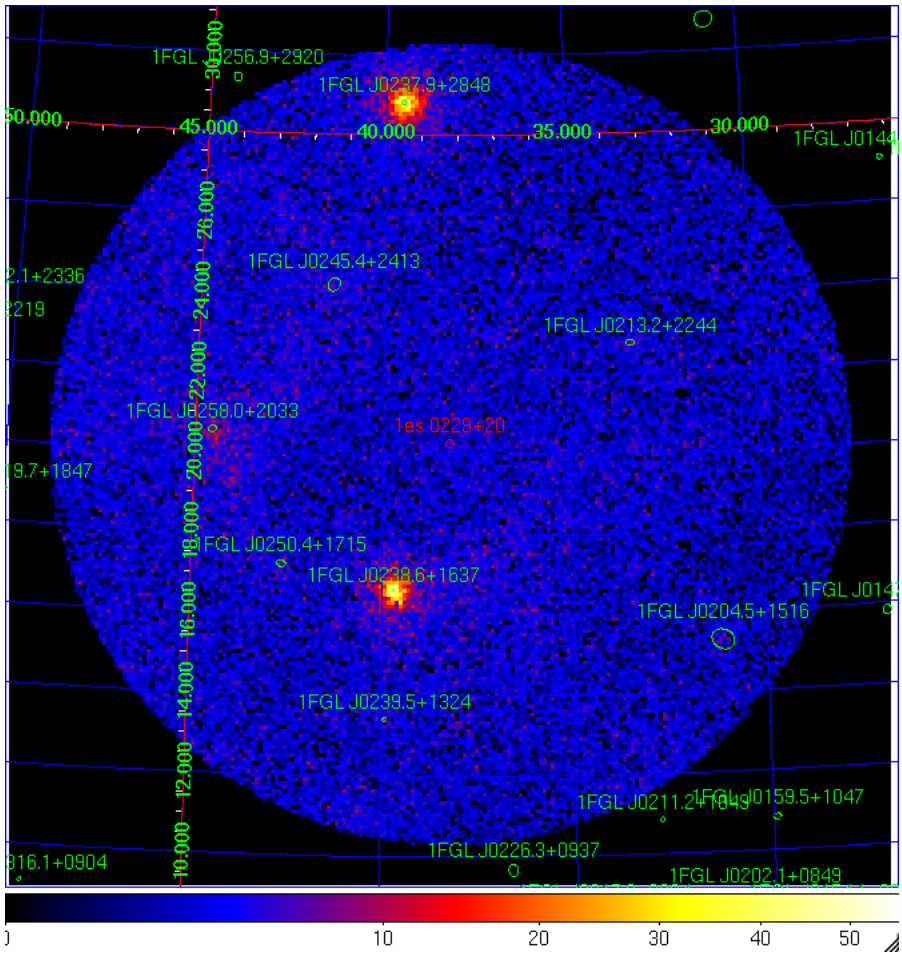

Figure 4.5 Counts map of source 1ES 0229+200 for photons with energy between 200 MeV and 300 GeV. Overlaid on the counts map are the neighborhood sources from the LAT 2 year point source catalog, along with the RA and DEC in degrees.

In this work, we make frequent use of the source properties in individual energy bins. The size of the energy bin is always chosen to be much larger than the LAT energy resolution. The upper bound on the bin size is typically set by the requirement that the number of photon counts is much larger than one and there is a reasonable expectation that within a given energy bin, the flux can be approximated by a simple power law. To satisfy these requirements, we have chosen the size of the bins to be between one and two bins per decade. To

determine the spectral parameters of the source in each energy bin, the following steps are performed:

1. Select events with energies in the given bin from the EDFs
2. Fix all background sources to their fluxes and spectral indices found in maximal likelihood optimization of the source and its neighborhood over its entire energy range.
3. Run the *gtlike* tool to determine the spectral parameters of the source in question in the given bin.

The last step can be performed using three different strategies. a) Both spectral index and integral flux in the bin are free parameters for optimization b) the spectral index is fixed to the value in the fit for the full energy range while the integral flux remains a free parameter c) the spectral index is fixed to the value derived from simulations of the source in question, while the integral flux is a free parameter. The last strategy c) is particularly important for the data analysis developed by us in this study, and it is different from strategy b), which is normally used for the derivation of the source spectral energy density utilized by typical LAT data users.

4.2 IACT (VERITAS) Overview: A VHE Gamma-Ray Detector

In this work, we utilize the observations of three major ground based gamma-ray observatories VERITAS[2], HESS[3], and MAGIC[4]. An overview of these in-

[2] https://veritas.sao.arizona.edu/
[3] http://www.mpi-hd.mpg.de/hfm/HESS/
[4] https://magic.mpp.mpg.de/

struments is provided in this section, based on the example of the VERITAS observatory. A significant fraction of the data used in this study was obtained by VERITAS and analyzed by us and our collaborators. VERITAS is an array of four IACTs located at the base camp of the Fred Lawrence Whipple Observatory in southern Arizona, 1268 m above sea level (see Fig 4.6). In the following, we describe the major hardware and online software components, summarize the VERITAS performance, and explain the generic features of the VERITAS data reduction and data analysis chain.

Figure 4.6 VERITAS ground based gamma-ray observatory installation at the Fred Lawrence Whipple Observatory in Southern AZ.

4.2.1 The VERITAS Instrument

The VERITAS observatory consists of 4 IACTs which detect a short flash of UV light with a duration of about 6 ns which is produced by the secondary particles in the electromagnetic cascade in the atmosphere. The cascades may be generated by gamma-rays, but also by the much more abundant (by at least a factor of 10^4) cosmic rays-electrons, protons, and heavier nuclei. The duration of the pulse is relatively independent from the originating particle type, and mostly depends on the atmospheric density profile and on the distance of the shower core (the location where the gamma-ray would strike the ground if it were to pierce through the atmosphere) from the telescope observing it. The discrimination power of the IACTs comes from the technology known as imaging. In short, each IACT makes a photograph of the electromagnetic cascade, with an exposure of roughly 10 ns, and with the imaging resolution determined by the pixel size of the camera. The VERITAS camera contains 499 photomultiplier tubes (PMTs), with a physical diameter of 2.86 cm and angular separation of 0.15°. As shown through simulations, gamma-ray initiated showers and hadronic cosmic ray initiated showers have a very distinct morphology (see Fig. 4.7), and therefore, they can be efficiently distinguished based on the analysis of the recorded images. Further advancement of the imaging atmospheric technique has been accomplished through simultaneous imaging of the cascades from multiple positions by several telescopes, which is known as stereoscopic observations. Highly azimuthally asymetric hadronic showers-due to a large transverse momentum of secondary products acquired in the hadronic interactions-results in significant differences of the image of a hadronic cascade viewed from different directions. QED interactions which govern the development of photon cascades (and unfortunately also by cascades initiated by electrons and positrons) produce a highly collimated

structure in all images. Figure 4.8 shows the difference to illustrate the point. The pixel size of the camera needs to be small enough to resolve structures in the images of the cascades, and for the current generation of IACTs it is limited by the desired telescope cost. With the given pixel size, the optical system (OS) of the telescope must meet the minimal requirement to not degrade the imaging resolution. From the point of view of an optical telescope, an IACT is a single light collector with a very large aperture $\gtrsim$ 10 m to detect sparse Cherenkov photons from atmospheric cascades.

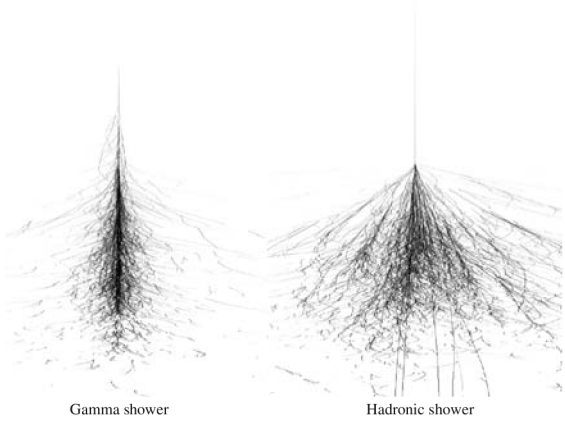

Figure 4.7 Simulation of a gamma ray shower and hadronic shower in the atmosphere. In general, the gamma shower is compact and to lowest approximation axially symmetric about the direction of the primary. Hadronic showers are irregular and may contain electromagnetic subshowers (simulation by [Ber08]).

Misalignment of mirrors is primarily due to limitations in the alignment technique as well as gravitational deformations of the OS which change as the telescopes slew in elevation and shift the mirrors out of alignment. The mirror alignment is configured to achive the optimal PSF at 65° elevation where most observations are made. The light collected by the optical system is focused into the camera, which contains 499 photomultiplier tubes (PMTs), with a physical diameter of 2.86 cm and angular separation of 0.15°.

Each VERITAS telescope utilizes the segmented Davies-Cotton optical system [DC57], with one primary optical reflector, which consists of 342 identical hexagonal mirror facets having a total mirror area of $\sim$ 106 m^2. Each mirror facet is 61 cm edge-to-edge with a spherical figure of radius of curvature of 24 m. The glass mirrors are coated with anodized aluminum that achieves 85 % reflectivity between 280 nm - 450 nm and 92 % reflectance at 320 nm [RIP08]. The size of the primary mirror and the reflectivity have direct implications on the energy threshold of the observatory.

The ideal point spread function (PSF) of the VERITAS OS has a FWHM of 0.037° and 0.088° for field angles of 0 and 1 degree respectively. At the edge of the VERITAS camera field of view (field angle of 1.75 deg), the PSF is comparable to the pixel size of 0.15 deg. Due to non-idealicities in the OS, the FWHM is generally larger than its theoretical ideal value with misalignment of the individual mirror facets as the primary cause of this [FV05]. Normally, a telescope is aligned at 65° elevation, where most of the observations are made. As the telescope moves in azimuth and elevation, gravitational deformations in the telescope structure

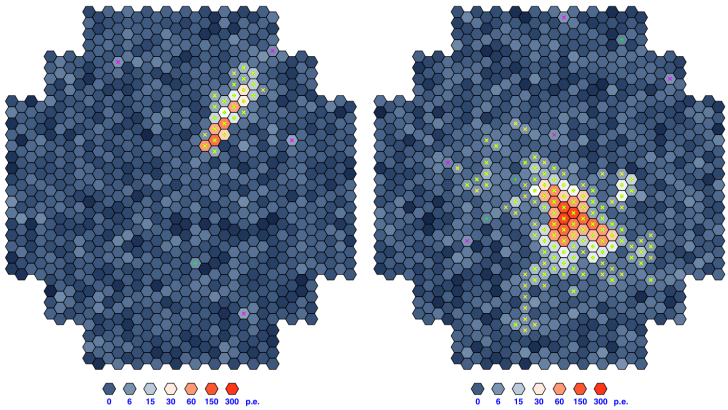

Figure 4.8 Difference between gamma ray and cosmic ray showers as imaged in the focal plane of the telescope camera (simulation by [Ber08]).

relative to the 65° position induce tolerable degredation of the PSF. The angular resolution of the ground based IACT observatories, or gamma-ray point spread function, represents a very important performance parameter for this study. It is determined not only by the pixel size, optical psf, and imaging resolution but also by the number of telescopes observing an event. Typically, a high gamma-ray angular resolution can be achieved by applying geometry selection criteria. However, this is done at the cost of reduced gamma-ray collecting area.

The VERITAS cameras utilize fast electronics to record signals from the PMTs to determine the charge which is proportional to the number of Cherenkov photons collected by a pixel. Each PMT pulse is amplified, and copies of it are sent to both the trigger and the data acquisition (DAQ) subsystems. To optimize the detection of the short-duration Cherenkov flashes of light from cascades in the atmosphere, a three-level trigger system is employed by VERITAS. The three levels of the trigger system operate at the pixel level, camera level, and array level respectively, and the main goals of the trigger are to reject night sky background fluctuations and muons which are characterized by rings or incomplete arcs of light-rather than compact patches-in the image. For each event that passes the trigger, the arrival time of the photons determined by the GPS clock shared between telescopes is recorded with an accuracy better than 1 μs. The input to the VERITAS DAQ system is a second copy of the amplified signal from the PMT. For events which pass the array trigger, a readout sequence is initiated, and the digitized PMT waveform, the pixel trigger pattern, the array event number, and other parameters are collected into a single "event" and compressed into a single raw VERITAS Bank File (VBF) format for each data run. A typical VBF file for a 20 minute run is about 4-6 GB in size, depending on the array trigger rate. These raw VBF files then become the input to the VERITAS analysis software.

4.2.2 VERITAS Performance

The performance indicators for each of the three current generation IACT observatories (VERITAS, HESS, and MAGIC) are similar, although there are some performance differences which have very little effect on the detection of electromagnetic cascades from TeV gamma-rays. In this section, the sensitivity and performance of VERITAS is described. The main performance parameters of VERITAS are summarized as the following:

- Energy range: $\sim$100 GeV - $>$ 30 TeV
- Energy resolution: $\sim$15 % at 1 TeV
- Peak effective area: 10^5 m^2
- Angular resolution: 68 % containment of 0.1° at 1 TeV, 0.14° at 200 GeV
- Source localization: 50 arcseconds
- Point source Sensitivity: 1 % Crab-like source in $<$ 30 hours, 10 % Crab in 30 min[5].
- Observation time per year: 750 hours of quality data.

These performance parameters of VERITAS are slightly affected by several quantities which will vary from source to source-the zenith angle, azimuthal angle of the observations, the energy spectrum of the gamma-rays being observed, and the night sky background rate (affected by cloud cover, moonlight, stray light, etc.). The effective area is the detector cross section to a uniform gamma-ray flux. Figure 4.9 shows the effective area as a function of energy at three

[5]The Crab Nebula is the standard candle in VHE astronomy, characterized by a power law spectrum and consistently producing a relatively constant rate of VHE gamma-rays.

different zenith angles for two different types of analyses: "standard cuts" and "soft cuts". The standard cuts are derived for the detection of sources with harder spectral characteristics like the Crab Nebula, while soft cuts are tuned to detect astrophysical sources with significantly softer spectrum (greater relative flux at lower energies), which is a typical characteristic of extragalactic sources. The effect of these cuts will be further described in the following section.

The VERITAS point spread function (PSF) is a measure of how well the instrument can reconstruct the direction of incident gamma-rays. Figure 4.10 shows a plot of the 68 % containment radius of gamma-rays derived from simulations for observations made at a zenith angle of 20°. The black line illustrates the PSF of standard cuts and the red line is derived for soft cuts.

The VERITAS energy resolution is the ability of the instrument to correctly reconstruct the true energy of the gamma-ray, and is of critical importance to measuring the spectrum of a source. For typical VERITAS analyses, the spectral reconstruction begins around an energy of about 150 GeV (effective instrument energy threshold), and usually runs out of statistics around 10 TeV. Figure 4.11 shows the VERITAS energy resolution in terms of the percent accuracy vs. the true energy of incident gamma-rays at a zenith angle of 20°. For most of the relevant energy range, the energy resolution remains around 15 - 20 %.

4.2.3 VERITAS Data Analysis

The raw "event" data, or collections of the readout of all the PMTs within a given time interval defined by the trigger recorded by VERITAS and saved to the VBF files, become the input for the analysis of gamma-ray data. The analysis of VERITAS data which becomes the basis of collaboration publications is typically done using one of the two standard analysis packages of the collaboration:

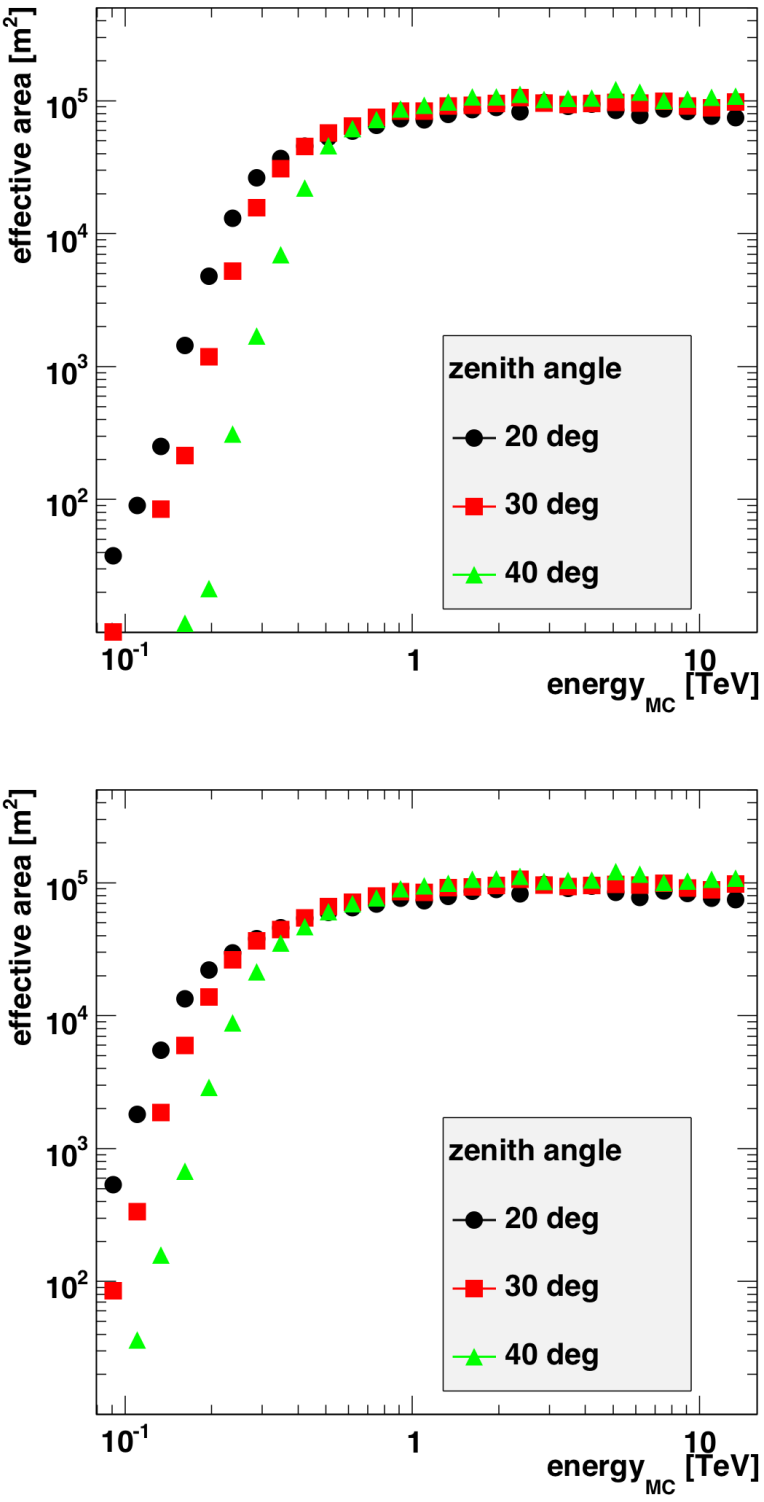

Figure 4.9 VERITAS effective area for three different zenith angles with (top) standard cuts analysis and (bottom) for soft cuts analysis.

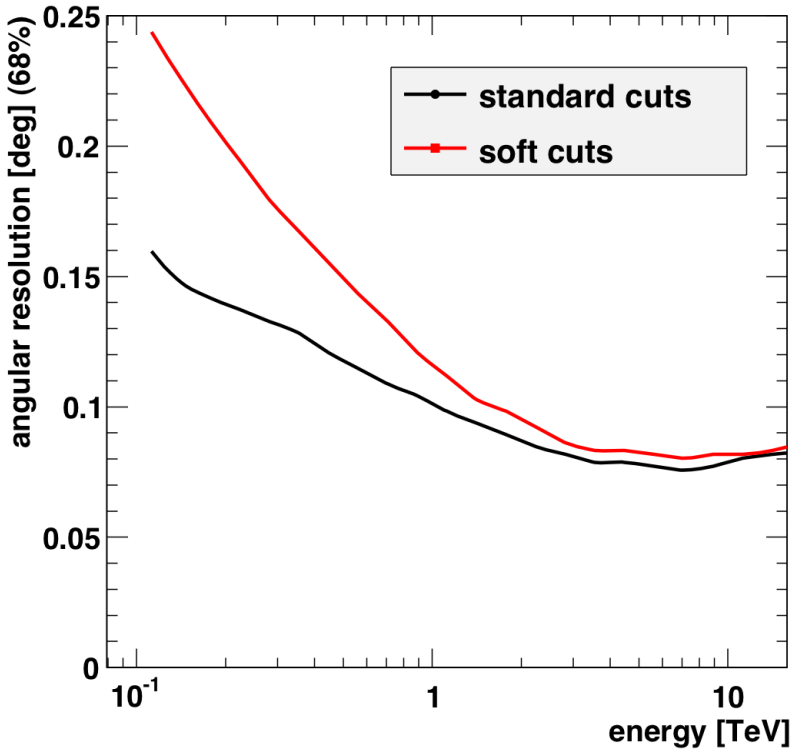

Figure 4.10 VERITAS Angular Resolution plot as a function of the incident photon energy for both standard cuts and soft cuts.

the VERITAS Gamma-Ray Analysis Suite (*VEGAS*) or *EventDisplay*. In what follows, some generic features of the analysis of VERITAS data relevant to the study of the secondary cascade emisison from photons interacting in intergalactic space are described.

The main goal of the analysis of raw data from an IACT is to determine which images of atmospheric particle showers originated from the much more numerous cosmic ray nuclei, and which were initiated by gamma-rays. Because energetic cosmic rays undergo hadronic interactions with the particles in the atmosphere producing neutral and charged pions, the image of a hadronic shower differs from that of a gamma-ray shower which is entirely electromagnetic. This is primarily

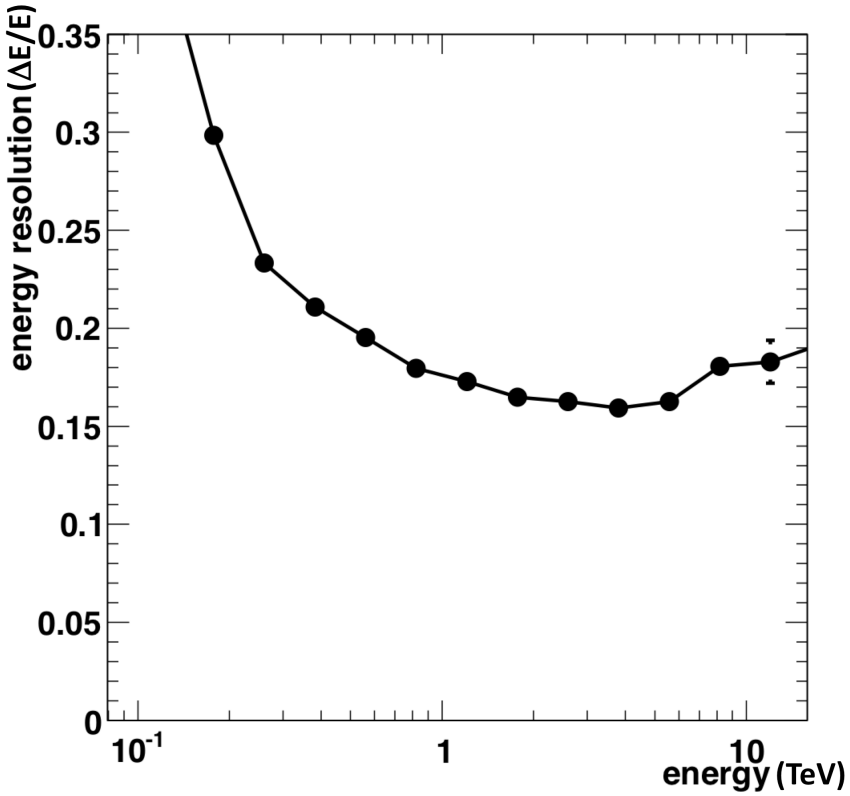

Figure 4.11 VERITAS Energy Resolution plot as a function of the incident photon energy.

due to the larger transverse momentum transfer acquired in hadronic interactions, resulting in broad and irregularly shaped shower images, as discussed in section 4.2.1. Because of these differences, suitable "cuts" can be optimized based on Monte Carlo simulations to preferentially select gamma ray showers and reject cosmic ray showers. The efficiency of such rejection is relatively high, on the order of 10^3, and it depends on the energy of the event. The set of cuts identifying cosmic rays and gamma-rays is collectively known as particle discrimination cuts. After the application of these selection cuts, the data set of reconstructed gamma-rays is used to derive source significance, spectral properties, light curves, and other analyzed parameters given enough statistics. The analysis is typically

performed as follows:

- After lower-level *image cleaning* is performed to extract a uniform image of the shower, they are parameterized to then calculate the direction, shower core location, and energy of the shower-initiating particle.
- The source and background are modeled based on the distribution of reconstructed event parameters.
- A subset of events is chosen to extract the small subset of events most likely to have been originated by gamma-rays.
- The intrinsic flux and spectral energy density are modeled using Monte Carlo simulations and spectral reconstruction techniques.

Event Parameterization and Reconstruction

The shape of the image of the Cherenkov light formed in the plane of the camera carries important information regarding the properties of the particle inducing the air shower. Once cleaned, the telsecope images are used to calculate a set of parameters for each event including the focal plane image moments, the 3D trajectory of the shower primary, the shower energy, and the discrimination parameters for the Cosmic Ray background rejection. The parameterization of the image begins by computing the *size*-the total amount of light collected by the telescope, the *length*-the major axis of the ellipse image, the *width*-the minor axis of the ellipse image, and the *distance*-the separation from the centroid to the center of the field of view (see Fig 4.12).

The 3D trajectory of the shower primary is characterized by its arrival direction, $\mathbf{e}$ and "core" location $\mathbf{R}$ (defined as the location of the shower on the

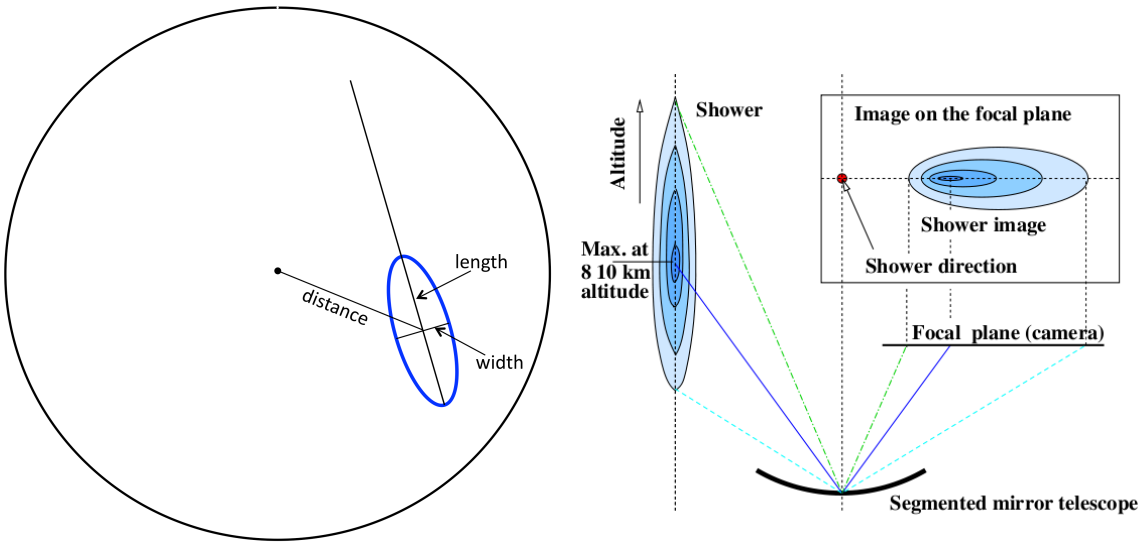

Figure 4.12 (left) Illustration of parameters used to image the event in the focal plane of the camera. (right) Shower development in the atmosphere and imaged in the focal plane of the telescope camera. (Figure taken from [VB09]).

ground, had the gamma-ray penetrated the atmosphere). Because the major axis of the parameterized ellipse is a projection of the shower axis (see Fig 4.12), the direction of the primary gamma-ray will lie along this direction. By combining multiple images simultaneously obtained by different telescopes (typically three or four) onto a common plane, the intersection of axes from separate images aids in reconstructing the shower direction and core position. More elaborate reconstruction methods can also be employed, and a summary of these algorithms can be found in [VF05].

The ability to reconstruct the primary particle energy which initiates the Cherenkov air shower is essential for the spectral analysis of gamma-ray sources. Because of the important property of air showers that the brightness scales as a function of the number of secondary particles produced, the total light in the image can be used to determine the energy of the shower primary. The highly non-uniform Cherenkov emission pattern on the ground as a function of energy

and distance of the primary however, must be accounted for. The size of events with radius > 125 m decreases rapidly with impact distance. Additionally, other factors such as the noise level, zenith angle, azimuthal angle, offset between the source and the pointing direction, and the telescope must be taken into account. Thus, Monte Carlo simulations are used to determine an energy estimator lookup table, from which an event can be assigned a most probable energy based on the event geometry and image size observed in multiple telescopes.

Source Detection and Spectral Reconstruction

Following the gamma-ray selection cuts to the sample of events, a skymap of the distribution of event directions is produced. The event distribution may still be dominated in some energy bins by the residual (approximately uniform-once the camera acceptance and zenith angle have been accounted for) cosmic-ray background events, which have survived the selection cuts. A gamma-ray source is found by searching for a significant deviation of the counts in the skymap from the expected background counts. The standard observation strategy used by VERITAS incorporates the *wobble* technique, whereby the putative source position is offset from the telescope pointing by a fixed amount (generally $0.5°$) along one of the four cardinal directions (N,S,E,W) in the camera FoV. Once the camera acceptance is accounted for, the significance and amplitude of a gamma-ray excess is then determined at a given point generally using the *ring-background* method. The second primary method is used in spectral modeling and is called the *reflected-region* method. A schematic of each method is shown in Fig 4.13.

The PSF of the IACTs such as the VERITAS instrument can be modeled as

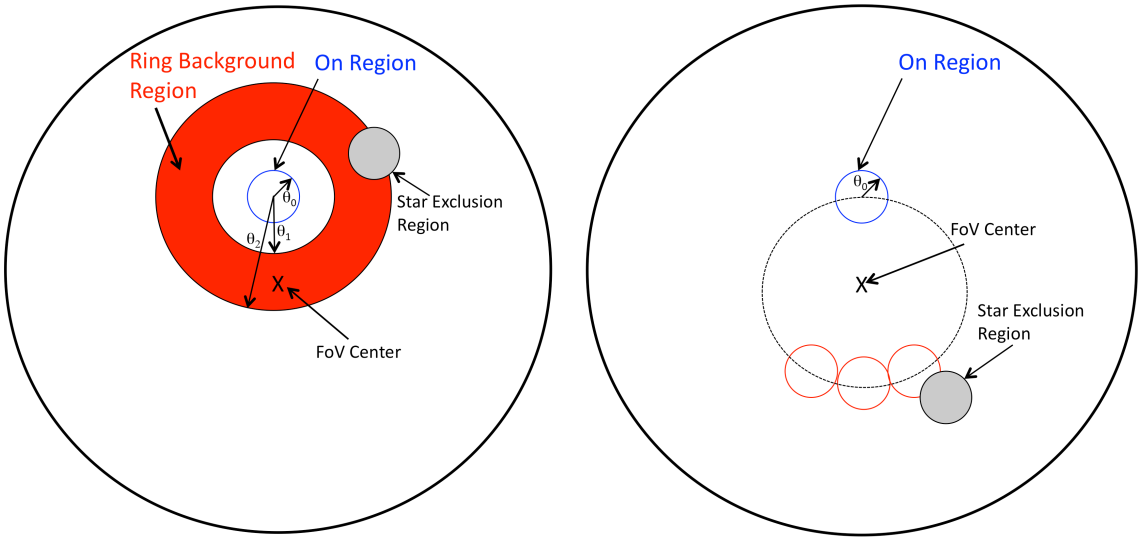

Figure 4.13 Illustration of the ON and OFF regions in the camera FoV used in (left) the reflected-region background method and (right) ring-background background method.

an azimuthally symmetric two-component gaussian distribution given by

$$\frac{dP}{d\theta^2} = \frac{\alpha}{\sigma_1^2} e^{-\theta^2/(2\sigma_1^2)} + \frac{(1-\alpha)}{\sigma_2^2} e^{-\theta^2/(2\sigma_2^2)} \tag{4.1}$$

where θ is the angle between the true and reconstructed direction, σ_1 and σ_2 are parameters describing the width of the core and tail components respectively, and α is a parameter controlling the relative amplitude of these components.

In order to detect the presence of a point-source of gamma-rays, the excess of counts near the source must be significantly greater than in other parts of the FoV, nearly all of which are background cosmic ray events. To determine the amount of excess counts in a region near the source (the "ON" region), the total number of counts within this region are computed (N_{on}). In the *reflected-region* method, the number of counts which are expected due to the background are estimated as follows: an "OFF" region is defined as the set of non-overlapping equal radius

regions located at the same wobble distance away from the center of the FoV as the ON region (see Fig. 4.13). Known gamma-ray sources and stars are excluded from this OFF region, and the total number of counts are summed N_{off}. In the *ring-background* method, an annulus surrounding the source is constructed and the number of counts in this OFF region is found (see Fig. 4.13). The number of excess counts in the ON region is given by

$$N_e = N_{on} - \alpha N_{off}$$

where α is the ratio of solid angles of the ON region to the OFF region. To determine how statistically significant the excess number of counts is, the likelihood ratio is formed for two hypothesis-the null hypothesis and the non-zero hypothesis assuming Poisson statistics. The logarithm of this ratio can be used to evaluate the significance of the detection, which comes out to be [LM83],

$$\sigma = \sqrt{2}\left[N_{on}\ln\left(\frac{1+\alpha}{\alpha}\frac{N_{on}}{N_{on}+N_{off}}\right) + N_{off}\ln\left((1+\alpha)\frac{N_{on}}{N_{on}+N_{off}}\right)\right]^{1/2}.$$

In TeV astronomy, a significance of 5σ is generally required to claim a source detection. An example of an excess counts map for an important source of this study, 1ES 0229+200, is given in figure 4.14.

From the measured set of reconstructed event energies, E', along with a model for the effective collecting area of the VERITAS instrument, it is possible to unfold the source spectrum in true gamma-ray energy, E which has produced the signal. In terms of logarithmic energy $x = \log(E)$, the reconstructed spectrum dN_{rec}/dx', is related to the true spectrum dF/dx by

$$\frac{dN_{rec}}{dx'} = \tau \int \frac{dR}{dx'} A_{eff}(x) \frac{dF}{dx} \tag{4.2}$$

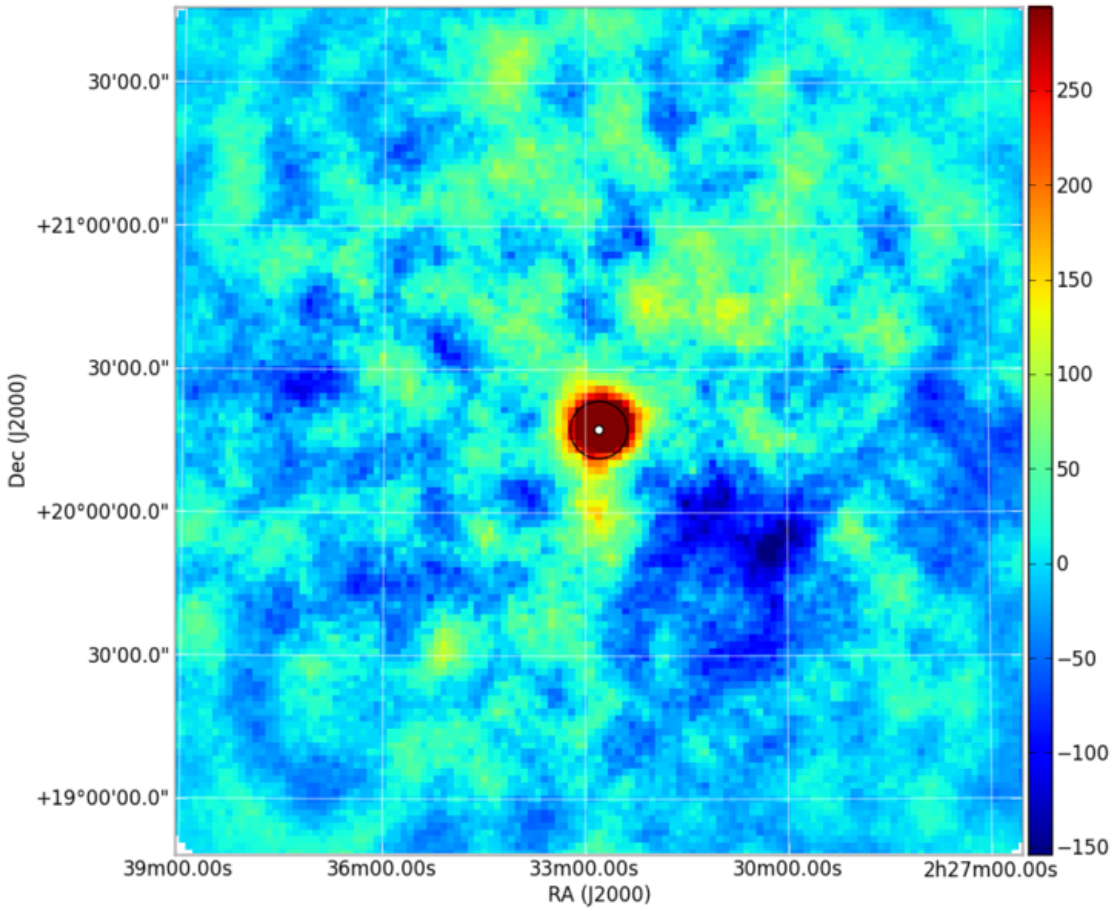

Figure 4.14 Excess counts map from VERITAS analysis of source 1ES0229+200 for a total of 54 hours from 2009 - 2012.

where τ is the livetime (exposure), $A_{eff}(x)$ is the gamma-ray effective area (determined from simulations), and dR/dx' is the energy response function (or the ability of the analysis to correctly reconstruct the true energy of the gamma-ray). At the end of the analysis of a given source, one will have the differential flux energy spectrum of a source in terms of dF/dE vs. E, under the assumption of a point source, with error bars primarily determined by the residual background rate of cosmic rays.

CHAPTER 5

Constraining the IGMF Through Spectral Fits of HE and VHE Data

In this chapter, a detailed investigation into the possibility of deriving lower limits on the IGMF from the non-detection of cascade radiation in the GeV energy band is undertaken. As reviewed in section 1.4, some authors have argued that a lower limit on the IGMF strength may be derived based on present gamma-ray data from the *Fermi*-LAT and IACTs. In most of those works, a number of assumptions, approximations, and model-dependent results were used to present the justification for arguing for the interpretation of the data which requires a lower limit on the IGMF strength. Therefore, we aim to use our recently developed Monte Carlo code to investigate these assumptions and determine whether the data is incompatible with the "$B_{IGMF} = 0$ hypothesis" (in this chapter, hereafter referred to as $H0$). Because of the differences in the two types of instruments which span the GeV - TeV data range, considerations regarding how each instrument treats the cascade emission data must be separately analyzed. Section 5.1 describes the simulation of the detector response to the cascade radiation as well as the methodology that we employ to determine whether a given source's data is consistent with a given B_{IGMF} value (primarily though, with $H0$). Section 5.2 describes the data used in this chapter. The chapter concludes with a detailed analysis of the spectral fits of each source in section 5.3, as well as a detailed

investigation of the multiple systematic and astrophysical uncertainties, which affect the lower limit of B_{IGMF}.

The content in this chapter draws heavily from a recently submitted publication, [AVW12], whose primary goal was to provide precise numerical verification of the constraints on the IGMF as reported in prior studies [NV10, TGF10, DKO11, DCR11, TVN11]. In contrast to any previous study of this kind, particular attention in this chapter is given to establishing the robustness of the magnetic field limit when various systematics are taken into consideration.

5.1 Data Analysis Approach

Under the assumption of $B_{IGMF} = 0$ ($H0$), the secondary gamma-rays of the cascade obtain an angular extension due only to the QED pair production and IC scattering angles, not from magnetic deflection of the electrons and positrons, and this angular extension is much smaller than the 68 % containment radius (R_{68}) of any current gamma-ray instrument. However, when the effect of magnetic deflection of the electron/positron pairs becomes important, it is possible to approximate the effect that this angular extension has, in the context of the spectral energy density measurements of the point source analyses of the HE and VHE data.

5.1.1 Simulating the Detector Response for Spectral Analysis

To predict how the IACT instruments and the *Fermi*-LAT will reconstruct the spectrum of secondary gamma rays arriving at the earth, some care is needed when the point source assumption breaks down, due to the angular spread induced in the secondary emission by the IGMF. According to the following chapter,

the angular extension in the VHE domain becomes comparable to R_{68} when $B_{IGMF} \gtrsim 10^{-15}$ G, and in the HE domain when $B_{IGMF} \gtrsim 10^{-17}$ G, so that for each type of instrument, the point source assumption is valid for smaller magnetic fields than this, in particular, under the assumption of $H0$. To model the spectral reconstruction of this non-point source emission, the instrument's PSF is used to determine the probability that the photon will be reconstructed within some angular distance from the point source and thus interpreted by the analysis as having originated from the source. This models the presence of an angular extension in a more robust and accurate way than previous studies of the kind. Previous studies, (e.g. [NV10]) which aimed to set a lower limit on the IGMF by comparing the VHE and HE spectral energy density measurements of AGN, counted the secondary photon in the flux measurement if the photon simulated (or computed with a semi-analytic calculation) had an arrival angle of less than R_{68} of the instrument at the given energy. The approach taken in the present work goes a significant step further-using the instrument's PSF to re-weight the arrival photon's flux according to the probability of the photon being reconstructed within the instrument's R_{68}. For example, a secondary photon at an arrival angle of strictly 0° would be weighted by 0.68, because it has a 68 % chance of being reconstructed within R_{68}. First we work out the analytic formula for this re-weighting for the IACT PSF, then we describe the changes performed in the case of the LAT.

As described in section 4.2.3, the PSF of the IACT is modeled as

$$dP = \left[\frac{(1-\alpha)}{\theta_1^2} \exp\left(-\frac{\theta^2}{\theta_1^2}\right) + \frac{\alpha}{\theta_2^2} \exp\left(-\frac{\theta^2}{\theta_2^2}\right) \right] d\theta^2.$$

The i^{th} photon from the simulation will arrive with polar angle θ_i and azimuthal angle φ_θ. The non-ideal PSF of the instrument will reconstruct it as offset from

this position by the amount θ, φ, which will lead to a reconstructed photon FoV coordinate of θ', φ'.

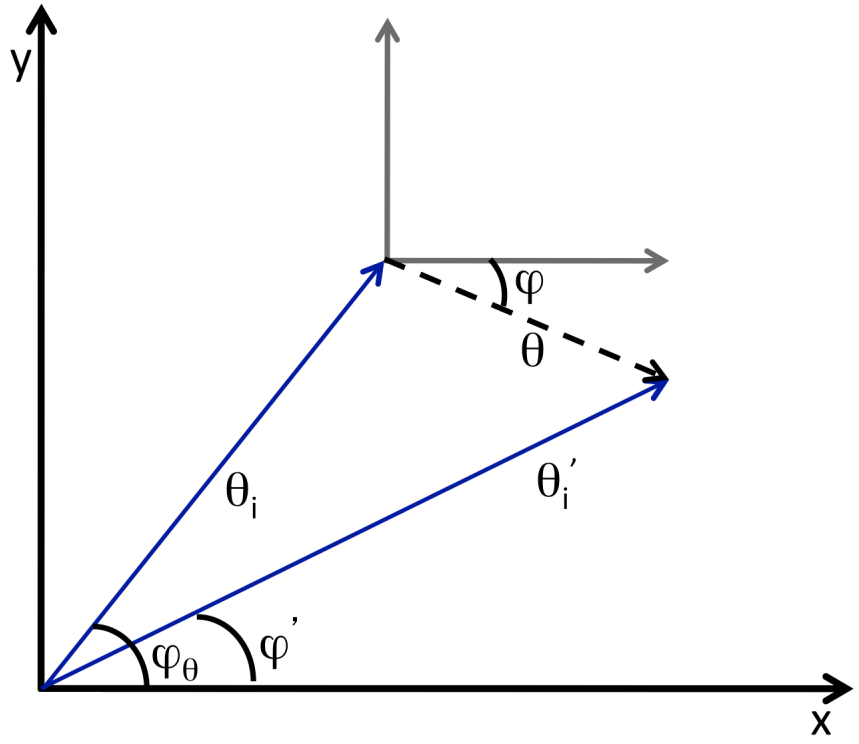

Figure 5.1 Geometry for photon reconstruction in the instrument FoV.

The strategy employed is to integrate over the psf in order to determine the probability ($\Phi(\theta')$) that the photon is reconstructed within R_{68}, and is thus counted in the determination of the spectral energy density. Thus, the following integral is to be evaluated

$$\frac{d}{d\theta'^2}\Phi(\theta'^2) = \int_0^\infty \delta\left(\theta'^2 - \theta_i^2 - \theta^2 - 2\left(\boldsymbol{\theta}_i \cdot \boldsymbol{e}\right)\right) dP \frac{d\varphi}{2\pi}, \tag{5.1}$$

where $\boldsymbol{\theta}_i = \theta_i(\cos\varphi, \sin\varphi)$ is the vector of the incident photon arrival angles. For each simulated set of source and magnetic field parameters, there are on the order of millions of secondary photons simulated. Thus, it would be very slow

and impractical to integrate Eq 5.1 numerically for each photon. To analytically integrate this, properties of the delta function are used to rewrite the integral over φ to an integral over θ'.

$$d\Phi\left(\theta'^2\right) = \frac{1}{\pi}\int_0^\infty \frac{d\theta'^2}{2\theta\theta_i\sqrt{1-\left(\frac{\theta'^2-\theta_i^2-\theta^2}{2\theta\theta_i}\right)^2}} dP, |\theta_i - \theta| \leq \theta' \leq |\theta_i + \theta|.$$

Due to the restriction on θ' and the form of the integrand, it turns out there will actually be three distinct cases that the above integral will be evaluated under. The complete details of this are worked out in the internal memo called "Photon Blurring For IACT and Fermi-LAT". In the case of the LAT, the integration is complicated by the fact that there is a difference in the PSF between front-converted and back-converted photons. There is an option in the code to use only front, back, or both sets of photons, which allows us to test these differences. For the remainder of this chapter, the data is analyzed using both front and back converted photons.

5.1.2 Comparison of Data and Model

To compare the predictions of the Monte Carlo simulations to the data, we combine both the HE and VHE spectral energy density data to compute a χ^2-like parameter, detailed in this section. The simulated effective point-source flux is used as the model expectation value, and we assume that the statistical error of the vast amount of simulations is negligible compared to the observational error. The point-source fluxes derived with the use of the *Fermi* tools as explained above or obtained from IACT publications are used as data. The observational error obtained or reported is taken to be the primary source of discrepancy between the data and the model. A χ^2-like parameter is used to estimate the goodness-

of-fit of a given model and χ^2 statistics is used to convert it to a confidence level (or the probability of the model exclusion). For this conversion, an explicit assumption is being made, that the errors in both the HE and VHE regimes are dominated by statistics with a gaussian distribution. Throughout this analysis, our sole goal is to test the null hypothesis, $H0$, that $B_{IGMF} = 0$ is incompatible with the data and the simulations. The confidence level is the probability that the measurement cannot be obtained with the assumption of the given model. In what follows, we take the model to be incompatible if the confidence level exceeds 95 %, corresponding to a 2σ deviation for a normal distribution. We do not claim any meaningful interpretation of a higher confidence level, due to the unknown behavior in the tails of the distribution of errors of each instrument.

The model spectral energy density is derived based on the full Monte Carlo simulations computed for monoenergetic primary photons with 8 bins per decade, of equal width in logarithmic space. The simulated spectral energy density data are equally binned with 8 bins per decade and each bin is centered on the energy of the primary photon monoenergetic line. The VHE data are reported in different publications at different energies and with different binning. We use simulated data to interpolate the flux value to the reported positions of the bins and their widths. In the 3 decades of the HE regime, 4-6 energy bins are generated depending on the given source luminosity and statistics. The simulated data are then used to interpolate the flux value to these energy bins. Moreover, we use the simulated data to find the spectral index for the power law distribution of photons at each energy bin. This spectral index is taken to be fixed when we find the flux value and its error utilizing the *Fermi* tools.

To compare the HE and VHE data of each source with the simulations, the effective point source fluxes are generated for a set of gamma-ray source models

with fixed values of four parameters-α, ϵ_c, Γ, and θ_v. For each model, α is chosen in the range (1.0, 2.5) with a step of 0.1, and ϵ_c is chosen in the range (600 GeV, 60 TeV) with 8 bins per decade, equally spaced in logarithmic energy. Each model is characterized with default values of $\theta_v = 0$, and $\Gamma = 10$, unless otherwise stated. Therefore, for each source, we test 240 individual source models.

The remaining three parameters of the seven parameter source model were determined as follows. Two of these parameters, the break energy ϵ_B and the spectral index γ are relevant only to the HE part of the spectrum. They were chosen by minimizing the χ^2_{HE} value, by allowing ϵ_B to vary between $\gtrsim$ 10 GeV to the lower edge of the lowest energy VHE data bin and γ between -5 and 5. This interval for the break energy is motivated by the fact that IACT instruments become insensitive in this energy regime and *Fermi* runs out of photon statistics, therefore allowing a possible knee feature in the spectrum to be undetectable. The spectral index γ in the HE regime may or may not be constrained by minimization of the χ^2_{HE} value. It is evident that when secondary, cascade emission dominates in this energy regime, it is sufficient for γ to be larger than some value to keep prompt emission negligible. The flux normalization factor, F_0, is the only optimization parameter for a given model which is relevant to the χ^2_{VHE} and which may or may not be relevant to the χ^2_{HE}, depending on the relationship between the prompt and secondary emission of the source. We chose to determine F_0 by minimization of the VHE part of χ^2 by solving $\partial\chi^2_{VHE}/\partial F_0 = 0$ independently from the behavior of χ^2_{HE}. Effectively, this means that we have made a stringent requirement of compatibility of the source model with the VHE data and have excluded some models which would be highly incompatible with the VHE measurements, but would allow statistical compatibility with an overall $\chi^2 = \chi^2_{HE} + \chi^2_{VHE}$, just because of an increased number of data points and therefore number of degrees of freedom. We view this weighting procedure of HE

and VHE parts of χ^2 in determination of F_0 as better physically motivated, since the highest energy data points in the VHE regime are of extreme importance for the production of the cascade emission, but from a statistical point of view, they are equal to any other point of N_{HE} or N_{VHE} measurements.

The χ^2 value for each model with four fixed parameters (α, ϵ_c, Γ, and θ_v) was converted into a confidence level, using χ^2 statistics with $N_{HE} - 2 + N_{VHE} - 1$ degrees of freedom, assuming that three parameters were optimized for each model (F_0, ϵ_B, γ). We make no attempt in our studies to evaluate the confidence intervals of the latter three parameters of each model. Our goal is exclusively to find a model or a set of source models which are compatible with $H0$.

As an illustration of a typical result of the data and model comparison, Figure 5.6a shows the χ^2 confidence level of the differential Flux Energy Density (dFED), E^2dF/dE vs. E, assuming four fixed and three free parameters for each model tested within the given range of α and ϵ_c parameters. The most favored model with value of $\alpha = 1.8$ and $\epsilon_c = 3.16$ TeV is incompatible with the data at the level of about 75 %. If this choice of parameters α and ϵ_c is considered as an optimization process, in which case the number of free parameters in the model is 5, then this model is incompatible with the data at the level of 88 %. Figure 5.6b shows the data points for the dFED and the best fit simulation result with these α, ϵ_c parameters. For this source's dFED, below 10 GeV the spectrum is dominated by cascade emission, while above 10 GeV, it is dominated by prompt radiation.

5.2 Data Used in Spectral Fitting

The data used in this section to investigate $H0$ are described in this section. In

Table 5.1. Data of RGB J0710+591 are taken by VERITAS [AAA10]. Source 1ES 1218+304 was observed by VERITAS and the results were published in two separate submissions [AAB10, AAA09a]. This source was also detected during a six day period around MJD 53750 by the MAGIC collaboration [AAA06], at a level similar to that of the reported flux by VERITAS about one year later. Observations of 1ES 0229+200, 1ES 0347-121, 1ES 1101-232, H 2356-309, and RGB J0152+017 were taken prior to the launch of the *Fermi* satellite, and are reported by the HESS collaboration [AAB07a, AAB07b, AAB07d, AAB06a, AAB08].

IACT data summary

Source	z	IACT	Flux [10^{-12}cm^{-2} s^{-1}]	index	MJD (approx)	Hrs
RGB J0710+591	0.125	VERITAS	($>$ 300 GeV) 3.9 $\pm$ 0.8	2.7 $\pm$ 0.3	54882-54892	22.1
1ES 1218+304	0.182	VERITAS	($>$ 200 GeV) 18.4 $\pm$ 0.9	3.1 $\pm$ 0.3	54829-54944	27.2
1ES 1218+304	0.182	VERITAS	($>$ 200 GeV) 12.2 $\pm$ 2.6	3.1 $\pm$ 0.1	54070-54220	17.4
1ES 0229+200	0.14	HESS	($>$ 580 GeV) 0.94 $\pm$ 0.24	2.5 $\pm$ 0.2	53614-53649, 53967-54088	41.8
1ES 0347-121	0.188	HESS	($>$ 250 GeV) 3.91 $\pm$ 1.1	3.1 $\pm$ 0.3	53948-54100	25
1ES 1101-232	0.186	HESS	($>$ 200 GeV) 4.5 $\pm$ 1.2	2.9 $\pm$ 0.2	53111-53445	43
H 2356-309	0.165	HESS	($>$ 200 GeV) 4.1 $\pm$ 0.5	3.1 $\pm$ 0.3	53157-53370	40
RBG J0152+017	0.08	HESS	($>$ 300 GeV) 2.7 $\pm$ 1.0	2.9 $\pm$ 0.5	54403-54418	15

the HE regime (High Energy; 100 MeV $\lesssim$ E $\lesssim$ 100 GeV), the data were obtained by the *Fermi*-LAT instrument and processed using the publically available tools, version v9r23p1, with the update from November 6, 2011. The P7_V6 version of the processed data were used, which is the latest version available from Feb. 23, 2012 up until the time of the writing of the present work. For the VHE regime (Very High Energy; E $\gtrsim$ 100 GeV), data previously reported by the Imaging Atmospheric Cherenkov Telescopes (IACT) VERITAS and HESS are used.

The VHE data set used in this paper is summarized in Table 5.1. The data sets of the first three sources (RGB J0710+591, 1ES 1218+304, and 1ES 0229+200) are identical to those used in [TVN11], except that an additional data set for 1ES 1218+304 obtained by the VERITAS Collaboration just before the launch of the *Fermi* satellite (on August 4, 2008 or MJD 54682) is considered in this study. As reported in [AAB10], the activity of the source is nearly identical during these non-overlapping periods, except for an elevated flux of the source peaking at the level of $\sim$20 % Crab over a few nights of observations. The data set for 1ES 0229+200 was also obtained prior to the launch of the *Fermi* satellite. Based on the report from [PV10], the activity of the source as measured by VERITAS during the second year of the *Fermi* mission, appeared to resemble the reported SED by the HESS collaboration prior to the launch of *Fermi* satellite [AAB07a]. VERITAS has continued monitoring this source since the Fermi launch and tentatively detected flux variations on a sub-yearly time scale (private communication, J.S. Perkins and VERITAS collaboration). There will also be a forthcoming paper from the VERITAS collaboration summarizing VERITAS observations of this source in the near future. Finally, the data sets for four other extreme TeV blazars (1ES 0347-121, 1ES 1101-232, H 2356-309, and RGB J0152+017) were taken from the discovery publications by the HESS collaboration, and all of these sources were observed prior to the start of the *Fermi* mission. The *Fermi*-LAT

data for these sources are re-analyzed and are collected from the mission start time Aug 4, 2008 to February 14, 2012, and the updated P7SOURCE IRFs are used along with the Pass 7 data. The models for extragalactic and diffuse backgrounds were used together with the standard gamma-ray selection constraint of zenith angle $< 100^{\circ}$ which eliminates earth limb gamma-rays.

To compare simulated differential fluxes from an effective point source to the *Fermi*-LAT data, the standard analysis tools were applied but with a notable important distinction from previous studies. Since in the HE regime, the flux of gamma-ray photons can be dominated by either prompt or secondary emission, we first derive the spectral index in each energy bin from simulations. This index is then used as a fixed parameter for the maximal likelihood evaluation[1] of the flux in each energy bin in the *Fermi* data, within the 10° region of interest (ROI) which also includes all nearby sources from the 2 year point source catalog and diffuse backgrounds. The HE point source fluxes or upper limits are then derived using this procedure.

5.3 Results of Spectral Fits to VHE and HE Data

This section presents the results of the fits of the HE and VHE spectral data of the sources described in the previous section, under the hypothesis that $B_{IGMF} = 0$ ($H0$) unless otherwise stated. First, the analysis framework described in section 5.1.2 is applied to four hard-spectrum TeV sources which had been observed prior to the start of the *Fermi* mission, and had been considered in prior works which aimed at a constraint on the IGMF [NV10, EAK10, TGB11]. Next, three sources (RGB J0710+591, 1ES 1218+304, and 1ES 0229+200) are investigated which have IACT spectral data published during the *Fermi* mission, and which

[1] http://fermi.gsfc.nasa.gov/ssc/data/analysis/

have been reported as having provided constraints on the IGMF, in the recent comprehensive study of [TVN11] (and references within). Hereafter, we refer back to this important paper multiple times, since we will be especially interested in contrasting their analysis of these three sources with our analysis of these same sources.

Perhaps the main source of uncertainty in placing constraints on the IGMF stems from the unknown duty cycle of TeV blazars and particularly, the history of the highest energy TeV emission, as has been pointed out in [DCR11]. The sampling of the VHE activity of these sources reported by IACTs is limited to a few tens of hours dispersed over a period of a few weeks to a few years. In the regime of very low IGMF ($B_{IGMF} < 10^{-20}$ G), most of the secondary radiation from intergalactic cascades with energy > 100 MeV, which originates from the primary VHE flux sampled by IACTs, would have reached the earth and would be detected by the *Fermi*-LAT (see Fig. 3.4) within a few hours. This assumes that the HE flux from a given source sampled by the *Fermi*-LAT over the period of the mission (about 4 years) could be viewed as "contemporaneous" to IACT measurements, for the purposes of verification of $H0$. This explicitly assumes, however, that the duty cycle of a given source in the VHE regime $= 1$ over this same period, which we take as a default premise unless otherwise stated.

Analysis of 1ES 0347-121

Source 1ES 0347-121 was first detected at VHE energies by the HESS collaboration [AAB07b], over the period of August - December 2006, during which time 25.4 hours exposure was acculumlated, and a time-averaged dFED for 7 bins over the energy range from 250 GeV - 3.67 TeV was derived. Because this source was strongly detected in VHE energies with a relatively hard spectral index (~ 3),

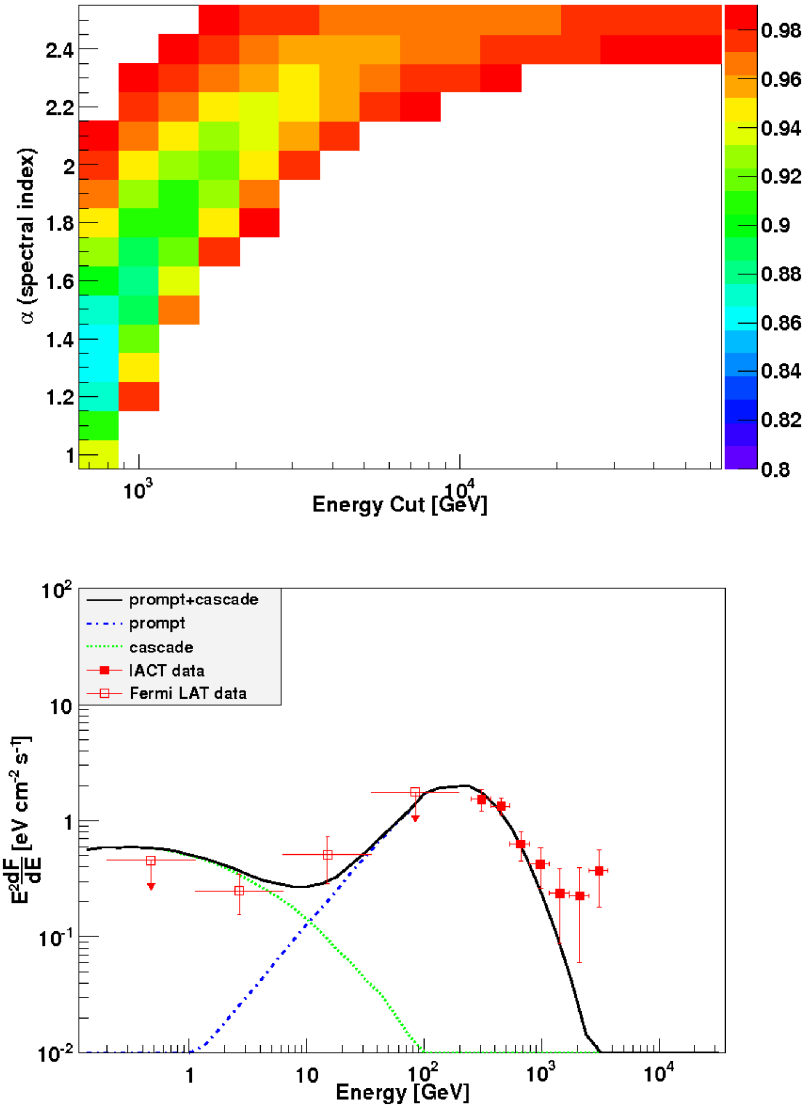

Figure 5.2 Source 1ES 0347-121 analyzed under the assumption of $H0$. (top) Confidence level, or the probability of exclusion of the gamma-ray source model (with fixed α and ϵ_c), where the remaining three parameters of the model (γ, ϵ_B, and F_0, see Eq. 3.9) are chosen so as to minimize χ^2. (bottom) Simulated dFED of the best fit model of $\alpha = 1.3$, $\epsilon_c = 0.75$ TeV, showing both the prompt and secondary cascade contributions to the total dFED, along with the HE and VHE data.

is located at high redshift ($z = 0.188$), and was not present in the *Fermi*-LAT first or second year point source catalog, it is a good candidate to constrain the IGMF, since its VHE spectral features would predict a high flux of secondary radiation in the HE regime. For the HE energy regime, four energy bins were used spanning 200 MeV to 200 GeV. The flux found in the first and fourth bins is weak (TS < 9) for all spectral indices tested, allowing only an upper limit to be established. The flux in the second and third bins is typically found with $9 <$ TS < 25 for the simulated models where the secondary flux dominates the total flux. Figure 5.2a shows the confidence level of simulated models obtained for $H0$. The best fit models in the α - ϵ_C plane are found at ϵ_C values near 1 TeV, which is incompatible with $H0$ at the $\lesssim 86$ % confidence level, and the dFED for one of these models is illustrated in Figure 5.2b. The relatively low confidence level of the 1ES 0347-121 simulated models is partially due to the poor fit of the highest energy bins of the VHE regime where the reported dFED tentatively exhibits a feature of increasing energy density. This trend in the dFED is not accounted for in the set of simulated models investigated. A similar spectral feature appears to be even more pronounced in the VHE data set of 1ES 1101-232, which perhaps may signal unmodeled physics process(es) or a systematic error in the data analyses. However, for all models with confidence level < 95 %, the cascade flux dominates over the prompt flux in the HE energy regime, suggesting this may be a good candidate for future IGMF studies if the power emitted in the VHE energy regime remains about as high as it was during the HESS observations in 2006.

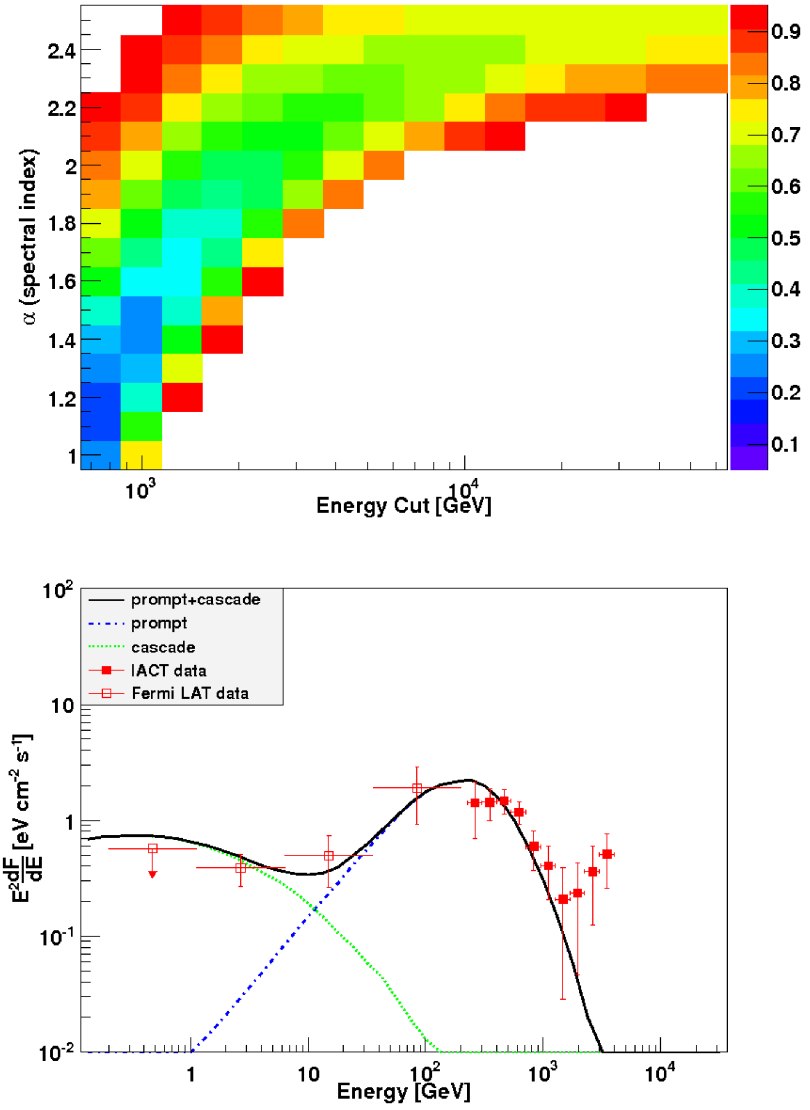

Figure 5.3 Source 1ES 1101-232 analyzed under the assumption of $H0$. (top) Confidence level, or the probability of exclusion of the gamma-ray source model (with fixed α and ϵ_c), where the remaining three parameters of the model (γ, ϵ_B, and F_0, see Eq. 3.9) are chosen so as to minimize χ^2. (bottom) Simulated dFED of the best fit model of $\alpha = 1.2$, $\epsilon_c = 0.75$ TeV, showing both the prompt and secondary cascade contributions to the total dFED, along with the HE and VHE data.

Analysis of 1ES 1101-232

The blazar 1ES 1101-232 was first detected by the HESS collaboration in 2005 [AAB07d], and their published data set consists of 3 periods of observations spanning from April 2004 - March 2005, for a total of 43 hours. The time-averaged dFED is reported for 10 bins over the energy range 225 GeV - 4 TeV. Due to its relatively high redshift ($z = 0.186$) and hard spectral index, it was used in one of the first studies which used TeV observations to constrain the EBL [AAB06b]. This source is present in the second Fermi point source catalog, but only detected at the level of 5.18 σ, which suggests that it may be a good candidate for IGMF studies. The *Fermi*-LAT dFED was computed using four energy bins, equal in log space, spanning from 200 MeV to 200 GeV. The first bin allows a determination of only an upper limit (TS < 9) for all simulated models tested, whereas the remaining bins are typically characterized by $9 <$ TS < 25. Figures 5.3a and b illustrate the compatibility of the 1ES 1101-232 VHE and HE data sets with $H0$. The best fit model, shown in Fig. 5.3b is incompatible with $H0$ at the very low level of only < 15 %, despite the fact that the previously described feature in the highest energy bins of the VHE regime is not well fitted by the models. However, for many of the models which are compatible with $H0$, the cascade flux dominates the prompt flux at GeV energies, suggesting that 1ES 1101-232 may be a good candidate for future IGMF studies, if the power emitted in the VHE energy band remains near the level of the HESS observations in 2004-2005.

Analysis of H 2356-309

Observations of H 2356-309 were carried out by the HESS collaboration over the period of June - September 2004, for a total exposure of 40 hours, resulting in the first detection of this source at VHE energies. The time-averaged dFED

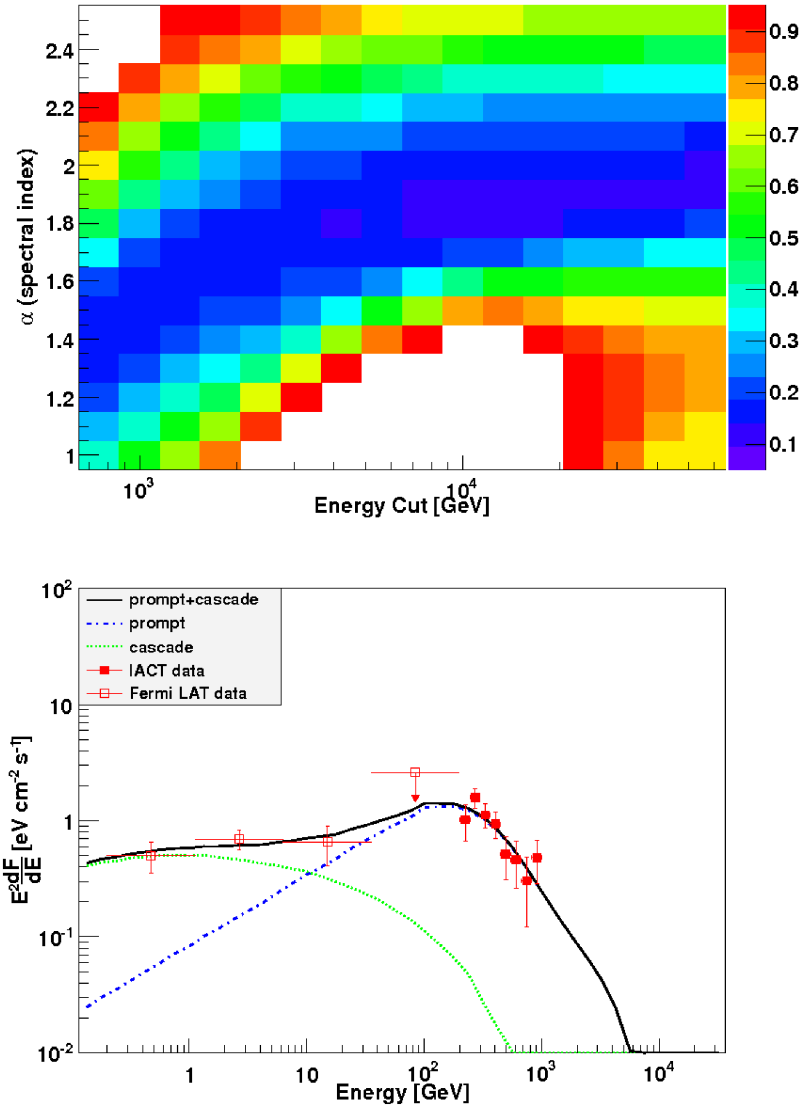

Figure 5.4 Source H 2356-309 analyzed under the assumption of $H0$. (top) Confidence level, or the probability of exclusion of the gamma-ray source model (with fixed α and ϵ_c), where the remaining three parameters of the model (γ, ϵ_B, and F_0, see Eq. 3.9) are chosen so as to minimize χ^2. (bottom) Simulated dFED of the best fit model of $\alpha = 1.8$, $\epsilon_c = 4.22$ TeV, showing both the prompt and secondary cascade contributions to the total dFED, along with the HE and VHE data.

was provided for eight bins over the energy range from 200 GeV - 1.23 TeV ([AAB06a]). Because of its relatively hard spectral index and high redshift ($z = 0.165$), this source was thought to be a good candidate to constrain the IGMF. It is also detected in the *Fermi* second year catalog at the relatively weak level of 7.1 σ. For the HE dFED, four energy bins, equally distant in log space, from 200 MeV - 200 GeV. The flux in the first energy bin is weakly detected for most simulated models ($9 < \mathrm{TS} < 25$), but the second and third bins exhibit a strong detection ($\mathrm{TS} > 25$). An upper limit is derived for the fourth bin in the HE dFED due to a weak signal present ($\mathrm{TS} < 9$). As illustrated in Figure 5.4, this source has a very large set of models compatible with the $H0$. Most of these models, however, suggest that the flux in the two lowest energy bins of the HE regime is dominated by secondary radiation. If the VHE luminosity remains at nearly the level reported here or higher, it may be a good source for future studies of the IGMF.

Analysis of RGB J0152+017

The HESS collaboration discovered RGB J0152+017 over the period of October 30 - November 14 2007, observing the source for a total exposure of 14.7 hours. The time averaged dFED was reported for six bins over the energy range of 240 GeV - 3.6 TeV ([AAB06a]). Its intermediate redshift ($z = 0.08$) and moderately hard spectral index (~ 3), combined with the fact that it is weakly detected in the *Fermi* second year source catalog, at the level of 8.9σ suggests the possibility that the source may be candidate to constrain the IGMF. The dFED of the *Fermi* energy range was derived using 6 energy bins equal in logarithmic energy, over the range of 200 MeV - 200 GeV. The flux in all but the first energy bin of the *Fermi* data is strongly detected ($\mathrm{TS} > 25$) for the majority of simulated

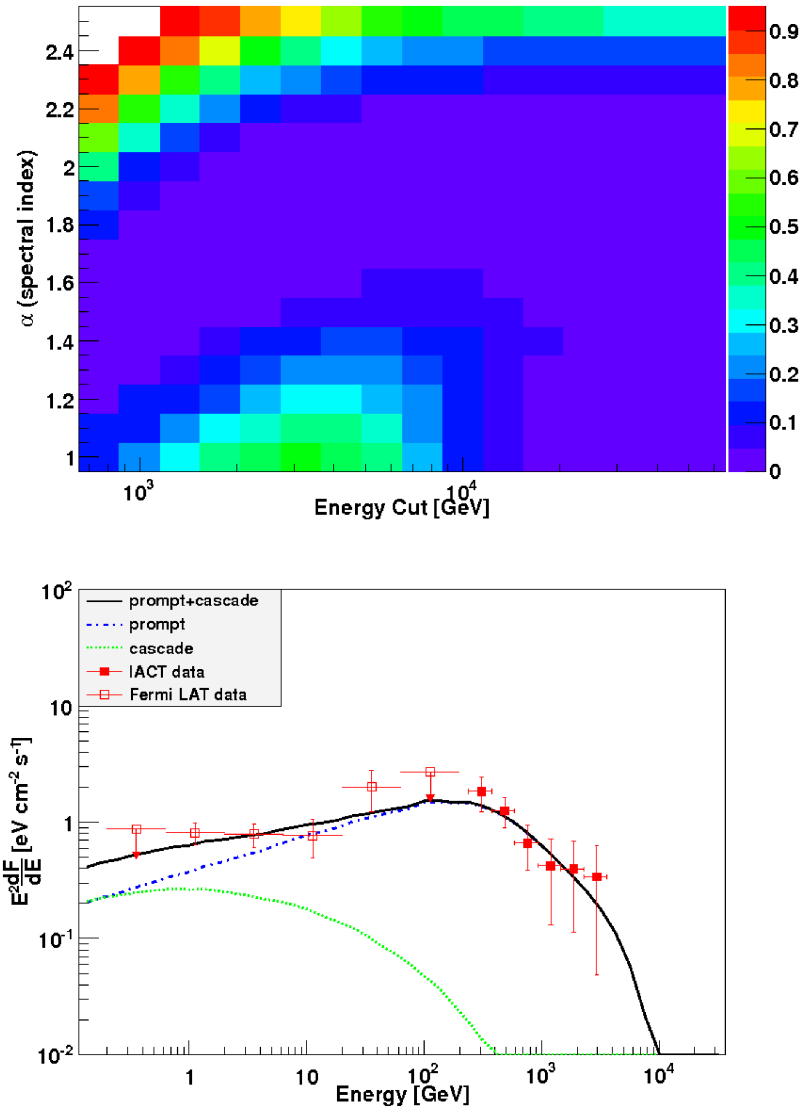

Figure 5.5 RGB J0152+017 (top) Confidence level, or the probability of exclusion of the gamma-ray source model (with fixed α and ϵ_c), where the remaining three parameters of the model (γ, ϵ_B, and F_0, see Eq. 3.9) are chosen so as to minimize χ^2. (bottom) Simulated dFED of the best fit model of $\alpha = 1.9$, $\epsilon_c = 3.16$ TeV, showing both the prompt and secondary cascade contributions to the total dFED, along with the HE and VHE data.

models. Figure 5.5 a and b illustrate that this source provides the weakest constraints on the IGMF with nearly the entire parameter space of simulated models compatible with the VHE and HE spectral data. In only some of these models, the HE part of the spectrum is dominated by the primary emission, so for future investigations into the IGMF using the spectral data or attempting to detect an angular extension, it is not as likely to be a viable candidate.

Analysis of RGB J0710+591 Data

The VHE observations of RGB J0710+591 are summarized in Table 5.1. They include 5 energy data points reported by the VERITAS collaboration in [AAA10], observed during the time period December 2008 - March 2009 for a total of 22 hours. For the HE regime, 6 energy bins were used spanning from 200 MeV to 200 GeV. In each energy bin, if TS $>$ 9, the flux point and 1σ error bars are displayed. Otherwise, an upper limit was computed. It is important to note that with this strategy and extended data set as compared to previously used in [TVN11], the flux in the lowest energy bin now constitutes a flux point rather than an upper limit. This data point had been critical for rejecting $H0$.

Figure 5.6a shows the confidence level for rejecting $H0$, for a set of models characterized by the range of ϵ_c and α described in section 5.1.2. It identifies the best fit model with values of $\alpha = 1.8$ and $\epsilon_c = 3.16$ TeV, which is incompatible with $H0$ at < 75 % confidence level assuming three free parameters, and < 88 % assuming 5 free parameters. The range of models in the vicinity of this point is not incompatible with $H0$. The fit of the simulated dFED and observations is shown in Figure 5.6b. It appears that the conclusion of [TVN11] that $H0$ is ruled out at the 98.8 % level is invalidated primarily due to two factors. First, the *Fermi*-LAT dataset underwent revision from the old pass 6 version (P6) to

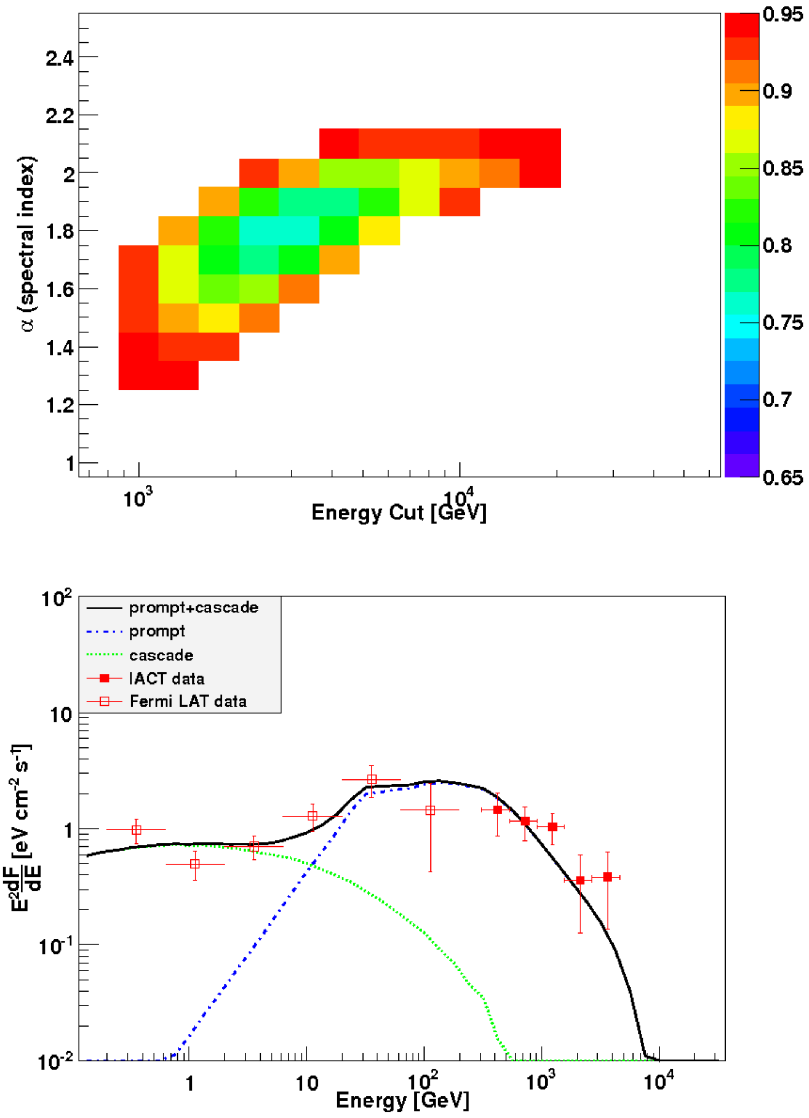

Figure 5.6 Source RGB J0710+591 analyzed under the assumption of $H0$. (top) Confidence level, or the probability of exclusion of the gamma-ray source model (with fixed α and ϵ_c), where the remaining three parameters of the model (γ, ϵ_B, and F_0, see Eq. 3.9) are chosen so as to minimize χ^2. (bottom) Simulated dFED of the best fit model, of $\alpha = 1.8$, $\epsilon_c = 3.16$ TeV, showing both the prompt and secondary cascade contributions to the total dFED, along with the HE and VHE data.

the current pass 7 (P7) and this allowed a detection to be made in the lowest energy bin, which is higher than the previously computed upper limit. The second factor may be due to the fitting algorithm which is different from that adopted in [TVN11], in which the flux or upper limit determination in a given energy bin was fixed to the best fit index over the entire energy range.

Furthermore, the geometrical orientation of the jet with respect to the observer and the jet boost factor represents another source of uncertainty, and tuning these parameters can further improve the goodness of the χ^2 fit. For example, [TVN11] assumes a viewing angle of 2° and an effective jet opening angle of 6°, corresponding to a boost factor of ~ 10. As shown in Figure 3.7, however, lower boost factors or smaller viewing angles lead to lower total power of the jet at the highest energies, and therefore lead to reduced secondary flux.

Analysis of 1ES 1218+304 Data

The VHE observations of 1ES 1218+304 are summarized in Table 5.1, which includes 2 data sets. The first set, obtained during December 2008 - May 2009, is based on 27 hours of data and has 9 energy data points reported by the VERITAS collaboration in [AAB10]. This data set was used in [TVN11], and for consistency it is also used in this study. The *Fermi*-LAT data for this source were produced in the same way as for RGB J0710+591, with 6 energy bins spanning from 200 MeV to 200 GeV. This source has excellent statistics in each *Fermi*-LAT energy bin, with TS > 25. It is important to note that the extended exposure and updated pass 7 data set used in this work shows no statistically significant difference compared to the Pass 6 data analyzed in [TVN11].

Figure 5.7a shows the confidence level for rejecting the $H0$ hypothesis on the α-ϵ_c plane. It suggests a best fit model with values of $\alpha = 1.8$, $\epsilon_c = 3.16$ TeV,

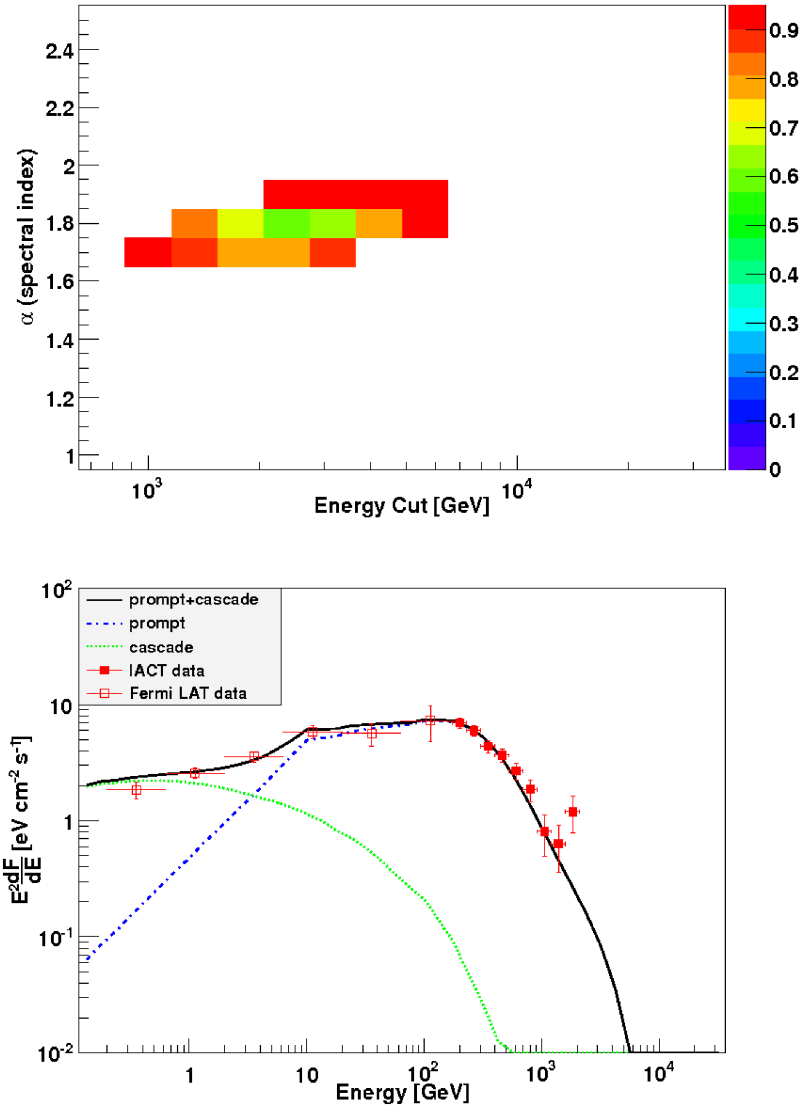

Figure 5.7 Source 1ES 1218+304 analyzed under the assumption of $H0$. (top) Confidence level, or the probability of exclusion of the gamma-ray source model (with fixed α and ϵ_c), where the remaining three parameters of the model (γ, ϵ_B, and F_0, see Eq. 3.9) are chosen so as to minimize χ^2. (bottom) simulated dFED of the best fit model, of $\alpha = 1.8$, $\epsilon_c = 3.16$ TeV, showing both the prompt and secondary cascade contributions to the total dFED, along with the HE and VHE data.

a spectral break energy of $\epsilon_B = 10$ GeV, and an index below the break energy of $\gamma = 1.0$, which is incompatible with $H0$ at the less than 65 % confidence level, assuming three, and less than 80 % assuming five free model parameters. The fit of the simulated dFED and observations is shown in Figure 5.7b. It is evident that the conclusion of [TVN11], that $H0$ is ruled out with more than 99.99 % probability, is purely due to the assumption that a single source spectral index holds for over five orders of magnitude in energy. Allowing a spectral break energy and an intrinsic spectral index below the break energy to vary as detailed in section 3.3.1 makes it possible to interpret the 1ES 1218+304 data set as compatible with $H0$.

The amount of secondary radiation strongly depends on the power output of the TeV blazar at the highest energies. For this source, more so than the others, IACT observations demonstrate strong variability in the VHE spectrum. The VERITAS collaboration reports that the 1ES 1218+304 data were sampled sparsely over a period of 115 days in late 2008 - 2009, and while the majority of the data are consistent with a steady baseline flux, the data set also includes a statistically significant flare which peaked at $\sim$ 20 % Crab, and lasted a few nights. The flux at the peak of the flare was 3-4 times higher than the baseline flux and it significantly increases the average flux value observed over the entire period. Furthermore, evidence for variability of this source can be inferred from the VERITAS publication covering its 2 year activity which occurred prior to the *Fermi* mission ([AAA09a]). The flux observed at that time constitutes about 60-70 % of that reported in the second data set (see Table 5.1). Overall, the IACT data to date suggest that the average observed VHE flux of this souce could be lower than used in [TVN11], yet the assumption of the higher average VHE flux is still compatible with $H0$.

Analysis of 1ES 0229+200 Data

The parameters of the data set of 1ES 0229+200 are given in Table 5.1 and include two sets of observations by the HESS collaboration during the period from September 1, 2005 to December 19, 2006, accumulating 41.8 hours exposure ([AAB07a]). This data set provides the time-averaged dFED for 8 bins over the energy range spanning from 500 GeV to 16 TeV. This same data set was used in the previous study of [TVN11]. The *Fermi*-LAT dFED for 1ES 0229+200 utilizes four evenly spaced bins in log space in the range from 420 MeV to 300 GeV. Only the first energy bin in this data set provides a strong detection (TS $>$ 25), for all simulated models in which the secondary flux dominates the total flux. The TS for all other energy bins is typically found at $>$ 9 for the majority of simulated models but in some cases, only the upper limit can be established (TS $<$ 9). This indicates that the source detection in the HE regime is weak. Perhaps more so than for any other source, the dFED of 1ES 0229+200 does not resemble a power law in the HE energy regime, making the χ^2 fits relatively poor.

To evaluate the goodness of fit of the data to the Monte Carlo simulations, we assume that the data accumulated by the HESS collaboration over 2005-2006 is representative of the source activity during the first 3.5 years of the *Fermi*-LAT data used in this work. The χ^2 fit obtained under this assumption and for $H0$ is shown in Figure 5.8a. We confirm the result of [TVN11] and others that this source does not have a viable source model that explains the combined HE-VHE data set and agree that $H0$ is ruled out at the 99.5 % confidence level. The best fit ($\alpha = 1.3$, $\epsilon_c = 1$ TeV) model requires a dramatic spectral break just below 100 GeV and the dFED of 1ES 0229+200 below this energy is completely dominated by secondary flux as shown in Figure 5.8b.

Since the zero IGMF hypothesis is not consistent with the data, it is necessary

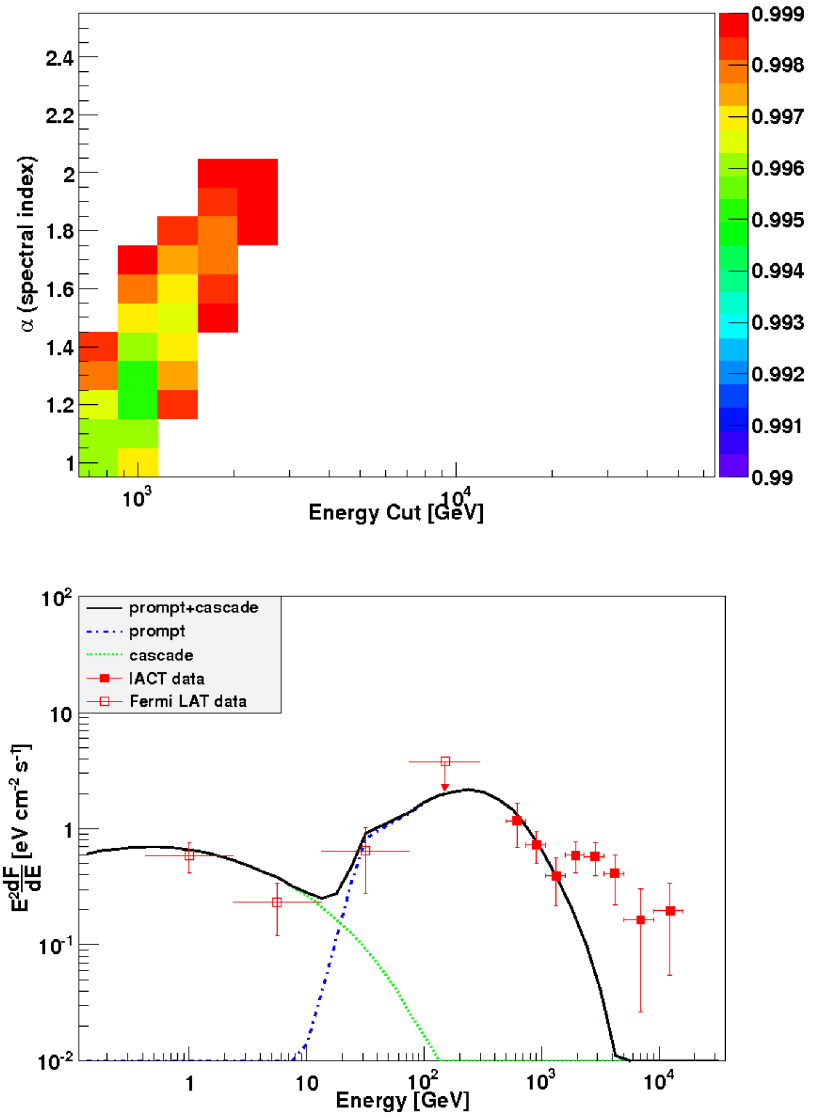

Figure 5.8 Source 1ES 0229+200 analyzed under the assumption of $H0$. (top) Confidence level, or the probability of exclusion of the gamma-ray source model (with fixed α and ϵ_c), where the remaining three parameters of the model (γ, ϵ_B, and F_0, see Eq. 3.9) are chosen so as to minimize χ^2. (bottom) Simulated dFED of the best fit model (C.L. = 0.995) of $\alpha = 1.3$, $\epsilon_c = 1$ TeV, showing both the prompt and secondary cascade contributions to the total dFED, along with the HE and VHE data.

to ask what the source of discrepancy is. The observations may be reconciled with $H0$ if either there was some source of astrophysical or systematic uncertainty unaccounted for in the present analysis, or if the IGMF strength is greater than some value strong enough to isotropize many of the electrons responsible for creating the IC scattered secondary radiation. The former will be explored in the next section, while the latter possibility is now considered. We begin with the assumption that the HESS dataset from 2005 - 2006 is a reliable estimate of the VHE activity of this source over the past three years since the start of the *Fermi* observations. Under this scenario, fig. 5.9a shows the confidence level for incompatibility of the given model, for the lowest possible magnetic field where source models are present with less than 95 % confidence level. One of the best fit models to this data is with a spectral index of 1.2 and cutoff energy of 5.6 TeV. This model is displayed in fig. 5.9b, and is incompatible at the level of only < 30 %. Under these assumptions, the limit on the magnetic field from 1ES 0229+200 data, is $B_{IGMF} < 10^{-17}$ G, consistent with [TVN11].

Systematic and Astrophysical Uncertainties for 1ES 0229+200

The effects of two systematic uncertainties, viewing angle $\theta_{\rm v}$ and Doppler factor Γ, can be considered in our analysis. The default assumptions in the analysis are $\theta_{\rm v} = 0$ and $\Gamma = 10$. Increasing the viewing angle, e.g. $\theta_{\rm v} = 2^{\circ}$ as done in [TVN11], would further overproduce radiation in the HE regime (see Figure 3.7a). Increasing the Doppler factor, Γ, combined with the $\theta_{\rm v} = 0$ assumption would imply that the overall luminosity of the jet in the VHE band should be lower to fit the VHE observations since the jet is collimated into a smaller angle. Rescaling of the prompt radiation to fit the VHE data will however equally rescale secondary emission in the HE regime if the angular distribution of the prompt

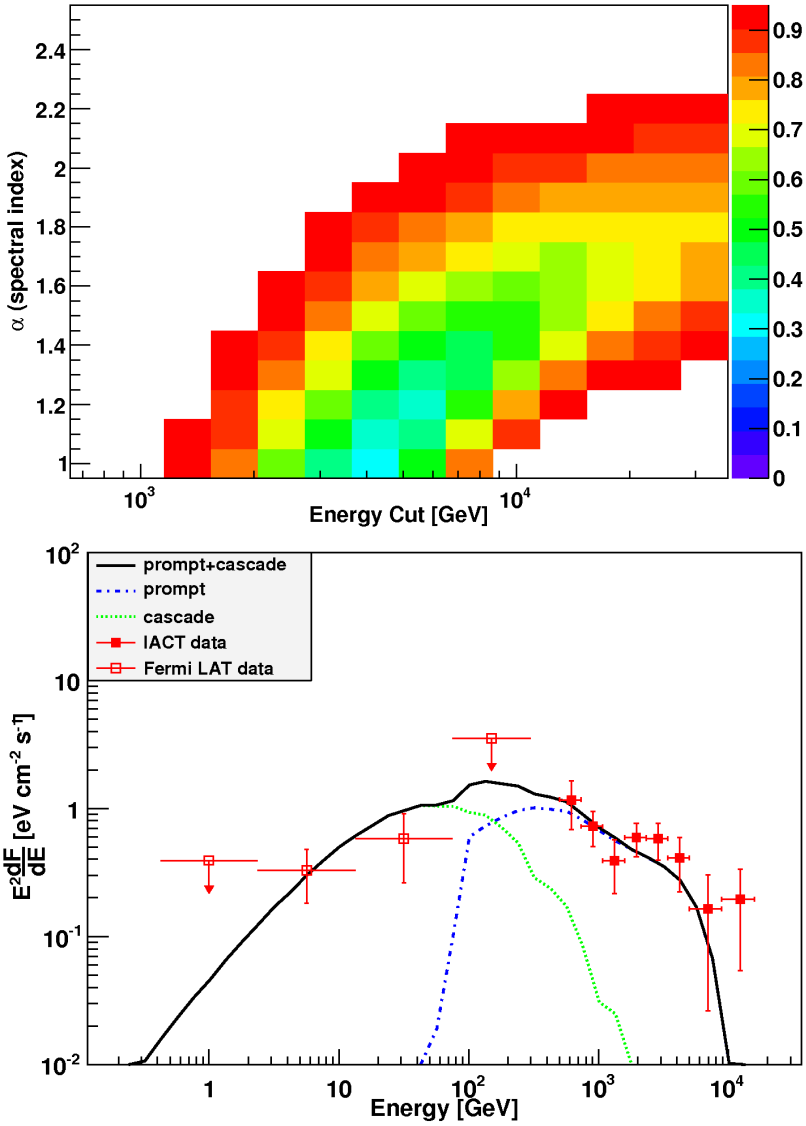

Figure 5.9 Source 1ES 0229+200 analyzed under the assumption of $H0$. (a) (left) Confidence level, or the probability of exclusion of the gamma-ray source model (with fixed α and ϵ_c), where the remaining three parameters of the model (γ, ϵ_B, and F_0, see Eq. 3.9) are chosen so as to minimize χ^2. (b) (right) Simulated dFED of the best fit model (C.L. = 0.995) of $\alpha = 1.3$, $\epsilon_c = 1$ TeV, showing both the prompt and secondary cascade contributions to the total dFED, along with the HE and VHE data.

photons is significantly wider than the characteristic scattering angles acquired in the QED processes. Therefore, for reasonable values of $\Gamma < 100$, the change in the secondary radiation above 100 MeV for the best fit model was found to be negligible. The effect becomes of order 10 % in the lower part of the HE spectral range only for $\Gamma \sim 10^4$ - 10^5, and it cannot be used to reconcile the observational data of 1ES 0229+200 with $H0$.

Since the energy density of the EBL directly affects the propagation length of VHE photons, the uncertainty in the EBL model represents a very important source of systematic error. To investigate this, two additional EBL models were generated, EBL model 2 & 3, shown in Figure 3.2. EBL model 2 is characterized by a considerably lower energy density in the far infrared peak of the dust emission. This model is motivated by the recently resolved lower limit on the EBL which is based on the galaxy counts in the data obtained with the Spitzer ([BDB10, DLP06]), Herschel ([BML10]), and AKARI ([MSK11]) satellites. This model corresponds to the lowest possible far infrared EBL energy density allowed within 2σ. It was found that even with such an extreme assumption about the far infrared EBL, the decrease of the secondary radiation in the model of 1ES 0229+200 was negligible. This conclusion is due to the fact that the source models providing the best χ^2 fits have high energy cutoffs, ϵ_c, below $\sim$ 5 TeV, and are thus insensitive to EBL photon wavelengths $\gtrsim 25\mu$m (kinematic threshold of pair production).

The EBL model 3 is based on the resolved EBL energy density of the starlight peak, which is derived from galaxy counts utilizing data from the HST ([MP00]) in the visible (from 0.36 - 2.2 μm), Spitzer in the near-IR (3.6 - 8 μm) ([FHA04]), and ISO in the mid-IR (15-24 μm) ([ECC02, PDE04]). As compared to the default model 1, this EBL model has an energy density in the visible reduced by

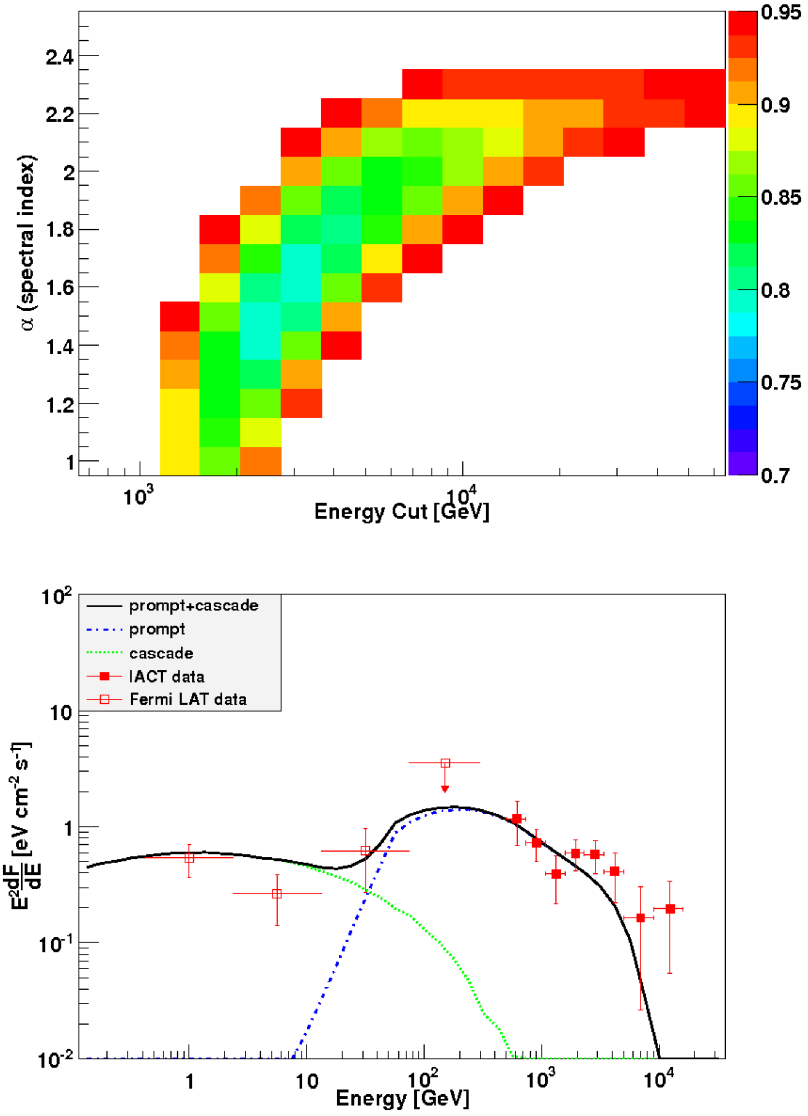

Figure 5.10 Source 1ES 0229+200 analyzed, assuming EBL Model 3 and $H0$. (top) Confidence level, or the probability of exclusion of the gamma-ray source model (with fixed α and ϵ_c), where the remaining three parameters of the model (γ, ϵ_B, and F_0, see Eq. 3.9) are chosen so as to minimize χ^2. (bottom) Simulated dFED of the best fit model (C.L. = 0.78) of $\alpha = 1.6$, $\epsilon_c = 3.16$ TeV, showing both the prompt and secondary cascade contributions to the total dFED, along with the HE and VHE data.

about 25% which is compatible with the galaxy counts results to within 1σ. The energy density in the near IR is reduced by about 50 %. At 3.6 μm, model 3 has an energy density of 4.0 nW m^{-2} sr^{-1} which is within the 2σ limit (3.5 nW m^{-2} sr^{-1}) from the galaxy counts result derived by [FHA04]. At 4.5 μm, model 3 has an energy density of 3.0 nW m^{-2} sr^{-1}, which is within the 1σ limit from the Fazio et. al. analysis. Given the uncertainty in the 5.8 and 8.0 μm galaxy counts by Fazio et. al. at the bright fluxes, [FRV08] reanalyzed the Spitzer data to conclude that at 8.0 μm the energy density of the EBL is 1.92 nW m^{-2} sr^{-1} with a 2σ lower bound of 1.23 nW m^{-2} sr^{-1}. The energy density of EBL model 3 is 1.4 nW m^{-2} sr^{-1} which is within the 2σ bound from the [FRV08] result. As has been pointed out by several authors ([MR07, KD10, DPR11]) the 5.8 μm result of [FHA04] is likely to have been also contaminated by excessive contributions from bright local galaxies, but it has not yet been re-analyzed, unlike the 8 μm point. Nevertheless, all of these authors have recognized that that the Fazio et. al. result at 5.8 μm should be corrected, and many have used the EBL energy density at this point, significantly lower than 3.6 nW m^{-2} sr^{-1} reported by [FHA04]. The 1σ lower bound used by [MR07] is 2.4 nW m^{-2} sr^{-1} and it is 2.5 nW m^{-2} sr^{-1} in [DPR11]. The 2.1 nW m^{-2} sr^{-1} assumed in model 3 is within the 2σ error bar from these later results. Thus, EBL model 3 is compatible with the galaxy counts results to within 2σ but it effectively does not allow any additional contribution to the EBL from unresolved or unknown sources. We do note, however, that more recent work has argued for a 1 sigma lower limit well above our EBL model 3 in the 0.1 - 0.8 μm range [SMS12], and ongoing work in this area will extend these limits out to 4 μm, which will have greater importance to this study. If the 2 sigma lower bounds on these more recent studies in the $\sim$ few to 10 μm range violate the EBL SED we take to be the lowest bound EBL model, EBL model 3, then this model must be re-evaluated and modified.

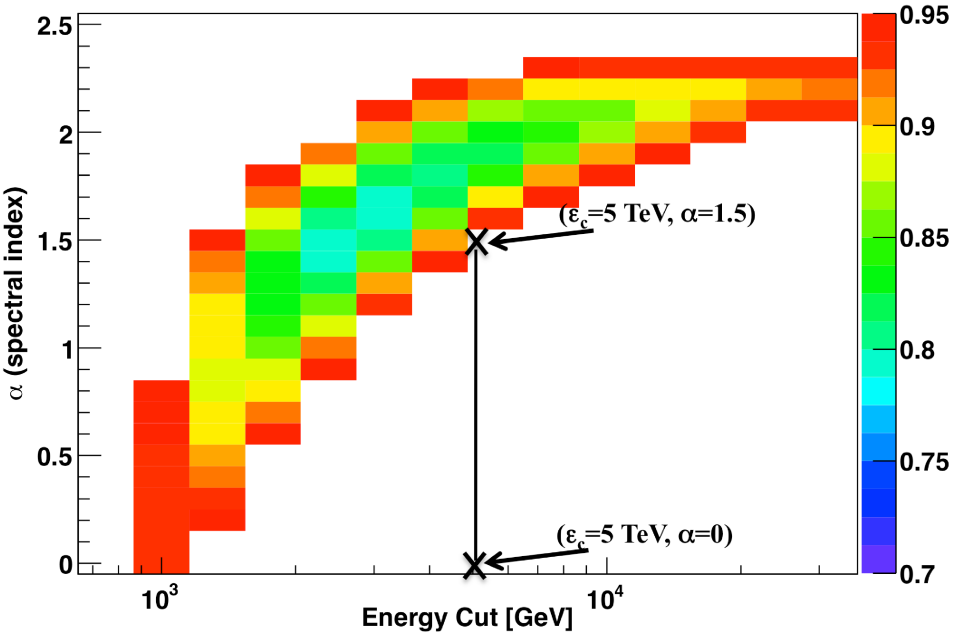

Figure 5.11 Confidence level, or the probability of exclusion of the gamma-ray source model (with fixed α and ϵ_c), where the remaining three parameters of the model (γ, ϵ_B, and F_0, see Eq. 3.9) are chosen so as to minimize χ^2, for source 1ES 0229+200 obtained under the assumption of EBL Model 3. The black line terminated with crosses represents the range of models analyzed in [VTS12].

The results of the simulations of intergalactic cascading for model 3 with $H0$ are shown in Figure 5.10a. It was found that a number of 1ES 0229+200 source models are compatible with the combined VHE and HE data set, and one of the best fit examples characterized by $\alpha = 1.6$, $\epsilon_c = 3.16$ TeV is shown in Figure 5.10b.

The strong sensitivity of the secondary photon flux to the EBL energy density in the near-IR combined with the conspicuous lack of a non-trivial EBL absorption feature in the VHE energy band ($\sim$ 200 GeV - 5 TeV) is due to the peculiar behavior of the EBL in this wavelength range. For $\lambda I_\lambda \propto \lambda^{-1}$, the optical depth is independent of the energy of a VHE photon (gray opacity). A small deviation from this proportionality results in a logarithmically slow dependence of the opti-

cal depth on the energy of the VHE photon, producing a power law, rather than exponential-like change in a blazar spectrum as discussed in [Vas00]. The behavior of the SED in the mid-IR exactly satisfies this condition and explains the "invisibility" of EBL absorption effects in a blazar dFED. The effect however is strong and reflected in the change of the spectral index of this blazar. In fact, this feature was used to derive upper limits on the EBL energy density in the mid-IR, which are taken to be the values of model 1, by assuming that the spectral index of the source 1ES 1101-232 cannot be harder than 1.5 (e.g. [AAB06b]). The 25 - 50% lower mid-IR density of model 2 significantly softens the intrinsic spectrum of 1ES 0229+200 reducing the total energy available for the development of the intergalactic cascade, and therefore the flux of the secondary photons. Thus, there are a range of EBL models with mid-IR energy density bounded by the lower limits on the EBL to some SED slightly below that of model 1 which are compatible with the EBL lower limits and $H0$.

In a recent study of the dual constraints on the EBL and IGMF it was found that an EBL model similar to model 3, is still incompatible with $H0$ and would require a lower bound of $B_{IGMF} = 6 \times 10^{-18}$ G ([VTS12]). All source models analyzed in that paper had a single cutoff energy $\epsilon_C = 5$ TeV and varied the spectral index α in the range of 0 - 1.5 with a single power law dFED over the entire VHE and HE energy range. A similar assumption of a steady flux from 1ES 0229+200 over the lifetime of the *Fermi*-LAT was made. Figure 5.11 illustrates the confidence level for a wider range of source models analyzed in this work together with the range of models considered by [VTS12]. The figure confirms the incompatibility of $H0$ with the data given assumptions about the source model used in that paper. However, in an extended parameter space of the 1ES 0229+200 models, $H0$ can be reconciled with observations of this source.

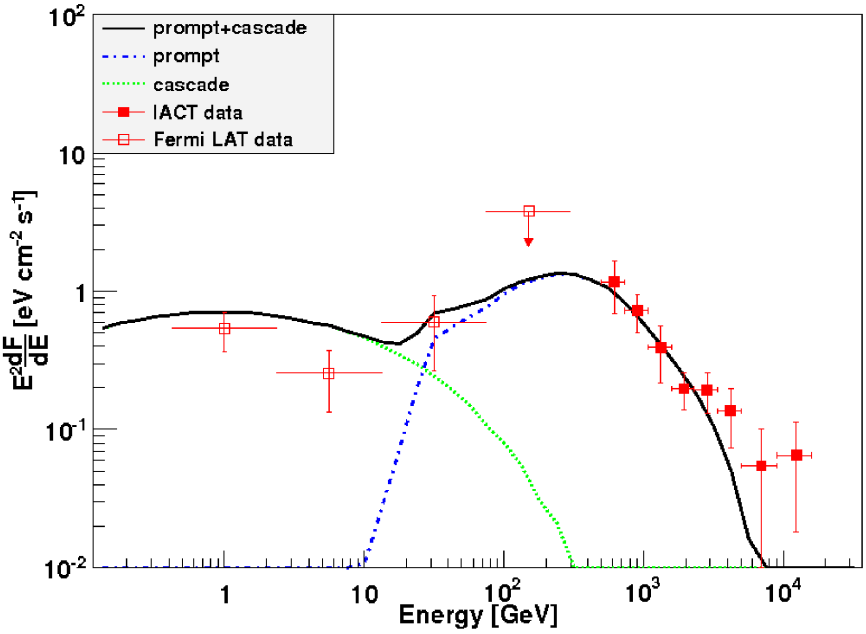

Figure 5.12 Spectral model of 1ES 0229+200 of $\alpha = 1.3$, $\epsilon_c = 1.78$ TeV (C.L. $\lesssim$ 0.8), utilized for the study of the effect of the duty cycle of the TeV data. The five highest energy data points are scaled down by $10^{-1/2}$ of their flux values to that reported in [AAB07a].

Another avenue to make the HE-VHE observational data of 1ES 0229+200 compatible with $H0$ is to question whether or not the VHE flux of the source reported is representative of the average flux during the *Fermi* mission. The HESS measurements were accumulated in 2005 (6.8 hrs) - 2006 (35 hrs) and are not strictly contemporaneous with the *Fermi* HE spectrum. The significance of the detection in 2005 reported is 2.7σ, while in 2006 it is 6.1σ with average photon fluxes above 580 GeV of 6.8 $\times 10^{-13}$ cm^{-2} s^{-1}, and 10 $\times 10^{-13}$ cm^{-2} s^{-1}, respectively. Due to the low flux of this source (1-2% of the Crab nebula flux), and the small data set in the original 1ES 0229+200 discovery paper, statistically significant flux variability as observed in 2005 and 2006 was not detected. Although these observations are compatible with a constant flux, the variability hypothesis cannot be ruled out, based on the statistical and systematic errors reported. Furthermore, observations of this source in 2009, as reported by VERITAS ([PV10]), were compatible with the average flux value of the HESS data set. However, the average flux obtained was dominated by a period of significantly higher "flaring" activity during a single dark run. In general, VHE observations above a few TeV (relevant for secondary photon production) require considerable integration time and so far, they are too sparse to claim that the HESS value of the flux is representative of the average flux during the *Fermi* mission. Further communication with the VERITAS Collaboration suggests that the flux level of 1ES 0229+200 has been steadily declining from 2009 - 2012 (private communication). To investigate the effect of a reduced duty cycle for 1ES 0229+200, the spectrum of this source was modified at the highest 5 energy points to half an order of magnitude of their reported values. It was found that the VHE - HE data set combined in this way does not rule out $H0$ at more than 95% confidence level. One of these compatible models, with $\alpha = 1.3$ $\epsilon_c = 1.78$ is shown in Figure 5.12. Therefore, the conclusion that the $H0$ is ruled out with

high significance heavily rests on the assumption that the HESS measurements are representative of the average flux for E $\gtrsim$ 2 TeV and a $\sim 10^{-1/2}$ change of the highest energy part of the spectrum invalidates this conclusion.

Therefore, we see that the lower limit on the IGMF of approximately 10^{-17} G rests on a number of important assumptions, but cannot be unequivocally confirmed at present. These assumptions are (at least): 1) That the long-term, multi-year time-averaged VHE spectral energy density measurements can be approximated as indentical to that measured and published by VHE instruments over a total exposure time of hours across several weeks or months. The flaring activity of most TeV blazars raises concerns regarding this assumption of a constant TeV flux. 2) That the EBL spectral energy density as modeled by authors such as [DPR11], is very close to the actual value. We have shown that the amount of cascade emission strongly depends on the assumed SED of the EBL in the near-IR, and this energy range of the EBL in particular has the greatest effect on the lower limits derived for the IGMF. 3) An additional assumption is made that the majority of the intergalactic cascade takes place in the voids, so that the IGMF is being measured, rather than taking place in filaments or other areas of gravitationally bound structures, with a higher associated magnetic field. If the locations of voids were well known and characterized out to the redshifts of these sources, then this consideration could be properly accounted for. Finally, an additional assumption being made which was not explored in the present chapter is that no other physical processes are at work other than the electomagnetic cascade, from gamma-rays launched directly from the source. As discussed in the final chapter of this thesis, a number of authors have proposed alternative interpretations of the data, the merits and validity of which are currently under intense scrutiny.

Future Spectral Measurements

Despite the challenges of constraining the IGMF under current generation instrumentation, there are many reasons to be hopeful that robust lower limits may be established on the IGMF using the spectral analysis of the combined GeV – TeV data through the use of future instrumentation. The capability of this method is limited not only by the astrophysical and systematic uncertainties, but also by the data itself-particularly the low sample of AGN with significant amout of power emitted at greater than a few TeV, so that the GeV cascade emission can be reasonably well-constrained. CTA, the next generation, ground-based gamma-ray observatory[2], will help establish a catalog of AGN with much improved sensitivity (better than an order of magnitude increase), smaller error bars, and extended coverage of the highest energies. Furthermore, HAWC[3], a future large field of view instrument, sensitive at greater than TeV energies, will help better constrain the long-term variability and time-averaged spectral properties of some of these brightest sources at the highest energy band ($\gtrsim$ few TeV) which is most relevant to this work. Therefore, although the evidence is premature to justify a robust lower limit at present, the future of this kind of work is very promising over the next few years.

[2] http://www.cta-observatory.org/
[3] http://www.hawc-observatory.org/

CHAPTER 6

Angular and Time Delay Effects of Cascading

In addition to the spectral signatures of the IGMF in the observational data of extragalactic sources as discussed in the last chapter, there are at least two other imprints of the IGMF which observations may uncover in the angular and temporal domains. The observational signatures of IGMFs, such as an angular extension or "halo" surrounding an otherwise point source of extragalactic gamma-rays, and a time delay in the arriving gamma-rays or "echo", are possibly detectable features if the amplitude of the magnetic fields is within some range. These potentially observational features are described in this chapter, as well as their detectability with current and future instrumentation.

6.1 Angular Domain Features

The initial study of the possibility of detecting a "halo" surrounding an otherwise point souce of gamma-rays was undertaken by [ACV94]. The authors considered the case where the magnetic field in the region of a few Mpc surrounding the source was of order 1 nG, and hence the electron positron pairs, if produced within this volume, were immediately isotropized, and thus the secondary radiation of the cascade is spread out over a 4π solid angle. The most likely scenario for detecting such a halo is if the VHE source spectral energy density is peaked near $E \gtrsim 100$ TeV, so that most of the initial photons pair produce within about 1

Mpc of the source, and the source would "glow" with this secondary radiation from the isotropized pair particles. In this case, the typical angular size of the halo scales with distance to the source, and all sources with sufficient power in the highest end of the energy spectrum would exhibit such halos, not only those AGN whose jets are pointed towards the observer. For typical estimates of the energy budget of the jets of AGN, the isotropization of such sources would make very weak VHE halos around AGNs, which so far have not been detected by any gamma-ray observatory.

In this section, we consider the case where the IGMF is not high enough to isotropize the electrons and positrons, and so the secondary emission is produced over solid angles $\ll 4\pi$, but the pair production can occur at distances much greater than 1 Mpc from the source, in the cosmic voids. In this case, the halo structure is significantly more complex and depends on a number of factors-the spectral characteristics of the source, the redshift, the IGMF value, the viewing angle of the observer to the jet axis, and the boost factor of the blazar jet. For example, figure 6.1 displays a simulation of the photon ($E > 1$ GeV) arrival angle distribution from a source at z = 0.13, with significant power emitted in the 10 - 30 TeV band, with gamma-ray source model parameters $\alpha = \gamma = 1.5$, $\epsilon_c = 30$ TeV, $\mathrm{B}_{IGMF} = 10^{-15}$ G, $\Gamma = 30$, at four different observing angles, $\theta_\mathrm{v} = 0°$, $2°$ $5°$, and $10°$ (see Eq. 3.9). The main trend in these figures is that the overall luminosity of the secondary emission rapidly declines as the observing angle increases, and that the photon distribution around the source becomes increasingly axially non-symmetric, when $\theta_\mathrm{v} \gtrsim 1/\Gamma$. The luminosity of the secondary photons declines with increasing angular distance from the source position. Thus, detecting non-axially symmetric halos around AGN with existing instrumentation may prove to be exciting but challenging. Figure 6.1 is in qualitative agreement with previously reported findings in a study of similar effects by [NSK10].

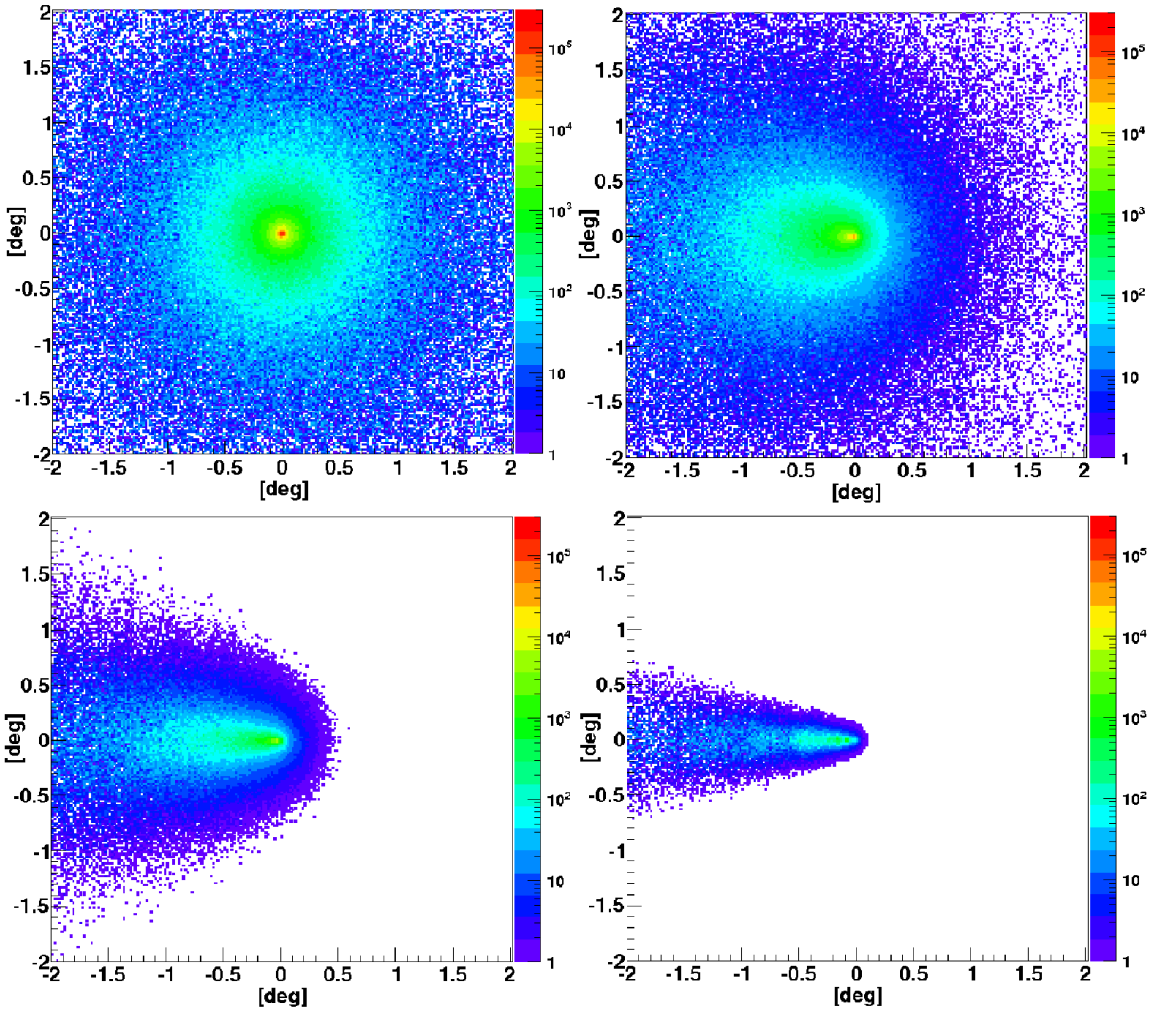

Figure 6.1 Skymaps of secondary emission due to intergalactic cascading for a source at z=0.13, with source model parameters $\alpha = 1.5$, $\epsilon_C = 30$ TeV, and $B_{IGMF}=10^{-15}$, $\theta_{obs} = 0°$ (upper left), 2° (upper right), 5° (lower left), 10° (lower right)

To understand the generic features of the halo structure, we choose typical values of the source model, for a source at $z = 0.13$, with a spectral index of $\alpha = \gamma = 2$, cutoff energy $\epsilon_C = 10$ TeV, bulk Lorentz factor $\Gamma = 10$, and viewing angle, $\theta_v = 0°$, and these parameters will be used throughout the remainder of this section, unless otherwise stated. The model is chosen such that the flux energy density of the intrinsic source spectrum is approximately constant throughout the entire

energy range of interest until 10 TeV. Figure 5.1 shows the 68 % containment radius of the halo flux for IGMF in the range of $10^{-18} - 10^{-13}$ G. The angular distribution of halo flux (especially at energies greater than around 10 GeV) will certainly depend on the spectral properties of the source, particularly at energies $\gtrsim$ 10 TeV, but this provides a good starting point to investigate the generic features. As illustrated in the figure, for $B_{IGMF} \lesssim 10^{-18}$ G, the angular spread is too small to be resolved by current instrumentation, falling within the point spread function of the LAT and IACTs (see chapter 4). However, for magnetic fields in the range, 10^{-17} G $< B_{IGMF} < 10^{-13}$ G, the halo may be detectable as an angular extension surrounding the source.

In order to assess the capabilities of current and future instruments to resolve this angular structure, we examine the angular resolution (that is the 68 % containment radius) of the *Fermi*-LAT which covers the HE energy range, and the next generation, ground-based IACT, the Cerenkov Telescope Array observatory (CTA)[1]. Fig. 6.2a shows a plot of the angular resolution of the *Fermi*-LAT and of two different configurations of the proposed CTA observatory, taken from the document, "Performance Requirements for CTA", an official internal collaboration memo (Ref. MAN-PO/121004). Two different configurations for CTA are described, "CTA-EU" and "CTA-US". CTA-EU is the baseline for the CTA cofiguration. CTA-US is the array configuration with an additional 36 telescopes contributed by US funding agencies, and is expected to be the one which is constructed. The LAT angular resolution is taken from section 4.1.1. It appears that the *Fermi*-LAT may be suitable to resolve the halo emission if the IGMF is within the range of around 10^{-17} – 10^{-15} G. For fields much greater than 10^{-14} G, too much of the halo emission would probably be isotropized and it would not be bright enough for the LAT to resolve. On the other hand, for the halo

[1] http://www.cta-observatory.org/

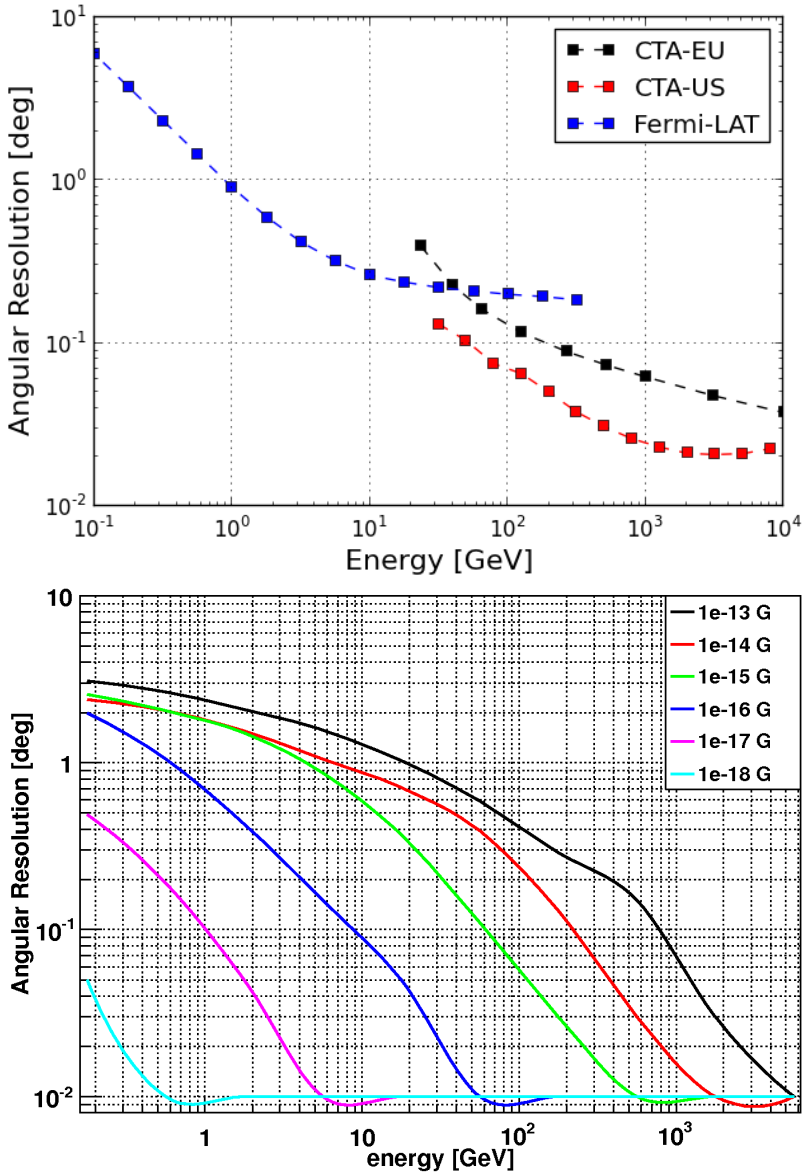

Figure 6.2 (top) Angular resolution (68 % containment radius) of the *Fermi*-LAT satellite, for front + back converting photons (see section 4.1.1), the CTA-EU configuration, and the CTA-US configuration of the CTA observatory (see text for details on these differences). (bottom) 68 % containment radius of the halo flux, for a range of magnetic fields, and for a source at z = 0.13, with a source spectrum defined by $\alpha = \gamma = 2$, cutoff energy $\epsilon_C = 10$ TeV, bulk Lorentz factor $\Gamma = 10$, and viewing angle, $\theta_v = 0°$.

with energies $\gtrsim$ 30 GeV, it appears that fields in the range of about 10^{-15} G -10^{-13} G (or higher) may be resolved. In this way, CTA and Fermi would be able to cover a large range of IGMF parameter space. Even more information about the IGMF could be extracted if the angular distribution was resolved in multiple energy bands. Figure 6.3 shows the angular distribution ($\theta dn/d\theta$ vs. θ) of the arrival angles of secondary cascade emission for various energy bins assuming an IGMF of 10^{-16} G and 10^{-14} G.

Further complicating the situation is the fact that there is in general the source's prompt (direct) radiation overlayed upon the secondary cascade halo flux, because the non-ideal PSF of the instrument will re-distribute gamma-rays arriving with angle 0° from the source position to some non-zero angle from the source position. Because of this, the prompt flux is an additional background upon which the halo emission must be detected. As all of these considerations show, there is clearly a complicated optimization problem here for detecting the angular extension of secondary gamma rays, involving some source spectral characteristics, range of B, z, θ, Γ, secondary energy range, instrument PSF, etc. This optimization problem is too compicated and the unknown parameters too poorly constrained to directly attack this problem. Instead, we outline some strategies that future observatories may employ to have the best chance of detecting the gamma-ray halo.

6.2 Strategy for Halo Search

The search for a halo surrounding individual sources in the GeV domain has so far been unsuccessful, limited by the sensitivity and angular resolution of the LAT. Because of this, the question of the detectability of the halo based on LAT data is not particularly promising at this stage. A source stacking analysis may be the

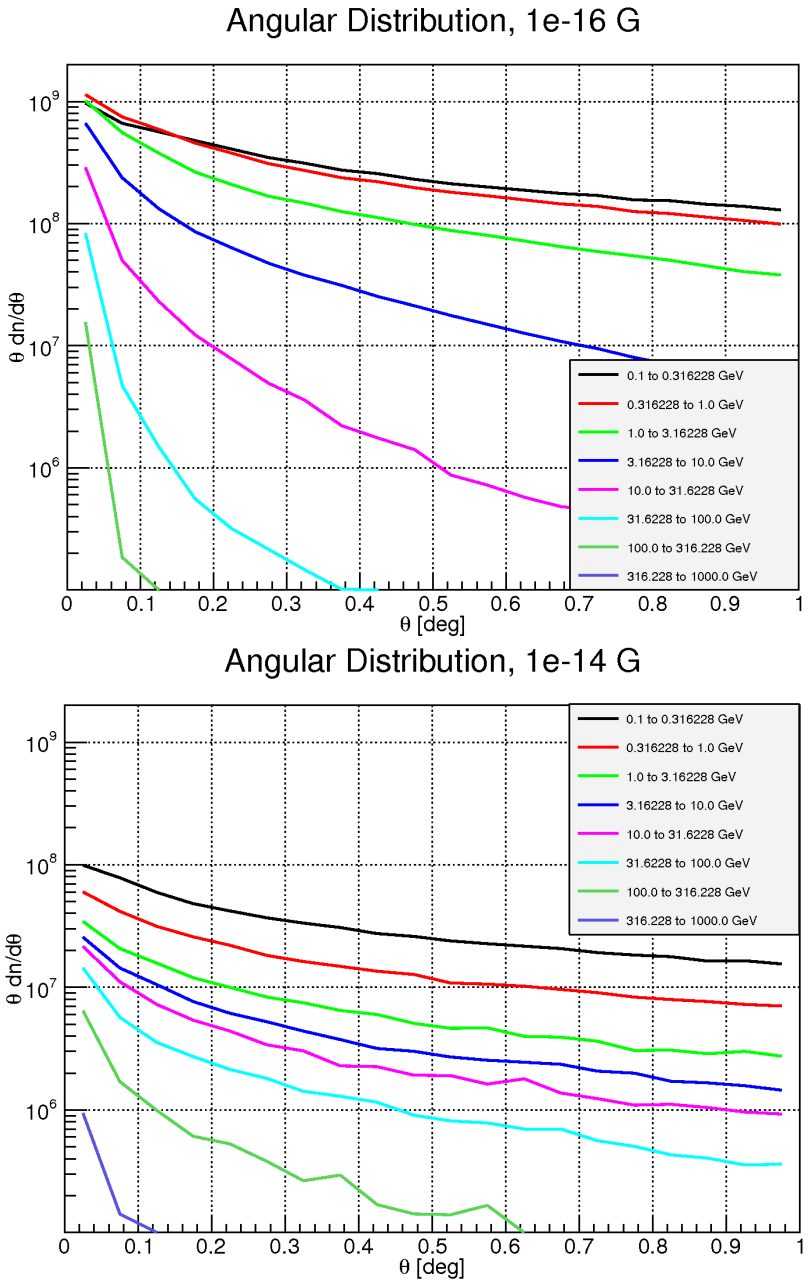

Figure 6.3 Angular distribution of the arrival angles of secondary gamma rays under the assumption of (top) $B_{IGMF} = 10^{-16}$ G and (bottom) $B_{IGMF} = 10^{-14}$ G.

best way to proceed, but the source selection criteria will be very important, since the catalog of TeV sources is not very high (relative to the number of sources detected in the GeV energy band) and in particular the spectral properties at high energies relevant to this study are not very well studied yet. CTA will help assemble a source list in which a more justified source selection criteria can be applied.

It is also important to consider the expected delay time of the angular emission, however. In chapter 3, Figure 3.4 shows the average arrival time of the secondary emission from a monoenergetic beam of 100 TeV primary photons, for different values of the IGMF, which is a good indicator of the average delay time of the secondary emission to arrive at the observer. For magnetic fields in the range where current instrumentation has the sensitivity to possibly detect their effects, namely from about 10^{-17} G to $\sim 10^{-13}$ G, the delay times of the secondary emission relative to the prompt emission ranges from years to 10^6 years. Therefore, one may expect halo emission to arrive from sources which are not visible today as AGN so the source selection would not necessarily be based on the current TeV catalog, but signatures from other wavebands, which may indicate a history of accretion activity from 10^5 – 10^6 years ago. The clues to search for this emission from "dead" blazars may be relics of a past jet and accretion in the galaxy.

It is important to ask the question of what can be learned about the IGMF if a halo is detected? How underdetermined would the IGMF be based on the detection of a halo from a single source or even a carefully chosen subset of sources? To answer this question of how well the magnetic field would be constrained, one would ideally resolve the angular extension in multiple energy bands. As shown in Fig. 6.3, the halo has a definite energy structure, and this may be the obser-

vational signature needed to make a very constraining limit on the IGMF. For some range of IGMF close to the upper limit of detectability (10^{-15} G $\sim$ 10^{-13} G), it may be possible to detect the angular extension in a higher energy range ($\gtrsim$ 30 GeV). At these energies, the *Fermi*-LAT has a very small collecting area ($\sim$ 1 m^2, see chapter 4) and thus very low sensitivity, even though it has very good angular resolution ($\sim$ 0.1°). This region overlaps with the lowest energy range where CTA may have good sensitivity, approximately 30 GeV - 100 GeV. Although the angular resolution will not be optimal here, $\sim$ 0.2 - 0.4°, the collecting area is much higher, $\sim$ 1 km^2, and thus, CTA may have a good chance of detecting an angular extension near 100 GeV, and detecting a signature of an IGMF in the vicinity of 10^{-14} G.

We mention one final way to use the basic ideas of cascading and "halo" formation to search for an IGMF signature. [VP13] have suggested that IGMF may leave an imprint on the angular anisotropy of the extragalactic gamma-ray background through its effect on the electromagnetic cascades, if sufficient power in the TeV band over a sufficiently long period of time occurs. A strong IGMF will isotropize the lower energy electrons in the cascade, thus introducing an anisotropy of the energy spectrum of the gamma-ray background. Significant uncertainties remain in the calculation of the anisotropies, however, and it is not clear what if anything can be concluded about the IGMF if no anisotropies are reliably detected.

6.3 Time Domain Features

The first to point out the possibility of detecting weak intergalactic magnetic fields through the time-delayed emission from "pulses of gamma-rays"-either from gamma-ray bursts or flares from blazars with significant power emitted in the

VHE band, was [Pla95]. His idea was that if there exists sources of gamma-rays with short, well-defined periods of elevated luminosity, the signal from this source would be decomposed into the "prompt" pulse of gamma-rays which does not interact with the EBL to pair produce, and a delayed after pulse, called "Field Induced Delay" (FID) of cascade photons arising from the electrons and positrons IC scattering with the background photon fields.

The reason for the FID, is that the electrons and positrons in the cascade which eventually upscatter photons to create secondary gamma rays, will travel a greater path length than photons arriving directly from the source. Furthermore, a secondary IC scattered photon produced in one of the first IC scatterings will experience a smaller time delay than a secondary photon produced after the electron has propagated many scattering lengths, because the electron has been more greatly deflected by the IGMF. The characteristic delay time for each energy band is also dependent on the IGMF strength, as shown for example, in chapter 3, figure 3.4, which makes it a potential observational probe of the IGMF. An approximate analytical formula for the average delay time of a secondary photon was worked out by [NS09], who estimated that the average delay time incurred by a secondary photon in the cascade scales as

$$T_{\rm delay} \propto \left(\frac{E_\gamma}{0.1\ {\rm TeV}}\right)^{-5/2} \left(\frac{B_0}{10^{-18}\ {\rm G}}\right)^2 \tag{6.1}$$

when the magnetic field coherence length is large compared to the electron/positron cooling length. A more precise calculation can be determined from simulations, where no analytical approximations are taken, and both the EBL and CMB photon fields are used in the determination of time delays, as shown in Fig. 3.4. In the 1 - 10 GeV band, where *Fermi*-LAT would have optimal sensitivity, for zero IGMF, the mean time delay due only to the scattering angle acquired by the QED

processes is of order 1 hour. The mean time delay in the same energy range for a 10^{-18} G field is of the order of tens of years, but most of the emission arrives in the first few days, with a very long tail in the arrival time distribution, as shown below (see, e.g. the daily lightcurve of Fig. 6.5, for $B_{IGMF} = 10^{-17}$).

It has taken some time for these ideas to be applied to real data, due to the sensitivity requirement to detect this delayed emission, and to date, these FID echos have eluded detection. So far, two papers have been published which have claimed evidence for a lower limit on the IGMF due to the non-detection of these delayed pulses of gamma-rays, by comparing the light curves of the VHE and HE band. The first study of [TMI12] used simultaneous GeV-TeV light curves of source Markarian 501 (Mrk 501) using VHE data from MAGIC and VERITAS, that included a TeV flare over three days from MJD 54953 – 54955 in 2009, with elevated flux levels of about 5 times over the rest of the observing period. Throughout this period, the *Fermi*-LAT conducted survey observations of Mrk 501 and a daily light curve of the LAT upper limits was derived and compared to the predicted cascade emission under a number of different magnetic field configurations. It was found that an IGMF at 10^{-20} G with coherence length of 1 kpc was excluded by the data at a relatively weak 90 % confidence level.

A second study, [TMI13] used long term lightcurves of blazar Mrk 421 from both the *Fermi*-LAT and the ARGO-YBJ experiment [TBB11] over a period of about 2 years to search for the delayed echo emission from isolated flares in the VHE band. From the non-detection of a certain level of GeV emission from these VHE flares, it was concluded that a magnetic field $B_{IGMF} < 10^{-20.5}$ G at a 1 kpc coherence length is excluded at the level of 4 σ. The result is scaled to other coherence lengths roughly as $B_{IGMF} \gtrsim 10^{-22}$ max$[(L_{coh}/350 \text{ kpc})^{-1/2}, 1]$ G.

6.3.1 Observational Signatures of Echo Emission

In this section, we discuss the observational features of echo emission, and main ideas behind the possible detection of this effect. The best and cleanest scenario for detection of an IGMF would appear to be the following: an IACT would detect a hard, rapid, isolated VHE flare, and the characteristic time delay could be searched for in follow up observations at lower energies, and possibly different energy bands. There have been a number of examples of hard, rapid flares, in the current generation of IACT detectors. Possibly the most well-known in the VHE gamma-ray community, was the detection by the HESS collaboration of a very hard rapid flare from source PKS 2155-304, a blazar at $z = 0.116$ [AAB07c]. During one night of extreme flaring activity, 2006 July 28, the flux level of this source increased by about 50 times its usual value, to about 7 times the Crab flux, with an EBL-corrected intrinsic spectral index of around 2.2 in the VHE band. Figure 6.4 shows the two hour lightcurve for this flare.

There have been at least two other notable cases where surprisingly rapid, isolated gamma-ray flares have been observed. Both of which occured for sources of the class of object called Flat Spectrum Radio Quasars (FSRQs) and were detected by MAGIC. The first such flare was detected from source 3C 279 in 2006, which has a redshift of 0.536. One night in particular, February 23, 2006, the source flared to nearly 1 Crab, as measured with an energy threshold above 100 GeV, with a differential spectral index of about 4.1 [MAA08]. This source is also noteworthy for being the most distant source detected by an IACT instrument to date. The second flare of interest to this study, was from the FSRQ 4C +21.35 (also known as PKS 1222+216) again, at a relatively distant redshift of 0.432 [AAA11]. During a 0.5 hour observation on June 17, 2010, the source flared to around a Crab level, with a soft observed photon index of about 3.75 above

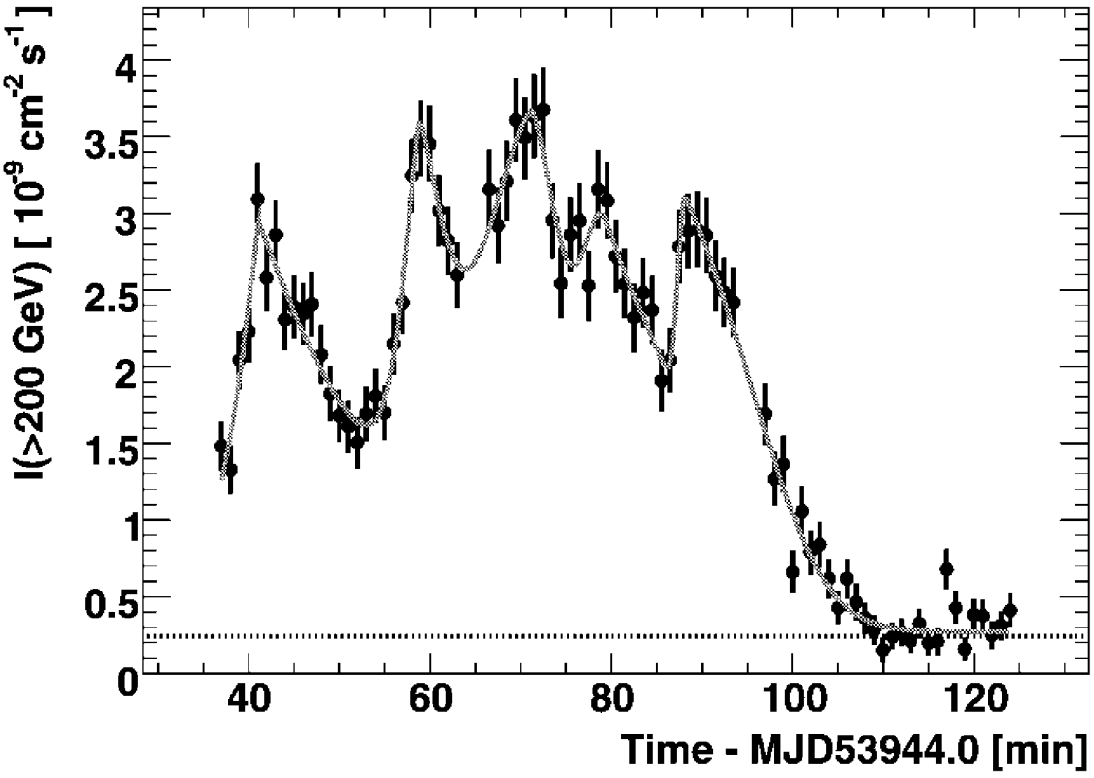

Figure 6.4 2 hour lightcurve for flare of PKS 2155-304, where the horizontal (dashed) line is the Crab flux. The flux level increased to about 50 times its average value, to about 7x the Crab flux.

100 GeV. This elevated flux level in the VHE band coincided with a flare in the HE band, as detected by the *Fermi*-LAT. According to the MAGIC publication, during the flare, the spectral index of this source, when EBL absorption-corrected, was well-fit by a single power law with differential spectral index of approximately 2.7, between 3 GeV and about 400 GeV. Unfortunately, both of these flares from FSRQs were probably too soft and the maximum energy detected was too low to claim a high level of cascade radiation which would provide an impetus for the search for GeV echo emission. However, harder and higher energy flares, of the type similar to PKS 2155-304 may be detected in the future, in particular by

more sensitive large FOV TeV survey instruments such as HAWC[2], or by CTA.

To provide an example of the type of observational echo signatures of these types of flares, we use a "PKS 2155-304-like flare", and examine the lightcurve which would be produced by the echo flux of the flare. Figure 6.5 shows the integral flux in daily time bins, determined by simulations in three different energy bands, for an IGMF of 10^{-17} G, for a flare with similar characteristics to PKS 2155-304, with the power law spectral index extending up to 32 TeV. One of the main features of the time delay distribution is that although there is a very long tail in the arrival time in each energy band, by far the greatest amount of daily flux occurs in the first few days after the flare. In these first few days, then, it is most desireable to search for the IGMF-dependent signal.

6.4 Prospects for Detection by Future Instruments

In addition to the challenge of serendipitously detecting an isolated VHE flare, it is also challenging to detect the quickly fading signal as shown in 6.5. Particularly difficult is the possibility of GeV survey instruments, such as the *Fermi*-LAT to detect flux variations on daily or sub-daily scales, as required by this technique. Because of this, we primarily consider the possibility of detection by the Cherenkov Telescope Array (CTA). Although the final design parameters have not yet been solidified, we consider two reasonable design configurations, which we denote "CTA-EU" and "CTA-US", as brifely discussed in section 6.1.

The secondary cascade radiation produced depends on the amount and distribution of photon flux in the VHE flare. To be specific, we choose to model the VHE flare spectrum as a power law plus exponential cutoff (see Eq. 3.8), nor-

[2] http://www.hawc-observatory.org/

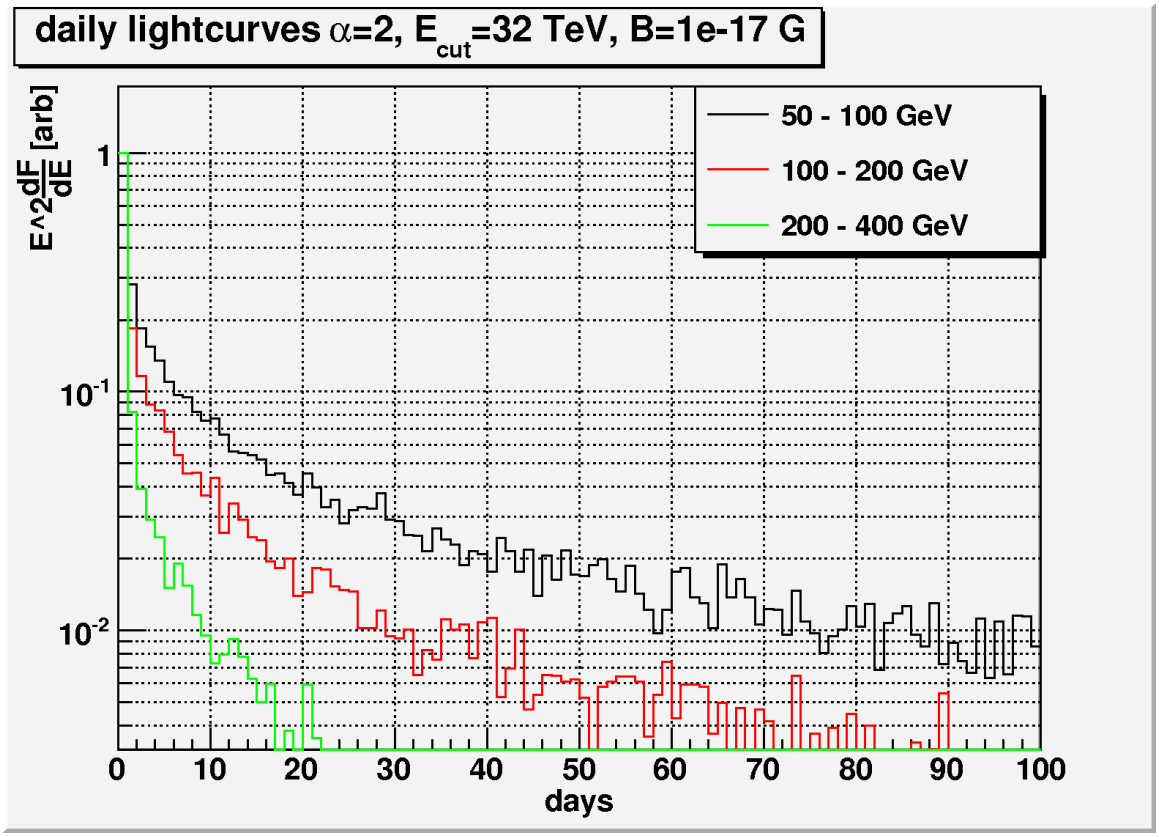

Figure 6.5 100 day lightcurve in three different energy bands, for a prompt flare with similar characteristics to source PKS 2155-304. The echo flux persists at the level of a few % over a period of a few weeks.

malized to the Crab flux at 400 GeV, with a moderately hard power law index of 1.75 and a cutoff energy of 10 TeV, for a source at redshift of 0.14. Figure 6.6 shows the time-averaged differential flux energy density (dFED) in several time bins for this flare under the assumption of $B_{IGMF} = 10^{-17}$ G and $B_{IGMF} = 10^{-18}$ G. As it turns out, a rather narrow range of IGMF is possible to probe using this technique ($10^{-18} \lesssim B_{IGMF} \lesssim 10^{-16}$ G) in the energy range where CTA would have good sensitivity. This is primarily due to the fact that the peak in the spectral energy density of the cascade flux in the following day time bin is strongly dependent on the magnetic field. However, combined with the studies

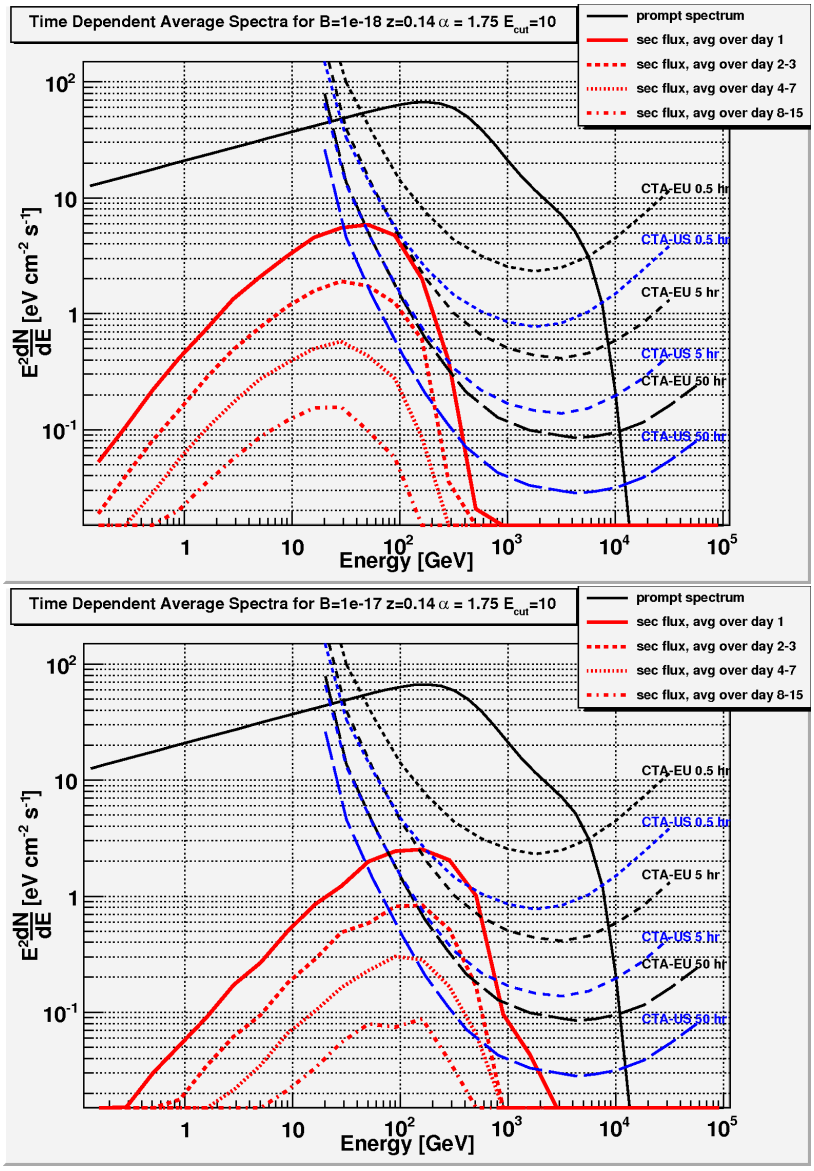

Figure 6.6 Simulated spectra for a source at z=0.14, for a flare with spectral index = 1.75, and cutoff energy 10 TeV, and (top) $B_{IGMF} = 10^{-18}$ G and (bottom) $B_{IGMF} = 10^{-17}$ G.

of the magnetic field in the angular domain, these two techniques would cover the fairly wide range of about 10^{-18} G – 10^{-13} G, more sensitive to such small IGMFs, than any other observational technique.

CHAPTER 7

Discussion and Conclusions

This thesis provides a detailed study of the phenomenon of VHE gamma-ray initiated electromagnetic cascading in intergalactic space, through the use of a 3 dimensional, particle tracking Monte Carlo code, incorporating all of the relevant QED and Cosmological physics, with the goal of constraining the IGMF. The three primary observational features of this cascade emission-"halo" emission, "echo" emission, and spectral modification features-have been described. Furthermore, a detailed statistical analysis of the energy flux spectrum of 7 TeV blazars has been presented which attempted to set a lower limit on the IGMF. This approach is promising, but we found that at present, an unambiguous determination of a lower bound on the IGMF cannot be established due to the many systematic and astrophysical uncertainties in the present data. Before making our closing remarks on this study, it is necessary to consider two alternative interpretations of the data which have been reported in the literature, and which may cloud the interpretation of IGMF limits from the detection of secondary gamma-ray emission from electromagnetic cascading.

7.1 Alternative Interpretation 1: Cosmic Ray Proton Source Emission Model

The first of these alternative scenarios is the possibility that the observed gamma-ray data from some sources, possibly the ones in question in this thesis, may be due to proton-initiated cascades, rather than from direct photons, if cosmic ray protons are also accelerated within the same source [EK10]. This scenario relies on the fact that the Universe is nearly transparent to $10^{16} - 10^{19}$ eV protons on spatial scales of hundreds of Mpc - Gpc, so that the majority of protons propagate without interacting with a background photon (EBL or CMB). However, a small percentage of them will interact in a random location along the line of sight, through the $p\gamma \rightarrow p\pi^0$ or $p\gamma \rightarrow n\pi^+$ channels, with the pions quickly decaying into photons and electrons, initiating an electromagnetic shower, with the observed gamma-rays putatively coming from these secondary interactions. Crossing small regions of intense magnetic fields such as those present in clusters and filaments represent difficulties for this mechanism since they rapidly destroy the correlations betwen the cosmic ray directions and the source. Moreover, it is likely a formidable task to devise a mechanism by which cosmic rays have been accelerated to nearly ultra high energies, in the source by intense magnetic fields satisfying the Hillas condition and then highly collimated along a particular direction, eventually entering regions of potentially small magnetic fields of voids without being significantly disrupted by the intermediate magnetic fields. If this mechanism takes place in nature, it has two distinct observational characteristics, namely that the VHE radiation produced should show little evidence for variability and correlations with other wavelength bands such as X-ray, etc. and most importantly, should be accompanied by higher energy gamma-rays, with energies above 10s of TeV in the VHE spectra of extreme blazars with z $\gtrsim$ 0.1. No such

observational evidence has been collected so far to necessitate considerations of this scenario, which also lacks an explanation of the origin of the collimation. This mechanism has been recently studied [MDT12] in the context of the source 1ES 0229+200 with the conclusion that the detection of larger than 25 TeV photons would provide an indication of acceleration of Ultra High Energy cosmic rays in this source.

7.2 Alternative Interpretation 2: Electron Beam Cooling due to Plasma Instability

A second scenario which may be of importance to this work is the possibility that beam-plasma instabilities could develop through the collective interaction with the electrons and positrons in the developing electromagnetic cascade, and the electrons of the plasma in the voids, as recently proposed by [BCP12]. If such a collective interaction between two populations of electrons indeed exists, the energy dissipation rate of electron positron pairs into modes of the plasma waves in voids may become significantly larger than the energy loss through IC scattering, and thus, the cascade would be rapidly suppressed, and attempts to measure or constrain the IGMF through its observation would be severely compromised. The amount of energy loss due to these instabilities as they propagate through the intergalactic medium depends on parameters of the highly energetic electron beam as well as the plasma medium which it propagates through. In what follows below, we provide an estimate of these parameters and discuss the regimes where this effect may become important.

Properties of the plasma in the voids are largely unknown. To estimate an upper limit on the plasma electron number density in the voids, we assume that

the mass of the baryonic matter in the voids does not exceed the difference between the baryonic mass identified through analysis of CMB fluctuations and the mass found in the galaxies and galaxy clusters. The cosmological density of the universe is 5.9 baryons m^{-3} of which 4.6 % represents baryonic matter. Ninety percent of the 2.7×10^{-7} baryons cm^{-3} were identified in filaments and clusters of galaxies filling about half the volume of the universe. Therefore, the amount of baryonic matter in the voids cannot exceed the remaining $\approx 0.5{\times}10$ %, making the density estimate of the electron plasma in the voids $n_e \approx 1.4 \times 10^{-8}$ cm^{-3} or lower. The plasma frequency of these electrons, $\omega_{p,e} = 2\pi f_{p,e} = (4\pi n_e e^2/m_e)^{1/2}$, is given by $f_{p,e} = 1$ Hz $(n_e/10^{-8})^{1/2}$.

To estimate the temperature of the electron plasma, we assume that the ionization of hydrogen in the voids occurs sometime during the end of the reionization epoch with redshift z between 6 – 10. At this point, the universe became mostly transparent to UV radiation, and UV photons from ionizing sources in galaxies could propagate to the voids. The photoionization cross section for hydrogen in the ground state by photons with energy $\varepsilon > \varepsilon_0 = 13.6$ eV, can be roughly approximated by $\sigma_i(\varepsilon/\varepsilon_0)^{-3}$ where $\sigma_i = 6.3 \times 10^{-18}$ cm^2. The ionization is suppressed at higher photon energies, suggesting that the characteristic kinetic energy of the plasma electrons acquired by an electron in the ionization process is of order ε_0. These electrons undergo cosmological expansion which reduces the kinetic energy by a factor of (1 + z), and they also transfer energy to CMB photons through the inverse Compton (IC) interaction. The heating of electrons by UV radiation accumulated and reprocessed in the EBL is negligible since the total energy density in the EBL (from the UV to far-IR) is an order of magnitude less than in the CMB. The average IC energy loss of non-relativistic electrons is given by

$$\frac{1}{E}\frac{dE}{dt} = \frac{8}{3}\sigma_{\rm T} c \frac{U_{cmb}}{m_e c^2} \tag{7.1}$$

where $\sigma_{\rm T}$ is the Thomson cross section and U_{cmb} is the CMB energy density which at the present epoch is $U_0 = 0.26$ eV/cm^3. In the context of cosmological expansion, the rate of IC energy loss of non-relativistic particles is given by

$$\ln\left(\frac{E(z)}{E(0)}\right) = \frac{8}{3}\sigma_{\rm T}\frac{c}{H_0}\frac{U_0}{m_e c^2}\int_0^z \frac{(1+z')^3 dz'}{\sqrt{\Omega_m(1+z')^3+\Omega_\Lambda}} \tag{7.2}$$

where H_0 is the Hubble constant. For z = 6, the RHS of this equation is equal to 1.1 and for z = 10, it is equal to 3.4. This, combined with the reduction of the kinetic energy due to cosmological expansion, suggests that the average kinetic energy of the plasma electrons is reduced by a factor of 5×10^{-2} (z = 6) or 3×10^{-3} (z = 10), from ε_0, implying that the present day temperature of the electron plasma in the voids is a few thousand K.

Given the temperature and density of the electron plasma in the voids, the screening Debye radius is

$$\lambda_D = \left(kT/8\pi n_e e^2\right)^{1/2} = 1.6 \times 10^6 \text{ cm}\sqrt{(T/10^3 \text{ K})\,(10^{-8}\text{cm}^{-3}/n_e)}.$$

We note that this screening radius is less than the typical distance between electrons in the beam, as estimated in our simulations shown in Figure 7.1. The bulk of the electrons in the beam is born near the threshold of pair production when a few hundred GeV primary photon interacts with the EBL. The typical Lorentz factor of the outgoing electon is $\sim 2 \times 10^5$. These electrons dissipate $\sim$ 90 % of their energy through IC scattering over the distance of $\sim$ 30 Mpc. For distances from the source larger than this, the typical separation of beam particles

is $n_b^{-1/3} \approx 10^6 - 10^7$ cm. It appears that electron positron pairs of the beam are significantly screened by the electrons of the plasma in the voids, and therefore, collective interactions to generate a higher rate of energy transfer to plasma oscillations should be strongly suppressed by screening, which was not accounted for in [BCP12]. The plasma condition at these relatively small distances from the source ($\sim$ few Mpc where the density of the beam may be higher) is likely to be different from those assumed here for the voids, and the Debye radius estimated may not be applicable in this region.

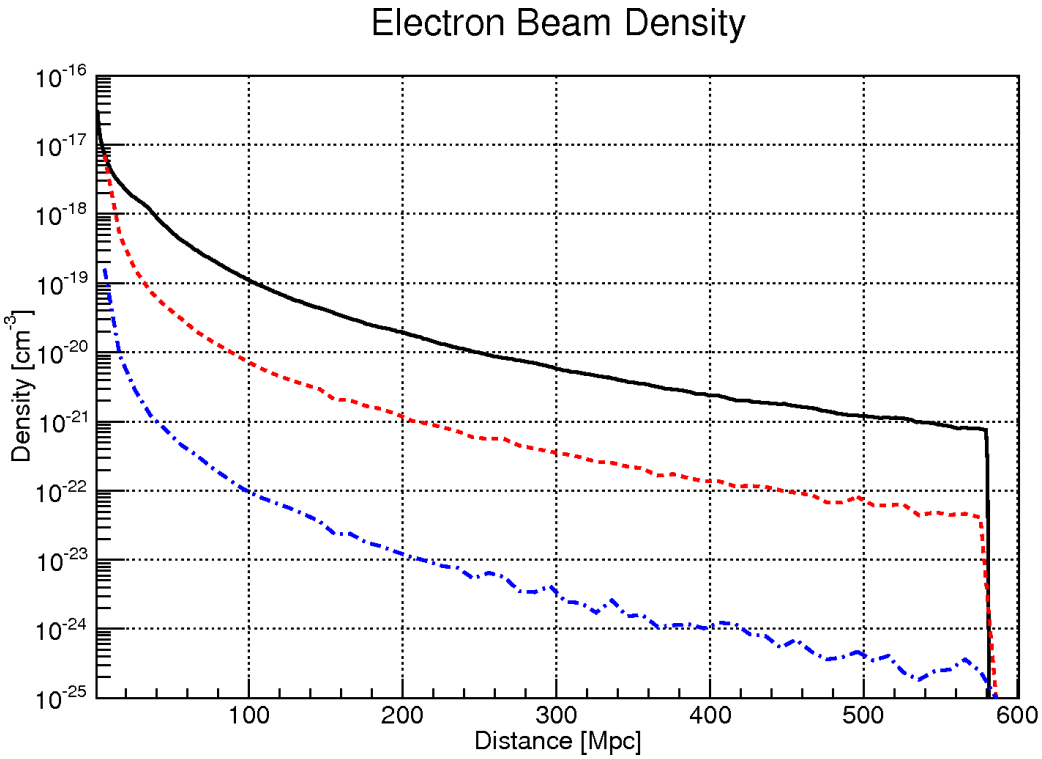

Figure 7.1 Electron Density as a function of distance from source 1ES 0229+200, assuming a normal EBL model (EBL model 1) and a spectral index in the VHE band (α) of 1.3 and cutoff energy (ε_c) 3.16 TeV. The black (solid) line traces the density of electrons with energies > 10 GeV, the red (dashed) line represents the density of electrons with energies > 100 GeV, and the blue (dot-dashed) line corresponds to energies > 1 TeV.

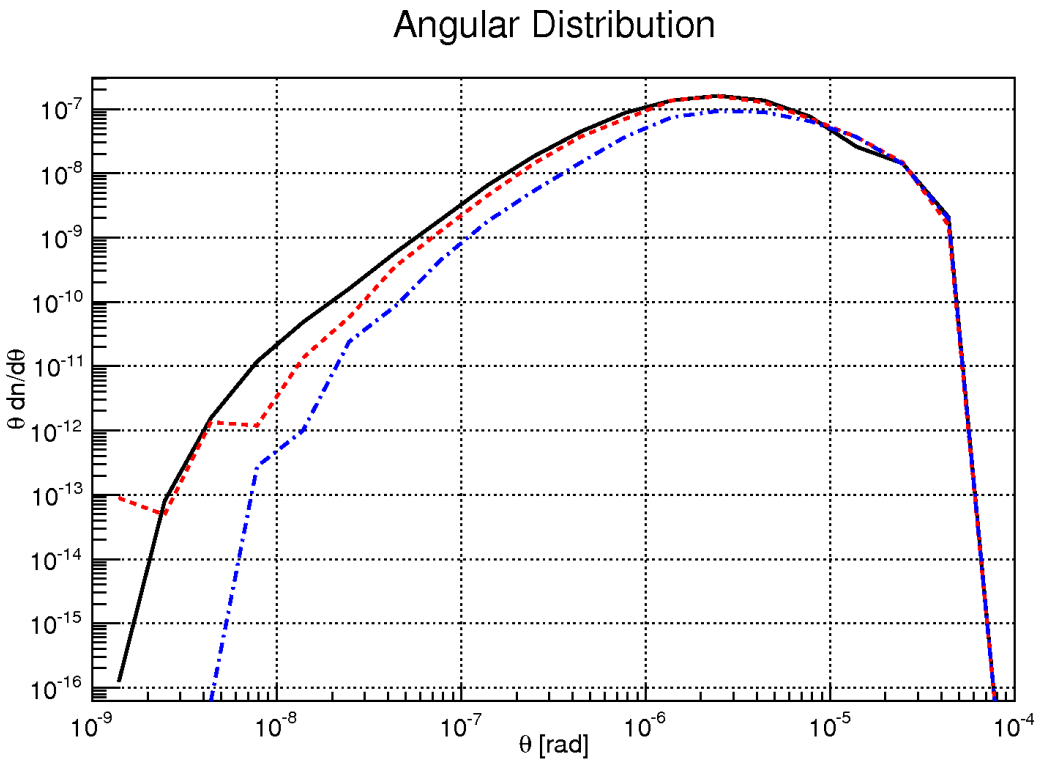

Figure 7.2 Electron angular distribution as a function of distance from the source 1ES 0229+200, assuming a normal EBL model (EBL model 1) and a spectral index in the VHE band (α) of 1.3 and cutoff energy (ε_c) 3.16 TeV. The angular distibution of electrons with energies above 10 GeV at 30 Mpc (black, solid), 100 Mpc (red, dashed), and 300 Mpc (blue, dot-dashed). The vicinity of the peak of the distribution can be well-represented as a $\log_{10}$-normal distribution peaking at $10^{-5.5}$ rad, with σ of 0.65.

One may argue that this screening effect can be alleviated if the density of electrons in the voids is considerably lower than the given upper bound estimate. Based on the results of simulations of density fluctuations quoted in [ME12], the present-day density of the electrons in objects with spatial scales of several tens of Mpc might be as low as $\approx 4 \times 10^{-10}$ cm^{-3}. This would make the Debye radius, $\lambda_D \approx 10^7$ cm, which suggests that screening effects remain critically important for the rate of the energy losses into the excitation of plasma waves. To estimate another critical paramter in the problem, namely, the effect of the

angular distribution of electrons in the beam, we consider a hydrodynamical approximation of the beam-plasma instability for the two populations of electrons with zero temperatures and one beam at relative velocity c. The dispersion relation for these waves is given by

$$1 = \frac{\omega_{p,e}^2}{\omega^2} + \frac{\omega_{p,b}^2}{(\mathbf{k}\cdot\mathbf{c}-\omega)^2} = \frac{1}{(x+iy)^2} + \frac{\kappa^2}{(z-x-iy)^2}, \tag{7.3}$$

where $\omega_{p,b}$ is the plasma frequency of the electrons and positrons in the beam, and where we introduced the dimensionless variables $x = Re(\omega)/\omega_{p,e}$, $y = Im(\omega)/\omega_{p,e}$, $z = \mathbf{k}\cdot\mathbf{c}/\omega_{p,e}$ and $\kappa = \omega_{p,b}/\omega_{p,e} = \sqrt{n_b/n_e} \ll 1$. The real and imaginary part of this equation can be separated, and the unstable (y $\neq$ 0) solution should satisfy

$$z^2 = \frac{(1+\varepsilon^2)}{(1-\varepsilon^2)}\frac{(1-\kappa\varepsilon)\,(\varepsilon-\kappa)}{\varepsilon}, \tag{7.4}$$

$$\frac{y^2}{x^2} = \varepsilon\frac{\kappa-\varepsilon^3}{1-\kappa\varepsilon}, \tag{7.5}$$

where $\varepsilon = \sqrt{z/x-1}$. The solution exists for $\kappa < \varepsilon < \kappa^{1/3}$ and for $0 < y/x < 3^{1/2}(\kappa/4)^{2/3}$. Since $\kappa \ll 1$, this would require that $|z|\,/\,|x| \sim 1$ and that $|z| \leq 1$. The last condition can only be satisfied for plasma waves with wave vector precisely perpendicular to the beam velocity. The cosine of this angle must satisfy the following condition $\cos\theta \leq (\lambda_D/c\omega_{p,e})(k\lambda_D)^{-1} = (k_BT/2m_ec^2)^{1/2}(k\lambda_D)^{-1} = 2.9\times10^{-4}(T/10^3\mathrm{K})^{1/2}(k\lambda_D)^{-1}$, in which $k\lambda_D \gg 1$ to enable collective interaction of plasma particles without significant screening. For the lowest estimate for n_e in the voids, we assume that $k\lambda_D \sim$ few, and therefore $\cos\theta$ may need to be less than 10^{-4}, but not significantly less than this.

According to our simulations, the angular distribution of electrons in the beam

is shown in Fig. 7.2. The bulk of the electrons is created with characteristic angles of order $1/\gamma \approx 5 \times 10^{-6}$. Although these electrons lose their energy through IC scattering, they retain the angular distribution of the parent particle, due to a small energy transfer to the CMB photons. Therefore, the angular distribution is relatively independent from the distance to the source, as illustrated in Fig. 7.2. Under the condition of the lowest electron density in the voids, maintaining perpendicularity of the wave vector of the plasma waves with respect to the beam, appears to be possible, and the approximation of the beam as completely collimated seems applicable here. All particles of the beam in this reactive regime of interaction will be involved into the energy transfer to the plasma waves making energy losses potentially higher. If $k\lambda_D$ becomes larger than about a few tens, then plasma waves will interact collectively only with a fraction of beam electrons in the kinetic regime of interaction, which has been pointed out in [ME12]. The energy losses in this regime are expected to be lower. Based on the parameters of the electron beam which we derived based on simulations, and reasonable assumptions about properties of electron plasma in the voids, we conclude that all effects of Debye screening and kinetic vs. reactive descriptions of two beam instabilities are important. Perhaps the most detailed to date study of the relaxation of beam plasma instabilities in cosmic voids has been reported in [ME12] with the conclusion that the relativistic pair beams of blazars remain stable on timescales much longer than the characteristic IC cooling time of electrons, and collective plasma-beam interaction effects in the voids are negligible. We find that the screening effects not accounted for in this work will only further validate their conclusions. However, the available parameter space in the regime of very low plasma density in the voids may enable the reactive interaction regime and therefore increase the energy loss rate, so without this direct knowledge of a map of the plasma number density distribution in the voids, it is not possible to com-

pute with certainty the importance of these instabilities in the electromagnetic cascade development.

7.3 Conclusions

Gamma-ray observations of TeV blazars will play a critically important role in measuring the IGMF, and hence in the understanding of primordial mangetic fields, unless pair-beam instabilities in cosmic voids are the dominant source of electron cooling (compared to IC losses), which is not likely to be the case, as we show in the previous section. Current generation instrumentation show hints of a non-zero IGMF, but the data is not conclusive enough to definitively demonstrate this due to a variety of uncertainties, discussed in chapter 5. However, next generation gamma-ray technology, specifically the proposed CTA observatory (and perhaps also the HAWC instrument) should have a much better chance of overcoming the uncertainties which obscure current analyses aiming to measure the IGMF.

Based on the studies performed in chapters 5 and 6, it appears that the range of IGMF that can be probed using gamma-ray observations is quite large, using a variety of observational features. The "Echo" emission using combined *Fermi*-LAT and (future) CTA data would be able to measure the IGMF if its magnitude is in the approximate range of 10^{-19} G $< B_{IGMF} < 10^{-17}$ G and if next generation instruments detect hard, rapid, VHE flares such as have occured about once per year using present day instrumentaion. "Halo" observations in the GeV energy band may probe fields of magnitude about 10^{-17} G $< B_{IGMF} < 10^{-13}$ G if TeV blazars are active for on average about 10^6 years or more. Finally, if the systematic uncertainties are properly accounted for, spectral observations may be able to set a lower limit on the IGMF of around 10^{-17} G. Since this is

the only method known to probe field strengths this low, continued gamma ray observations will provide valuable information regarding the IGMF and hence, help illuminate our understanding of primordial magnetic fields.

APPENDIX A

Target Photon Momentum Direction Integral

In this section, we show how equation 2.7 is evaluated rapidly and precisely. The integrals in the numerator and denominator are the same, differing only in their limits of integration. In order to speed up the computation, it is desirable to compute the integral in the denominator as rapidly as possible, rather than a brute force Simpson's rule type approach with a carefully chosen integration step size, which is employed for the evaluation of the numerator. To evaluate the denominator,

$$D(q,1) = \int_q^1 \left[\left(\frac{1}{\epsilon^2} + \frac{1}{\epsilon} - \frac{1}{2} \right) \ln \left(\frac{1+(1-\epsilon)^{1/2}}{1-(1-\epsilon)^{1/2}} \right) - \left(\frac{1}{\epsilon^2} + \frac{1}{\epsilon} \right) (1-\epsilon)^{1/2} \right] d\epsilon.$$

we first make the substitution, $t = \sqrt{1-\epsilon}$. Then, the integral can be partially performed and rewritten as

$$\begin{aligned} D(q,1) \;=\; & \frac{1}{2}\left[\ln^2(1-\sqrt{1-q}) - \ln^2(1+\sqrt{1-q}) \right] + \\ & \frac{(1-q)^2+1}{2q} \ln\left(\frac{1+\sqrt{1-q}}{1-\sqrt{1-q}} \right) - \frac{\sqrt{1-q}(2-q)}{q} + \\ & \int_0^{\sqrt{1-q}} \left[\frac{\ln(1+t)}{1-t} + \frac{\ln(1-t)}{1+t} \right] dt. \end{aligned}$$

Unfortunately, the final integral to be evaluated in the above does not have an analytic solution, but it is possible to cast it in terms of well-known integrals which have rapidly converging series solutions. In particular, the integral can be

solved in terms of the Dilogarithm function[1],

$$Li_2(x) = \int_x^0 \frac{\ln(1-t)}{t} dt = \sum_{k=1}^{\infty} \frac{z^k}{k^2}.$$

Making the substitutions, $\phi = \sqrt{1-q}$, $\eta_\pm = 1/2(1 \pm \phi)$,

$$\begin{aligned} D(q,1) &= \frac{1}{2}\left(\frac{\phi^4+1}{1-\phi^2}\right)\ln\left(\frac{1+\phi}{1-\phi}\right) - \frac{\phi+\phi^3}{1-\phi^2} + \\ & \quad Li_2(\eta_-) + \frac{1}{2}\ln^2(\eta_-) - Li_2(\eta_+) - \frac{1}{2}\ln^2(\eta_+) \end{aligned}$$

It turns out that the Dilogarithm function can be related to an integral which was already implemented to perform some integrals relating to the IC scattering step (see appendix C), called $PolyLog1(x) = PL1(x)$, defined as

$$PL1(x) = \int_1^x \frac{\ln(1+t)}{t} dt + \frac{\pi^2}{12} = -Li_2(-x)$$

So rather than re-programming and testing the Dilogarithm function into the code, we instead rewrite the function in terms of $PL1(x)$, and use the already written code to perform this work. In terms of the $PL1(x)$ function then, with the q-dependence back in, we have that

$$\begin{aligned} D(q,1) &= \left(\frac{q}{2} - 1 + \frac{1}{q}\right)\ln\left(\frac{1+\sqrt{1-q}}{1-\sqrt{1-q}}\right) - \sqrt{1-q}\left(\frac{2}{q} - 1\right) + \\ & \quad PL1\left(\frac{1-\sqrt{1-q}}{1+\sqrt{1-q}}\right) - PL1\left(\frac{1+\sqrt{1-q}}{1-\sqrt{1-q}}\right) + \ln\left(\frac{1-\sqrt{1-q}}{1+\sqrt{1-q}}\right)\ln\left(\frac{q}{4}\right). \end{aligned}$$

[1] Weisstein, Eric W. "Dilogarithm." From Mathworld-A Wolfram Web Resource. http://mathworld.wolfram.com/Dilogarithm.html

APPENDIX B

Evaluation of Mellin Integral Transform

Here is provided the derivation of equation 2.13 the Mellin integral transform for the total cross section for IC scattering, $\sigma(x)$. We begin with the integral definition of $\Sigma(\mu)$

$$\Sigma(\mu) = \int_0^\infty \frac{\sigma(x)}{\sigma_T} x^{\mu-1} dx,$$

and using equation 2.9 for $\sigma(x)$, and the fact that this integral converges for complex μ limited by $0 < \mathrm{Re}\,\mu < 1$. The integral is performed term by term below:

1) $\int_0^\infty \frac{1}{x} \ln(1+x)\, x^{\mu-1} dx = \int_0^\infty \ln(1+x) \frac{1}{\mu-1} dx^{\mu-1} = \frac{1}{\mu-1} \ln(1+x)\, x^{\mu-1}|_0^\infty -$
$\frac{1}{\mu-1} \int_0^\infty \frac{x^{\mu-1}}{(1+x)} dx = \frac{1}{1-\mu} \Gamma(\mu)\, \Gamma(1-\mu) = \frac{1}{1-\mu} \frac{\pi}{\sin \pi\mu}$

2) $-\int_0^\infty \frac{4}{x^2} (\ln(1+x) - x)\, x^{\mu-1} dx = -4 \int_0^\infty (\ln(1+x) - x) \frac{1}{\mu-2} dx^{\mu-2} =$
$-4 \frac{1}{\mu-2} (\ln(1+x) - x)\, x^{\mu-2}|_0^\infty + \frac{4}{\mu-2} \int_0^\infty x^{\mu-2} d(\ln(1+x) - x) =$
$\frac{4}{\mu-2} \int_0^\infty x^{\mu-2} \left(\frac{1}{(1+x)} - 1 \right) dx = \frac{4}{2-\mu} \int_0^\infty \frac{x^{\mu-1}}{(1+x)} dx = \frac{4}{2-\mu} \frac{\pi}{\sin \pi\mu}$

3) $-\int_0^\infty \frac{8}{x^3} \left(\ln(1+x) - x + \frac{1}{2}x^2\right) x^{\mu-1} dx = -\frac{8}{\mu-3} \int_0^\infty \left(\ln(1+x) - x + \frac{1}{2}x^2\right) dx^{\mu-3} =$
$-\frac{8}{\mu-3} \left(\ln(1+x) - x + \frac{1}{2}x^2\right) x^{\mu-3}|_0^\infty + \frac{8}{\mu-3} \int_0^\infty x^{\mu-3} \left(\frac{1}{(1+x)} - 1 + x \right) dx =$
$-\frac{8}{3-\mu} \int_0^\infty \frac{x^{\mu-1}}{(1+x)} dx = -\frac{8}{3-\mu} \frac{\pi}{\sin \pi\mu}$

4) $\int_0^\infty \frac{1}{2} \frac{2+x}{(1+x)^2} x^{\mu-1} dx = \frac{1}{2} \int_0^\infty \frac{x^{\mu-1}}{(1+x)} dx + \frac{1}{2} \int_0^\infty \frac{1}{(1+x)^2} x^{\mu-1} dx = \frac{1}{2} \frac{\pi}{\sin \pi\mu} + \frac{1}{2} \frac{\Gamma(\mu)\Gamma(2-\mu)}{\Gamma(2)} =$
$\frac{1}{2} \frac{\pi}{\sin \pi\mu} + \frac{1}{2} (1-\mu)\, \Gamma(\mu)\, \Gamma(1-\mu) = \left(1 - \frac{\mu}{2}\right) \frac{\pi}{\sin \pi\mu}$

Finally, we arrive at equation 2.13

$$\Sigma(\mu) = \int_0^\infty \frac{1}{\sigma_T}\sigma(x)\, x^{\mu-1} dx = \frac{3}{4}\left(\frac{1}{1-\mu} + \frac{4}{2-\mu} - \frac{8}{3-\mu} + \left(1 - \frac{\mu}{2}\right)\right)\frac{\pi}{\sin \pi\mu}.$$

APPENDIX C

Evaluation of IC Scattering Integral U

To compute $U\left(\frac{2\varepsilon}{m_e c^2}, \gamma\right)$ one needs to know two functions[1]

$$\frac{1}{x} f_1(x) = \frac{1}{2\pi i} \int_{\frac{1}{2}-i\infty}^{\frac{1}{2}+i\infty} \frac{1}{1-z} \Sigma(z)\, x^{-z} dz,$$

$$\frac{1}{x^2} f_2(x) = \frac{1}{2\pi i} \int_{\frac{1}{2}-i\infty}^{\frac{1}{2}+i\infty} \frac{1}{2-z} \Sigma(z)\, x^{-z} dz$$

$$\Sigma(z) = \frac{3}{4}\left(\frac{1}{1-z} + \frac{4}{2-z} - \frac{8}{3-z} + \left(1 - \frac{z}{2}\right)\right) \frac{\pi}{\sin \pi z}$$

$$\frac{1}{x} f_1(x) = \frac{1}{2\pi i} \int_{\frac{1}{2}-i\infty}^{\frac{1}{2}+i\infty} \frac{1}{1-z} \frac{3}{4} \left(\frac{1}{1-z} + \frac{4}{2-z} - \frac{8}{3-z} + \left(1 - \frac{z}{2}\right)\right) \frac{\pi}{\sin \pi z} \exp(-z \ln x)\, dz$$

1.) For $x < 1$ the sum over all first order poles $z = (-n + \varepsilon)$ where n is integer ≥ 0.

$$\frac{1}{1-(-n+\varepsilon)} \frac{3}{4} \left(\frac{1}{1-(-n+\varepsilon)} + \frac{4}{2-(-n+\varepsilon)} - \frac{8}{3-(-n+\varepsilon)} + \left(1 - \frac{(-n+\varepsilon)}{2}\right)\right) (-1)^n x^n \exp(-\varepsilon \ln x)$$
$$= \frac{3}{4} x^n \frac{(-1)^n}{n+1} \left(\frac{1}{2} n + \frac{1}{n+1} + \frac{4}{n+2} - \frac{8}{n+3} + 1\right)$$

[1]NOTE: In this section, the variable z is the standard complex variable, $z = x + iy$, where $x = \mathrm{Re}(z)$ and $y = \mathrm{Im}(z)$. In the chapter of the text, this variable is denoted as μ.

$\frac{3}{4}x^n\frac{(-1)^n}{n+1}\left(\frac{1}{2}n+\frac{1}{n+1}+\frac{4}{n+2}-\frac{8}{n+3}+1\right)\frac{1}{2\pi i}d\ln\varepsilon=\frac{3}{4}x^n\frac{(-1)^n}{n+1}\left(\frac{1}{2}n+\frac{1}{n+1}+\frac{4}{n+2}-\frac{8}{n+3}+1\right)$

$$\frac{1}{x}f_1(x)=\frac{3}{4}\sum_{n=0}^{\infty}x^n\frac{(-1)^n}{n+1}\left(\frac{1}{2}n+\frac{1}{n+1}+\frac{4}{n+2}-\frac{8}{n+3}+1\right)=$$

$$\frac{3}{4}\frac{1}{x}\sum_{n=1}^{\infty}x^n\frac{(-1)^{n-1}}{n}\left(\frac{1}{2}n+\frac{1}{n}+\frac{4}{n+1}-\frac{8}{n+2}+\frac{1}{2}\right)=$$

$$\frac{3}{4}\frac{1}{x}\sum_{n=1}^{\infty}(-1)^{n-1}x^n\left(\frac{1}{2}+\frac{1}{n^2}+\frac{4}{(n+1)n}-\frac{8}{(n+2)n}+\frac{1}{2n}\right)=$$

$$\frac{3}{4}\frac{1}{x}\sum_{n=1}^{\infty}(-1)^{n-1}x^n\left(\frac{1}{2}+\frac{1}{n^2}+4\left(\frac{1}{n}-\frac{1}{n+1}\right)-4\left(\frac{1}{n}-\frac{1}{n+2}\right)+\frac{1}{2n}\right)=$$

$$\frac{3}{4}\frac{1}{x}\sum_{n=1}^{\infty}(-1)^{n-1}x^n\left(\frac{1}{2}+\frac{1}{2n}-\frac{4}{n+1}+\frac{4}{n+2}+\frac{1}{n^2}\right)=$$

$$\sum_{n=1}^{\infty}(-1)^{n-1}x^n\left(\frac{1}{2}\right)=-\frac{1}{2}\left(\sum_{n=0}^{\infty}(-x)^n-1\right)=-\frac{1}{2}\left(\frac{1}{1+x}-1\right)=\frac{1}{2}\frac{x}{1+x}$$

$$\sum_{n=1}^{\infty}(-1)^{n-1}x^n\left(\frac{1}{2n}\right)=\frac{1}{2}\ln(1+x)$$

$$\sum_{n=1}^{\infty}(-1)^{n-1}x^n\left(-\frac{4}{n+1}\right)=4\frac{1}{x}\sum_{n=2}^{\infty}(-1)^{n-1}x^n\left(\frac{1}{n}\right)=\frac{4}{x}(\ln(1+x)-x)$$

$$\sum_{n=1}^{\infty}(-1)^{n-1}x^n\left(\frac{4}{n+2}\right)=4\frac{1}{x^2}\sum_{n=3}^{\infty}(-1)^{n-1}x^n\left(\frac{1}{n}\right)=\frac{4}{x^2}\left(\ln(x+1)-x+\frac{1}{2}x^2\right)$$

$$\frac{1}{x}f_1(x)=\frac{3}{4}\frac{1}{x}\left(\frac{1}{2}\frac{x}{1+x}+\frac{1}{2}\ln(1+x)+\frac{4}{x}(\ln(1+x)-x)+\frac{4}{x^2}\left(\ln(x+1)-x+\frac{1}{2}x^2\right)\right.$$
$$\left.+\sum_{n=1}^{\infty}\frac{(-1)^{n-1}}{n^2}x^n\right)$$

2.) For $x>1$ the sum over all first order poles $z=(n+\varepsilon)$ where n is integer >3.

$$I_{>3}(x)=\frac{1}{2\pi i}\int_{\frac{1}{2}-i\infty}^{\frac{1}{2}+i\infty}\frac{1}{1-z}\frac{3}{4}\left(\frac{1}{1-z}+\frac{4}{2-z}-\frac{8}{3-z}+\left(1-\frac{z}{2}\right)\right)\frac{\pi}{\sin\pi z}\exp(-z\ln x)\,dz$$

$\frac{1}{1-(n+\varepsilon)}\frac{3}{4}\left(\frac{1}{1-(n+\varepsilon)}+\frac{4}{2-(n+\varepsilon)}-\frac{8}{3-(n+\varepsilon)}+\left(1-\frac{(n+\varepsilon)}{2}\right)\right)(-1)^n x^{-n}\exp(-\varepsilon\ln x)=$
$\frac{3}{4}\frac{(-1)^n}{x^n(-n+1)}\left(-\frac{1}{2}n+\frac{1}{-n+1}+\frac{4}{-n+2}-\frac{8}{-n+3}+1\right)+O(\varepsilon)$

$$I_{>3}(x)=\frac{3}{4}\sum_{n=4}^{\infty}\frac{(-1)^n}{x^n(-n+1)}\left(-\frac{1}{2}n+\frac{1}{-n+1}+\frac{4}{-n+2}-\frac{8}{-n+3}+1\right)\frac{1}{2\pi i}\int_{\frac{1}{2}-i\infty}^{\frac{1}{2}+i\infty}d\ln\varepsilon$$

$\frac{1}{2\pi i}\int_{\frac{1}{2}-i\infty}^{\frac{1}{2}+i\infty}d\ln\varepsilon=-1$ (due to direction of countour to get correct result for inverse Mellin transform)

$$I_{>3}(x)=\frac{3}{4}\frac{1}{x}\sum_{n=4}^{\infty}(-1)^{n-1}\frac{x^{-n+1}}{-n+1}\left(\frac{1}{2}(-n+1)+\frac{1}{-n+1}+\frac{4}{-n+2}-\frac{8}{-n+3}+\frac{1}{2}\right)=$$
$$\frac{3}{4}\frac{1}{x}\sum_{n=3}^{\infty}(-1)^n\frac{x^{-n}}{n}\left(\frac{1}{2}n+\frac{1}{n}+\frac{4}{n-1}-\frac{8}{n-2}-\frac{1}{2}\right)=$$
$$\frac{3}{4}\frac{1}{x}\sum_{n=3}^{\infty}(-1)^n x^{-n}\left(\frac{1}{2}+\frac{1}{n^2}+\frac{4}{(n-1)n}-\frac{8}{(n-2)n}-\frac{1}{2n}\right)=$$
$$\frac{3}{4}\frac{1}{x}\sum_{n=3}^{\infty}(-1)^n x^{-n}\left(\frac{1}{2}+\frac{1}{n^2}+4\left(\frac{1}{n-1}-\frac{1}{n}\right)-4\left(\frac{1}{n-2}-\frac{1}{n}\right)-\frac{1}{2n}\right)=$$
$$\frac{3}{4}\frac{1}{x}\sum_{n=3}^{\infty}(-1)^n x^{-n}\left(\frac{1}{2}-\frac{1}{2n}+4\frac{1}{n-1}-4\frac{1}{n-2}+\frac{1}{n^2}\right)$$
$$\sum_{n=3}^{\infty}(-1)^n x^{-n}\left(\frac{1}{2}\right)=\frac{1}{2}\left(\sum_{n=0}^{\infty}\left(-\frac{1}{x}\right)^n-\sum_{n=0}^{2}\left(-\frac{1}{x}\right)^n\right)=\frac{1}{2}\left(\frac{1}{1+\frac{1}{x}}-\sum_{n=0}^{2}\left(-\frac{1}{x}\right)^n\right)=$$
$\frac{1}{2}\left(\frac{x}{1+x}-\frac{1}{x^2}+\frac{1}{x}-1\right)$
$$\sum_{n=3}^{\infty}(-1)^n x^{-n}\left(-\frac{1}{2n}\right)=\sum_{n=3}^{\infty}(-1)^{n-1}x^{-n}\left(\frac{1}{2n}\right)=\frac{1}{2}\left(\ln\left(\frac{1}{x}+1\right)-\frac{1}{x}+\frac{1}{2x^2}\right)$$
$$\sum_{n=3}^{\infty}(-1)^n x^{-n}\left(4\frac{1}{n-1}\right)=\frac{1}{x}\sum_{n=2}^{\infty}(-1)^{n+1}x^{-n}\left(4\frac{1}{n}\right)=\frac{4}{x}\left(\ln\left(\frac{1}{x}+1\right)-\frac{1}{x}\right)$$

$$\sum_{n=3}^{\infty}(-1)^n x^{-n}\left(-4\frac{1}{n-2}\right)=\frac{1}{x^2}\sum_{n=1}^{\infty}(-1)^{n-1}x^{-n}\left(4\frac{1}{n}\right)=\frac{4}{x^2}\ln\left(\frac{1}{x}+1\right)$$

$$\sum_{n=3}^{\infty}\frac{(-1)^n}{n^2}x^{-n}=-\sum_{n=1}^{\infty}\frac{(-1)^{n-1}}{n^2}x^{-n}-\left(\frac{1}{4x^2}-\frac{1}{x}\right)$$

$$I_{>3}(x)=\frac{3}{4}\frac{1}{x}\left(\frac{1}{2}\frac{x}{1+x}+\frac{1}{2}\ln\left(\frac{1}{x}+1\right)+\frac{4}{x}\ln\left(\frac{1}{x}+1\right)+\frac{4}{x^2}\ln\left(\frac{1}{x}+1\right)+\left(\frac{1}{x}-\frac{9}{2x^2}-\frac{1}{2}\right)\right.$$
$$\left.-\sum_{n=1}^{\infty}\frac{(-1)^{n-1}}{n^2}x^{-n}\right)$$

For $x>1$ the second order pole $z=(3+\varepsilon)$:

$$\frac{1}{2\pi i}\int\limits_{\frac{1}{2}-i\infty}^{\frac{1}{2}+i\infty}\frac{1}{1-z}\frac{3}{4}\left(\frac{1}{1-z}+\frac{4}{2-z}-\frac{8}{3-z}+\left(1-\frac{z}{2}\right)\right)\frac{\pi}{\sin\pi z}\exp\left(-z\ln x\right)dz$$

$$\frac{1}{1-(3+\varepsilon)}\frac{3}{4}\left(\frac{1}{1-(3+\varepsilon)}+\frac{4}{2-(3+\varepsilon)}+\frac{8}{\varepsilon}+\left(1-\frac{(3+\varepsilon)}{2}\right)\right)\frac{(-1)}{x^3}\exp\left(-\varepsilon\ln x\right)=$$

$$\frac{3}{x^3\varepsilon}-\frac{3}{4x^3}\left(4\ln x+\frac{9}{2}\right)-\frac{3}{4x^3}\varepsilon\left(-\frac{9}{2}\ln x-2\ln^2 x-\frac{33}{8}\right)+O\left(\varepsilon^2\right)$$

$$-\frac{3}{4x^3}\left(4\ln x+\frac{9}{2}\right)\frac{1}{2\pi i}\int\limits_{\frac{1}{2}-i\infty}^{\frac{1}{2}+i\infty}d\ln\varepsilon=\frac{3}{x^3}\left(\ln x+\frac{9}{8}\right)$$

For $x>1$ the second order pole $z=(2+\varepsilon)$:

$$\frac{1}{1-(2+\varepsilon)}\frac{3}{4}\left(\frac{1}{1-(2+\varepsilon)}-\frac{4}{\varepsilon}-\frac{8}{3-(2+\varepsilon)}+\left(1-\frac{(2+\varepsilon)}{2}\right)\right)\frac{1}{x^2}\exp\left(-\varepsilon\ln x\right)=$$

$$\frac{3}{x^2\varepsilon}+\frac{3}{4x^2}\left(-4\ln x+5\right)+\frac{3}{4x^2}\varepsilon\left(-5\ln x+2\ln^2 x+\frac{5}{2}\right)+O\left(\varepsilon^2\right)$$

$$+\frac{3}{4x^2}\left(-4\ln x+5\right)\frac{1}{2\pi i}\int\limits_{\frac{1}{2}-i\infty}^{\frac{1}{2}+i\infty}d\ln\varepsilon=\frac{3}{x^2}\left(\ln x-\frac{5}{4}\right)$$

For $x>1$ the third order pole $z=(1+\varepsilon)$:

$$\frac{-1}{\varepsilon}\frac{3}{4}\left(-\frac{1}{\varepsilon}+\frac{4}{2-(1+\varepsilon)}-\frac{8}{3-(1+\varepsilon)}+\left(1-\frac{(1+\varepsilon)}{2}\right)\right)\frac{-1}{x}\exp\left(-\varepsilon\ln x\right)=$$

$$-\frac{3}{4x\varepsilon^2}+\frac{3}{4x\varepsilon}\left(\ln x+\frac{1}{2}\right)+\frac{3}{4x}\left(-\frac{1}{2}\ln x-\frac{1}{2}\ln^2 x+\frac{3}{2}\right)+O\left(\varepsilon\right)$$

$$\frac{3}{4x}\left(-\frac{1}{2}\ln x-\frac{1}{2}\ln^2 x+\frac{3}{2}\right)\frac{1}{2\pi i}\int\limits_{\frac{1}{2}-i\infty}^{\frac{1}{2}+i\infty}d\ln\varepsilon=\frac{3}{8x}\left(\ln x+\ln^2 x-3\right)$$

$$\frac{1}{x}f_1(x) = \frac{3}{4}\frac{1}{x}\left(\frac{1}{2}\frac{x}{1+x} + \frac{1}{2}\ln\left(\frac{1}{x}+1\right) + \frac{4}{x}\ln\left(\frac{1}{x}+1\right) + \frac{4}{x^2}\ln\left(\frac{1}{x}+1\right) + \left(\frac{1}{x} - \frac{9}{2x^2} - \frac{1}{2}\right)\right.$$
$$\left. -\sum_{n=1}^{\infty}\frac{(-1)^{n-1}}{n^2}x^{-n}\right) + \frac{3}{x^3}\left(\ln x + \frac{9}{8}\right) + \frac{3}{x^2}\left(\ln x - \frac{5}{4}\right) + \frac{3}{8x}\left(\ln x + \ln^2 x - 3\right) =$$

$$f_1(x) = \frac{3}{4}\left(\frac{1}{2}\frac{x}{1+x} + \frac{1}{2}\ln(1+x) + \frac{4}{x}\ln(1+x) + \frac{4}{x^2}\ln(1+x) + \left(-\frac{4}{x} - 2\right) + \frac{1}{2}\ln^2 x\right.$$
$$\left. -\sum_{n=1}^{\infty}\frac{(-1)^{n-1}}{n^2}x^{-n}\right)$$

or for $x > 1$

$$f_1(x) = \frac{3}{4}\left(\frac{1}{2}\frac{x}{1+x} + \frac{1}{2}\ln(1+x) + \frac{4}{x}\left(\ln(1+x) - x\right) + \frac{4}{x^2}\left(\ln(1+x) - x + \frac{1}{2}x^2\right) + \right.$$
$$\left. \frac{1}{2}\ln^2 x - \sum_{n=1}^{\infty}\frac{(-1)^{n-1}}{n^2}x^{-n} + \frac{1}{12}\pi^2\right)$$

and for $x < 1$

$$f_1(x) = \frac{3}{4}\left(\frac{1}{2}\frac{x}{1+x} + \frac{1}{2}\ln(1+x) + \frac{4}{x}\left(\ln(1+x) - x\right) + \frac{4}{x^2}\left(\ln(x+1) - x + \frac{1}{2}x^2\right) + \right.$$
$$\left. \sum_{n=1}^{\infty}\frac{(-1)^{n-1}}{n^2}x^{n} - \frac{1}{12}\pi^2\right)$$

check:

$$\frac{d}{dx}\left(\frac{1}{2}\ln^2 x - \sum_{n=1}^{\infty}\frac{(-1)^{n-1}}{n^2}x^{-n}\right) = \frac{1}{x}\ln x + \frac{1}{x}\ln\left(\frac{1}{x}+1\right) = \frac{1}{x}\ln(1+x)$$

$$\frac{d}{dx}\left(\sum_{n=1}^{\infty}\frac{(-1)^{n-1}}{n^2}x^{n}\right) = \frac{1}{x}\ln(x+1)$$

$$\sum_{n=1}^{\infty}\frac{(-1)^{n-1}}{n^2} = \frac{1}{12}\pi^2$$

Let us introduce the function

$$PLog(x) = \int_1^x \frac{1}{x}\ln(1+x)\,dx$$

so that

$$PLog(x)=\begin{cases}\frac{1}{2}\ln^2 x-\sum\limits_{n=1}^{\infty}\frac{(-1)^{n-1}}{n^2}x^{-n}+\frac{1}{6}\pi^2; & x\geq 1\\ \sum\limits_{n=1}^{\infty}\frac{(-1)^{n-1}}{n^2}x^{n}; & x\leq 1\end{cases}.$$

$PLog(-\frac{1}{2})=-\sum\limits_{n=1}^{\infty}\frac{1}{n^2 2^n}=\frac{1}{2}\ln^2 2-\frac{1}{12}\pi^2$

$PLog(y)=\ln y\ln(1+y)-\frac{1}{2}\ln^2(1+y)+\frac{1}{6}\pi^2+PLog(-\frac{1}{1+y})$

then

$f_1(x)=\frac{3}{4}\Bigg(\frac{1}{2}\frac{x}{1+x}+\frac{1}{2}\ln(1+x)+\frac{4}{x}\left(\ln(1+x)-x\right)+\frac{4}{x^2}\left(\ln(x+1)-x+\frac{1}{2}x^2\right)+PLog(x)\Bigg)$

$$\frac{1}{x}f_1(x)=\frac{1}{2\pi i}\int\limits_{\frac{1}{2}-i\infty}^{\frac{1}{2}+i\infty}\frac{1}{1-z}\Sigma(z)\,x^{-z}dz,$$

and

$f_2(x)=\frac{3}{4}\Bigg(\left(1+x\right)\ln(1+x)-\frac{x}{2}\left(\frac{2+x}{1+x}\right)+8\ln(1+x)+8\frac{1}{x}\left(\ln(1+x)-x\right)-4PLog(x)\Bigg),$

$$\frac{1}{x^2}f_2(x)=\frac{1}{2\pi i}\int\limits_{\frac{1}{2}-i\infty}^{\frac{1}{2}+i\infty}\frac{1}{2-z}\Sigma(z)\,x^{-z}dz.$$

Limits:

$$PLog(x)=\begin{cases}\frac{1}{2}\ln^2 x+\frac{1}{6}\pi^2; & x\to\infty\\ x-\frac{1}{4}x^2; & x\to 0\end{cases}.$$

$f_1(x)=\frac{3}{4}\Bigg(\frac{1}{2}\frac{x}{1+x}+\frac{1}{2}\ln(1+x)+\frac{4}{x}\left(\ln(1+x)-x\right)+$

$\frac{4}{x^2}\left(\ln(x+1)-x+\frac{1}{2}x^2\right)+PLog(x)\Big)$,

$$f_1(x)=x-\frac{1}{2}x^2,\quad x\to 0$$

$$f_1(x)=\frac{3}{8}\ln^2 x+\frac{3}{8}\ln x+\frac{2}{16}\pi^2-\frac{9}{8},\quad x\to\infty$$

$f_2(x)=\frac{3}{4}\Big((1+x)\ln(1+x)-\frac{x}{2}\left(\frac{2+x}{1+x}\right)+8\ln(1+x)+8\frac{1}{x}\left(\ln(1+x)-x\right)-4PLog(x)\Big)$,

$$f_2(x)=\frac{3}{4}\left(x\ln x-\frac{x}{2}+8\ln x-8-2\ln^2 x-\frac{2}{3}\pi^2\right),\quad x\to\infty$$

$$f_2(x)=\frac{1}{2}x^2,\quad x\to 0$$

($f_1(x)$ and $f_2(x)$ are checked, see below)

$\frac{1}{x^2}f_2(x)=\frac{1}{2\pi i}\int\limits_{\frac{1}{2}-i\infty}^{\frac{1}{2}+i\infty}\frac{1}{2-z}\frac{3}{4}\left(\frac{1}{1-z}+\frac{4}{2-z}-\frac{8}{3-z}+\left(1-\frac{z}{2}\right)\right)\frac{\pi}{\sin\pi z}\exp(-z\ln x)\,dz$

1.) For $x<1$ the sum over all first order poles $z=(-n+\varepsilon)$ where n is integer ≥ 0.

$\frac{1}{2-(-n+\varepsilon)}\frac{3}{4}\left(\frac{1}{1-(-n+\varepsilon)}+\frac{4}{2-(-n+\varepsilon)}-\frac{8}{3-(-n+\varepsilon)}+\left(1-\frac{(-n+\varepsilon)}{2}\right)\right)(-1)^n x^n\exp(-\varepsilon\ln x)=\frac{3}{4}x^n\frac{(-1)^n}{n+2}\left(\frac{1}{2}n+\frac{1}{n+1}+\frac{4}{n+2}-\frac{8}{n+3}+1\right)+O(\varepsilon)$

$\frac{3}{4}x^n\frac{(-1)^n}{n+2}\left(\frac{1}{2}n+\frac{1}{n+1}+\frac{4}{n+2}-\frac{8}{n+3}+1\right)\frac{1}{2\pi i}\int\limits_{\frac{1}{2}-i\infty}^{\frac{1}{2}+i\infty}d\ln\varepsilon$

$\frac{1}{x^2}f_2\left(x\right)=\frac{3}{4}\sum_{n=0}^{\infty}x^n\frac{\left(-1\right)^n}{n+2}\left(\frac{1}{2}n+\frac{1}{n+1}+\frac{4}{n+2}-\frac{8}{n+3}+1\right)=$

$\frac{3}{4}\frac{1}{x^2}\sum_{n=0}^{\infty}x^{n+2}\frac{\left(-1\right)^{n+2}}{n+2}\left(\frac{1}{2}\left(n+2\right)+\frac{1}{n+2-1}+\frac{4}{n+2}-\frac{8}{n+2+1}\right)$

$f_2\left(x\right)=\frac{3}{4}\sum_{n=2}^{\infty}x^n\frac{\left(-1\right)^n}{n}\left(\frac{1}{2}n+\frac{1}{n-1}+\frac{4}{n}-\frac{8}{n+1}\right)=$

$\frac{3}{4}\sum_{n=2}^{\infty}\left(-1\right)^n x^n\left(\frac{1}{2}+\frac{1}{(n-1)n}+\frac{4}{n^2}-\frac{8}{(n+1)n}\right)$

$f_2\left(x\right)=\frac{3}{4}\sum_{n=2}^{\infty}\left(-1\right)^n x^n\left(\frac{1}{2}+\left(\frac{1}{n-1}-\frac{1}{n}\right)+\frac{4}{n^2}-8\left(\frac{1}{n}-\frac{1}{n+1}\right)\right)=$

$\frac{3}{4}\sum_{n=2}^{\infty}\left(-1\right)^n x^n\left(\frac{1}{2}+\frac{1}{n-1}-9\frac{1}{n}+8\frac{1}{n+1}+\frac{4}{n^2}\right)$

$f_2\left(x\right)=\frac{3}{4}\sum_{n=2}^{\infty}\left(-1\right)^n x^n\left(\frac{1}{2}+\frac{1}{n-1}-9\frac{1}{n}+8\frac{1}{n+1}+\frac{4}{n^2}\right)$

$\frac{3}{4}\sum_{n=2}^{\infty}\left(-1\right)^n x^n\left(\frac{1}{2}\right)=\frac{3}{4}\frac{1}{2}\left(\frac{1}{1+x}-\sum_{n=0}^{1}\left(-x\right)^n\right)=\frac{3}{8}\left(x+\frac{1}{x+1}-1\right)=\frac{3}{8}x\left(1+\frac{-1}{x+1}\right)=$

$\frac{3}{8}\frac{x^2}{x+1}$

$\frac{3}{4}\sum_{n=2}^{\infty}\left(-1\right)^n x^n\left(\frac{1}{n-1}\right)=\frac{3}{4}x\sum_{n=1}^{\infty}\frac{\left(-1\right)^{n+1}}{n}x^n=\frac{3}{4}x\ln\left(x+1\right)$

$\frac{3}{4}\sum_{n=2}^{\infty}\left(-1\right)^n x^n\left(-9\frac{1}{n}\right)=\frac{3}{4}9\left(\ln\left(x+1\right)-x\right)$

$\frac{3}{4}\sum_{n=2}^{\infty}\left(-1\right)^n x^n\left(8\frac{1}{n+1}\right)=\frac{3}{4}\sum_{n=3}^{\infty}\left(-1\right)^{n-1}x^{n-1}\left(8\frac{1}{n}\right)=3x+\frac{6}{x}\ln\left(x+1\right)-6$

$\frac{3}{4}\sum_{n=2}^{\infty}\left(-1\right)^n x^n\left(\frac{4}{n^2}\right)=\frac{3}{4}\left(-4\sum_{n=1}^{\infty}\frac{\left(-1\right)^{n-1}}{n^2}x^n+4x\right)$

$f_2(x)=\frac{3}{4}\left(\left(1+x\right)\ln\left(1+x\right)-\frac{x}{2}\left(\frac{2+x}{1+x}\right)+8\ln\left(1+x\right)+8\frac{1}{x}\left(\ln\left(1+x\right)-x\right)-4PLog(x)\right)$

$$U\left(\frac{2\varepsilon}{m_e c^2},\gamma\right)=\frac{1}{2\pi i}\int\limits_{\frac{1}{2}-i\infty}^{\frac{1}{2}+i\infty}\Sigma\left(z\right)\left[\left(\frac{2\varepsilon}{m_e c^2}\right)^{-z}\Pi\left(\gamma,z\right)\right]dz,$$

$$\Pi\left(\gamma,z\right)=\frac{\gamma}{\left(\gamma^{2}-1\right)^{\frac{3}{2}}}\left[\begin{array}{c}\frac{1}{2-z}\left(\left(\gamma+\sqrt{\gamma^{2}-1}\right)^{2-z}+\left(\frac{1}{\gamma+\sqrt{\gamma^{2}-1}}\right)^{2-z}-2\left(\frac{1}{\gamma}\right)^{2-z}\right)\\ -\frac{1}{1-z}\frac{1}{\gamma}\left(\left(\gamma+\sqrt{\gamma^{2}-1}\right)^{1-z}+\left(\frac{1}{\gamma+\sqrt{\gamma^{2}-1}}\right)^{1-z}-2\left(\frac{1}{\gamma}\right)^{1-z}\right)\end{array}\right]$$

$$U\left(\frac{2\varepsilon}{m_{e}c^{2}},\gamma\right)=\frac{\gamma}{\left(\gamma^{2}-1\right)^{\frac{3}{2}}\left(\frac{2\varepsilon}{m_{e}c^{2}}\right)^{2}}\left[\begin{array}{c}f_{2}\left(\frac{2\varepsilon}{m_{e}c^{2}}\left(\gamma+\sqrt{\gamma^{2}-1}\right)\right)+f_{2}\left(\frac{\frac{2\varepsilon}{m_{e}c^{2}}}{\gamma+\sqrt{\gamma^{2}-1}}\right)-\\ 2f_{2}\left(\frac{2\varepsilon}{\gamma m_{e}c^{2}}\right)-\left(\frac{2\varepsilon}{\gamma m_{e}c^{2}}\right)\left[f_{1}\left(\frac{2\varepsilon}{m_{e}c^{2}}\left(\gamma+\sqrt{\gamma^{2}-1}\right)\right)\right.\\ \left.+f_{1}\left(\frac{\frac{2\varepsilon}{m_{e}c^{2}}}{\gamma+\sqrt{\gamma^{2}-1}}\right)-2f_{1}\left(\frac{2\varepsilon}{\gamma m_{e}c^{2}}\right)\right]\end{array}\right].$$

APPENDIX D

Derivation of Particle Tracking Equations

We begin with the generalized momentum of the particle, Eq 2.23

$$p_0 = \frac{ma^2 v}{\sqrt{1 - \frac{a^2}{c^2} v^2}} = \text{const}$$

which allows the determination of the particle's speed as a function of time

$$\upsilon(t) = \frac{c}{a\,(t)} \frac{\left(\frac{p_0}{mca(t)}\right)}{\sqrt{1 + \left(\frac{p_0}{mca(t)}\right)^2}}.$$

Rewriting the equation of motion (2.22) as

$$\frac{d}{dt}\left(p_0 \frac{1}{\upsilon} \frac{d\vec{r}}{dt}\right) = e\left[\frac{1}{\upsilon}\frac{d\vec{r}}{dt} \times \upsilon a^2 \vec{B}\right] \tag{D.1}$$

Introducing the following definitions

$\vec{\beta} = \frac{\vec{B}}{\left|\vec{B}\right|}$; $\left(\vec{\beta} \cdot \vec{\beta}\right) = 1$, unit vector in the direction of $\vec{B}$ and

$\vec{\nu} = \frac{1}{\upsilon}\frac{d\vec{r}}{dt}$; $(\vec{\nu} \cdot \vec{\nu}) = 1$, unit vector in the direction of $\vec{v}$.

then we have for equation D.1

$$\frac{d}{dt}(\vec{\nu}) = \frac{ea^2 \left|\vec{B}\right| \upsilon}{p_0}\left[\vec{\nu} \times \vec{\beta}\right] = \vec{\omega}(t)\left[\vec{\nu} \times \vec{\beta}\right]$$

where we have defined an angular frequency by

$$\omega(t) = \frac{ea^2\left|\vec{B}\right|}{p_0}\upsilon\left(t\right) = \frac{e\sqrt{\left(\vec{B}_0,\vec{B}_0\right)}}{p_0}\upsilon\left(t\right)$$

$$\phi(t) = \int_{t_e}^{t}\omega(t)dt = \frac{e\sqrt{\left(\vec{B}_0,\vec{B}_0\right)}}{p_0}\int_{t_e}^{t}\upsilon\left(t\right)dt = \varkappa_0 l\left(t,t_e\right)$$

where $\varkappa_0 = e\sqrt{\left(\vec{B}_0\cdot\vec{B}_0\right)}/p_0$, and $l\left(t,t_e\right) = \int_{t_e}^{t}\upsilon\left(t\right)dt$ is the propagation track length in the comoving reference frame.

Then we can write

$$\frac{d}{d\phi}\left(\vec{\nu}\right) = \left[\vec{\nu}\times\vec{\beta}\right]$$

with solution

$$\vec{\nu}\left(t\right) = \left(\vec{\nu}\left(t_e\right) - \left(\vec{\nu}\left(t_e\right)\cdot\vec{\beta}\right)\vec{\beta}\right)\cos\left(\phi(t)\right) + \left[\vec{\nu}\left(t_e\right)\times\vec{\beta}\right]\sin\left(\phi(t)\right) + \left(\vec{\nu}\left(t_e\right)\cdot\vec{\beta}\right)\vec{\beta}.$$

This solution gives a comoving velocity of

$$\begin{aligned}\frac{d\vec{r}}{dt} &= \upsilon\left(t\right)\cos\left(\phi(t)\right)\left(\vec{\nu}\left(t_e\right) - \left(\vec{\nu}\left(t_e\right)\cdot\vec{\beta}\right)\vec{\beta}\right) + \\ &\quad \upsilon\left(t\right)\sin\left(\phi(t)\right)\left[\vec{\nu}\left(t_e\right)\times\vec{\beta}\right] + \upsilon\left(t\right)\left(\vec{\nu}\left(t_e\right)\cdot\vec{\beta}\right)\vec{\beta}\end{aligned} \tag{D.2}$$

and comoving position

$$\begin{aligned}\vec{r}\left(t\right) = \vec{r}\left(t_e\right) &+ \int_{t_e}^{t}\upsilon\left(t\right)\cos\left(\phi(t)\right)dt\left(\vec{\nu}\left(t_e\right) - \left(\vec{\nu}\left(t_e\right)\cdot\vec{\beta}\right)\vec{\beta}\right) + \\ &\int_{t_e}^{t}\upsilon\left(t\right)\sin\left(\phi(t)\right)dt\left[\vec{\nu}\left(t_e\right)\times\vec{\beta}\right] + \int_{t_e}^{t}\upsilon\left(t\right)dt\left(\vec{\nu}\left(t_e\right)\cdot\vec{\beta}\right)\vec{\beta}.\end{aligned}$$

Since $\int_{t_e}^{t}\upsilon\left(t\right)\sin\left(\phi(t)\right)dt = \int_0^l dl\sin\left(\varkappa_0 l\right)$ and $\int_{t_e}^{t}\upsilon\left(t\right)\cos\left(\phi(t)\right)dt = \int_0^l dl\cos\left(\varkappa_0 l\right)$,

we have that

$$\vec{r}\,(t) = \vec{r}\,(t_e) + \frac{\sin\left(\varkappa_0 l\right)}{\varkappa_0}\left(\vec{\nu}\,(t_e) - \left(\vec{\nu}\,(t_e)\cdot\vec{\beta}\right)\vec{\beta}\right) - \frac{\left(1-\cos\left(\varkappa_0 l\right)\right)}{\varkappa_0}\left[\vec{\nu}\,(t_e)\times\vec{\beta}\right] + l\left(\vec{\nu}\,(t_e)\cdot\vec{\beta}\right)\vec{\beta}$$

$$\Delta\vec{r} = \vec{r}\,(t) - \vec{r}(t_e) = \vec{\nu}(t_e)l + \left(\vec{\nu}(t_e) - \left(\vec{\nu}(t_e)\cdot\vec{\beta}\right)\vec{\beta}\right)\left[\frac{\sin(\varkappa_0 l) - \varkappa_0 l}{\varkappa_0}\right] + \left(\vec{\nu}(t_e)\times\vec{\beta}\right)\left[\frac{1-\cos(\varkappa_0 l)}{\varkappa_0}\right]$$

Hence, the propagated track length is

$$l = \int_{t_e}^{t} \upsilon\,(t)\,dt = \int_{t_e}^{t} \frac{c}{a\,(t)} \frac{\left(\frac{p_0}{mca(t)}\right)}{\sqrt{1+\left(\frac{p_0}{mca(t)}\right)^2}} dt = \frac{p_0}{m}\int_{t_e}^{t} \frac{(1+z)^2}{\sqrt{1+\left(\frac{p_0}{mc}\right)^2(1+z)^2}} \frac{dt}{dz} dz$$

And since

$$\frac{dt}{dz} = -\frac{1}{H_0}\frac{1}{1+z}\frac{1}{Q\,(z)}$$

we have the final expression for the propagated track length in terms of redshift

$$l\,(z, z_e) = \frac{c}{H_0}\int_{z}^{z_e} \frac{(1+z)}{\sqrt{\left(\frac{mc}{p_0}\right)^2 + (1+z)^2}} \frac{1}{Q\,(z)} dz \Rightarrow$$

$$l\,(z, z_e) = R_H \int_{z}^{z_e} \frac{(1+z)}{\sqrt{(\frac{mc}{p_o})^2 + (1+z)^2}} \frac{dz}{Q(z)}. \tag{D.3}$$

References

[AAA06] J. Albert, E. Aliu, H. Anderhub, P. Antoranz, A. Armada, M. Asensio, C. Baixeras, J. A. Barrio, M. Bartelt, H. Bartko, D. Bastieri, S. R. Bavikadi, W. Bednarek, K. Berger, C. Bigongiari, A. Biland, E. Bisesi, R. K. Bock, T. Bretz, I. Britvitch, M. Camara, A. Chilingarian, S. Ciprini, J. A. Coarasa, S. Commichau, J. L. Contreras, J. Cortina, V. Curtef, V. Danielyan, F. Dazzi, A. De Angelis, R. de los Reyes, B. De Lotto, E. Domingo-Santamaría, D. Dorner, M. Doro, M. Errando, M. Fagiolini, D. Ferenc, E. Fernández, R. Firpo, J. Flix, M. V. Fonseca, L. Font, N. Galante, M. Garczarczyk, M. Gaug, M. Giller, F. Goebel, D. Hakobyan, M. Hayashida, T. Hengstebeck, D. Höhne, J. Hose, P. Jacon, O. Kalekin, D. Kranich, A. Laille, T. Lenisa, P. Liebing, E. Lindfors, F. Longo, J. López, M. López, E. Lorenz, F. Lucarelli, P. Majumdar, G. Maneva, K. Mannheim, M. Mariotti, M. Martínez, K. Mase, D. Mazin, M. Meucci, M. Meyer, J. M. Miranda, R. Mirzoyan, S. Mizobuchi, A. Moralejo, K. Nilsson, E. Oña-Wilhelmi, R. Orduña, N. Otte, I. Oya, D. Paneque, R. Paoletti, M. Pasanen, D. Pascoli, F. Pauss, N. Pavel, R. Pegna, M. Persic, L. Peruzzo, A. Piccioli, M. Poller, E. Prandini, W. Rhode, J. Rico, B. Riegel, M. Rissi, A. Robert, S. Rügamer, A. Saggion, A. Sánchez, P. Sartori, V. Scalzotto, R. Schmitt, T. Schweizer, M. Shayduk, K. Shinozaki, S. N. Shore, N. Sidro, A. Sillanpää, D. Sobczyńska, A. Stamerra, L. S. Stark, L. Takalo, P. Temnikov, D. Tescaro, M. Teshima, N. Tonello, A. Torres, D. F. Torres, N. Turini, H. Vankov, A. Vardanyan, V. Vitale, R. M. Wagner, T. Wibig, W. Wittek, and J. Zapatero. "Discovery of Very High Energy Gamma Rays from 1ES 1218+30.4." *ApJL*, **642**:L119–L122, May 2006.

[AAA09a] V. A. Acciari, E. Aliu, T. Arlen, M. Beilicke, W. Benbow, S. M. Bradbury, J. H. Buckley, V. Bugaev, Y. Butt, K. L. Byrum, O. Celik, A. Cesarini, L. Ciupik, Y. C. K. Chow, P. Cogan, P. Colin, W. Cui, M. K. Daniel, T. Ergin, A. D. Falcone, S. J. Fegan, J. P. Finley, P. Fortin, L. F. Fortson, A. Furniss, G. H. Gillanders, J. Grube, R. Guenette, G. Gyuk, D. Hanna, E. Hays, J. Holder, D. Horan, C. M. Hui, T. B. Humensky, A. Imran, P. Kaaret, N. Karlsson, M. Kertzman, D. B. Kieda, J. Kildea, A. Konopelko, H. Krawczynski, F. Krennrich, M. J. Lang, S. LeBohec, G. Maier, A. McCann, M. McCutcheon, P. Moriarty, R. Mukherjee, T. Nagai, J. Niemiec, R. A. Ong, D. Pandel, J. S. Perkins, M. Pohl, J. Quinn, K. Ragan, L. C. Reyes, P. T. Reynolds, H. J. Rose, M. Schroedter, G. H. Sembroski, A. W. Smith, D. Steele,

S. P. Swordy, J. A. Toner, L. Valcarcel, V. V. Vassiliev, R. Wagner, S. P. Wakely, J. E. Ward, T. C. Weekes, A. Weinstein, R. J. White, D. A. Williams, S. A. Wissel, M. Wood, and B. Zitzer. "VERITAS Observations of the BL Lac Object 1ES 1218+304." *ApJ*, **695**:1370–1375, April 2009.

[AAA09b] W. B. Atwood, A. A. Abdo, M. Ackermann, W. Althouse, B. Anderson, M. Axelsson, L. Baldini, J. Ballet, D. L. Band, G. Barbiellini, and et al. "The Large Area Telescope on the Fermi Gamma-Ray Space Telescope Mission." *ApJ*, **697**:1071–1102, June 2009.

[AAA10] V. A. Acciari, E. Aliu, T. Arlen, T. Aune, M. Bautista, M. Beilicke, W. Benbow, M. Böttcher, D. Boltuch, S. M. Bradbury, and et al. "The Discovery of γ-Ray Emission from the Blazar RGB J0710+591." *ApJL*, **715**:L49–L55, May 2010.

[AAA11] J. Aleksić, L. A. Antonelli, P. Antoranz, M. Backes, J. A. Barrio, D. Bastieri, J. Becerra González, W. Bednarek, A. Berdyugin, K. Berger, E. Bernardini, A. Biland, O. Blanch, R. K. Bock, A. Boller, G. Bonnoli, D. Borla Tridon, I. Braun, T. Bretz, A. Cañellas, E. Carmona, A. Carosi, P. Colin, E. Colombo, J. L. Contreras, J. Cortina, L. Cossio, S. Covino, F. Dazzi, A. De Angelis, E. De Cea del Pozo, B. De Lotto, C. Delgado Mendez, A. Diago Ortega, M. Doert, A. Domínguez, D. Dominis Prester, D. Dorner, M. Doro, D. Elsaesser, D. Ferenc, M. V. Fonseca, L. Font, C. Fruck, R. J. García López, M. Garczarczyk, D. Garrido, G. Giavitto, N. Godinović, D. Hadasch, D. Häfner, A. Herrero, D. Hildebrand, D. Höhne-Mönch, J. Hose, D. Hrupec, B. Huber, T. Jogler, S. Klepser, T. Krähenbühl, J. Krause, A. La Barbera, D. Lelas, E. Leonardo, E. Lindfors, S. Lombardi, M. López, E. Lorenz, M. Makariev, G. Maneva, N. Mankuzhiyil, K. Mannheim, L. Maraschi, M. Mariotti, M. Martínez, D. Mazin, M. Meucci, J. M. Miranda, R. Mirzoyan, H. Miyamoto, J. Moldón, A. Moralejo, D. Nieto, K. Nilsson, R. Orito, I. Oya, D. Paneque, R. Paoletti, S. Pardo, J. M. Paredes, S. Partini, M. Pasanen, F. Pauss, M. A. Perez-Torres, M. Persic, L. Peruzzo, M. Pilia, J. Pochon, F. Prada, P. G. Prada Moroni, E. Prandini, I. Puljak, I. Reichardt, R. Reinthal, W. Rhode, M. Ribó, J. Rico, S. Rügamer, A. Saggion, K. Saito, T. Y. Saito, M. Salvati, K. Satalecka, V. Scalzotto, V. Scapin, C. Schultz, T. Schweizer, M. Shayduk, S. N. Shore, A. Sillanpää, J. Sitarek, D. Sobczynska, F. Spanier, S. Spiro, A. Stamerra, B. Steinke, J. Storz, N. Strah, T. Surić, L. Takalo, F. Tavecchio, P. Temnikov, T. Terzić, D. Tescaro, M. Teshima, M. Thom, O. Ti-

bolla, D. F. Torres, A. Treves, H. Vankov, P. Vogler, R. M. Wagner, Q. Weitzel, V. Zabalza, F. Zandanel, R. Zanin, MAGIC Collaboration, Y. T. Tanaka, D. L. Wood, and S. Buson. "MAGIC Discovery of Very High Energy Emission from the FSRQ PKS 1222+21." *ApJL*, **730**:L8, March 2011.

[AAB06a] F. Aharonian, A. G. Akhperjanian, A. R. Bazer-Bachi, M. Beilicke, W. Benbow, D. Berge, K. Bernlöhr, C. Boisson, O. Bolz, V. Borrel, I. Braun, F. Breitling, A. M. Brown, R. Bühler, I. Büsching, S. Carrigan, P. M. Chadwick, L.-M. Chounet, R. Cornils, L. Costamante, B. Degrange, H. J. Dickinson, A. Djannati-Ataï, L. O'C. Drury, G. Dubus, K. Egberts, D. Emmanoulopoulos, P. Espigat, F. Feinstein, E. Ferrero, G. Fontaine, S. Funk, S. Funk, Y. A. Gallant, B. Giebels, J. F. Glicenstein, P. Goret, C. Hadjichristidis, D. Hauser, M. Hauser, G. Heinzelmann, G. Henri, G. Hermann, J. A. Hinton, W. Hofmann, M. Holleran, D. Horns, A. Jacholkowska, O. C. de Jager, B. Khélifi, N. Komin, A. Konopelko, I. J. Latham, R. Le Gallou, A. Lemière, M. Lemoine-Goumard, T. Lohse, J. M. Martin, O. Martineau-Huynh, A. Marcowith, C. Masterson, T. J. L. McComb, M. de Naurois, D. Nedbal, S. J. Nolan, A. Noutsos, K. J. Orford, J. L. Osborne, M. Ouchrif, M. Panter, G. Pelletier, S. Pita, G. Pühlhofer, M. Punch, B. C. Raubenheimer, M. Raue, S. M. Rayner, A. Reimer, O. Reimer, J. Ripken, L. Rob, L. Rolland, G. Rowell, V. Sahakian, L. Saugé, S. Schlenker, R. Schlickeiser, U. Schwanke, H. Sol, D. Spangler, F. Spanier, R. Steenkamp, C. Stegmann, G. Superina, J.-P. Tavernet, R. Terrier, C. G. Théoret, M. Tluczykont, C. van Eldik, G. Vasileiadis, C. Venter, P. Vincent, H. J. Völk, S. J. Wagner, and M. Ward. "Discovery of very high energy γ-ray emission from the BL Lacertae object H 2356-309 with the HESS Cherenkov telescopes." *A&A*, **455**:461–466, August 2006.

[AAB06b] F. Aharonian, A. G. Akhperjanian, A. R. Bazer-Bachi, M. Beilicke, W. Benbow, D. Berge, K. Bernlöhr, C. Boisson, O. Bolz, V. Borrel, I. Braun, F. Breitling, A. M. Brown, P. M. Chadwick, L.-M. Chounet, R. Cornils, L. Costamante, B. Degrange, H. J. Dickinson, A. Djannati-Ataï, L. O. Drury, G. Dubus, D. Emmanoulopoulos, P. Espigat, F. Feinstein, G. Fontaine, Y. Fuchs, S. Funk, Y. A. Gallant, B. Giebels, S. Gillessen, J. F. Glicenstein, P. Goret, C. Hadjichristidis, D. Hauser, M. Hauser, G. Heinzelmann, G. Henri, G. Hermann, J. A. Hinton, W. Hofmann, M. Holleran, D. Horns, A. Jacholkowska, O. C. de Jager, B. Khélifi, S. Klages, N. Komin, A. Konopelko, I. J. Latham, R. Le Gallou, A. Lemière, M. Lemoine-Goumard, N. Leroy, T. Lohse,

J. M. Martin, O. Martineau-Huynh, A. Marcowith, C. Masterson, T. J. L. McComb, M. de Naurois, S. J. Nolan, A. Noutsos, K. J. Orford, J. L. Osborne, M. Ouchrif, M. Panter, G. Pelletier, S. Pita, G. Pühlhofer, M. Punch, B. C. Raubenheimer, M. Raue, J. Raux, S. M. Rayner, A. Reimer, O. Reimer, J. Ripken, L. Rob, L. Rolland, G. Rowell, V. Sahakian, L. Saugé, S. Schlenker, R. Schlickeiser, C. Schuster, U. Schwanke, M. Siewert, H. Sol, D. Spangler, R. Steenkamp, C. Stegmann, J.-P. Tavernet, R. Terrier, C. G. Théoret, M. Tluczykont, C. van Eldik, G. Vasileiadis, C. Venter, P. Vincent, H. J. Völk, and S. J. Wagner. "A low level of extragalactic background light as revealed by γ-rays from blazars." *Nature*, **440**:1018–1021, April 2006.

[AAB07a] F. Aharonian, A. G. Akhperjanian, U. Barres de Almeida, A. R. Bazer-Bachi, B. Behera, M. Beilicke, W. Benbow, K. Bernlöhr, C. Boisson, O. Bolz, V. Borrel, I. Braun, E. Brion, A. M. Brown, R. Bühler, T. Bulik, I. Büsching, T. Boutelier, S. Carrigan, P. M. Chadwick, L.-M. Chounet, A. C. Clapson, G. Coignet, R. Cornils, L. Costamante, M. Dalton, B. Degrange, H. J. Dickinson, A. Djannati-Ataï, W. Domainko, L. O'C. Drury, F. Dubois, G. Dubus, J. Dyks, K. Egberts, D. Emmanoulopoulos, P. Espigat, C. Farnier, F. Feinstein, A. Fiasson, A. Förster, G. Fontaine, S. Funk, M. Füßling, Y. A. Gallant, B. Giebels, J. F. Glicenstein, B. Glück, P. Goret, C. Hadjichristidis, D. Hauser, M. Hauser, G. Heinzelmann, G. Henri, G. Hermann, J. A. Hinton, A. Hoffmann, W. Hofmann, M. Holleran, S. Hoppe, D. Horns, A. Jacholkowska, O. C. de Jager, I. Jung, K. Katarzyński, E. Kendziorra, M. Kerschhaggl, B. Khélifi, D. Keogh, N. Komin, K. Kosack, G. Lamanna, I. J. Latham, A. Lemière, M. Lemoine-Goumard, J.-P. Lenain, T. Lohse, J. M. Martin, O. Martineau-Huynh, A. Marcowith, C. Masterson, D. Maurin, G. Maurin, T. J. L. McComb, R. Moderski, E. Moulin, M. de Naurois, D. Nedbal, S. J. Nolan, S. Ohm, J.-P. Olive, E. de Oña Wilhelmi, K. J. Orford, J. L. Osborne, M. Ostrowski, M. Panter, G. Pedaletti, G. Pelletier, P.-O. Petrucci, S. Pita, G. Pühlhofer, M. Punch, S. Ranchon, B. C. Raubenheimer, M. Raue, S. M. Rayner, M. Renaud, J. Ripken, L. Rob, L. Rolland, S. Rosier-Lees, G. Rowell, B. Rudak, J. Ruppel, V. Sahakian, A. Santangelo, R. Schlickeiser, F. Schöck, R. Schröder, U. Schwanke, S. Schwarzburg, S. Schwemmer, A. Shalchi, H. Sol, D. Spangler, Ł. Stawarz, R. Steenkamp, C. Stegmann, G. Superina, P. H. Tam, J.-P. Tavernet, R. Terrier, C. van Eldik, G. Vasileiadis, C. Venter, J. P. Vialle, P. Vincent, M. Vivier, H. J. Völk, F. Volpe, S. J. Wag-

ner, M. Ward, A. A. Zdziarski, and A. Zech. "New constraints on the mid-IR EBL from the HESS discovery of VHE γ-rays from 1ES 0229+200." *A&A*, **475**:L9–L13, November 2007.

[AAB07b] F. Aharonian, A. G. Akhperjanian, U. Barres de Almeida, A. R. Bazer-Bachi, B. Behera, M. Beilicke, W. Benbow, K. Bernlöhr, C. Boisson, O. Bolz, V. Borrel, I. Braun, E. Brion, A. M. Brown, R. Bühler, T. Bulik, I. Büsching, T. Boutelier, S. Carrigan, P. M. Chadwick, L.-M. Chounet, A. C. Clapson, G. Coignet, R. Cornils, L. Costamante, M. Dalton, B. Degrange, H. J. Dickinson, A. Djannati-Ataï, W. Domainko, L. O'C. Drury, F. Dubois, G. Dubus, J. Dyks, K. Egberts, D. Emmanoulopoulos, P. Espigat, C. Farnier, F. Feinstein, A. Fiasson, A. Förster, G. Fontaine, S. Funk, M. Füßling, Y. A. Gallant, B. Giebels, J. F. Glicenstein, B. Glück, P. Goret, C. Hadjichristidis, D. Hauser, M. Hauser, G. Heinzelmann, G. Henri, G. Hermann, J. A. Hinton, A. Hoffmann, W. Hofmann, M. Holleran, S. Hoppe, D. Horns, A. Jacholkowska, O. C. de Jager, I. Jung, K. Katarzyński, E. Kendziorra, M. Kerschhaggl, B. Khélifi, D. Keogh, N. Komin, K. Kosack, G. Lamanna, I. J. Latham, A. Lemière, M. Lemoine-Goumard, J.-P. Lenain, T. Lohse, J. M. Martin, O. Martineau-Huynh, A. Marcowith, C. Masterson, D. Maurin, G. Maurin, T. J. L. McComb, R. Moderski, E. Moulin, M. de Naurois, D. Nedbal, S. J. Nolan, S. Ohm, J.-P. Olive, E. de Oña Wilhelmi, K. J. Orford, J. L. Osborne, M. Ostrowski, M. Panter, G. Pedaletti, G. Pelletier, P.-O. Petrucci, S. Pita, G. Pühlhofer, M. Punch, S. Ranchon, B. C. Raubenheimer, M. Raue, S. M. Rayner, M. Renaud, J. Ripken, L. Rob, L. Rolland, S. Rosier-Lees, G. Rowell, B. Rudak, J. Ruppel, V. Sahakian, A. Santangelo, R. Schlickeiser, F. Schöck, R. Schröder, U. Schwanke, S. Schwarzburg, S. Schwemmer, A. Shalchi, H. Sol, D. Spangler, Ł. Stawarz, R. Steenkamp, C. Stegmann, G. Superina, P. H. Tam, J.-P. Tavernet, R. Terrier, C. van Eldik, G. Vasileiadis, C. Venter, J. P. Vialle, P. Vincent, M. Vivier, H. J. Völk, F. Volpe, S. J. Wagner, M. Ward, A. A. Zdziarski, and A. Zech. "Discovery of VHE γ-rays from the distant BL Lacertae 1ES 0347-121." *A&A*, **473**:L25–L28, October 2007.

[AAB07c] F. Aharonian, A. G. Akhperjanian, A. R. Bazer-Bachi, B. Behera, M. Beilicke, W. Benbow, D. Berge, K. Bernlöhr, C. Boisson, O. Bolz, V. Borrel, T. Boutelier, I. Braun, E. Brion, A. M. Brown, R. Bühler, I. Büsching, T. Bulik, S. Carrigan, P. M. Chadwick, A. C. Clapson, L.-M. Chounet, G. Coignet, R. Cornils, L. Costamante, B. Degrange, H. J. Dickinson, A. Djannati-Ataï, W. Domainko, L. O.

Drury, G. Dubus, J. Dyks, K. Egberts, D. Emmanoulopoulos, P. Espigat, C. Farnier, F. Feinstein, A. Fiasson, A. Förster, G. Fontaine, S. Funk, S. Funk, M. Füßling, Y. A. Gallant, B. Giebels, J. F. Glicenstein, B. Glück, P. Goret, C. Hadjichristidis, D. Hauser, M. Hauser, G. Heinzelmann, G. Henri, G. Hermann, J. A. Hinton, A. Hoffmann, W. Hofmann, M. Holleran, S. Hoppe, D. Horns, A. Jacholkowska, O. C. de Jager, E. Kendziorra, M. Kerschhaggl, B. Khélifi, N. Komin, K. Kosack, G. Lamanna, I. J. Latham, R. Le Gallou, A. Lemière, M. Lemoine-Goumard, J.-P. Lenain, T. Lohse, J. M. Martin, O. Martineau-Huynh, A. Marcowith, C. Masterson, G. Maurin, T. J. L. McComb, R. Moderski, E. Moulin, M. de Naurois, D. Nedbal, S. J. Nolan, J.-P. Olive, K. J. Orford, J. L. Osborne, M. Ostrowski, M. Panter, G. Pedaletti, G. Pelletier, P.-O. Petrucci, S. Pita, G. Pühlhofer, M. Punch, S. Ranchon, B. C. Raubenheimer, M. Raue, S. M. Rayner, M. Renaud, J. Ripken, L. Rob, L. Rolland, S. Rosier-Lees, G. Rowell, B. Rudak, J. Ruppel, V. Sahakian, A. Santangelo, L. Saugé, S. Schlenker, R. Schlickeiser, R. Schröder, U. Schwanke, S. Schwarzburg, S. Schwemmer, A. Shalchi, H. Sol, D. Spangler, Ł. Stawarz, R. Steenkamp, C. Stegmann, G. Superina, P. H. Tam, J.-P. Tavernet, R. Terrier, C. van Eldik, G. Vasileiadis, C. Venter, J. P. Vialle, P. Vincent, M. Vivier, H. J. Völk, F. Volpe, S. J. Wagner, M. Ward, and A. A. Zdziarski. "An Exceptional Very High Energy Gamma-Ray Flare of PKS 2155-304." *ApJL*, **664**:L71–L74, August 2007.

[AAB07d] F. Aharonian, A. G. Akhperjanian, A. R. Bazer-Bachi, M. Beilicke, W. Benbow, D. Berge, K. Bernlöhr, C. Boisson, O. Bolz, V. Borrel, I. Braun, E. Brion, A. M. Brown, R. Bühler, I. Büsching, T. Boutelier, S. Carrigan, P. M. Chadwick, L.-M. Chounet, G. Coignet, R. Cornils, L. Costamante, B. Degrange, H. J. Dickinson, A. Djannati-Ataï, L. O'C. Drury, G. Dubus, K. Egberts, D. Emmanoulopoulos, P. Espigat, C. Farnier, F. Feinstein, E. Ferrero, A. Fiasson, G. Fontaine, S. Funk, S. Funk, M. Füßling, Y. A. Gallant, B. Giebels, J. F. Glicenstein, B. Glück, P. Goret, C. Hadjichristidis, D. Hauser, M. Hauser, G. Heinzelmann, G. Henri, G. Hermann, J. A. Hinton, A. Hoffmann, W. Hofmann, M. Holleran, S. Hoppe, D. Horns, A. Jacholkowska, O. C. de Jager, E. Kendziorra, M. Kerschhaggl, B. Khélifi, N. Komin, K. Kosack, G. Lamanna, I. J. Latham, R. Le Gallou, A. Lemière, M. Lemoine-Goumard, T. Lohse, J. M. Martin, O. Martineau-Huynh, A. Marcowith, C. Masterson, G. Maurin, T. J. L. McComb, E. Moulin, M. de Naurois, D. Nedbal, S. J. Nolan, A. Noutsos, J.-P. Olive, K. J.

Orford, J. L. Osborne, M. Panter, G. Pelletier, P.-O. Petrucci, S. Pita, G. Pühlhofer, M. Punch, S. Ranchon, B. C. Raubenheimer, M. Raue, S. M. Rayner, J. Ripken, L. Rob, L. Rolland, S. Rosier-Lees, G. Rowell, V. Sahakian, A. Santangelo, L. Saugé, S. Schlenker, R. Schlickeiser, R. Schröder, U. Schwanke, S. Schwarzburg, S. Schwemmer, A. Shalchi, H. Sol, D. Spangler, F. Spanier, R. Steenkamp, C. Stegmann, G. Superina, P. H. Tam, J.-P. Tavernet, R. Terrier, M. Tluczykont, C. van Eldik, G. Vasileiadis, C. Venter, J. P. Vialle, P. Vincent, H. J. Völk, S. J. Wagner, and M. Ward. "Detection of VHE gamma-ray emission from the distant blazar 1ES 1101-232 with HESS and broadband characterisation." *A&A*, **470**:475–489, August 2007.

[AAB08] F. Aharonian, A. G. Akhperjanian, U. Barres de Almeida, A. R. Bazer-Bachi, B. Behera, M. Beilicke, W. Benbow, K. Bernlöhr, C. Boisson, V. Borrel, I. Braun, E. Brion, J. Brucker, R. Bühler, T. Bulik, I. Büsching, T. Boutelier, S. Carrigan, P. M. Chadwick, R. C. G. Chaves, L.-M. Chounet, A. C. Clapson, G. Coignet, R. Cornils, L. Costamante, M. Dalton, B. Degrange, H. J. Dickinson, A. Djannati-Ataï, W. Domainko, L. O'C. Drury, F. Dubois, G. Dubus, J. Dyks, K. Egberts, D. Emmanoulopoulos, P. Espigat, C. Farnier, F. Feinstein, A. Fiasson, A. Förster, G. Fontaine, M. Füßling, S. Gabici, Y. A. Gallant, B. Giebels, J.-F. Glicenstein, B. Glück, P. Goret, C. Hadjichristidis, D. Hauser, M. Hauser, G. Heinzelmann, G. Henri, G. Hermann, J. A. Hinton, A. Hoffmann, W. Hofmann, M. Holleran, S. Hoppe, D. Horns, A. Jacholkowska, O. C. de Jager, I. Jung, K. Katarzyński, S. Kaufmann, E. Kendziorra, M. Kerschhaggl, D. Khangulyan, B. Khélifi, D. Keogh, N. Komin, K. Kosack, G. Lamanna, I. J. Latham, J.-P. Lenain, T. Lohse, J.-M. Martin, O. Martineau-Huynh, A. Marcowith, C. Masterson, D. Maurin, T. J. L. McComb, R. Moderski, E. Moulin, M. Naumann-Godo, M. de Naurois, D. Nedbal, D. Nekrassov, S. J. Nolan, S. Ohm, J.-P. Olive, E. de Oña Wilhelmi, K. J. Orford, J. L. Osborne, M. Ostrowski, M. Panter, G. Pedaletti, G. Pelletier, P.-O. Petrucci, S. Pita, G. Pühlhofer, M. Punch, A. Quirrenbach, B. C. Raubenheimer, M. Raue, S. M. Rayner, M. Renaud, F. Rieger, J. Ripken, L. Rob, S. Rosier-Lees, G. Rowell, B. Rudak, J. Ruppel, V. Sahakian, A. Santangelo, R. Schlickeiser, F. M. Schöck, R. Schröder, U. Schwanke, S. Schwarzburg, S. Schwemmer, A. Shalchi, H. Sol, D. Spangler, Ł. Stawarz, R. Steenkamp, C. Stegmann, G. Superina, P. H. Tam, J.-P. Tavernet, R. Terrier, C. van Eldik, G. Vasileiadis, C. Venter, J.-P. Vialle, P. Vincent, M. Vivier, H. J. Völk, F. Volpe,

S. J. Wagner, M. Ward, A. A. Zdziarski, and A. Zech. "Discovery of VHE γ-rays from the high-frequency-peaked BL Lacertae object RGB J0152+017." *A&A*, **481**:L103–L107, April 2008.

[AAB10] V. A. Acciari, E. Aliu, M. Beilicke, W. Benbow, D. Boltuch, M. Böttcher, S. M. Bradbury, V. Bugaev, K. Byrum, A. Cesarini, L. Ciupik, P. Cogan, W. Cui, R. Dickherber, C. Duke, A. Falcone, J. P. Finley, G. Finnegan, L. Fortson, A. Furniss, N. Galante, D. Gall, K. Gibbs, R. Guenette, G. H. Gillanders, S. Godambe, J. Grube, D. Hanna, C. M. Hui, T. B. Humensky, A. Imran, P. Kaaret, N. Karlsson, M. Kertzman, D. Kieda, H. Krawczynski, F. Krennrich, M. J. Lang, S. LeBohec, G. Maier, S. McArthur, A. McCann, P. Moriarty, T. Nagai, R. A. Ong, A. N. Otte, D. Pandel, J. S. Perkins, A. Pichel, M. Pohl, J. Quinn, K. Ragan, L. C. Reyes, P. T. Reynolds, E. Roache, H. J. Rose, M. Schroedter, G. H. Sembroski, A. W. Smith, D. Steele, S. P. Swordy, M. Theiling, S. Thibadeau, V. V. Vassiliev, S. Vincent, S. P. Wakely, T. C. Weekes, A. Weinstein, T. Weisgarber, D. A. Williams, and VERITAS Collaboration. "Discovery of Variability in the Very High Energy γ-Ray Emission of 1ES 1218+304 with VERITAS." *ApJL*, **709**:L163–L167, February 2010.

[ABB07] W. B. Atwood, R. Bagagli, L. Baldini, R. Bellazzini, G. Barbiellini, F. Belli, T. Borden, A. Brez, M. Brigida, G. A. Caliandro, C. Cecchi, J. Cohen-Tanugi, A. de Angelis, P. Drell, C. Favuzzi, Y. Fukazawa, P. Fusco, F. Gargano, S. Germani, R. Giannitrapani, N. Giglietto, F. Giordano, T. Himel, M. Hirayama, R. P. Johnson, H. Katagiri, J. Kataoka, N. Kawai, W. Kroeger, M. Kuss, L. Latronico, F. Longo, F. Loparco, P. Lubrano, M. M. Massai, M. N. Mazziotta, M. Minuti, T. Mizuno, A. Morselli, D. Nelson, M. Nordby, T. Ohsugi, N. Omodei, M. Ozaki, M. Pepe, S. Rainò, R. Rando, M. Razzano, D. Rich, H. F.-W. Sadrozinski, G. Scolieri, C. Sgrò, G. Spandre, P. Spinelli, M. Sugizaki, H. Tajima, H. Takahashi, T. Takahashi, S. Yoshida, C. Young, and M. Ziegler. "Design and initial tests of the Tracker-converter of the Gamma-ray Large Area Space Telescope." *Astroparticle Physics*, **28**:422–434, December 2007.

[ACV94] F. A. Aharonian, P. S. Coppi, and H. J. Voelk. "Very high energy gamma rays from active galactic nuclei: Cascading on the cosmic background radiation fields and the formation of pair halos." *ApJL*, **423**:L5–L8, March 1994.

[Ahl11] M. Ahlers. "Gamma-ray halos as a measure of intergalactic magnetic

fields: A classical moment problem." *Phys. Rev. D*, **84**(6):063006, September 2011.

[AVW12] T. C. Arlen, V. V. Vassiliev, T. Weisgarber, S. P. Wakely, and S. Yusef Shafi. "Intergalactic Magnetic Fields and Gamma Ray Observations of Extreme TeV Blazars." *ArXiv e-prints*, October 2012.

[BBM96] G. Baym, D. Bödeker, and L. McLerran. "Magnetic fields produced by phase transition bubbles in the electroweak phase transition." *Phys. Rev. D*, **53**:662–667, January 1996.

[BCP12] A. E. Broderick, P. Chang, and C. Pfrommer. "The Cosmological Impact of Luminous TeV Blazars. I. Implications of Plasma Instabilities for the Intergalactic Magnetic Field and Extragalactic Gamma-Ray Background." *ApJ*, **752**:22, June 2012.

[BDB10] M. Béthermin, H. Dole, A. Beelen, and H. Aussel. "Spitzer deep and wide legacy mid- and far-infrared number counts and lower limits of cosmic infrared background." *A&A*, **512**:A78, March 2010.

[Ber08] K. Bernlöhr. "Simulation of imaging atmospheric Cherenkov telescopes with CORSIKA and sim_telarray." *Astroparticle Physics*, **30**:149–158, October 2008.

[BF99] E. G. Blackman and G. B. Field. "Resolution of an Ambiguity in Dynamo Theory and Its Consequences for Back-Reaction Studies." *ApJ*, **521**:597–601, August 1999.

[Bit04] J. A. Bittencourt. *Fundamentals of Plasma Physics*. Springer-Verlag, 2004.

[BML08] M. L. Bernet, F. Miniati, S. J. Lilly, P. P. Kronberg, and M. Dessauges-Zavadsky. "Strong magnetic fields in normal galaxies at high redshift." *Nature*, **454**:302–304, July 2008.

[BML10] S. Berta, B. Magnelli, D. Lutz, B. Altieri, H. Aussel, P. Andreani, O. Bauer, A. Bongiovanni, A. Cava, J. Cepa, A. Cimatti, E. Daddi, H. Dominguez, D. Elbaz, H. Feuchtgruber, N. M. Förster Schreiber, R. Genzel, C. Gruppioni, R. Katterloher, G. Magdis, R. Maiolino, R. Nordon, A. M. Pérez García, A. Poglitsch, P. Popesso, F. Pozzi, L. Riguccini, G. Rodighiero, A. Saintonge, P. Santini, M. Sanchez-Portal, L. Shao, E. Sturm, L. J. Tacconi, I. Valtchanov, M. Wetzstein, and E. Wieprecht. "Dissecting the cosmic infra-red background with Herschel/PEP." *A&A*, **518**:L30, July 2010.

[BS05] A. Brandenburg and K. Subramanian. "Astrophysical magnetic fields and nonlinear dynamo theory." *Phys. Rep.*, **417**:1–209, October 2005.

[CO94] B. Cheng and A. V. Olinto. "Primordial magnetic fields generated in the quark-hadron transition." *Phys. Rev. D*, **50**:2421–2424, August 1994.

[COS96] B. Cheng, A. V. Olinto, D. N. Schramm, and J. W. Truran. "Constraints on the strength of primordial magnetic fields from big bang nucleosynthesis reexamined." *Phys. Rev. D*, **54**:4714–4718, October 1996.

[CST94] B. Cheng, D. N. Schramm, and J. W. Truran. "Constraints on the strength of a primordial magnetic field from big bang nucleosynthesis." *Phys. Rev. D*, **49**:5006–5018, May 1994.

[CT02] C. L. Carilli and G. B. Taylor. "Cluster Magnetic Fields." *ARAA*, **40**:319–348, 2002.

[DC57] J.E. Davies and E.S. Cotton. "Design of the quartermaster solar furnace." *Solar Energy*, **1**(23):16 – 22, 1957. The Proceedings of the Solar Furnace Symposium.

[DCR11] C. D. Dermer, M. Cavadini, S. Razzaque, J. D. Finke, J. Chiang, and B. Lott. "Time Delay of Cascade Radiation for TeV Blazars and the Measurement of the Intergalactic Magnetic Field." *ApJL*, **733**:L21, June 2011.

[DKO09] K. Dolag, M. Kachelrieß, S. Ostapchenko, and R. Tomàs. "Blazar Halos as Probe for Extragalactic Magnetic Fields and Maximal Acceleration Energy." *ApJ*, **703**:1078–1085, September 2009.

[DKO11] K. Dolag, M. Kachelriess, S. Ostapchenko, and R. Tomàs. "Lower Limit on the Strength and Filling Factor of Extragalactic Magnetic Fields." *ApJL*, **727**:L4+, January 2011.

[DL90] R. A. Daly and A. Loeb. "A possible origin of galactic magnetic fields." *ApJ*, **364**:451–455, December 1990.

[DLP06] H. Dole, G. Lagache, J.-L. Puget, K. I. Caputi, N. Fernández-Conde, E. Le Floc'h, C. Papovich, P. G. Pérez-González, G. H. Rieke, and M. Blaylock. "The cosmic infrared background resolved by Spitzer. Contributions of mid-infrared galaxies to the far-infrared background." *A&A*, **451**:417–429, May 2006.

[DN13] R. Durrer and A. Neronov. "Cosmological Magnetic Fields: Their Generation, Evolution and Observation." *ArXiv e-prints*, March 2013.

[DPR11] A. Domínguez, J. R. Primack, D. J. Rosario, F. Prada, R. C. Gilmore, S. M. Faber, D. C. Koo, R. S. Somerville, M. A. Pérez-Torres, P. Pérez-González, J.-S. Huang, M. Davis, P. Guhathakurta, P. Barmby, C. J. Conselice, M. Lozano, J. A. Newman, and M. C. Cooper. "Extragalactic background light inferred from AEGIS galaxy-SED-type fractions." *MNRAS*, **410**:2556–2578, February 2011.

[EAK10] W. Essey, S. Ando, and A. Kusenko. "Determination of intergalactic magnetic fields from gamma ray data." *ArXiv e-prints*, December 2010.

[ECC02] D. Elbaz, C. J. Cesarsky, P. Chanial, H. Aussel, A. Franceschini, D. Fadda, and R. R. Chary. "The bulk of the cosmic infrared background resolved by ISOCAM." *A&A*, **384**:848–865, March 2002.

[EK10] W. Essey and A. Kusenko. "A new interpretation of the gamma-ray observations of distant active galactic nuclei." *Astroparticle Physics*, **33**:81–85, March 2010.

[Fer49] E. Fermi. "On the Origin of the Cosmic Radiation." *Physical Review*, **75**:1169–1174, April 1949.

[FHA04] G. G. Fazio, J. L. Hora, L. E. Allen, M. L. N. Ashby, P. Barmby, L. K. Deutsch, J.-S. Huang, S. Kleiner, M. Marengo, S. T. Megeath, G. J. Melnick, M. A. Pahre, B. M. Patten, J. Polizotti, H. A. Smith, R. S. Taylor, Z. Wang, S. P. Willner, W. F. Hoffmann, J. L. Pipher, W. J. Forrest, C. W. McMurty, C. R. McCreight, M. E. McKelvey, R. E. McMurray, D. G. Koch, S. H. Moseley, R. G. Arendt, J. E. Mentzell, C. T. Marx, P. Losch, P. Mayman, W. Eichhorn, D. Krebs, M. Jhabvala, D. Y. Gezari, D. J. Fixsen, J. Flores, K. Shakoorzadeh, R. Jungo, C. Hakun, L. Workman, G. Karpati, R. Kichak, R. Whitley, S. Mann, E. V. Tollestrup, P. Eisenhardt, D. Stern, V. Gorjian, B. Bhattacharya, S. Carey, B. O. Nelson, W. J. Glaccum, M. Lacy, P. J. Lowrance, S. Laine, W. T. Reach, J. A. Stauffer, J. A. Surace, G. Wilson, E. L. Wright, A. Hoffman, G. Domingo, and M. Cohen. "The Infrared Array Camera (IRAC) for the Spitzer Space Telescope." *ApJS*, **154**:10–17, September 2004.

[FL01] S. R. Furlanetto and A. Loeb. "Intergalactic Magnetic Fields from Quasar Outflows." *ApJ*, **556**:619–634, August 2001.

[FRV08] A. Franceschini, G. Rodighiero, and M. Vaccari. "Extragalactic optical-infrared background radiation, its time evolution and the cosmic photon-photon opacity." *A&A*, **487**:837–852, September 2008.

[FV05] S.J. Fegan and V.V. Vassiliev. "Optical Ray-Tracing for VERITAS." *VERITAS Collaboration Memo*, 2005.

[GR96] D. Grasso and H. R. Rubinstein. "Revisiting nucleosynthesis constraints on primordial magnetic fields." *Physics Letters B*, **379**:73–79, February 1996.

[GR01] D. Grasso and H. R. Rubinstein. "Magnetic fields in the early Universe." *Phys. Rep.*, **348**:163–266, July 2001.

[GS67] R. J. Gould and G. P. Schréder. "Opacity of the Universe to High-Energy Photons." *Physical Review*, **155**:1408–1411, March 1967.

[HK97] A. M. Howard and R. M. Kulsrud. "The Evolution of a Primordial Galactic Magnetic Field." *ApJ*, **483**:648, July 1997.

[Hog83] C. J. Hogan. "Nucleation of cosmological phase transitions." *Physics Letters B*, **133**:172–176, December 1983.

[HWA11] H. Huan, T. Weisgarber, T. Arlen, and S. P. Wakely. "A New Model for Gamma-Ray Cascades in Extragalactic Magnetic Fields." *ApJL*, **735**:L28+, July 2011.

[IIT08] K. Ichiki, S. Inoue, and K. Takahashi. "Probing the Nature of the Weakest Intergalactic Magnetic Fields with the High-Energy Emission of Gamma-Ray Bursts." *ApJ*, **682**:127–134, July 2008.

[ITO06] K. Ichiki, K. Takahashi, H. Ohno, H. Hanayama, and N. Sugiyama. "Cosmological Magnetic Field: A Fossil of Density Perturbations in the Early Universe." *Science*, **311**:827–829, February 2006.

[ITS07] K. Ichiki, K. Takahashi, N. Sugiyama, H. Hanayama, and H. Ohno. "Magnetic Field Spectrum at Cosmological Recombination." *ArXiv Astrophysics e-prints*, January 2007.

[JGP97] W.N. Johnson, J. E. Grove, B.F. Philips, J.P. Norris, and A. A. Moiseev. "A CsI(Tl) hodoscopic calorimeter for the GLAST mission." In *Nuclear Science Symposium, 1997. IEEE*, pp. 27–31 vol.1, 1997.

[JKO98] K. Jedamzik, V. Katalinić, and A. V. Olinto. "Damping of cosmic magnetic fields." *Phys. Rev. D*, **57**:3264–3284, March 1998.

[KD10] T. M. Kneiske and H. Dole. "A lower-limit flux for the extragalactic background light." *A&A*, **515**:A19, June 2010.

[KPZ92] P. P. Kronberg, J. J. Perry, and E. L. H. Zukowski. "Discovery of extended Faraday rotation compatible with spiral structure in an intervening galaxy at Z = 0.395 - New observations of PKS 1229 - 021." *ApJ*, **387**:528–535, March 1992.

[Kro94] P. P. Kronberg. "Mapping the Milky Way." *Nature*, **370**:179–180, July 1994.

[KSV96] P. J. Kernan, G. D. Starkman, and T. Vachaspati. "Big bang nucleosynthesis constraints on primordial magnetic fields." *Phys. Rev. D*, **54**:7207–7214, December 1996.

[KT90] E. W. Kolb and M. S. Turner. *The early universe.* Addison-Wesley, 1990.

[Kul05] R. M. Kulsrud. *Plasma physics for astrophysics.* Princeton University Press, 2005.

[KZ08] R. M. Kulsrud and E. G. Zweibel. "On the origin of cosmic magnetic fields." *Reports on Progress in Physics*, **71**(4):046901, April 2008.

[LM83] T.-P. Li and Y.-Q. Ma. "Analysis methods for results in gamma-ray astronomy." *ApJ*, **272**:317–324, September 1983.

[MAA08] MAGIC Collaboration, J. Albert, E. Aliu, H. Anderhub, L. A. Antonelli, P. Antoranz, M. Backes, C. Baixeras, J. A. Barrio, H. Bartko, D. Bastieri, J. K. Becker, W. Bednarek, K. Berger, E. Bernardini, C. Bigongiari, A. Biland, R. K. Bock, G. Bonnoli, P. Bordas, V. Bosch-Ramon, T. Bretz, I. Britvitch, M. Camara, E. Carmona, A. Chilingarian, S. Commichau, J. L. Contreras, J. Cortina, M. T. Costado, S. Covino, V. Curtef, F. Dazzi, A. De Angelis, E. D. Cea del Pozo, R. de los Reyes, B. De Lotto, M. De Maria, F. De Sabata, C. D. Mendez, A. Dominguez, D. Dorner, M. Doro, M. Errando, M. Fagiolini, D. Ferenc, E. Fernández, R. Firpo, M. V. Fonseca, L. Font, N. Galante, R. J. García López, M. Garczarczyk, M. Gaug, F. Goebel, M. Hayashida, A. Herrero, D. Höhne, J. Hose, C. C. Hsu, S. Huber, T. Jogler, T. M. Kneiske, D. Kranich, A. La Barbera, A. Laille, E. Leonardo, E. Lindfors, S. Lombardi, F. Longo, M. López, E. Lorenz, P. Majumdar, G. Maneva, N. Mankuzhiyil, K. Mannheim, L. Maraschi, M. Mariotti, M. Martínez, D. Mazin, M. Meucci, M. Meyer, J. M. Miranda, R. Mirzoyan, S. Mizobuchi,

M. Moles, A. Moralejo, D. Nieto, K. Nilsson, J. Ninkovic, N. Otte, I. Oya, M. Panniello, R. Paoletti, J. M. Paredes, M. Pasanen, D. Pascoli, F. Pauss, R. G. Pegna, M. A. Perez-Torres, M. Persic, L. Peruzzo, A. Piccioli, F. Prada, E. Prandini, N. Puchades, A. Raymers, W. Rhode, M. Ribó, J. Rico, M. Rissi, A. Robert, S. Rügamer, A. Saggion, T. Y. Saito, M. Salvati, M. Sanchez-Conde, P. Sartori, K. Satalecka, V. Scalzotto, V. Scapin, R. Schmitt, T. Schweizer, M. Shayduk, K. Shinozaki, S. N. Shore, N. Sidro, A. Sierpowska-Bartosik, A. Sillanpää, D. Sobczynska, F. Spanier, A. Stamerra, L. S. Stark, L. Takalo, F. Tavecchio, P. Temnikov, D. Tescaro, M. Teshima, M. Tluczykont, D. F. Torres, N. Turini, H. Vankov, A. Venturini, V. Vitale, R. M. Wagner, W. Wittek, V. Zabalza, F. Zandanel, R. Zanin, and J. Zapatero. "Very-High-Energy gamma rays from a Distant Quasar: How Transparent Is the Universe?" *Science*, **320**:1752–, June 2008.

[MDT12] K. Murase, C. D. Dermer, H. Takami, and G. Migliori. "Blazars as Ultra-high-energy Cosmic-ray Sources: Implications for TeV Gamma-Ray Observations." *ApJ*, **749**:63, April 2012.

[ME12] F. Miniati and A. Elyiv. "Relaxation of Blazar Induced Pair Beams in Cosmic Voids: Measurement of Magnetic Field in Voids and Thermal History of the IGM." *ArXiv e-prints*, August 2012.

[MHO07] A. A. Moiseev, R. C. Hartman, J. F. Ormes, D. J. Thompson, M. J. Amato, T. E. Johnson, K. N. Segal, and D. A. Sheppard. "The anti-coincidence detector for the GLAST large area telescope." *Astroparticle Physics*, **27**:339–358, June 2007.

[MP00] P. Madau and L. Pozzetti. "Deep galaxy counts, extragalactic background light and the stellar baryon budget." *MNRAS*, **312**:L9–L15, February 2000.

[MR07] D. Mazin and M. Raue. "New limits on the density of the extragalactic background light in the optical to the far infrared from the spectra of all known TeV blazars." *A&A*, **471**:439–452, August 2007.

[MSK11] S. Matsuura, M. Shirahata, M. Kawada, T. T. Takeuchi, D. Burgarella, D. L. Clements, W.-S. Jeong, H. Hanami, S. A. Khan, H. Matsuhara, T. Nakagawa, S. Oyabu, C. P. Pearson, A. Pollo, S. Serjeant, T. Takagi, and G. J. White. "Detection of the Cosmic Far-infrared Background in AKARI Deep Field South." *ApJ*, **737**:2, August 2011.

[MTI08] K. Murase, K. Takahashi, S. Inoue, K. Ichiki, and S. Nagataki. "Probing Intergalactic Magnetic Fields in the GLAST Era through Pair Echo Emission from TeV Blazars." *ApJL*, **686**:L67–L70, October 2008.

[NAA12] P. L. Nolan, A. A. Abdo, M. Ackermann, M. Ajello, A. Allafort, E. Antolini, W. B. Atwood, M. Axelsson, L. Baldini, J. Ballet, and et al. "Fermi Large Area Telescope Second Source Catalog." *ApJS*, **199**:31, April 2012.

[NS09] A. Neronov and D. V. Semikoz. "Sensitivity of γ-ray telescopes for detection of magnetic fields in the intergalactic medium." *Phys. Rev. D*, **80**(12):123012–+, December 2009.

[NSK10] A. Neronov, D. Semikoz, M. Kachelriess, S. Ostapchenko, and A. Elyiv. "Degree-scale GeV "Jets" from Active and Dead TeV Blazars." *ApJL*, **719**:L130–L133, August 2010.

[NV10] A. Neronov and I. Vovk. "Evidence for Strong Extragalactic Magnetic Fields from Fermi Observations of TeV Blazars." *Science*, **328**:73–, April 2010.

[Par70] E. N. Parker. "The Origin of Magnetic Fields." *ApJ*, **160**:383, May 1970.

[Par71] E. N. Parker. "The Generation of Magnetic Fields in Astrophysical Bodies. II. The Galactic Field." *ApJ*, **163**:255, January 1971.

[Par79] E. N. Parker. *Cosmical magnetic fields: Their origin and their activity*. Oxford University Press, 1979.

[PDE04] C. Papovich, H. Dole, E. Egami, E. Le Floc'h, P. G. Pérez-González, A. Alonso-Herrero, L. Bai, C. A. Beichman, M. Blaylock, C. W. Engelbracht, K. D. Gordon, D. C. Hines, K. A. Misselt, J. E. Morrison, J. Mould, J. Muzerolle, G. Neugebauer, P. L. Richards, G. H. Rieke, M. J. Rieke, J. R. Rigby, K. Y. L. Su, and E. T. Young. "The 24 Micron Source Counts in Deep Spitzer Space Telescope Surveys." *ApJS*, **154**:70–74, September 2004.

[PF11] Daniela Paoletti and Fabio Finelli. "CMB constraints on a stochastic background of primordial magnetic fields." *Phys. Rev. D*, **83**:123533, Jun 2011.

[Pla95] R. Plaga. "Detecting intergalactic magnetic fields using time delays in pulses of γ-rays." *Nature*, **374**:430–432, March 1995.

[PS95] M. E. Peskin and D. V. Schroeder. *An Introduction to Quantum Field Theory*. Westview Press, 1995.

[PV10] J. S. Perkins and VERITAS Collaboration. "Probing the Extragalactic Background Light with Very High Energy Blazars." In *AAS/High Energy Astrophysics Division #11*, volume 42 of *Bulletin of the American Astronomical Society*, p. 708, February 2010.

[QLS89] J. M. Quashnock, A. Loeb, and D. N. Spergel. "Magnetic field generation during the cosmological QCD phase transition." *ApJL*, **344**:L49–L51, September 1989.

[RIP08] E. Roache, R. Irvin, J. S. Perkins, and et al. "Mirror Facets for the VERITAS Telescopes." In *International Cosmic Ray Conference*, volume 3 of *International Cosmic Ray Conference*, pp. 1397–1400, 2008.

[RS68] M. J. Rees and G. Setti. "Model for the Evolution of Extended Radio Sources." *Nature*, **219**:127–131, July 1968.

[RSS88] A. A. Ruzmaikin, D. D. Sokolov, and A. M. Shukurov, editors. *Magnetic fields of galaxies*, volume 133 of *Astrophysics and Space Science Library*, 1988.

[Shu91] F. H. Shu. *Physics of Astrophysics, Vol. I.* University Science Books, 1991.

[SMS12] F. W. Stecker, M. A. Malkan, and S. T. Scully. "A Determination of the Intergalactic Redshift-dependent Ultraviolet-Optical-NIR Photon Density Using Deep Galaxy Survey Data and the Gamma-Ray Opacity of the Universe." *ApJ*, **761**:128, December 2012.

[SOJ97] G. Sigl, A. V. Olinto, and K. Jedamzik. "Primordial magnetic fields from cosmological first order phase transitions." *Phys. Rev. D*, **55**:4582–4590, April 1997.

[TBB11] The ARGO-YBJ Collaboration, B. Bartoli, P. Bernardini, X. J. Bi, C. Bleve, I. Bolognino, P. Branchini, A. Budano, A. K. Calabrese Melcarne, P. Camarri, Z. Cao, A. Cappa, R. Cardarelli, S. Catalanotti, C. Cattaneo, P. Celio, S. Z. Chen, T. L. Chen, Y. Chen, P. Creti, S. W. Cui, B. Z. Dai, G. D'Alí Staiti, Danzengluobu, M. Dattoli, I. De Mitri, B. D'Ettorre Piazzoli, T. Di Girolamo, X. H. Ding, G. Di Sciascio, C. F. Feng, Z. Feng, Z. Feng, F. Galeazzi, P. Galeotti, E. Giroletti,

Q. B. Gou, Y. Q. Guo, H. H. He, H. Hu, H. Hu, Q. Huang, M. Iacovacci, R. Iuppa, I. James, H. Y. Jia, Labaciren, H. J. Li, J. Y. Li, X. X. Li, G. Liguori, C. Liu, C. Q. Liu, J. Liu, M. Y. Liu, H. Lu, X. H. Ma, G. Mancarella, S. M. Mari, G. Marsella, D. Martello, S. Mastroianni, P. Montini, C. C. Ning, A. Pagliaro, M. Panareo, B. Panico, L. Perrone, P. Pistilli, X. B. Qu, E. Rossi, F. Ruggieri, P. Salvini, R. Santonico, P. R. Shen, X. D. Sheng, F. Shi, C. Stanescu, A. Surdo, Y. H. Tan, P. Vallania, S. Vernetto, C. Vigorito, B. Wang, H. Wang, C. Y. Wu, H. R. Wu, B. Xu, L. Xue, Y. X. Yan, Q. Y. Yang, X. C. Yang, Z. G. Yao, A. F. Yuan, M. Zha, H. M. Zhang, J. Zhang, J. Zhang, L. Zhang, P. Zhang, X. Y. Zhang, Y. Zhang, Zhaxiciren, Zhaxisangzhu, X. X. Zhou, F. R. Zhu, Q. Q. Zhu, and G. Zizzi. "Long-term monitoring of the TeV emission from Mrk 421 with the ARGO-YBJ experiment." *ArXiv e-prints*, June 2011.

[TBD95] D. J. Thompson, D. L. Bertsch, B. L. Dingus, J. A. Esposito, A. Etienne, C. E. Fichtel, D. P. Friedlander, R. C. Hartman, S. D. Hunter, D. J. Kendig, J. R. Mattox, L. M. McDonald, C. von Montigny, R. Mukherjee, P. V. Ramanamurthy, P. Sreekumar, J. M. Fierro, Y. C. Lin, P. F. Michelson, P. L. Nolan, S. K. Shriver, T. D. Willis, G. Kanbach, H. A. Mayer-Hasselwander, M. Merck, H.-D. Radecke, D. A. Kniffen, and E. J. Schneid. "The Second EGRET Catalog of High-Energy Gamma-Ray Sources." *ApJS*, **101**:259, December 1995.

[TGB11] F. Tavecchio, G. Ghisellini, G. Bonnoli, and L. Foschini. "Extreme TeV blazars and the intergalactic magnetic field." *MNRAS*, **414**:3566–3576, July 2011.

[TGF10] F. Tavecchio, G. Ghisellini, L. Foschini, G. Bonnoli, G. Ghirlanda, and P. Coppi. "The intergalactic magnetic field constrained by Fermi/Large Area Telescope observations of the TeV blazar 1ES0229+200." *MNRAS*, **406**:L70–L74, July 2010.

[TIO05] K. Takahashi, K. Ichiki, H. Ohno, and H. Hanayama. "Magnetic Field Generation from Cosmological Perturbations." *Physical Review Letters*, **95**(12):121301, September 2005.

[TMI12] K. Takahashi, M. Mori, K. Ichiki, and S. Inoue. "Lower Bounds on Intergalactic Magnetic Fields from Simultaneously Observed GeV-TeV Light Curves of the Blazar Mrk 501." *ApJL*, **744**:L7, January 2012.

[TMI13] K. Takahashi, M. Mori, K. Ichiki, S. Inoue, and H. Takami. "Robust Lower Bounds on Magnetic Fields in Intergalactic Voids from Long-

Term GeV-TeV Light Curves of the Blazar Mrk 421." *ArXiv e-prints*, March 2013.

[TVN11] A. M. Taylor, I. Vovk, and A. Neronov. "Extragalactic magnetic fields constraints from simultaneous GeV-TeV observations of blazars." *A&A*, **529**:A144, May 2011.

[Vac91] T. Vachaspati. "Magnetic fields from cosmological phase transitions." *Physics Letters B*, **265**:258–261, August 1991.

[Vas00] V. V. Vassiliev. "Extrgalactic background light absorption signal in the TeV gamma-ray spectra of blazars." *Astroparticle Physics*, **12**:217–238, January 2000.

[VB09] H. J. Völk and K. Bernlöhr. "Imaging very high energy gamma-ray telescopes." *Experimental Astronomy*, **25**:173–191, August 2009.

[VF05] V.V. Vassiliev and S.J. Fegan. "Event Reconstruction and Parameterization for VERITAS." *VERITAS Collaboration Memo*, 2005.

[VP13] T. M. Venters and V. Pavlidou. "Probing the intergalactic magnetic field with the anisotropy of the extragalactic gamma-ray background." *MNRAS*, **432**:3485–3494, July 2013.

[VR72] S. I. Vainshtein and A. A. Ruzmaikin. "Generation of the Large-Scale Galactic Magnetic Field. II." *Soviet Ast.*, **16**:365, October 1972.

[VTS12] I. Vovk, A. M. Taylor, D. Semikoz, and A. Neronov. "Fermi/LAT Observations of 1ES 0229+200: Implications for Extragalactic Magnetic Fields and Background Light." *ApJL*, **747**:L14, March 2012.

[Wid02] L. M. Widrow. "Origin of galactic and extragalactic magnetic fields." *Reviews of Modern Physics*, **74**:775–823, 2002.

[WRS12] L. M. Widrow, D. Ryu, D. R. G. Schleicher, K. Subramanian, C. G. Tsagas, and R. A. Treumann. "The First Magnetic Fields." *Space Sci. Rev.*, **166**:37–70, May 2012.